GENERAL ATOMIC

GA-A13868
UC-77

# GAS-COOLED FAST BREEDER REACTOR

## QUARTERLY PROGRESS REPORT
## FOR THE PERIOD FEBRUARY 1, 1976 THROUGH APRIL 30, 1976

by

Project Staff

Prepared under
Contract E(04-3)-167
Project Agreement No. 23
for the
San Francisco Operations Office
U.S. Energy Research and Development Administration



General Atomic Project 3228

Date Published: May 31, 1976

[redacted]

---

PROGRESS REPORT SERIES

| | |
|---|---|
| GA-5537 | November 1, 1963 through July 31, 1964 |
| GA-6667 | August 1, 1964 through July 31, 1965 |
| GA-7645 | August 1, 1965 through July 31, 1966 |
| GA-8107 | August 1, 1966 through July 31, 1967 |
| GA-8787 | August 1, 1967 through July 31, 1968 |
| GA-8895 | August 1, 1968 through October 31, 1968 |
| GA-9229 | November 1, 1968 through January 31, 1969 |
| GA-9359 | February 1, 1969 through April 30, 1969 |
| GA-9639 | May 1, 1969 through July 31, 1969 |
| GA-9811 | August 1, 1969 through October 31, 1969 |
| GA-9838 | November 1, 1969 through January 31, 1970 |
| GA-10517 | February 1, 1970 through January 31, 1971 |
| GA-10645 | February 1, 1971 through April 30, 1971 |
| GA-A10803 | May 1, 1971 through July 31, 1971 |
| GA-A10906 | August 1, 1971 through October 31, 1971 |
| GA-A12003 | November 1, 1971 through January 31, 1972 |
| GA-A12252 | May 1, 1972 through July 31, 1972 |
| GA-A12421 | August 1, 1972 through October 31, 1972 |
| GA-A12530 | November 1, 1972 through January 31, 1973 |
| GA-A12635 | February 1, 1973 through April 30, 1973 |
| GA-A12728 | May 1, 1973 through July 31, 1973 |
| GA-A12824 | August 1, 1973 through October 31, 1973 |
| GA-A12894 | November 1, 1973 through January 31, 1974 |
| GA-A13021 | February 1, 1974 through April 30, 1974 |
| GA-A13148 | May 1, 1974 through July 31, 1974 |
| GA-A13238 | August 1, 1974 through October 31, 1974 |
| GA-A13379 | November 1, 1974 through January 31, 1975 |
| GA-A13458 | February 1, 1975 through April 30, 1975 |
| GA-A13565 | May 1, 1975 through July 31, 1975 |
| GA-A13766 | August 1, 1975 through October 31, 1975 |
| GA-A13815 | November 1, 1975 through January 31, 1976 |

## ABSTRACT

The tasks of the gas-cooled fast breeder reactor (GCFR) program that are supported by the U.S. Energy Research and Development Administration include development of GCFR fuel, blanket, and control elements; development of the pressure equalization system for GCFR fuel; out-of-pile loop facility test program planning; fuels and materials development; fuel, blanket, and control rod analyses and development; nuclear analysis and reactor physics for GCFR core design; shielding requirements for the GCFR; reactor engineering to assess the thermal, hydraulic, and structural performance of the core and the core support structure; plant systems control; development of reactor components, including reactor vessel, control and locking mechanisms, fuel handling equipment, core support structure, shielding assemblies, main helium circulator, steam generator, and auxiliary circulator; development of a helium circulator test facility; and reactor safety, including an in-pile safety evaluation program.

CONTENTS

FIGURES

FIGURES (Continued)

FIGURES (Continued)



TABLES

TABLES (Continued)

# 1. INTRODUCTION

The various tasks of the gas-cooled fast breeder reactor (GCFR) program for the period February 1, 1976 through April 30, 1976 sponsored by the U.S. Energy Research and Development Administration (ERDA) are discussed in this quarterly progress report. The GCFR utility program, which is supported by a large number of electric utility companies, rural electric cooperatives, and General Atomic, is primarily directed toward the development of a GCFR demonstration plant. The utility-sponsored work and the ERDA-sponsored work are complementary.

Analytical, experimental, and fabrication development is being accomplished under the core element development task to establish the basis for the design of GCFR fuel, blanket, and control element assemblies. Analytical methods development for structural and thermal-hydraulic analyses is discussed, and the results of structural analysis of the fuel assembly components and thermal-hydraulic analysis of the blanket element during low power are presented. Current progress on rod spacer interaction tests, fuel element seismic and vibration test planning, and development of assembly fabrication techniques is also presented. The various subtasks of core element development and the work accomplished during this reporting period are discussed in Section 2.

The technology to support the design and construction of the pressure equalization system for GCFR fuel is being developed. This includes (1) the development of analytical models and computer codes that will be verified by test programs and testing of materials and seals and (2) the development of fabrication processes for the pressure equalization system. These are discussed in Section 3.

To demonstrate the ability of GCFR fuel, control, and blanket assembly designs to meet design goals and verify predictions of analytical models, a series of out-of-pile simulation tests will be performed. The emphasis of the tests will be on obtaining thermal-structural data for steady-state, transient, and margin conditions using electrically heated rod bundles in a dynamic helium loop. These are discussed in Section 4.

In the fuels and materials development program, thermal flux and fast flux irradiation programs are being conducted to establish conditions and design features specific to GCFR fuel rods, such as vented fuel, fission product traps, and surface-roughened cladding. In addition, a test program of smooth and surface-roughened GCFR cladding specimens is being conducted to determine how materials behave under irradiation. The fuels and materials tests, the analytical studies, and the results to date are presented in Section 5.

Under the fuel rod engineering task, performance of the fuel and blanket rods under steady-state and transient conditions is being evaluated to determine performance characteristics, operating limits, and design criteria. In addition, surveillance of the fuel rod and blanket rod technology of other programs is being carried out. These studies are presented in Section 6.

The objectives of the nuclear analysis and reactor physics task are to verify and validate the nuclear design methods which will be applied to the GCFR core design. A critical assembly experimental program is being carried out on the ZPR-9 facility at Argonne National Laboratory for this purpose. Critical assembly design, analysis, and methods development are discussed in Section 7.

Verification of the physics and engineering analytical methods and the data for design of the GCFR shields is being conducted under the shielding requirements task along with an evaluation of the effectiveness of various shield configurations. The results of radial shield analyses and the work being done on structural analysis are presented in Section 8.

To assess the thermal-hydraulic performance of the GCFR reactor core, analytical methods and models are being developed and utilized to define operating strategies. These, together with the development of GCFR plant control systems and an evaluation of the capability of the PCRV internal structures to provide postaccident fuel containment, are discussed in Section 9.

Section 10 presents the evaluation and development of the main components of the GCFR which are currently in progress, including reactor vessel, control and locking mechanisms, fuel handling, core support structure, shielding assemblies, main helium circulator, steam generator, and auxiliary circulator.

Development of a test facility for qualification testing of the main helium circulator is discussed in Section 11. This task includes the responsibility for (1) evaluation studies of alternative test facility concepts, (2) preparation of specifications for the selected facility, and (3) final design, construction, and checkout of the facility.

The objective of the reactor safety task, which is discussed in Section 12, is to study the safety aspects of the GCFR using logical probabilistic methods to determine the probabilities associated with accident initiation and progression sequences.

The gas reactor in-pile safety test (GRIST) program is being studied as a potential follow-on to the analytical and experimental programs covering design basis accidents. The objective of the GRIST program is to provide information related to beyond-design-basis accidents, particularly the behavior of melted cladding and fuel. Progress in test assembly analysis and design is discussed in Section 13.

# 2. CORE ELEMENT DEVELOPMENT (189a No. SU006)

## 2.1. FUEL AND CONTROL ASSEMBLY ANALYSIS

### 2.1.1. Introduction

The analytical basis, in conjunction with experimental evaluation, for the design and development of the GCFR fuel and control assemblies is being developed. Because complete prototype in-pile tests cannot be conducted, a strong analytical base supported by development tests is required to design the core assemblies. The current effort is devoted to the development of an adequate steady-state and transient analysis capability in the areas of thermal-hydraulic and structural steady-state and transient analyses to provide a basis for assembly design criteria and specific test requirements.

During the previous quarter, the subroutine for calculating the first-order outer flow rates in FLOMAX was developed, and some debugging is still in progress. The chopped cosine power distribution was incorporated in the code, and preparations were begun for programming the inner solutions. The thermal-hydraulic analysis for the previous quarter concentrated on a more accurate determination of the effect of the rod-to-duct spacing of the fuel assembly. A calculational scheme was developed using the rough rod data from the Swiss Federal Institute as a basis, but further analysis is required for this complicated problem.

During this quarter, the programming of the outer solutions in FLOMAX was completed, except for some debugging, and the results for simple problems corresponded well with the COBRA predictions. For the inner solutions, a problem arose with respect to the appropriate scaling; this problem was resolved. Calculations of the subchannel temperatures of two channels gave

good agreement with COBRA. The thermal analysis continued with the application of rough rod data to a model of the fuel assembly. This model was used to study the variation of the power-to-flow ratio of the fuel assembly for a constant maximum cladding temperature. A structural analysis model was initiated to study the interaction of the guide tube and the duct of the control rod assembly.

### 2.1.2. Analytical Methods Development

Work continued on the development of the thermal-hydraulic subchannel analysis code FLOMAX. The mathematical problem of rod bundle codes is to determine for each subchannel i, and as a function of the axial coordinate x, the mass velocities $G_i(x)$, the temperatures $T_i(x)$, and the pressures $P_i(x)$. In FLOMAX, this is done by expanding these variables into the asymptotic series

$$G_i(x) \sim G_{oi} + \sigma G_{1i}(x) + \sigma g_i(\xi) + O(\varepsilon) \quad ,$$

$$T_i(x) \sim T_o(x) + \sigma T_{1i}(x) + \sigma t_i(\xi) + O(\varepsilon) \quad ,$$

$$P_i(x) \sim P_o(x) + \sigma P_1(x) + \sigma^2 p(\xi) + O(\varepsilon) \quad ,$$

where the upper case letters denote outer variables, which are valid away from the inlet, geometry transitions, and spacers; the lower case letters denote inner variables, which are valid near the inlet, transitions, and spacers; the Greek letters denote small parameters; and the stretched coordinate is $\xi = x/\sigma$.

2.1.2.1. The Outer Solutions. The programming of the outer solutions $G_{oi}$, $T_o$, and $T_{1i}$ was previously completed. During this quarter, the $P_1$ and $G_{1i}$ solutions were programmed. To check these solutions, two problems with two subchannels were executed. In the first problem, the subchannel areas and friction perimeters were the same, and equal

amounts of heat were added with a flat and a chopped cosine axial power function. The resulting subchannel flows, temperatures, and pressures were in excellent agreement with a COBRA execution of the same problem. In the second problem, subchannel 1 was much smaller than subchannel 2 (area ratio = 0.1), but the same amount of heat was added to both subchannels. This means that subchannel 1 is much hotter than subchannel 2, thus providing a stringent test of the asymptotic solution.

During the last quarter, it was observed that FLOMAX tended to overpredict the COBRA temperature where there was a positive axial power gradient. The opposite occurred for a negative gradient. This was due to neglecting $T_{2i}(x)$ in the following series:

$$T_i(x) \sim T_o(x) + \sigma T_{1i}(x) + \sigma^2 T_{2i}(x) + \ldots$$

To emphasize this behavior, a problem was executed with a hypothetical triangular-shaped axial power profile. The results are shown in Fig. 2-1. For subchannel 1, the equation for $T_{2i}(x)$ has a forcing function proportional to the negative axial power gradient; thus, for a positive constant gradient, $T_{2i}$ would be approximately a constant negative number which would shift the $T_i(x) \sim T_o(x) + T_{1i}(x)$ solution downward, approximately parallel to itself. The opposite would occur for a negative gradient. It can be seen that this is the behavior of the curves in Fig. 2-1 if the COBRA integration is regarded as the exact solution. Thus, it is possible to obtain a refined solution by adding the $T_{2i}(x)$ functions. However, the above problem with different areas is an extreme example, and the programming of the $T_{2i}$ functions will be done only as a code improvement task if warranted for actual fuel assembly calculations.

In FLOMAX, the calculation of the outer solutions follows the following sequence:

1. $T_o(x)$ is determined based on the axial power function.

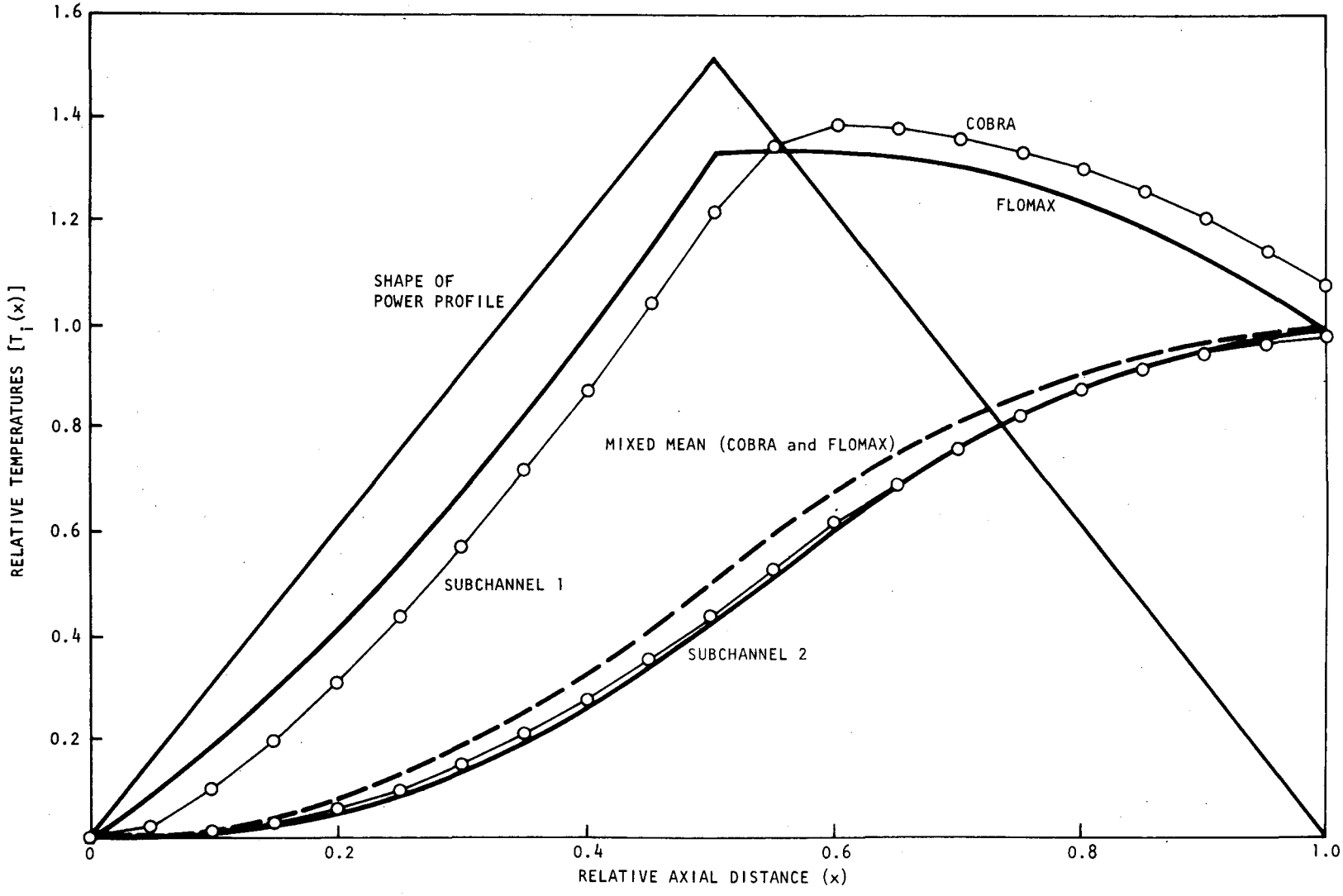


Fig. 2-1 Comparison of FLOMAX outer subchannel temperatures with COBRA results for a triangular shaped axial power distribution

2. $P_o(x)$ and $G_{oi}$ values are determined based on $T_o(\bar{x})$.

3. $T_{1i}(x)$ values are determined based on $T_o(x)$, $G_{oi}$, and the power functions.

4. $P_1(x)$ and $G_{1i}(x)$ values are determined based on $T_{1i}(x)$, $G_{oi}$, and $P_o(x)$.

5. $T_{2i}(x)$ values would be based on all the above solutions.

Subchannel velocities and pressures were also calculated for the two-channel problem, including the programmed solutions $P_1(x)$ and $G_{1i}(x)$. Figure 2-2 shows the pressure drop profile in comparison with COBRA results. The agreement is excellent. There is considerable acceleration loss in this example as shown by comparison with the unheated profile. In COBRA and FLOMAX, the pressures were identical in the two subchannels. The mass fluxes of the two heated channels are shown in Fig. 2-3. The agreement for the small subchannel 1 is not so good. As expected, FLOMAX and COBRA reduce the mass flux in the hot channel below the unheated value, but COBRA reduces it more than FLOMAX. To check if this disagreement is due to a programming error, the two-channel velocities will be manually calculated for comparison. The curvature of the COBRA solution at the inlet occurred because of the way in which COBRA determines inlet velocities to produce equal subchannel pressure drops. As shown in Fig. 2-4, the Reynolds numbers were also compared. It can be seen that the errors in the asymptotic approximations of the velocities and temperatures tend to compensate such that the Reynolds numbers agree very well. The Reynolds numbers decrease with axial distance because the viscosity increases with temperature. With the subchannel temperatures and Reynolds numbers thus determined, the rod surface temperatures can be calculated. The programming of this calculation was initiated. The Stanton numbers (St) for the subchannels are determined as functions of the Reynolds numbers in a special subroutine with user-supplied correlations in a manner similar to that

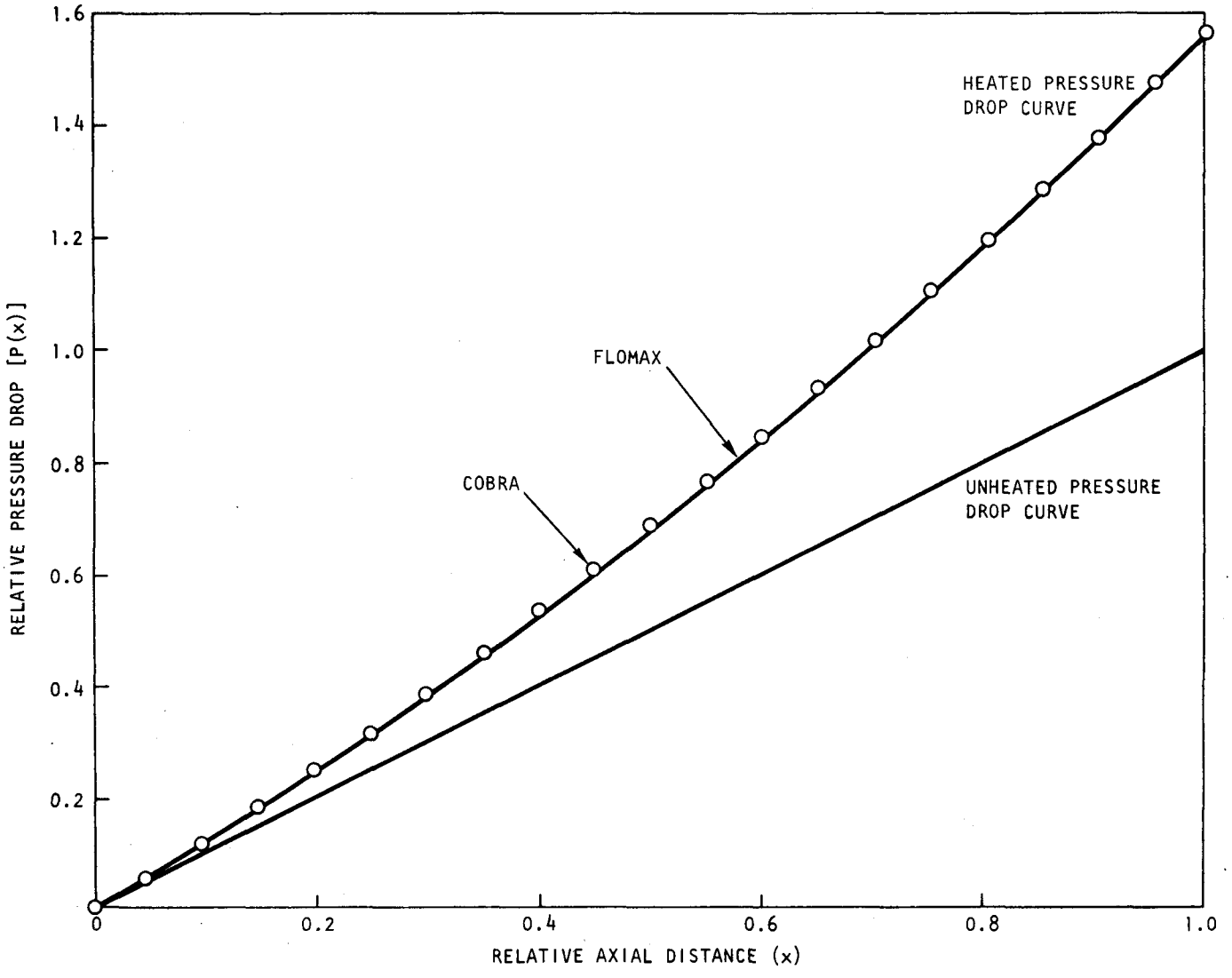


Fig. 2-2 Comparison of pressure drop calculations for a flat power profile and constant friction factors

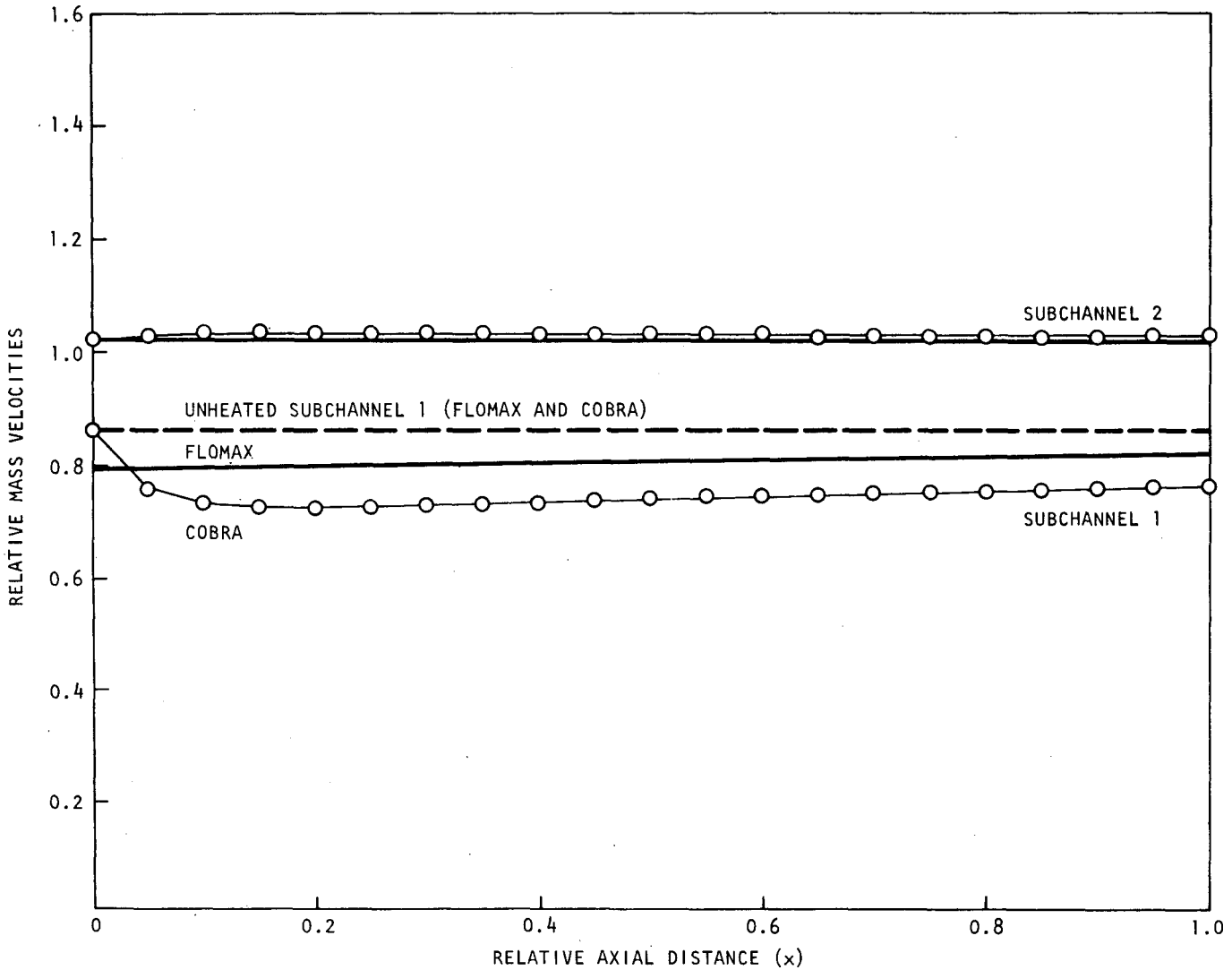


Fig. 2-3 Comparison of mass flux calculations for a flat power profile and axial friction factors

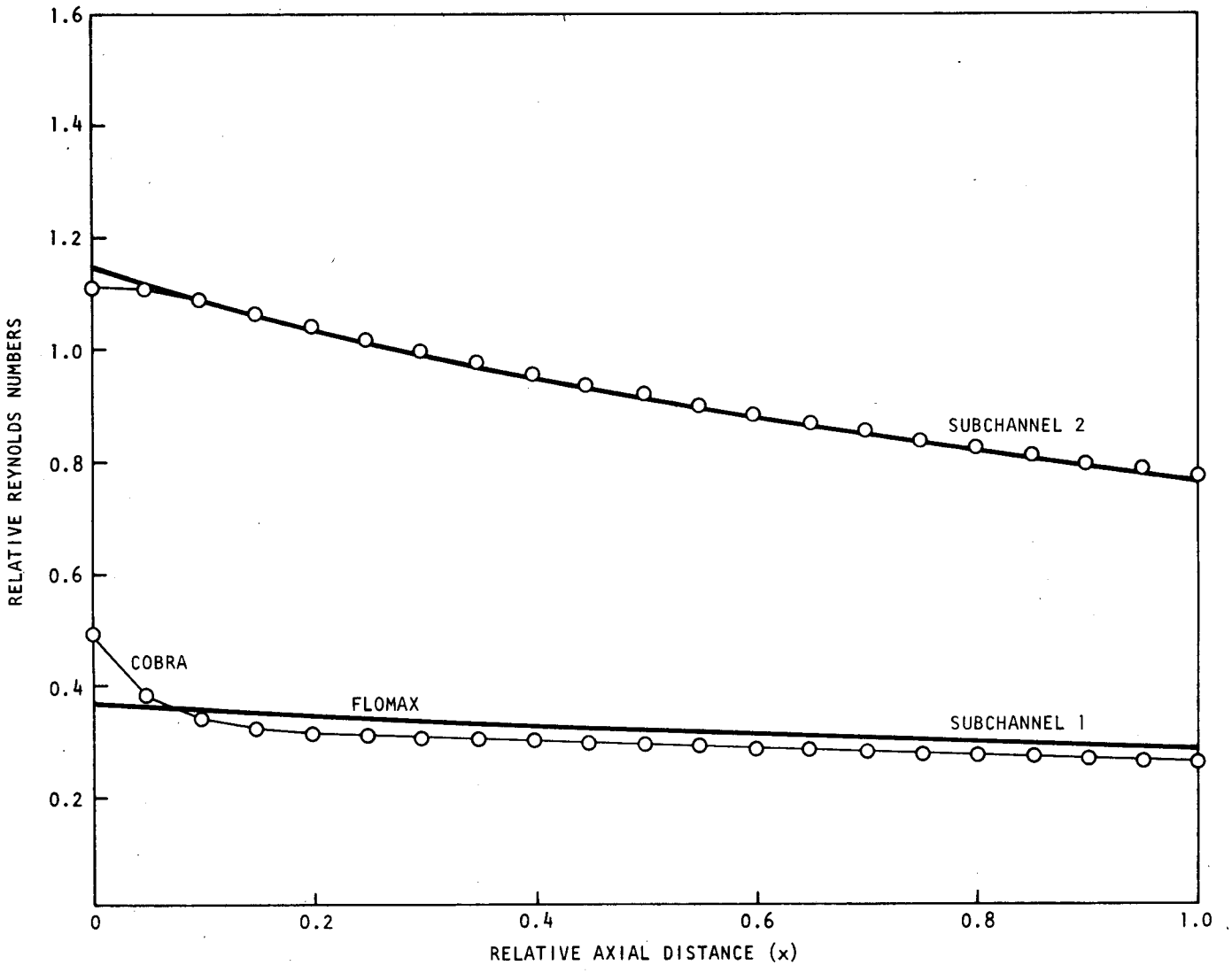


Fig. 2-4 Comparison of Reynolds number calculations for a flat power profile and constant friction factors

for the friction factors. The surface temperatures are then determined from the formula

$$q = h(T_s - T) \quad ,$$

where $q$ = rod heat flux,

$h$ = heat transfer coefficient ($C_p G\ St$),

$T_s$ = rod surface temperature,

$T$ = subchannel bulk temperature.

The above calculations were programmed and are now being debugged. The surface temperatures and the above outer solutions will be compared with COBRA for actual models of parts of the GCFR fuel rod assembly. Then, FLOMAX will be used with refined models of the assemblies to determine flows and temperatures near the edge of the assemblies. Such a model is described in Section 2.1.3.

2.1.2.2. The Inner Solutions. In the development of the outer solutions, it was found that the correct expansion parameter was $\sigma = \varepsilon/\lambda$, where $\lambda$ is associated with a characteristic friction factor of the assembly, instead of the parameter $\varepsilon$ as previously thought. In the development of the inner solutions, the stretched variable $\zeta = x/\varepsilon$ was previously used, but this led to an incorrect flow and temperature development. During this quarter, a correct analytical solution for the temperature development was obtained in terms of $\xi = x/\sigma$, and it was verified by manual calculations for a two-channel problem.

Previously, the axial momentum equation was written in the follow-form:

$$\varepsilon\left(\begin{matrix}\text{acceleration}\\ \text{term}\end{matrix}\right) + \omega\left(\begin{matrix}\text{cross-flow}\\ \text{term}\end{matrix}\right) + \lambda\left(\begin{matrix}\text{pressure gradient,}\\ \text{friction, and mixing}\\ \text{terms}\end{matrix}\right) = 0 \quad ,$$

where $\omega$ is an arbitrary scaling factor for the cross-flow velocities. For the inner solutions, this factor was selected as $\omega = \lambda$. Thus, dividing through by $\lambda$, the descriptive FLOMAX differential equations were written in the following form:

Conservation of mass

$$\sigma\begin{pmatrix}\text{axial change}\\ \text{in mass flow}\end{pmatrix} + \begin{pmatrix}\text{cross flow}\end{pmatrix} = 0 \quad , \tag{2-1}$$

Conservation of axial momentum

$$\sigma\begin{pmatrix}\text{acceleration}\end{pmatrix} + \begin{pmatrix}\text{cross flow}\end{pmatrix} + \begin{pmatrix}\text{pressure gradient,}\\ \text{friction, and mixing}\end{pmatrix} \tag{2-2}$$

Conservation of thermal energy

$$\sigma\begin{pmatrix}\text{axial change}\\ \text{in heat flow}\end{pmatrix} + \begin{pmatrix}\text{cross flow}\end{pmatrix} + \begin{pmatrix}\text{mixing}\end{pmatrix} = \sigma\begin{pmatrix}\text{heat}\\ \text{generation}\end{pmatrix} \quad , \tag{2-3}$$

Conservation of transverse momentum

$$\begin{pmatrix}\text{transverse}\\ \text{pressure gradient}\end{pmatrix} = \varepsilon^2\begin{pmatrix}\text{transverse}\\ \text{acceleration}\end{pmatrix} + \frac{\varepsilon^2}{\sigma}\begin{pmatrix}\text{transverse}\\ \text{friction}\end{pmatrix} \quad . \tag{2-4}$$

In the asymptotic series of FLOMAX, terms will be included to the order of magnitude of $\sigma$, and possibly of $O(\sigma^2)$, if warranted as code improvements. However, terms of $O(\varepsilon) = 10^{-3}$, and certainly those of $O(\varepsilon^2) = 10^{-6}$, will be neglected. Thus, Eq. 2-4 is not required, and the subchannel pressures will be equal at each axial position. This means that the spacer pressure losses in FLOMAX will be treated as an integral loss for the whole spacer. The adequacy of this approximation will be verified by comparison with COBRA calculations.

The inner solutions $t_i(\xi)$ and $g_i(\xi)$ are required at the rod bundle inlet and smooth-rough surface transitions, and they are determined by

substituting the expansions into Eqs. 2-1 to 2-3. For $t_i(\xi)$, this resulted in the following linear equation:

$$(G_o A)_{(i)} \frac{dt_i}{d\xi} + C_{ik} (sYG_o \Delta t)_k = 0 \quad .$$

This equation was formally solved as an eigenvalue problem by setting $t_i(\xi) = a_i e^{-\alpha\xi}$. For the two-channel sample problem, the single eigenvalue $\alpha$ was determined by manual calculations. The result for a flat axial power profile is shown in Fig. 2-5, and it agrees satisfactorily with COBRA. A similar equation for the $g_i$ values is presently being obtained. In the FLOMAX code, eigenvalues will be numerically determined for n subchannels, and the corresponding solutions will be added to the presently programmed outer solutions.

### 2.1.3. Thermal-Hydraulic Analysis

During this quarter, work continued on the development of appropriate friction factor and Stanton number correlations for various fuel element subchannel configurations for input to the COBRA and FLOMAX thermal-hydraulic analysis computer codes. Additional annulus test data have been evaluated using several transformation methods which allow single-rod data to be adapted for use with fuel rod bundles. The procedures for defining rod bundle sub-subchannels and the transformation methods were discussed in the last quarterly report (Ref. 2-1).

Figure 2-6 shows a section of a strip through a 271-rod GCFR fuel element. The bottom, horizontal line represents the duct wall, and the vertical lines are lines of symmetry. The side channel was divided into eight subchannels to provide a better description of the relationship of the friction factor (f) and the Stanton number (St) to the Reynolds number (Re). Annulus flow test data were transformed, and the effects of relative

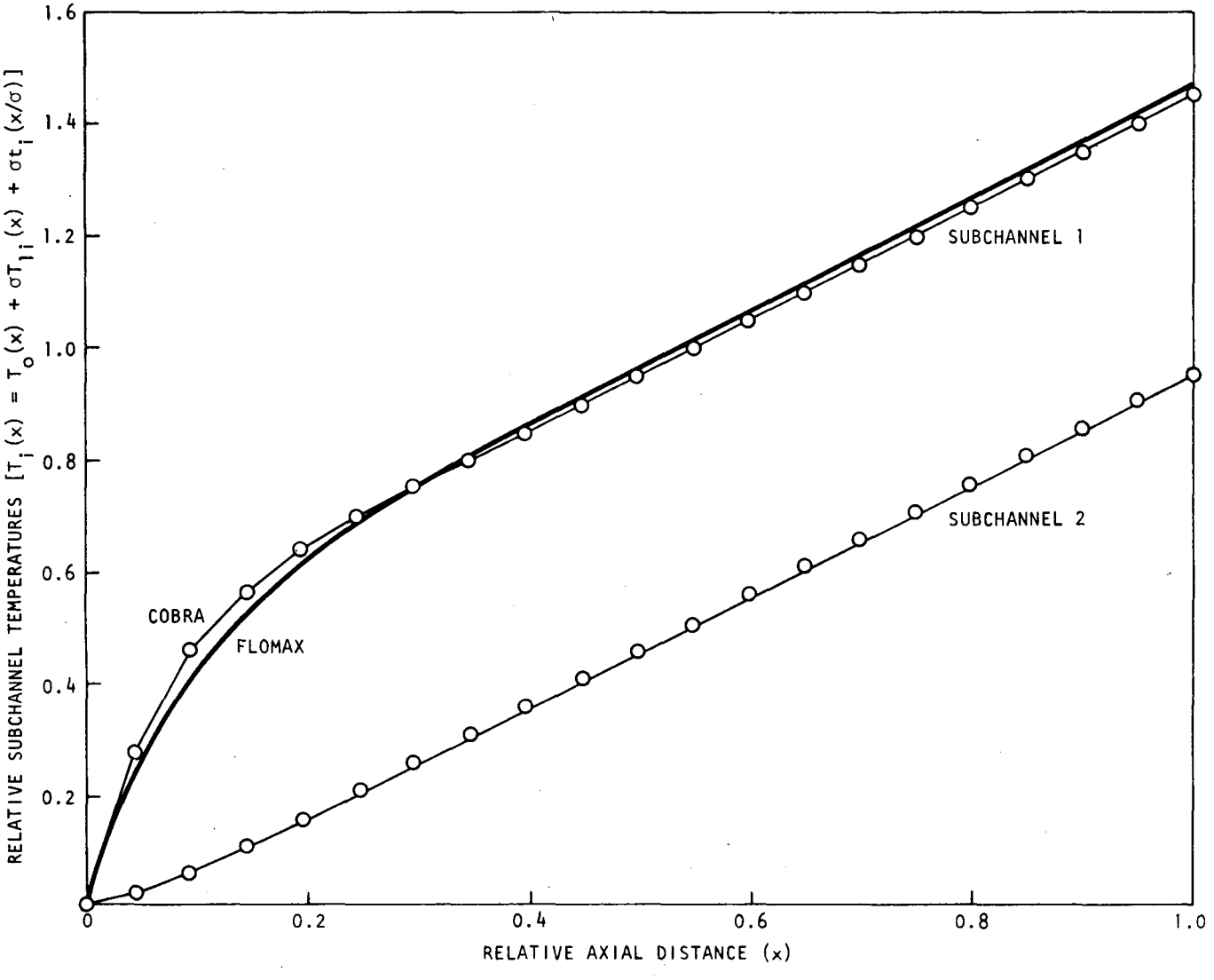


Fig. 2-5 Comparison of subchannel temperatures with COBRA for a flat axial power profile, including the inner solutions $t_i(\xi)$

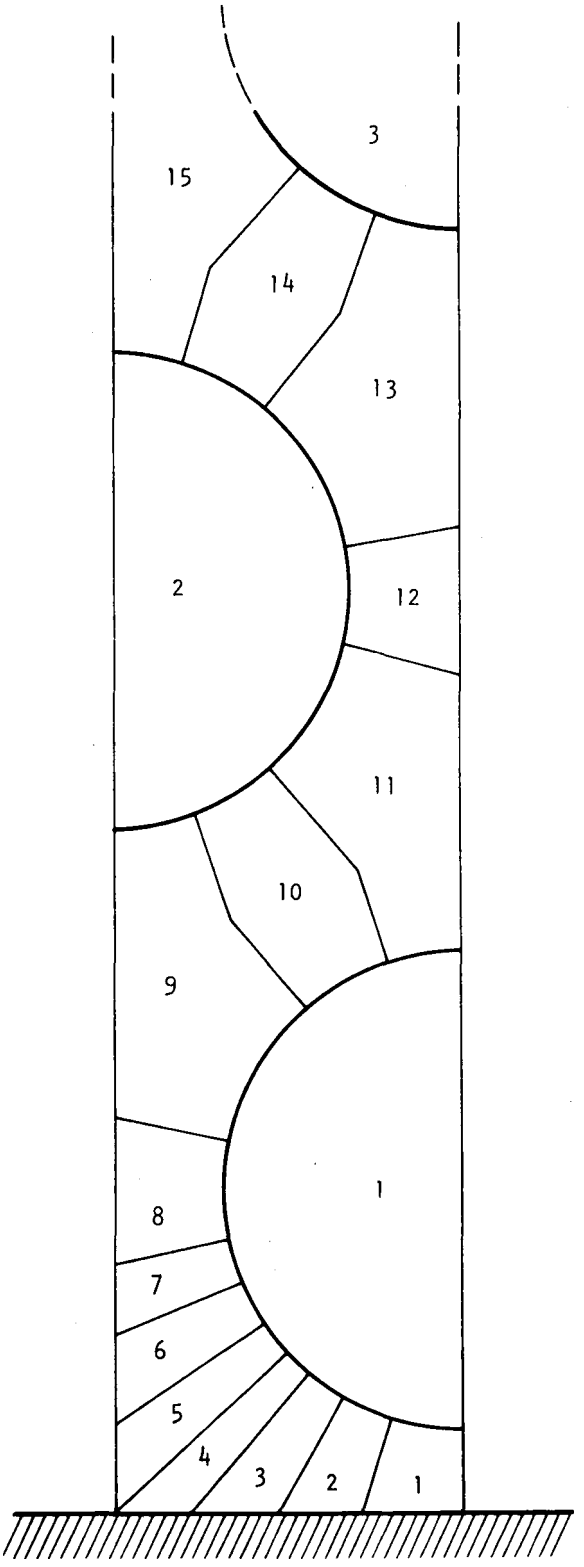


Fig. 2-6 Subchannel layout for studying the effect of rod-to-duct spacing

roughness and Re were separated using the procedures described in Ref. 2-1. These data were then used with the strip model geometry and the inverse transformation equations to calculate f and St as functions of Re for the 10 different subchannels.

For use with the FLOMAX code, the data for each subchannel i were correlated in the form

$$f_i = a_i + b_i Re^{c_i} \quad ,$$

$$St_i = d_i + e_i Re^{g_i} \quad ,$$

and the parameters $a_i$, $b_i$, ... were directly input to the code for each of the 10 different subchannel types. The FLOMAX code is presently being executed with these correlations, but the results have not yet been evaluated. In the COBRA code, the f and St data for subchannels 1 to 8 were combined into one side subchannel, as described in Ref. 2-1.

The strip model of the fuel element was analyzed with COBRA-IV to determine the power-flow relationship at different power levels. A rod--to-wall gap which was 40% of the rod-to-rod gap was used, and a temperature of 700°C (1292°F) at the midwall of the cladding was maintained. Figure 2-7 shows a plot of the power-to-flow ratio as a function of power. At 10% power, the flow is not yet laminar. The coolant flow distribution between the central and the side subchannels is also shown in terms of the ratio of the respective mass fluxes $G_c/G_s$. The performance of the element at low powers and laminar flow conditions must still be analyzed.

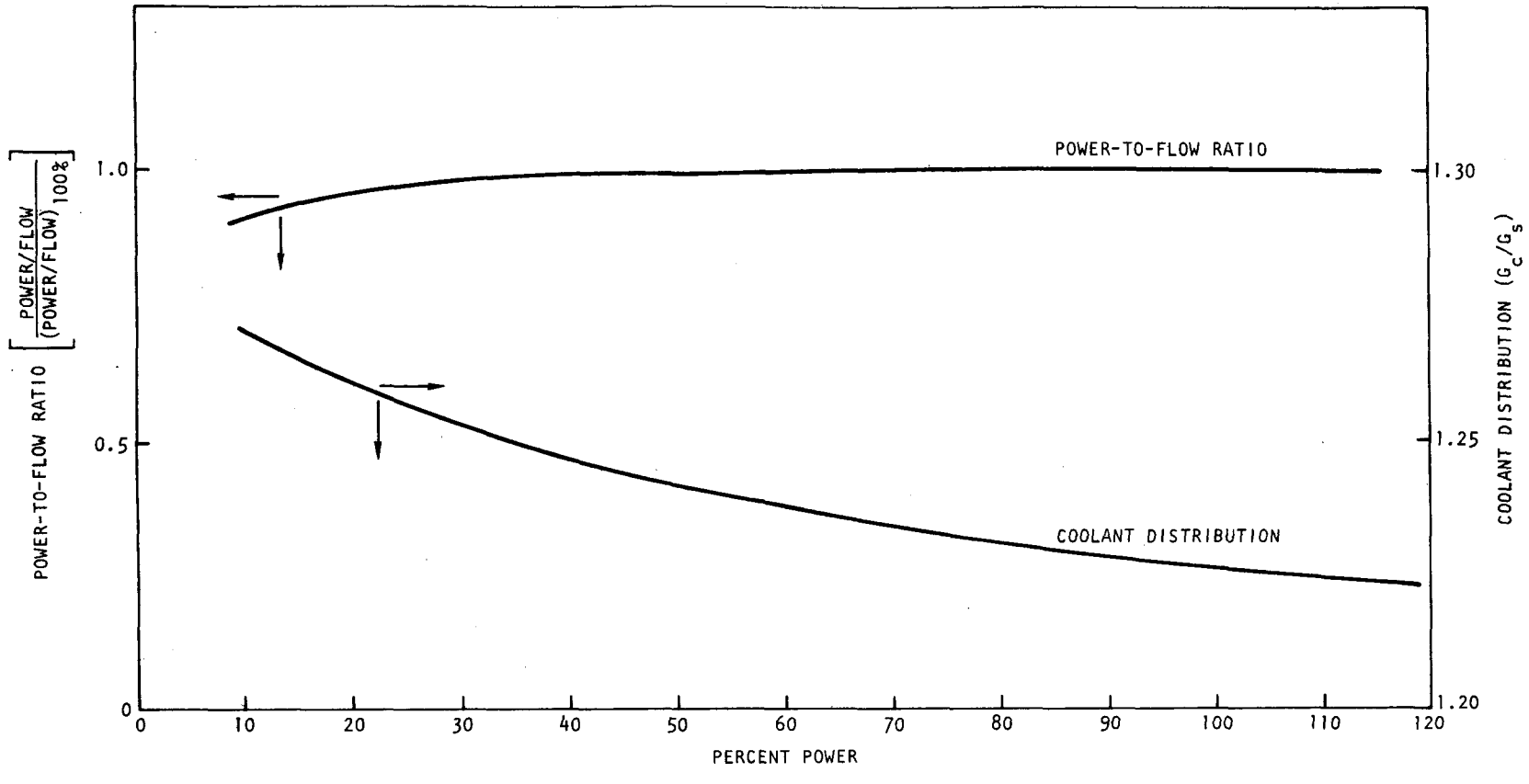


Fig. 2-7 Variation of power-to-flow ratio and coolant distribution with percent of full power for a constant maximum cladding temperature of 700°C (1292°F)

### 2.1.4. Structural Analysis

A study has been initiated to evaluate the bowing deformation of the control rod guide tube, taking into account the coupling effect of a single connection at the lower end of the control assembly. The MARC computer program will be used in the analysis. A model consisting of 38 beam elements of hexagonal cross section has been formulated. The analysis will consider time-dependent bowing due to differential swelling and thermal gradients. The analysis will initially be performed in two dimensions and the results compared with CRASIB analyses on less exact (no duct guide tube coupling) models. The present models possess the capability of including other support grids along the element axis.

## 2.2. BLANKET ASSEMBLY ANALYSIS

The purpose of this task is to develop and verify the analytical techniques for blanket assembly analysis. These analytical techniques will be applied to obtain preliminary and final designs of the blanket assembly and to determine the design margin requirements. This task includes thermal-hydraulic, structural, and dynamic analyses and evaluation of handling and shipping of the blanket assembly.

During the previous quarter, an evaluation of the proposed design of the GCFR radial blanket assembly compared with the reference design was performed, and a new configuration and management scheme for the radial blanket were proposed, reviewed, and approved. Some aspects (e.g., pressure drop) of the thermal-hydraulics of the new reference design of the GCFR radial blanket assembly were also analyzed.

### 2.2.1. Thermal-Hydraulic Analysis

The new reference design (Ref. 2-1) consists of a wire-wrapped blanket rod. The pressure drop for this configuration is given by the following correlation proposed in Ref. 2-2:

$$\Delta P = M f_s \frac{L}{D_e} \frac{\rho V^2}{2g} \quad , \tag{2-5}$$

where $$M = \left( \frac{1.034}{(P/D)^{0.124}} + \frac{29.7\ (P/D)^{6.94}\ Re^{0.086}}{(H/D)^{2.239}} \right)^{0.885} \quad ,$$

$\Delta P$ = pressure drop (Pa),

$f_s$ = smooth tube friction factor,

$L$ = length of rod bundle (m),

$D_e$ = equivalent hydraulic diameter of flow cell (m),

$p$ = coolant density ($g/cm^3$),

$V$ = bulk flow velocity (m/s),

$g$ = gravitational constant ($m/s^2$)

$P$ = pitch of rod bundle (m),

$D$ = rod diameter (m),

$H$ = wire wrap pitch (m).

The above correlation, also called the FFTF correlation, is adequate for analysis in the turbulent flow range. However, additional literature search and experiments are necessary for analysis in the laminar flow range.

For p/d = 1.05 of the GCFR radial blanket assembly, the friction factor multiplier M in Eq. 2-5 reduces to

$$M = \left( 1.03 + \frac{41.6\ Re^{0.086}}{(H/D)^{2.239}} \right)^{0.885} \quad . \tag{2-6}$$

Structural analysis of the blanket assembly has shown that a pitch of 30 cm (1 ft) is desirable for the wire wrap. For this pitch of the wire wrap, Eq. 2-6 becomes

$$M = \left( 1.03 + 0.11\ Re^{0.086} \right)^{0.885} \quad . \tag{2-7}$$

Using this relation, the pressure drop in the peak powered blanket assembly was calculated as 0.068 MPa (9.8 psi). This pressure drop is much smaller than the pressure drop across the fuel assemblies.

## 2.3. ASSEMBLY MECHANICAL TESTING

The objective of this task is to conduct mechanical tests of core element assembly components and assemblies to simulate mechanical loads expected during normal and abnormal reactor operating conditions. The current phase of the assembly mechanical testing program involves testing of fuel element assembly components. The fuel rod/spacer interaction test is the initial long-term component test. Additional tests are being planned for FY 77.

### 2.3.1. Fuel Rod/Spacer Interaction Test

The purpose of the rod/spacer interaction test is to evaluate the interaction between the rod and the spacer in the ranges of temperature and impurity levels (primarily water and hydrogen) expected in the GCFR helium coolant. These interactions arise from the relative motion between the rod and the spacer due to temperature variations during reactor transients. These tests will provide a data base for standards of acceptable friction and wear and elimination of the possibility of adhesion between the rod and the spacer.

Initially, combinations of pressed spacers with convex contact surfaces and smooth or ribbed rods were tested. Spacers and rods were made of type 316 stainless steel. Adhesion was observed in tests on smooth rods in an environment containing 900/90 μatm of $H_2/H_2O$ in helium. No adhesion was observed when the $H_2/H_2O$ ratio was increased to 100 at the same absolute level of $H_2O$. Additional tests were conducted using spacers fabricated by the electrodischarge machining (EDM) technique. These spacers had flat or concave contact surfaces with 2 μm $R_a$ surface roughness. No adhesion was observed under the same conditions at which

pressed spacers showed adhesion. In addition, adhesion has not been observed with Inconel 718, Inconel 625, or Hastelloy spacers against type 316 stainless steel smooth rods.

During this quarter, the reproducibility tests on ribbed rods at 550°C (1022°F) were completed, and the results are given in Table 2-1. The ribs were fabricated by mechanical grinding at Kraftwerk Union (KWU) on the 20% cold-worked type 316 stainless steel tubing supplied by General Atomic (GA). The simulated spacers were fabricated by EDM machining by a U.S. vendor from 20% cold-worked type 316 stainless steel plate and had flat contact surfaces for bearing against the ribbed tube surface. The helium environment of the test furnace contained 3000 μatm of $H_2$ and 850 μatm of $H_2O$. The results indicate good reproducibility of the coefficient of friction and wear depth. Reproducibility tests at 750°C (1380°F) on ribbed rods are in progress, and preliminary test results are being analyzed. The results will be reported during the next quarter.

The long dwell time tests at 325°C (617°F) and 550°C (1022°F) on smooth tubes were completed. The test conditions were identical to those used for the reproducibility tests. The tests were performed with twenty-five 1-hr dwell times between strokes, followed by six 100-hr dwell times between strokes, followed by seventy 1-hr dwell times between strokes. The results are given in Table 2-2. Because of the limited number of tests, it is not realistic to compare the results with the results of reproducibility tests. However, the purpose of the tests was to determine if long dwell times between strokes might result in excessive sticking and adhesion. The adhesion never occurred, as evidenced by the load cell readings. Nevertheless, some indication of sticking is inferred from the higher coefficient of friction and the deeper wear grooves (comparing Tables 2-1 and 2-2), but the limited data do not permit definite conclusions.

Consideration has been given to planning a transient interaction test between the fuel rod and spacer, simulating abnormal operating conditions.

TABLE 2-1
FUEL ROD/SPACER INTERACTION TEST REPRODUCIBILITY RESULTS

| Stroke Length [mm (in.)] | Number of Strokes | Temperature [°C (°F)] | Coefficient of Friction | | Wear [μm (mils)] | |
|---|---|---|---|---|---|---|
| 3.8 (0.15) | 100 | 550 (1022) | 0.7 | Average = 0.53 | 13 | Average = 17.8 |
| | | | 0.5 | σ = 0.13 | 13 | σ = 5.9 |
| | | | 0.5 | | 25 | |
| | | | 0.4 | | 20 | |
| 0.76 (0.03) | 4000 | 550 (1022) | 0.9 | Average = 0.8 | 13 | Average = 14.8 |
| | | | 0.5 | σ = 0.2 | 13 | σ = 3.5 |
| | | | 0.9 | | 13 | |
| | | | 0.9 | | 20 | |

Note: EDM spacers and ribbed rods, $H_2/H_2O$ = 3000/800 μatm. σ is the standard deviation.

TABLE 2-2
LONG DWELL TIME TEST RESULTS

| Temperature [°C (°F)] | Rod Type | Coefficient of Friction | Wear [μm (mils)] |
|---|---|---|---|
| 325 (617) | Smooth | 0.9 | 25 (1) |
| 550 (1022) | Smooth | 1.1 | 62 (2.4) |
| 550 (1022) | Ribbed | 0.9 | 40 (1.6) |
| 750 (1380) | Ribbed | 0.9 | 38 (1.5) |

Note: $H_2/H_2O$ ratio = 3000/850 μatm.

Stroke length = 3.8 mm (0.15 in.).

EDM spacers and rods are made of 20% cold-worked type 316 stainless steel.

Twenty-five strokes of 1-hr dwell, six strokes of 100-hr dwell, seventy strokes of 1-hr dwell.

A conceptual design using a radio frequency (rf) induction heat source for transient heating has been developed. The major problem in the design is determination of a method for vertical support of the spacer during transient heating that will allow horizontal movement between interacting parts. Development of these testing techniques will be initiated during the FY 76 transition period.

### 2.3.2. Component Mechanical Testing

An experimental stress analysis was conducted on a fast test reactor (FTR) size hexagonal duct. The short duct section was instrumented on three walls with 4.5-mm (0.19-in.) strain gages at the midwall span and on the corners. For measuring wall deflections, two sensitive dial indicator gages were set at opposite midwall points, and two dial indicator gages were set at opposite corners. The duct was filled with water and then pressurized with helium from a safety-regulated gas cylinder. The test setup is shown in Fig. 2-8. The internal pressure was increased in intervals of 0.34 MPa (50 psi). The resulting stresses at the midwall and the corners as calculated from the measured strains are given in Fig. 2-9. The stresses are tension at the midwall and compression at the corners, as would be predicted. The measured tensile stresses can be compared with predicted stresses using the equation for a plate with fixed edges loaded in bending by a uniform pressure load (Ref. 2-3):

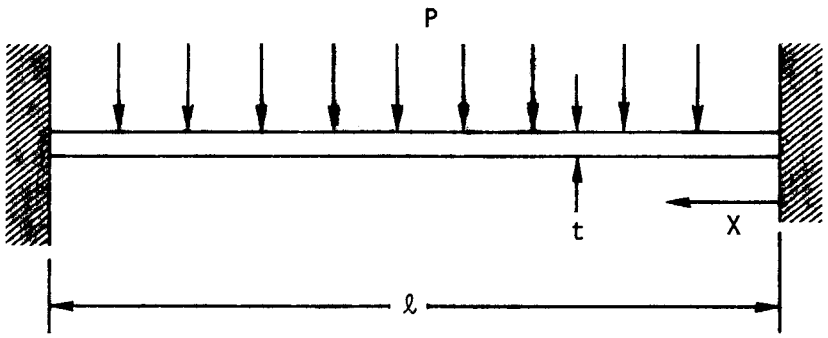


$$\sigma = \frac{MC}{I} \quad , \tag{2-8}$$

$$M = \frac{P\ell}{2}\left(X - \frac{X^2}{\ell} - \frac{1}{6}\ell\right) \text{ for unit depth} \quad , \tag{2-9}$$

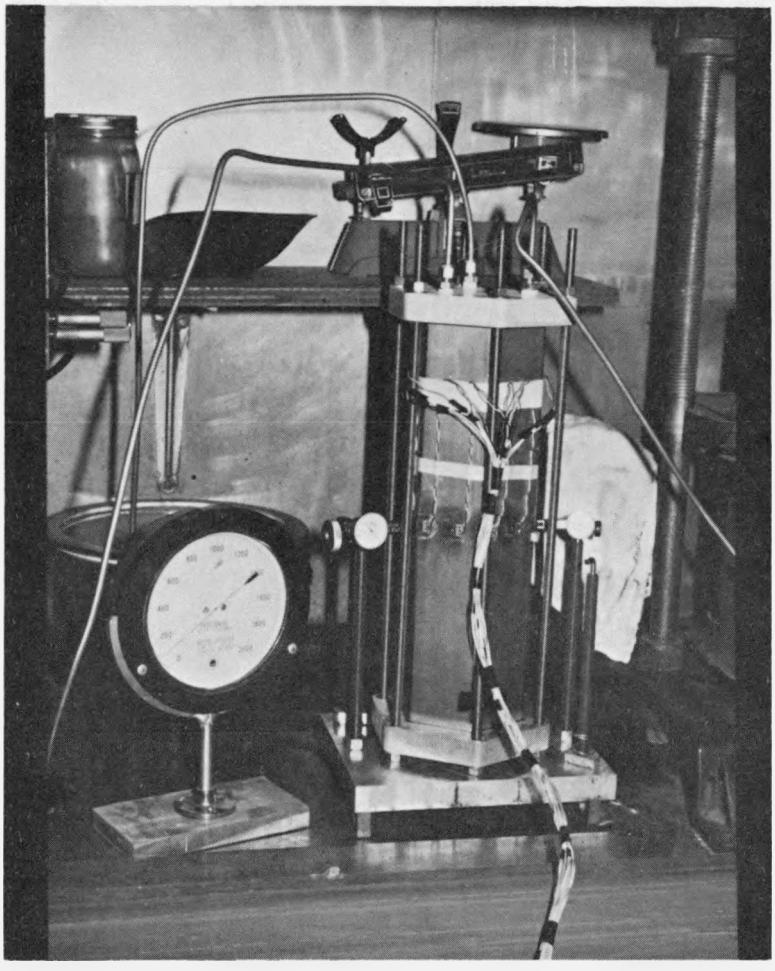

Fig. 2-8 Test setup

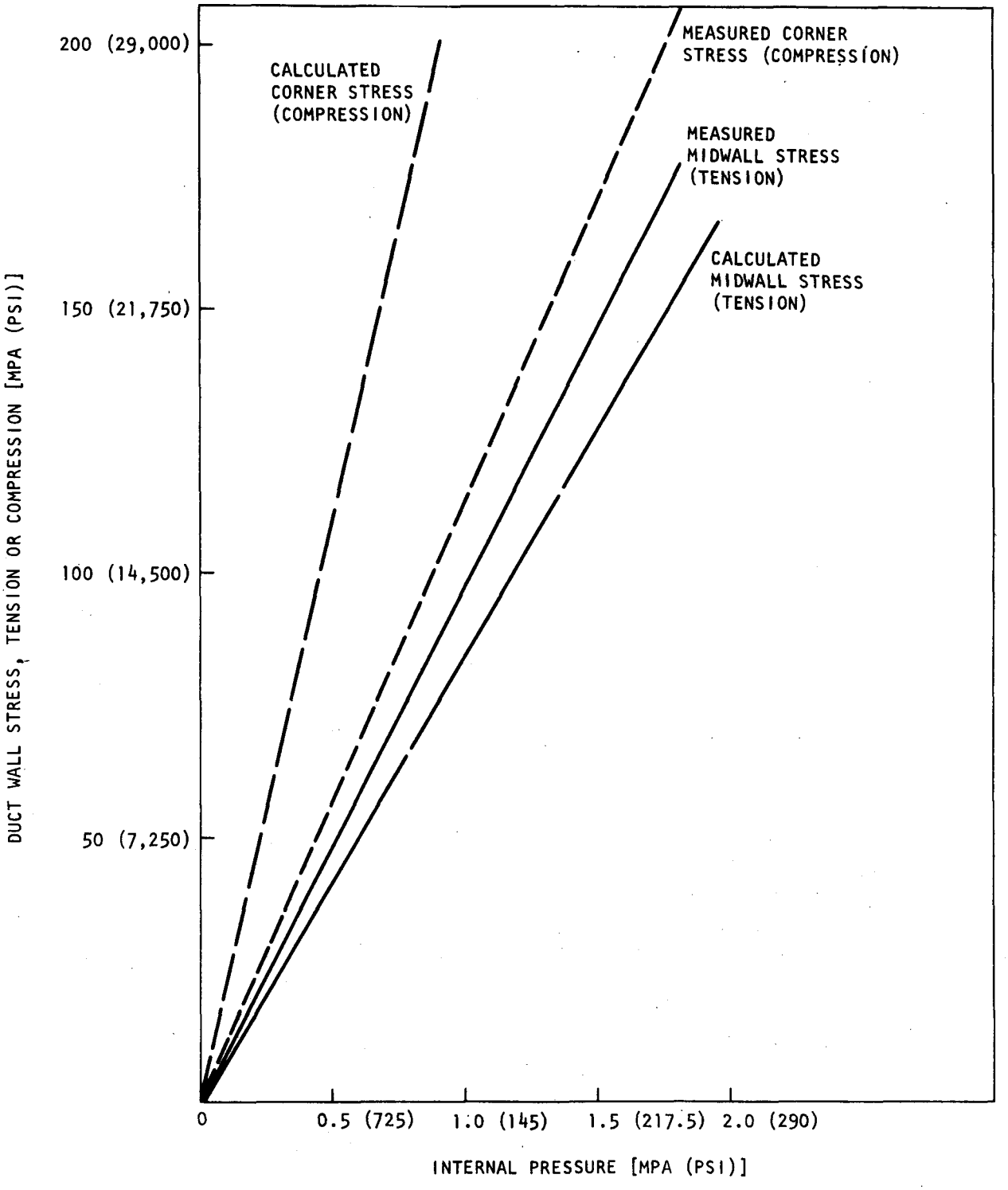


**Fig. 2-9 Pressure test of hexagonal duct**

where for case 33 of Table III in Ref. 2-3,

$t$ = wall thickness (mm),

$C = t/2$,

$\ell$ = duct wall flat length (mm),

$X$ = distance from corner (mm),

$I$ = moment of inertia $= \frac{t^3}{12}$ mm$^4$/mm,

$P$ = internal uniform gas pressure across wall (n/mm$^2$),

$C = t/2$.

The stresses at the midwall are obtained by substituting $X = \ell/2$ in Eq. 2-9 and M and I in Eq. 2-8 as follows:

$$\sigma = \frac{P\ell^2}{4t^2} \quad . \tag{2-10}$$

The stresses at the corners are obtained by substituting $X = 0$ and M and I into Eqs. 2-8 and 2-9 to give

$$\sigma = \frac{P\ell^2}{2t^2} \quad . \tag{2-11}$$

The predicted stresses at the midwall and the corners are also plotted in Fig. 2-9. It is noted that the agreement between the measured and predicted tensile midwall stresses is within 10%. However, the corner, or compressive, stress predicted from Eq. 2-11 is about 80% higher than the measured value. This is because the elementary beam model has pure fixed ends. In the actual case, the corner begins to rotate inward as the adjacent walls deflect outward; i.e., the hexagon is straining to become a cylinder again. The actual corner deflections were measured by dial indicator instruments and are shown along with the measured midwall or outward deflections in Fig. 2-10. The maximum midwall deflections are calculated from the following equation from Ref. 2-3:

$$Y_{max} = -\frac{1}{384}\frac{p\ell^4}{EI} \text{ at } X = \frac{\ell}{2} \quad ,$$

where E = Youngs modulus = $20.7 \times 10^4$ MPa ($30 \times 10^6$ psi) .

Calculated and measured midwall deflections are compared in Fig. 2-10. If the measured corner deflections are added to the midwall deflection to give total midwall deflections, then the agreement is between 10% and 12%.

It can be concluded from the above correlations that the elementary beam theory equations can be used to predict bending stresses and midwall deflections within 10%, but they predict too conservatively high stresses for corner stresses. However, a study was performed at Battelle Pacific Northwest Laboratories in which a detailed analysis was performed using a finite element shell model (Refs. 2-4, 2-5). In these results, the absolute value of the corner compressive stresses was about 30% higher than that of the midwall stresses. These test results predicted corner stresses which were about 10% higher in absolute value, and the elementary beam theory predicts corner stresses 100% higher. Thus, it is concluded that the finite element model should be used for calculating the corner stresses and strains for hexagonal ducts.

## 2.4. CORE TEMPERATURE MONITORING

Further conceptual designs were developed for the placing of the temperature sensing assembly in the center of the control element assembly. This concept requires a thermocouple guide or locating tube in the center of the upper control rod drive. The location appears to be feasible and will be considered in conceptual design studies. The location or guidance of the temperature sensor in the lower part of the control element assembly is more of a structural design problem because of the motion of the control rods. The tube must be structurally stiff and not interfere with control rod motion.

The possibilities of other sensors as an alternate to the thermocouple sensor has been studied. The two viable candidates are the infrared thermal

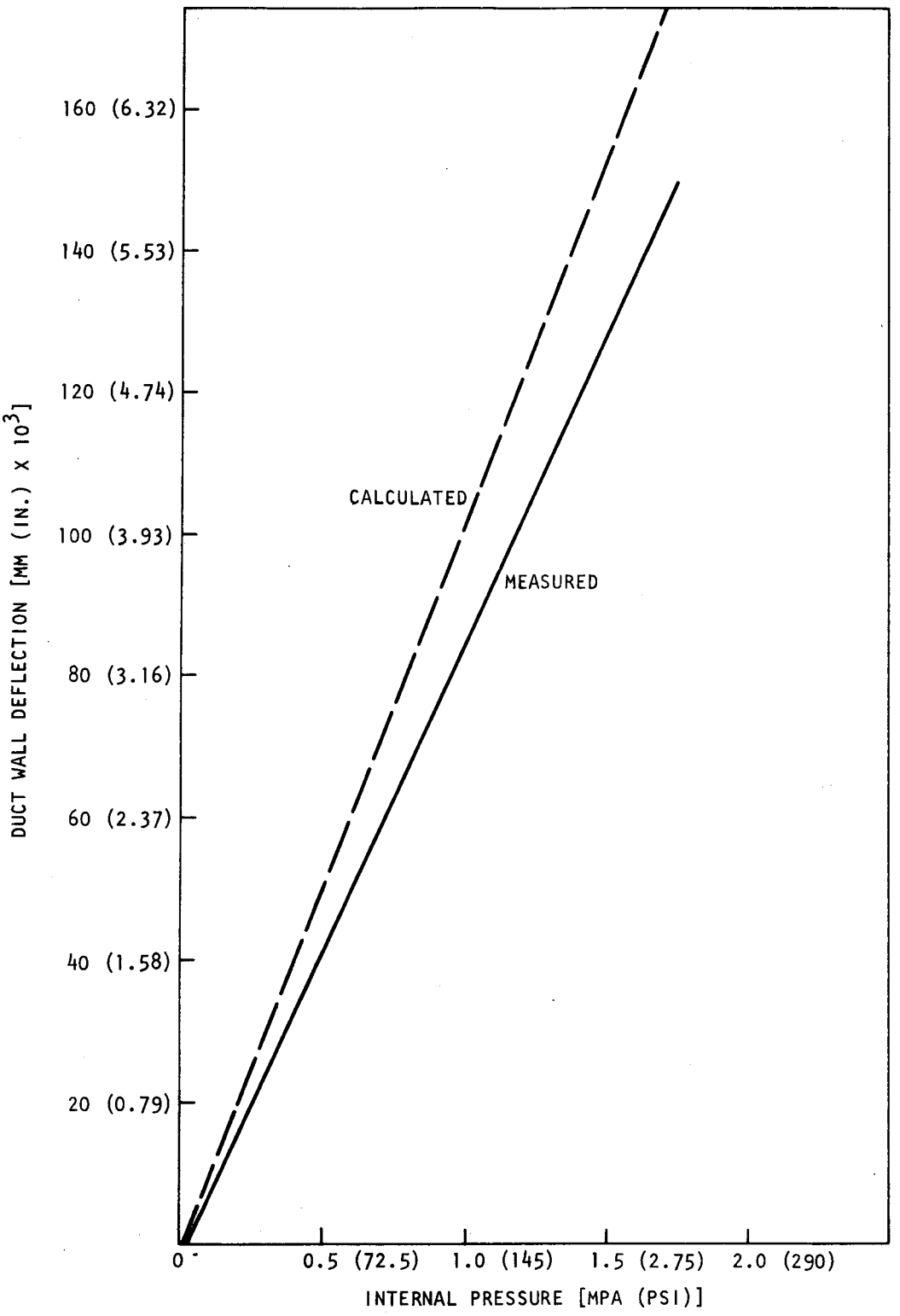


**Fig. 2-10 Pressure deflection test of hexagonal duct**

sensor and the Johnson noise thermometer. The infrared sensor concept is a system external to the core elements and is not part of the element assembly design. The Johnson noise thermometer measures the thermal noise power, which is a product of the radio frequency thermal noise voltage and the thermal noise current and a linear function of the absolute temperature of the sensor. The sensor itself is a resistor embedded in insulation inside a metal sheath that resembles a conventional thermocouple. In principle, it is extremely accurate and is unaffected by irradiation-induced changes such as wire resistance. The sensor is under development at ORNL primarily for fuel temperature measurement, i.e., above 1500°C (2732°F).

## 2.5. HEAT TRANSFER AND FLUID FLOW TESTING

The objective of this task for FY 76 is to initiate measurement of the pressure drop caused by components in the core element assemblies. The initial effort is to measure the pressure drop in the fuel element assembly inlet nozzle. To do this, a full-size plastic model of the inlet nozzle assembly has been designed. The detailed model design has been completed and the drawings reviewed and approved. The layout of the model is shown in Fig. 2-11. The fabrication of the model parts has been initiated. The hexagonal duct portion will be made by casting three sections, each 300 mm (1 ft) in length. The outer surface is cylindrical and the inner surface hexagonal. All other components such as shields, annular traps, and supports will be machined.

The pressure drop tests will be conducted at the GA Experimental Engineering Laboratory facility, where an air blower capability exists. The required air flow for simulation of helium flow is obtained by matching the Reynolds number for air to that for helium. Since the geometry and dimensions are exact for the model, the ratio of air flow to helium flow is simply a ratio of viscosities. The viscosity of air at standard conditions is $1.82 \times 10^{-5}$ N-s/m$^2$ (0.044 lb/ft-hr), and the viscosity of helium at design conditions of 322°C (617°F) and 9 MPa (1305 psia) is $3.22 \times 10^{-5}$ N-s/m$^2$ (0.078 lb/ft-hr). Thus, the required ratio of air flow

to helium flow is 0.565. The maximum helium flow rate in a 300-MW(e) GCFR core element is 6.6 kg/s (14.6 lb/s), so the required air flow is 3.7 kg/s (8.2 lb/s). The calculated pressure drop for this flow through the inlet nozzle assembly is 0.017 MPa (2.5 psia). The blower capability at the GA facility is 6.8 kg/s (15 lb/s) and a total pressure head of 0.031 MPa (4.5 psia).

The pressure losses will be measured by static pressure taps at the locations shown in Fig. 2-11. There are 24 taps located at 12 elevation levels in the outer nozzle wall (two at each elevation). Another set of 8 at 4 elevations is located in the central thermocouple tube. For the lower annular shield level, about 4 taps will penetrate the wall, support posts, and annular shield to measure pressures inside the annular shield. At the entrance to the grid manifold, a traversing pitot tube will be used to measure static and total pressures at various radial locations across the duct. There will be a short bundle of fuel-rod-size tubes below the manifold to give the flow a straightening section. This bundle length must be kept within a few millimeters because of the pressure head limitation of the blower. A pitot tube will be used to measure static and total pressure across the outlet of the bundle.

REFERENCES


2-1 "Gas-Cooled Fast Breeder Reactor Quarterly Progress Report for the Period November 1, 1975 Through January 31, 1976," ERDA Report GA-A13815, General Atomic, March 22, 1976.

2-2 Novendstern, E. H., "Pressure Drop Predictions for Fuel Assemblies with Wire Wrap Spacer System," Trans. Am. Nucl. Soc. 14, 660 (1971).

2-3 Roarke, R. J., Formula For Stress and Strain, 4th ed., McGraw-Hill, New York, 1965.

2-4 Mohr, C., P. Pankashee, and W. Anderson, "Gas Cooled Fast Reactor Fuel Duct and Spacer Mechanical Interaction Analysis," Battelle Pacific Northwest Laboratories Report TDO-610, July 1974.

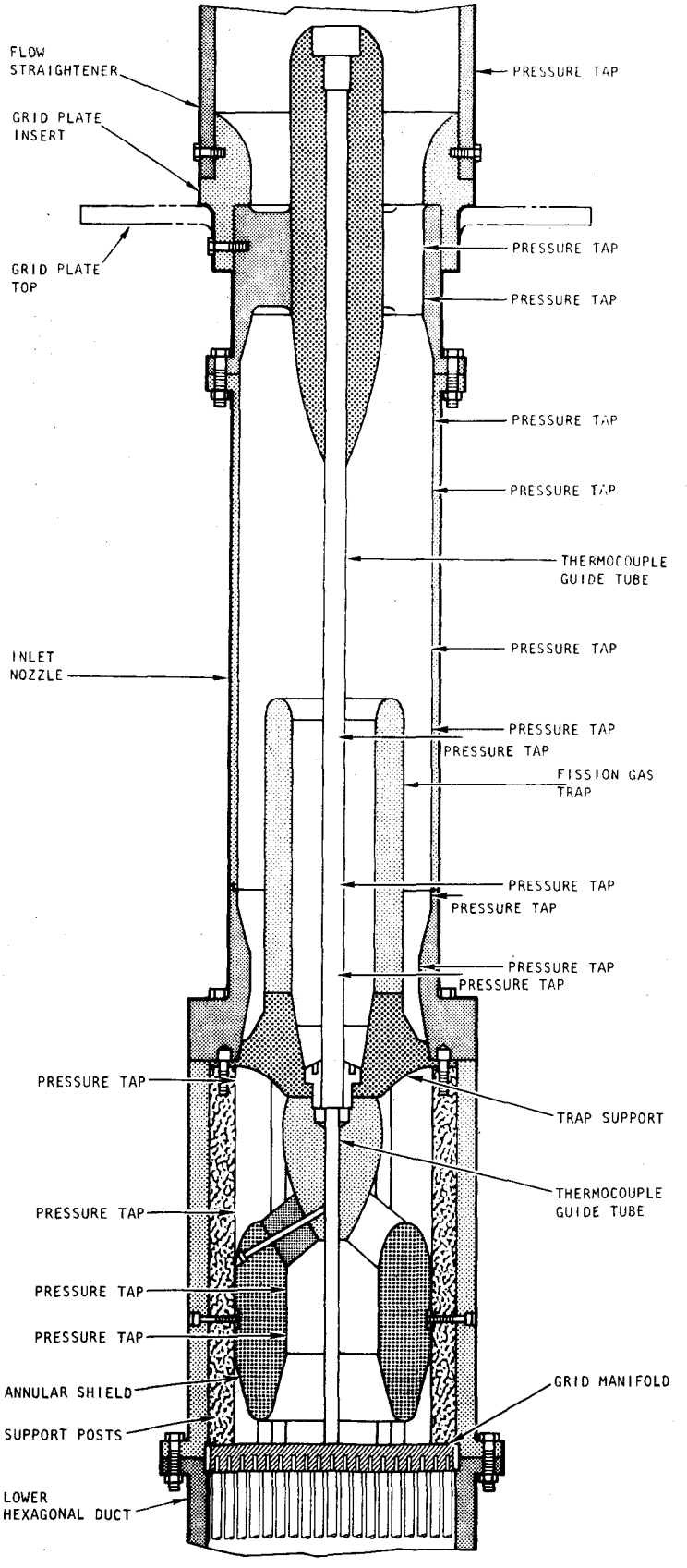


Fig. 2-11 Locations of static pressure taps

2-5 "Gas-Cooled Fast Breeder Reactor Quarterly Progress Report for the Period May 1, 1974 Through July 31, 1974," USAEC Report GA-A13148, General Atomic, September 26, 1974.

# 3. PRESSURE EQUALIZATION SYSTEM FOR FUEL (189a No. SU006)

## 3.1. FUEL ELEMENT AND VENT CONNECTION SEALS

In the GCFR reference design, the core elements (fuel, control, and blanket) and their vent connections are sealed to the grid plate by clamping the conical surfaces of the elements to the matching surfaces in the grid plate with a force sufficient to effect a seal and support the elements, which are cantilevered from the grid plate. These element seals must function at the coolant pressure difference between the reactor core inlet and exit plenums. The effectiveness of the seals over the life of the core is uncertain, not only because each element may be rotated or relocated several times over its useful life, but also because the seals must be effective in a high-purity, high-temperature helium environment while subject to mechanical, vibrational, and thermal effects. Most of the uncertainties are expected to be resolved in a two-part program: (1) a materials screening test program for the study of static adhesion of simulated fuel element and grid plate parts clamped together and (2) leakage tests of fuel element and vent connection seals to the grid plate. Current progress in these activities is described below.

### 3.1.1. Static Adhesion Tests

The alternate materials static adhesion testing phase of 3000 hr was completed, and the specimens will be given the post-test evaluation during the next quarter. There were no major problems during exposure of the test capsule.

### 3.1.2. Fuel Element Seal Leakage Tests

The reference design conical seal test parts were put back into the test autoclave for further side-load tests. The side bending moments

were applied to the element in small load increments, and helium leakage data were taken at various initial axial clamping loads. In addition, the increase in axial clamping load was measured as a function of increasing side load. Because of instrument limitations, the data are limited to leakages below 1.5 ℓ(stp)/s. The data are shown in Figs. 3-1 and 3-2, and the test method is shown in Fig. 3-3.

The side loading tests were again attempted after a rotation of 180 deg, but the seal parts leaked excessively (>1.6 ℓ/s). Examination of the surface showed a scored line on one side of the cone, which may have occurred from previous side load tests. The parts were sent to the shop and the cone surfaces reground to give a conical mismatch of 6.6 to 13.12 m. After rewelding the hex duct, the tests were run again in one position and again after a 180-deg rotation. The results of the leakage test in the first position were the same as those in Figs. 3-1 and 3-2. When the element seal part was rotated 180 deg, the results were the same as those in the previous test, i.e., excessive leakage associated with score marks. The side loading test results support the following two conclusions:

1. If conical metal-metal seals are to be utilized, then at least one of the materials should be harder than the 300 series stainless steel.

2. The moments that unseated the seal arise from forces in the range of forces that might be developed from element-to-element interferences resulting, for example, from irradiation swelling. As shown in Figs. 3-1 and 3-2, the load for unseating is about 2000 N for a clamp load of 13,300 N. Since the moment arm shown in Fig. 3-3 is 430 mm, the unseating moment is 860 N-m. For a full-length fuel element of 2780 mm, this unseating moment corresponds to a force of 310 N applied laterally at the bottom of the element.

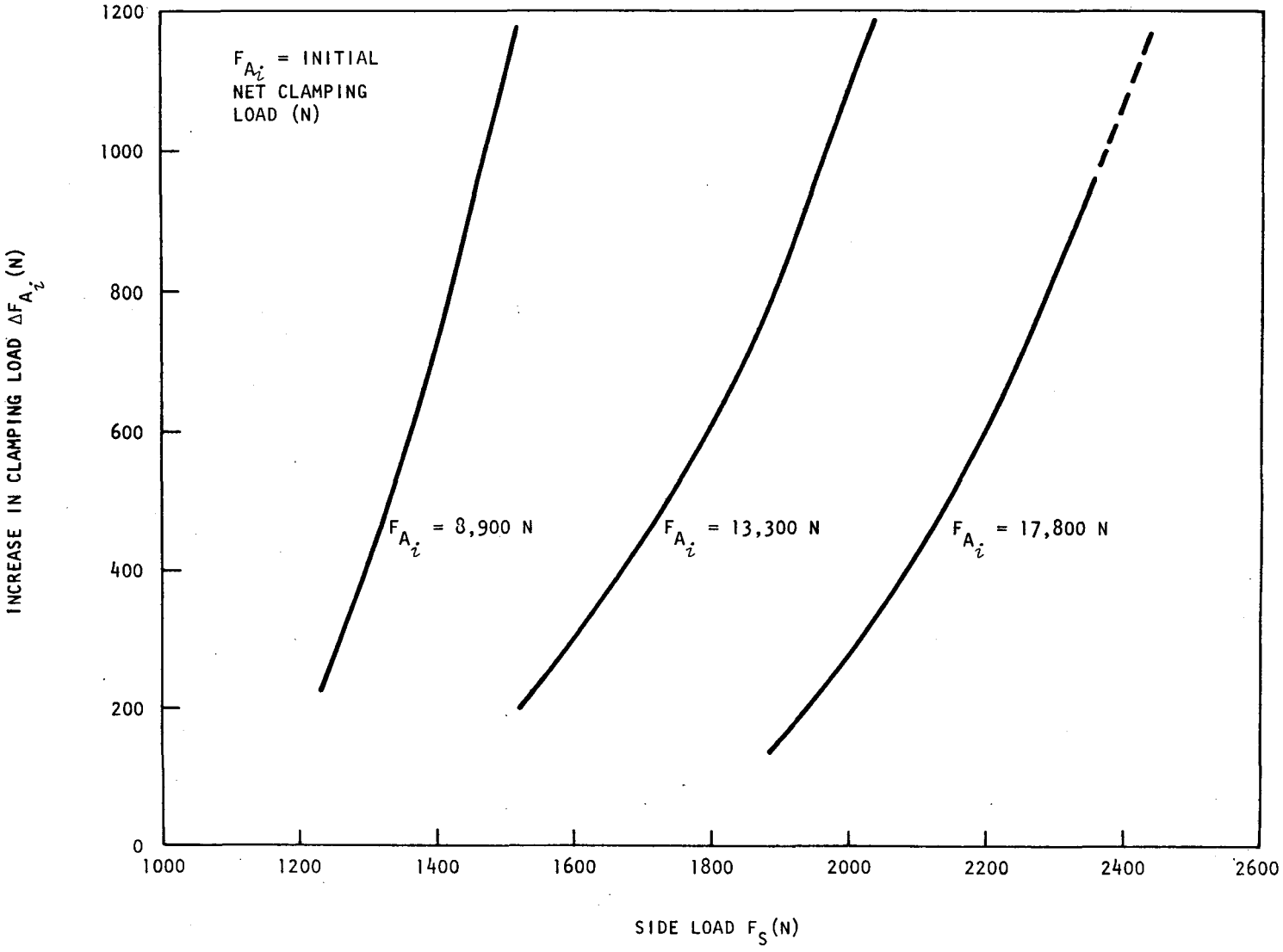


Fig. 3-1 Effect of side loading of fuel elements on their clamping load in the grid plate

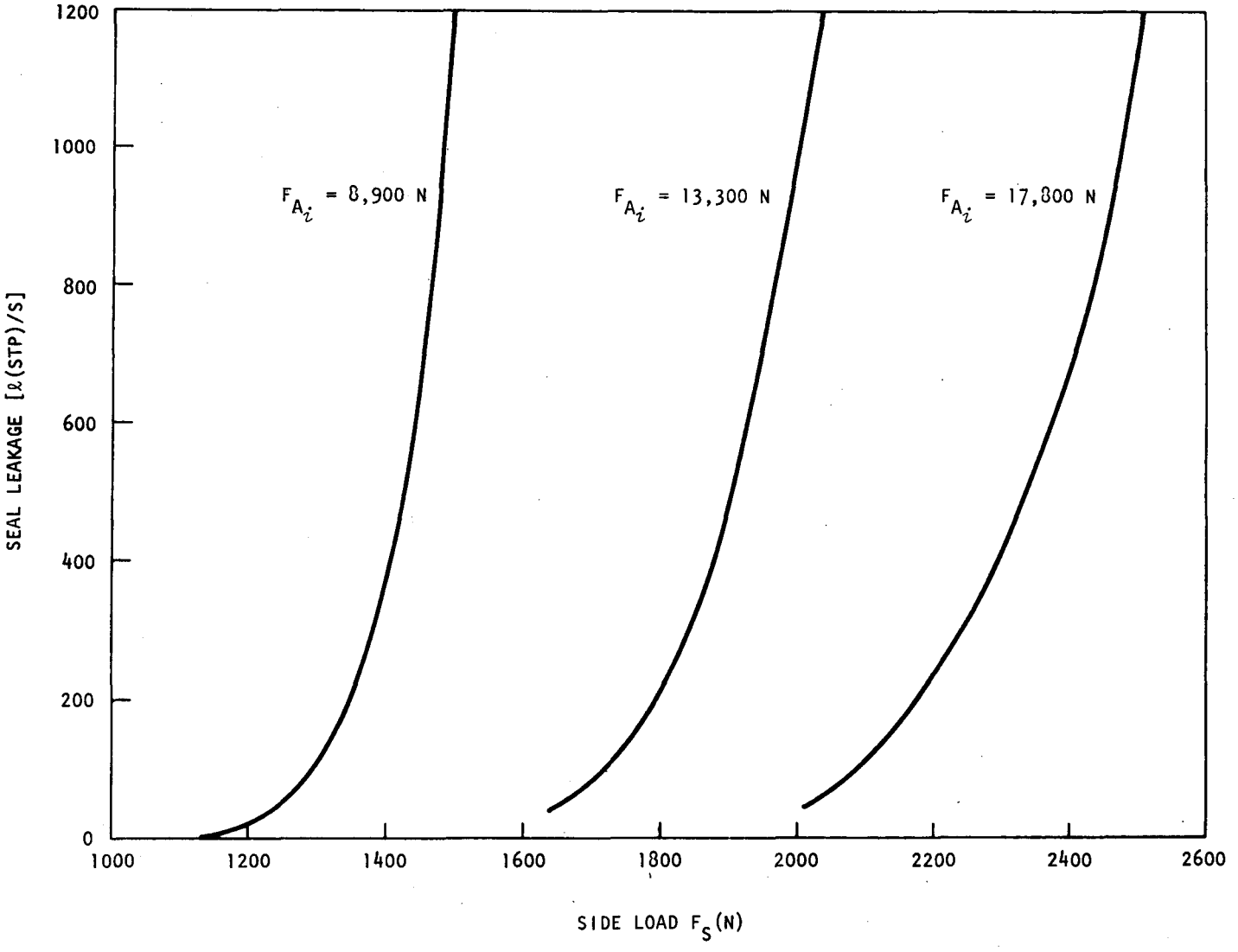


Fig. 3-2 Seal leakage as a function of side loading for various clamping forces

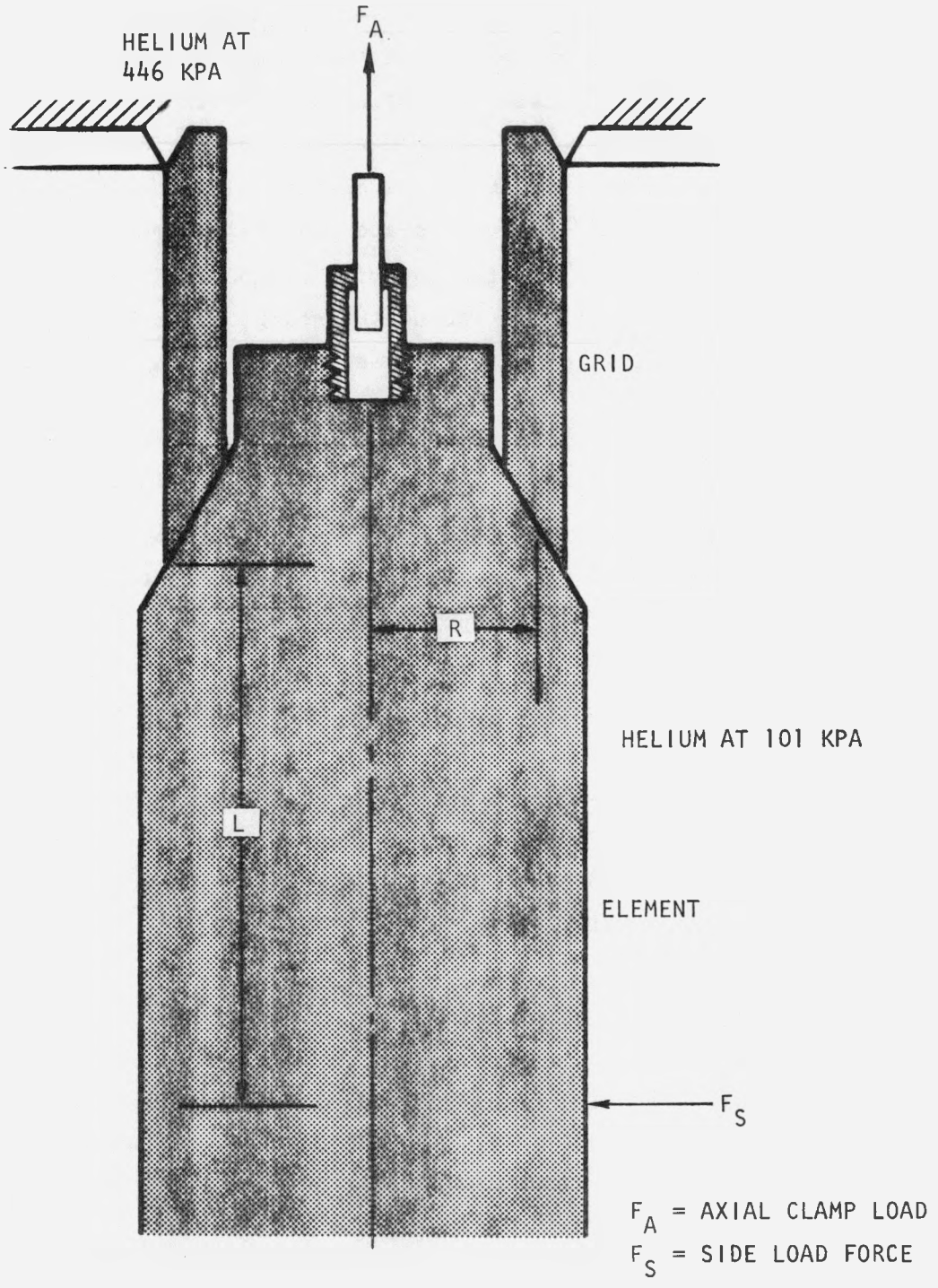


Fig. 3-3 Fuel element clamping into grid plate with unseating moment

### 3.1.3. Fuel Element Ring Seal Leakage Tests

An alternative to the conical metal-to-metal reference element seal design in which piston rings are used as sealing members is being developed. Piston ring seal tests are in preparation and are based on the design incorporated into the joint KWU-GA model core element being built by KWU in Germany. Test equipment and test grid plate and fuel elements parts used for metal-to-metal conical seal testing will be modified to test the piston ring seals. The test plan includes testing of the basic German design and piston ring designs, including three different ring materials, of two U.S. vendors.

The design of the apparatus for testing KWU piston seal rings was completed and the drawings approved. The assembly for testing in the autoclave is shown in Fig. 3-4. The apparatus also accommodates testing of U.S. piston ring designs. Dover Corporation and Stein Seal Company were selected to provide piston ring test assemblies. Dover has also supplied similar piston ring seals for the high-temperature gas-cooled reactor (HTGR) and the fast flux test facility (FFTF). Nine piston rings made of the three materials Inconel 718, type 410 stainless steel, and S-Monel were ordered from Dover. Three rings made of type 410 stainless steel were ordered from Stein Seal Company. All the piston rings will have electrodeposited chrome plating.

### 3.1.4. Vent Assembly Seals

A vent assembly is being developed for connecting the GCFR fuel elements to the vent passages in the grid plate and for sealing the vent port of the core elements when they are removed from the grid plate for handling, storage, and transport.

The design for testing the vent assembly in the element seal test autoclave depends on the method for mounting the vent assembly in the conical surface of the element. This mounting has not yet been designed.

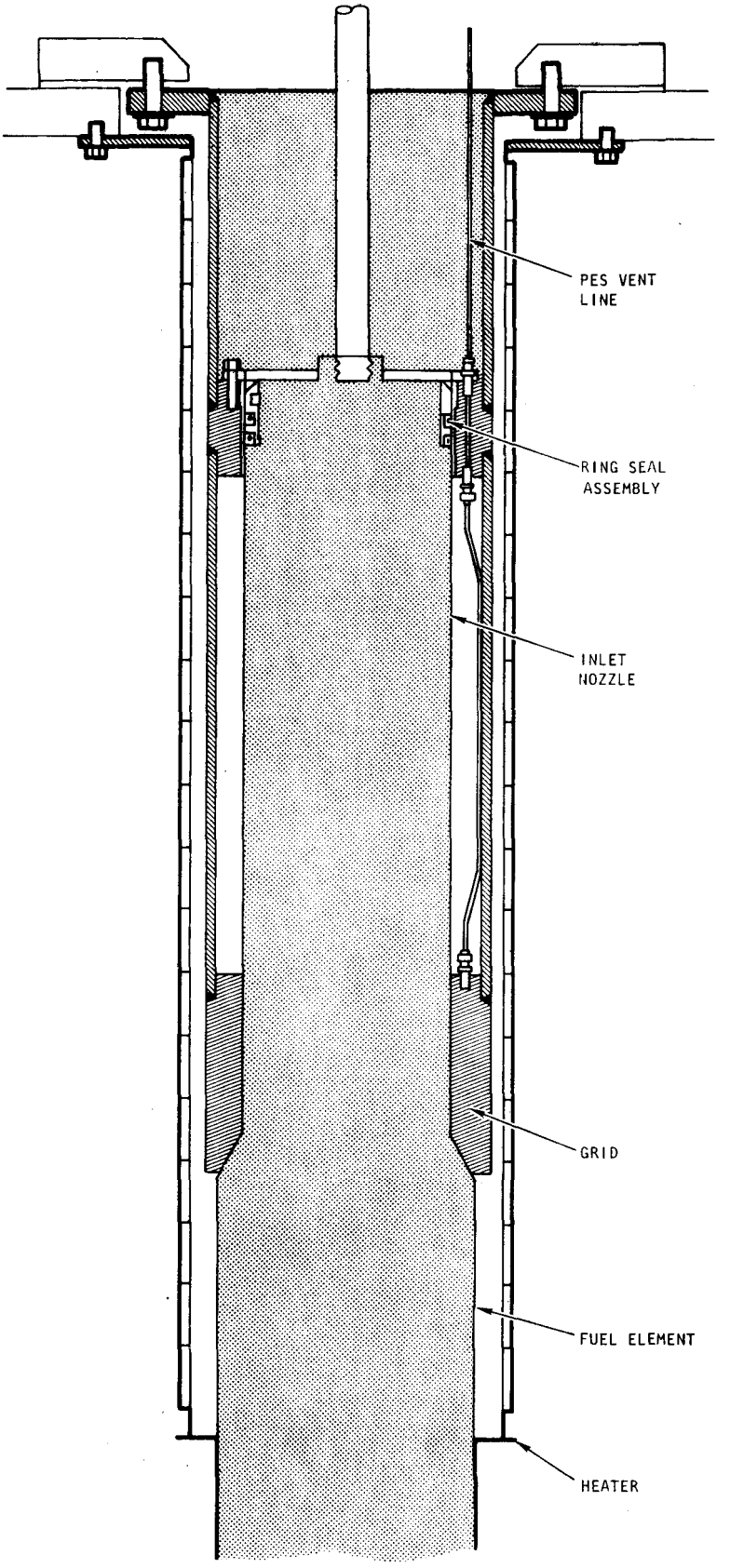


Fig. 3-4 Testing assembly

Welding development of the joint between the valve's seal bellows and the end cap was continued. Several successful seal welds were made using tungsten inert gas (TIG) welding methods with a copper chill block on the bellows. It was necessary to anneal the bellows prior to welding. This is acceptable since the bellows function only for sealing.

Parts were machined for attaching the vent assemblies for valve seat leakage testing to the apparatus previously assembled to test leakage of fuel rod joints to manifolds. The preliminary tests of the first port seal valve prototype were completed to temperatures of 300°C. The test setup is shown in Fig. 3-5, and the test results are shown in Figs. 3-6 and 3-7. The performance of the vent connection seal (across torus face of Fig. 3-5) is well within the specification of 135 mℓ stp/min, as shown in Fig. 3-6. The leakage through the port valve seal shown in Fig. 3-7 is considered to be high, although no specification for this leakage has been established. After leakage testing, the valve spring load was checked on the Instron load machine. The load had relaxed about 30%, which was not unexpected. The Belleville washers are rated for continuous operation to 260°C. It is this spring relaxation that resulted in higher room temperature leakage rates at the recheck points shown in Fig. 3-7. A higher alloy material will be needed for the final design. Belleville washers made of 17-7PH material, which has the capability of continuous operation at 370°C, have been ordered.

Two design changes are being made to improve the sealing of the port valve seal. The first change is to increase the cone angle mismatch from just a few minutes to a full degree to assure line contact sealing. The second change is to increase the spring preload from 177 to 444 N.

## 3.2. ANALYSIS, MODELS, AND CODE DEVELOPMENT

Development of a computer code for transient analysis of the PES flow network continued during this quarter.

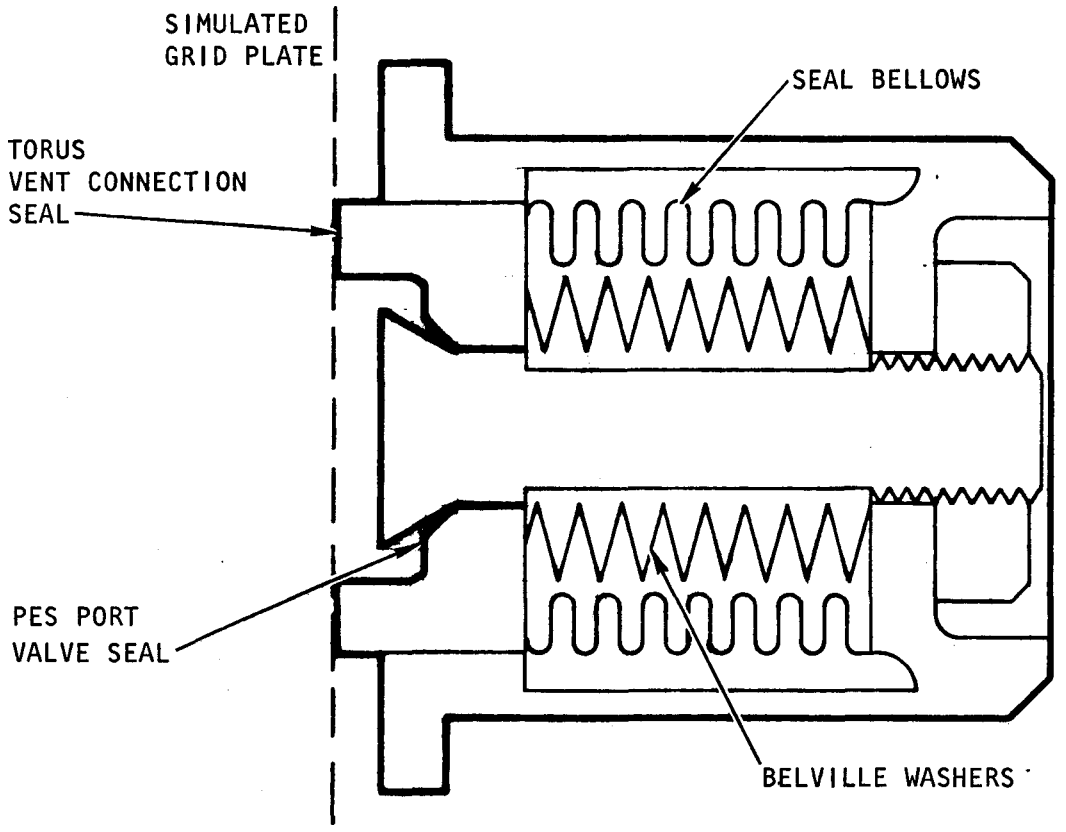


Fig. 3-5 PES vent connection seal and port valve assembly

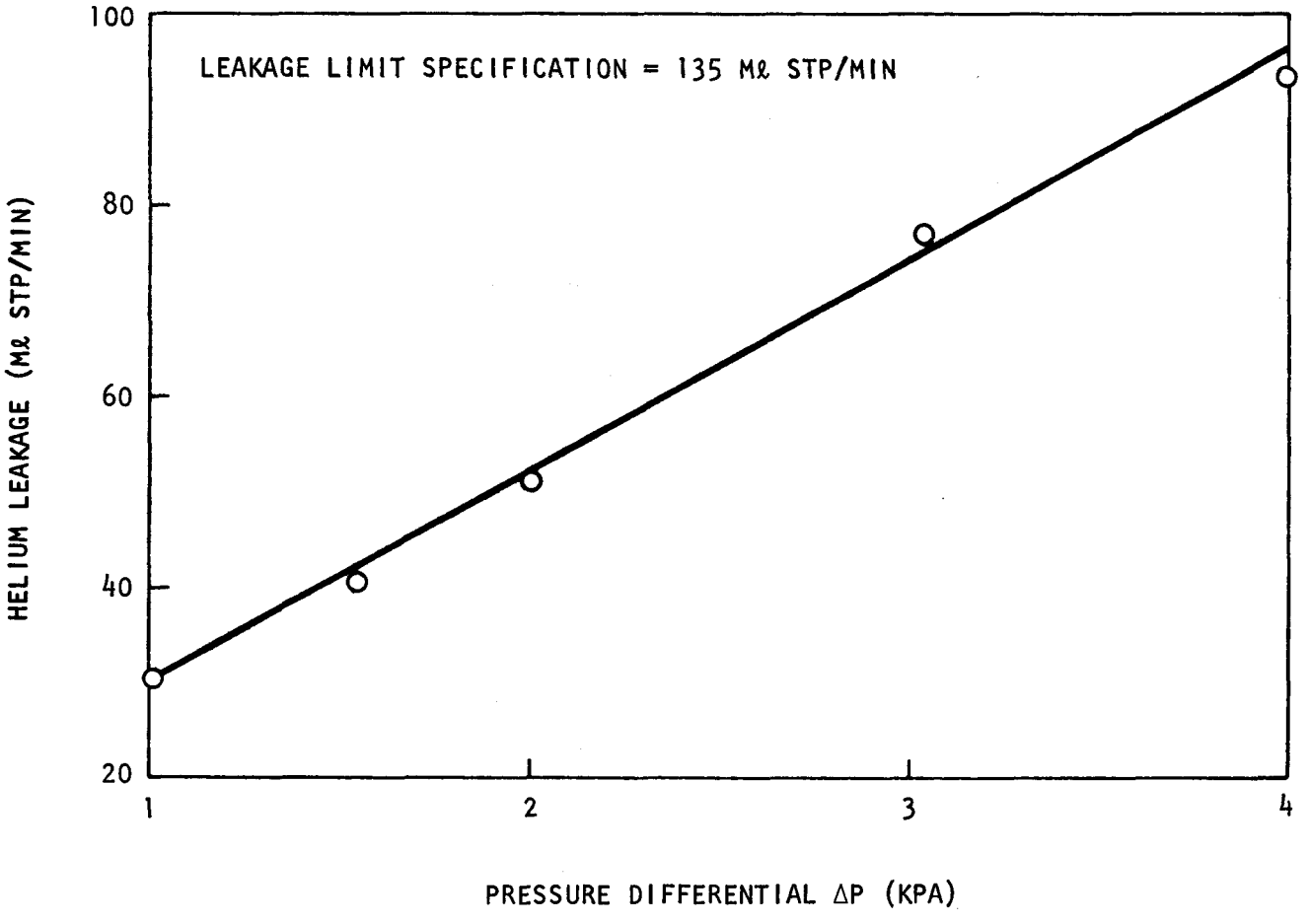


Fig. 3-6 PES vent connection leakage ambient temperature

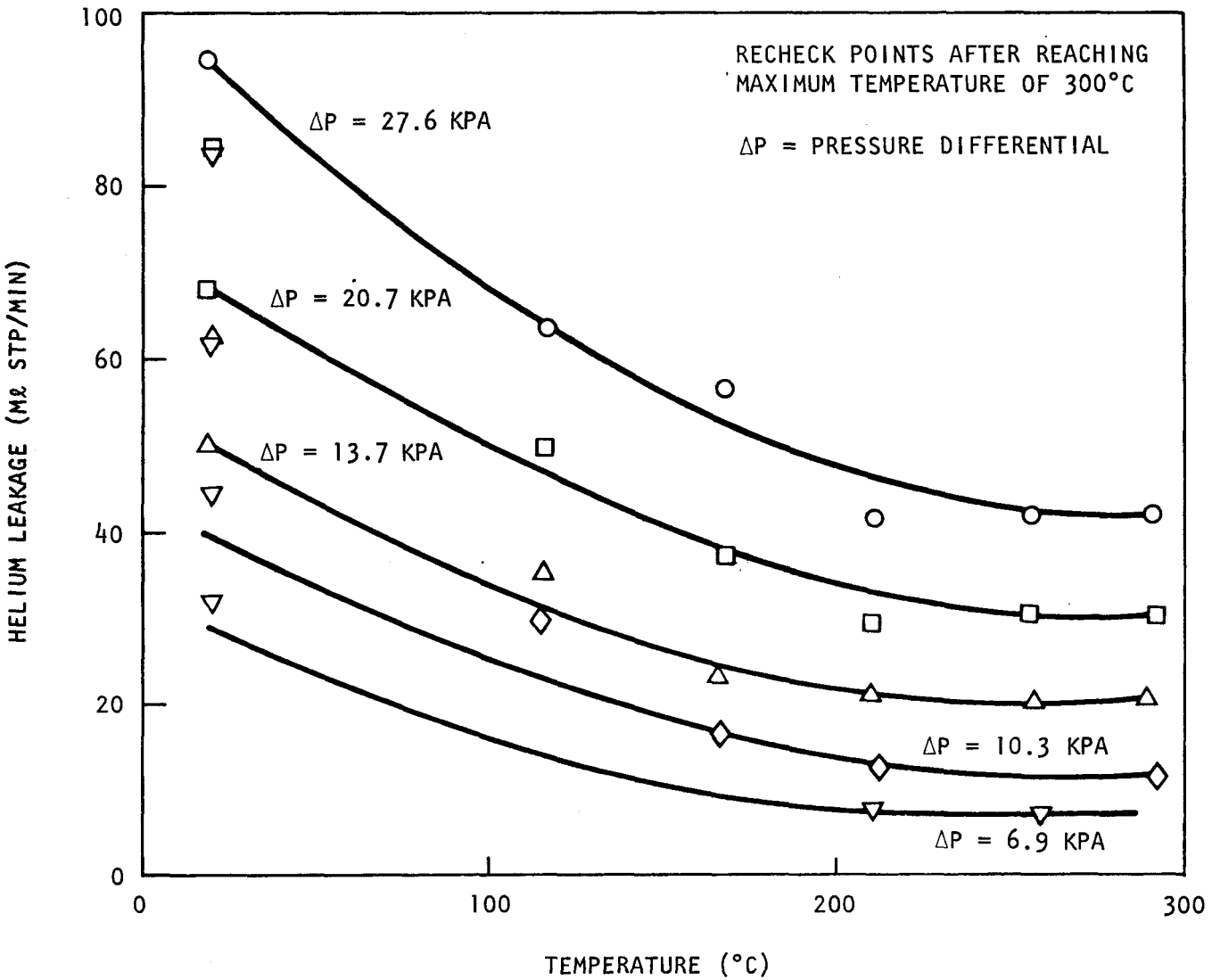


Fig. 3-7 Port seal valve leakage

During the previous quarter, the model for simulating the GCFR helium purification system (HPS) (reported in Ref. 3-1) was incorporated into a simplified representation of the GCFR PES. For the present simulation, the PES network has been reduced to a one-dimensional model, with volumes representing the fuel rod and the monitor line volumes and pipes representing the gas passages in the fuel element, the monitor lines, the suction holes, and the vent connection. This configuration will provide an initial trial for determining the transient flow of gas from nonleaking rods during normal, upset, and emergency transients. With some modification, this model will also handle leaking rods. The model has been programmed and has successfully compiled. However, so far, the steady-state routine has been unable to obtain a converged steady-state solution. The difficulties appear to result from an unusually large spread in the eigenvalues associated with the problem, causing the program to have difficulty in inverting the Jacobian matrix. Work is in progress to eliminate this problem.

Work was initiated to obtain a preliminary layout of the PES and HPS piping network so that pipe lengths and sizes could be modeled. This information is being incorporated into the simulation model.

To aid in establishing the minimum pressure drop required by the GCFR PES, the pressure drop and the flow of the Fort St. Vrain HPS (upon which the design of the GCFR HPS is currently based) were determined. Calculations were made to determine the pressure drop required of a system similar to that operating at Fort St. Vrain under GCFR pressure and flow. From this, the pressure drop requirement of the GCFR PES was estimated to be 99.3 kPa. It was also found that this could be reduced to the current available design $\Delta P$ of 65.5 kPa by an $\sim$20% reduction in PES flow. The reduced flow is well within the acceptable flow range for the demonstration plant.

## 3.3. PLATEOUT AND PLUGGING

During this quarter, work continued on the development of components that will make up the laboratory-size, high-pressure helium loop to be

used for plateout and plugging experiments. The work included measurement of water-vapor enhancement factors in the high-pressure water vapor saturator; endurance testing of the helium circulators; remeasurement of the circulator characteristic curve at high pressure; and design and construction of a gas heater.

### 3.3.1. High-Pressure Water Vapor Saturator

Preliminary experiments were performed to measure the enhancement factor for water vapor pressure over ice in high-pressure helium. At present, data have been acquired at an ice temperature of 253 K over a pressure range of 3.69 to 8.62 MPa. The data are presented in Table 3-1. The apparent constancy of the observed enhancement factor is suspect. From previous experiments with a GA dew-point hygrometer, it has been observed that at frost-point temperatures of <233 K, the instrument appears to give readings that are biased on the high side of the expected temperature. Further study is required to decide whether a problem exists and if so, the source of the problem.

### 3.3.2. Plateout and Plugging Test Loop Construction

3.3.2.1. Helium Circulators. The parallel arrangement of the diaphragm pumps has successfully operated in high-pressure helium ($P_T \geq 8.6$ MPa) for over 300 hr. At the conclusion of one 190-hr test, the loop gas was analyzed for impurities in an effort to determine if the pumps were adding contaminants to the system. The only impurities found were $H_2$, $N_2$, and $O_2$, which were already present in the gas source bottle.

Some problems were encountered in flow metering at the high pressures used in the loop. It was determined that the original flow measurements were in error, and the flow meter was replaced with a calibrated rotameter (in a pressure-equalized armor casing). As a result, the previously reported pump characteristic curve (Ref. 3-1) has been invalidated. The corrected pump characteristic curve is presented in Fig. 3-8 and was obtained with

TABLE 3-1
ENHANCEMENT FACTOR OF WATER VAPOR PRESSURE IN HIGH-PRESSURE HELIUM

| $P_T$ (MPa) | Predicted Saturation Vapor Pressure $e_s$ (Pa) | Observed Saturation Vapor Pressure $e_s'$ (Pa) | Enhancement Factor $e_s'/e_s$ |
|---|---|---|---|
| 8.62 ± 0.07 | 101.4 ± 0.9 | 115.8 ± 4.1 | 1.142 ± 0.051 |
| 7.20 ± 0.07 | 101.4 ± 0.9 | 116.5 ± 4.2 | 1.149 ± 0.052 |
| 5.31 ± 0.07 | 101.4 ± 0.9 | 115.8 ± 4.6 | 1.142 ± 0.056 |
| 3.69 ± 0.07 | 101.4 ± 0.9 | 116.3 ± 5.2 | 1.147 ± 0.062 |

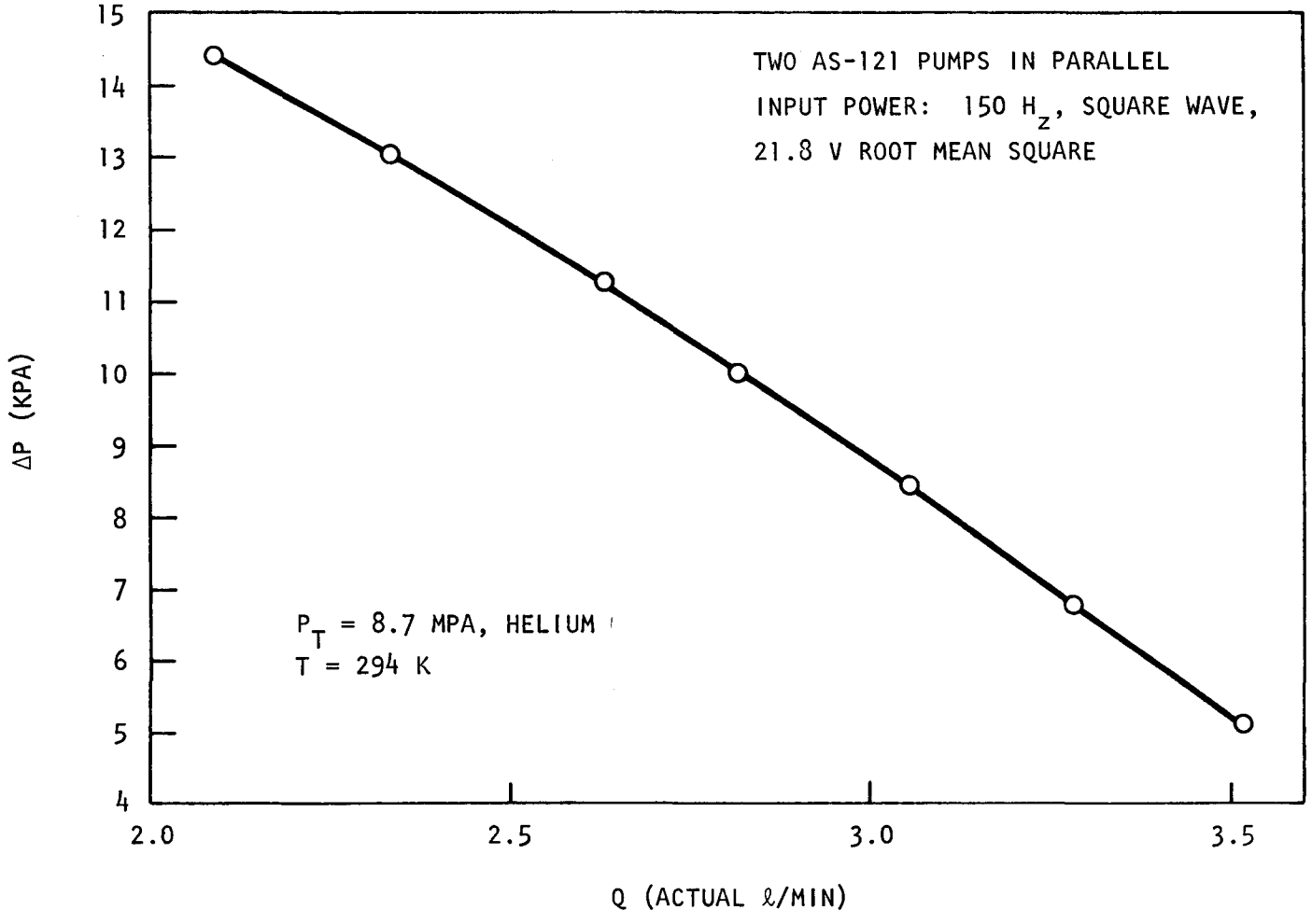


Fig. 3-8 Circulator characteristics

the calibrated rotameter. The data indicate that the pump will be able to deliver 2.5 ℓ(actual)/min of helium against a head of 12 kPa (at 8.6 MPa total pressure). Although this is slightly derated from the initial design criteria, it is believed to be adequate.

3.3.2.2. Gas Heaters. After a series of design calculations, a series arrangement, two-stage gas heater was built for the loop. Current experimentation is under way to test the heating and control capabilities of the heater.

## 3.4. PES MANIFOLD FABRICATION

Two sections cut from an investment cast 316 stainless steel manifold were exposed to helium containing 90 μatm of $H_2O$ and 900 μatm of $H_2$ for 3000 hr at 350°C. One specimen was in the as-received condition, the other was electrochemically etched for 15 min (at 12 A) in an Ionetics solution. The part exposed in the as-received condition showed a heavy dark oxide film on its surfaces. The section which had been etched prior to exposure exhibited a very bright shiny surface, just as it had prior to the exposure. Auger spectroscopy of the surfaces will be performed to determine what compositional differences can be detected in the two specimens.

Dimensional inspection of four one-third-segment investment cast manifolds [including three one-third-segment cast fission product manifolds into which fission gas passages were drilled by EDM, electrochemical machining (ECM), and gun drilling] and three full-size investment cast manifolds has been completed and the results are being analyzed. The results analyzed to date are summarized below.

The four one-third-segment and three full-size fission product investment cast manifolds were dimensionally checked upon receipt at GA. The measuring device used was a Cordax machine. The sensing probe on the Cordax is moved by the operator to a position on the part to be measured;

in this case, to the circular bosses on the manifold webs. After contacting each boss at three points approximately 120 deg apart, the Cordax computes the theoretical center and prints out the center location in an X-Y coordinate system plot. These Cordax plotted locations were then compared with the drawing locations, and the comparison results were plotted as a frequency diagram. Certain of the bosses near the edge of the manifold are not completely round (see Fig. 3-9), and the centers of these bosses were difficult or impossible to locate by the Cordax contacting three angular positions.

The deviations for the location of the bosses which are not round were not plotted when the value was excessive and obviously a measurement error. Some of the deviations in the X direction were out of tolerance on all webs, while the Y deviations shifted progressively to a complete out-of-tolerance situation for large values of Y. This indicates a problem in controlling shrinkage in the direction normal to the webs and a need for adjustment for the shrinkage in the design of the tooling for casting. The one-third-segment manifolds were then stress relieved at 400°C for 4 hr and remeasured. The deviations of boss locations after stress relief with respect to their locations in the as-received conditions are generally within a $\pm$0.13-mm band.

The results of the Cordax dimensional measurements for the full-size manifolds (see Fig. 3-10) show that the Y deviations are comparable in magnitude and direction to those for the one-third manifold segment above. Compared with the dimensional shift in the one-third segments, the shift in dimensions in the full-size manifolds is reversed because the full-size manifold was measured from left to right (+Y to -Y), while the one-third manifold segment was measured and plotted from right to left ($Y_o$ to $Y_{max}$ or +Y). The Y measurements on the right-hand side of the full-size manifold, however, indicate an excessive shrinkage or undercompensation for shrinkage in the pattern or tooling. The spread in values along the Y coordinate appears to be systematic, indicating an error reflected by a slight skew (~0.2 mm) in picking up the average attitude of the sides of the bosses in setting up to do the measurement. The full-size manifold

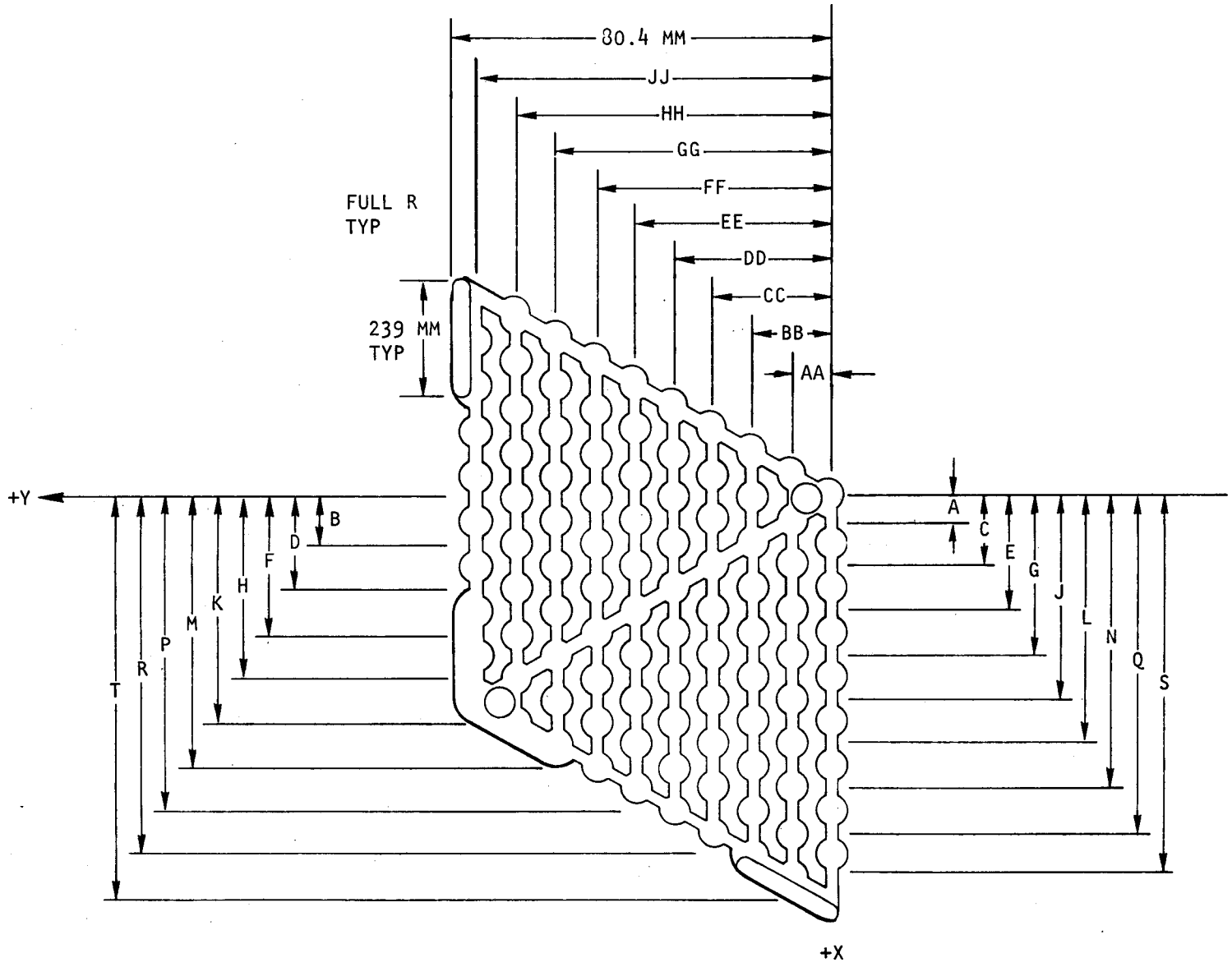


Fig. 3-9 Dimensions of one-third-segment manifold

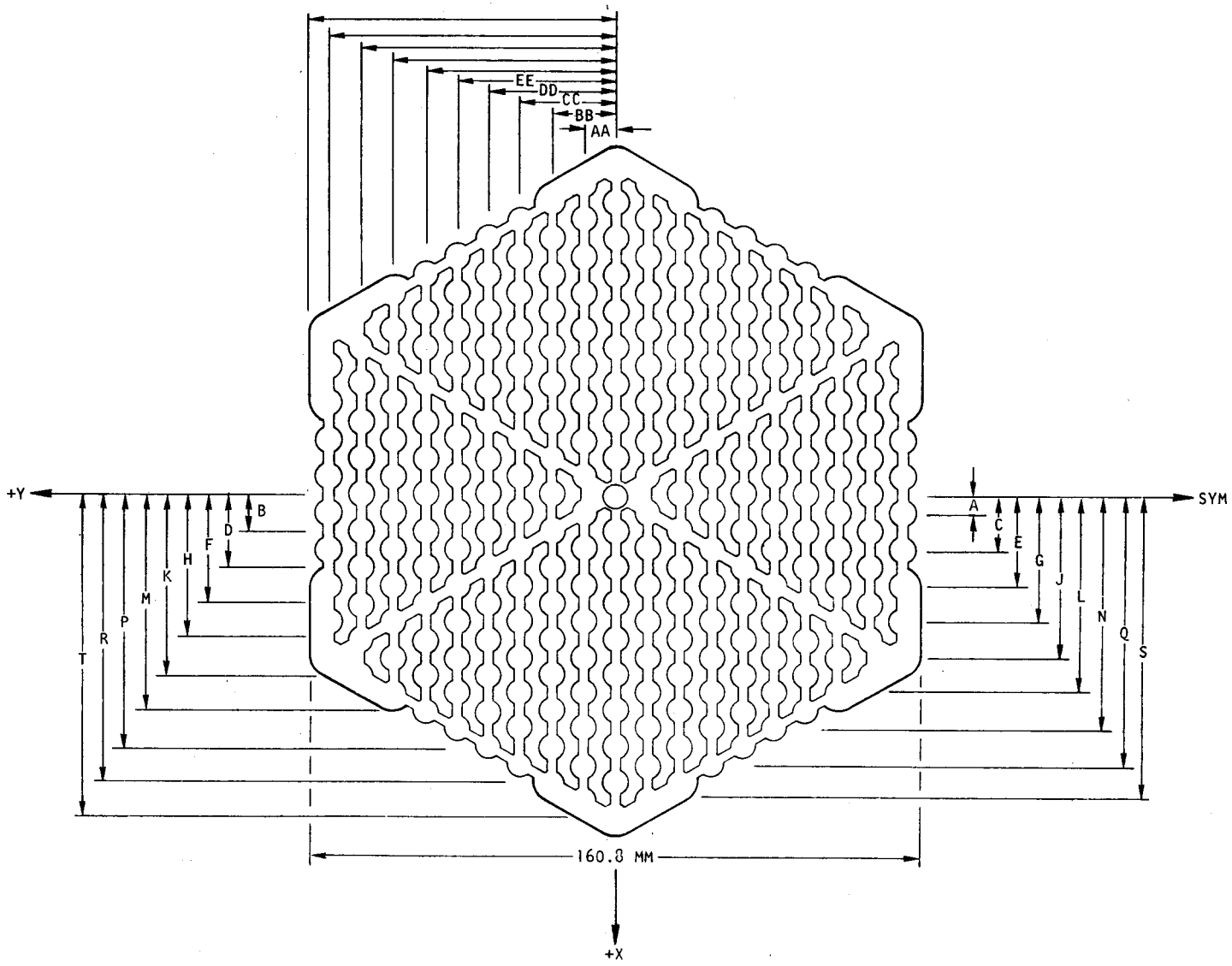


Fig. 3-10 Dimensions of full-size manifold

part was cast with the plane of the hex in a vertical position and the solidification front moving in the +Y direction. This could explain the progressive change in amount of shrinkage measured in the Y direction. Examination of deviations in the X direction shows a trend for these deviations to be greatest at the middle of the part (Y = 0) where the greatest amount of metal was solidifying during casting at one time. It is anticipated that in the future, the information obtained from these measurements could be used in the design of casting patterns and tooling to produce full-size manifold castings with shrinkage values within the established tolerances.

Work on preparation of a final summary report on manifold fabrication development has been initiated.

## 3.5. PES PROGRAM PLANNING

This task has been deleted owing to budget cuts.

## REFERENCE

3-1 "Gas-Cooled Fast Breeder Reactor Quarterly Progress Report for the Period November 1, 1975 Through January 31, 1976," ERDA Report GA-A13815, General Atomic, March 22, 1976.

# 4. CORE FLOW TEST LOOP PROGRAM (189a No. SU006)

A series of out-of-pile simulation tests will be performed (1) to demonstrate the ability of the GCFR fuel, control, and blanket assembly designs to meet design goals and (2) to verify predictions of analytical models that describe design operation and accident behavior. The test emphasis will be on obtaining thermal-structural data for steady-state, transient, and margin conditions using electrically heated rod bundles in a dynamic helium loop. The requirements include testing in the range of cladding melting and the consequences of local initiation of melting. The core flow test loop (CFTL) program plan (Ref. 4-1) contains the requirements for the test program to be conducted in the CFTL which will be constructed and operated by Oak Ridge National Laboratory (ORNL). The principal work accomplished during this quarter included

1. Initiation of work on a draft of revision 1 to Ref. 4-1.
2. Expansion of a computer code to aid in evaluating proposed transient test conditions.
3. Preparation for and participation in coordination and review meetings with ORNL.
4. Preparation of a preliminary draft of the Prototype Test Program Plan.

## 4.1. PROGRAM PLANNING

### 4.1.1. Program Plan

Reference 4-1 is undergoing a first revision which reflects the activities that have occurred since its initial issue in August 1974.

Major items are the inclusion of a detailed Section 7, "Test Analysis and Prediction Requirements;" conversion to the SI system of units; and removal of the test measurement information sheets (TMIS), which will be included or referenced in the test specifications.

### 4.1.2. GCFR and CFTL Schedule

The GCFR major milestone schedule (per ERDA funding guidelines) indicates that the CFTL tests will start in early 1980. The construction of the loop is considered by ORNL (based on ERDA funding) to be a line item for FY 78.

## 4.2. TEST ANALYSIS AND PREDICTION

### 4.2.1. Bundle Performance

The special-purpose computer code TSPEC, which was developed to aid in the preparation of test specifications and to predict test results from a simplified analytical approach to test bundle temperatures, pressures, and thermal expansion characteristics, has been expanded to cover transient test conditions. Reference 4-2 discusses the development of transient modeling. Table 4-1 lists test conditions and predicted results for a sample transient (scram) test. In this sample test, the power was linearly ramped down from 100% to 40% of the initial condition within 0.7 s, followed by a linear reduction to 10% in 2.2 s. The flow reduction was delayed 2 s beyond the start of power reduction. Flow was then linearly ramped down to 29% of the initial condition within 38 s, followed by a linear reduction to 10% in 39 s.

The first sheet of Table 4-1 lists the geometric input parameters to the computer code; the second sheet lists the power, helium flow, and input temperature conditions plus a summary of predicted thermal output, flow output, and thermal expansion parameters for test conditions prior to and following the scram; the third sheet lists the predicted initial and final values for pressure, power, and temperature (helium

TABLE 4-1

CFTL TEST SPECIFICATION FOR TEST SAMPLE TR 1, BUNDLE A

BUNDLE DESIGN

BUNDLE TYPE - FUEL

BUNDLE IDENTIFICATION - A

BUNDLE DATA

RODS PER BUNDLE = 37. HEATED = 31. UNHEATED = 6.

BUNDLE OD = 75.0 MM

DUCT WALL THICHNESS = 2.500 MM

BUNDLE FLOW AREA = 1613. MM**2

DUCT PERIMETER = 210.00 MM

AVG BUNDLE HYDRAULIC DIAMETER = 6.03 MM

ROD DATA

ROD DIAMETER = 7.40 MM

ROD PITCH = 10.00 MM

HEIGHT OF ROUGHENING = .100 MM

PITCH OF ROUGHENING = 1.20 MM

FLOW AREA PER ROD = 43.59 MM**2

H T PERIMETER PER ROD = 23.25 MM

LOCAL HYDRAULIC DIAMETER = 7.50 MM

UPPER BLANKET LENGTH = 650.5 MM

HEATED LENGTH = 1000.0 MM

LOWER BLANKET LENGTH = 450.0 MM

TOTAL LENGTH = 2100.5 MM

ROUGHENING DATA

ROUGHENED FRACTION OF HEATED LENGTH = .750

ROUGHENED LENGTH = 750.0 MM

FRICTION FACTOR MULTIPLIER = 3.00

HEAT TRANSFER MULTIPLIER = 2.00

REFERENCE REYNOLDS NO = 100000.

SPACER AND FLOW COEFFICIENT DATA

NUMBER OF SPACER = 10.

SPACER COEFFICIENT = .600

SPACER SOLIDITY = .179

INLET COEFFICIENT = .100

OUTLET COEFFICIENT = .500

HEATER AXIAL POWER PROFILE

AXIAL QMAX/QAVG = 1.210

QX/QMAX = COS( 1.049*(2*X/L - 1))

| X/L | QX/QMAX |
|---|---|
| .000 | .4984 |
| .100 | .6681 |
| .200 | .8084 |
| .300 | .9133 |
| .400 | .9781 |
| .500 | 1.0000 |
| .600 | .9781 |
| .700 | .9133 |
| .800 | .8084 |
| .900 | .6681 |
| 1.000 | .4984 |

## TABLE 4-1 (continued)

TRANSIENT TEST SERIES RUN NO. - 1

LINEAR POWER AND FLOW RAMP

| | FRACTION (1) | FRACTION (2) | FRACTION (3) | START TIME (S) | DECAY TIME (S) (2)-(1) | DECAY TIME (S) (3)-(2) |
|---|---|---|---|---|---|---|
| POWER | 1.000 | .400 | .100 | .2 | .7 | 2.2 |
| FLOW | 1.000 | .290 | .100 | 2.2 | 3.8 | 39.0 |

| | INITIAL CONDITIONS | FINAL CONDITIONS |
|---|---|---|
| **INPUT PARAMETERS** | | |
| TOTAL BUNDLE HEAT INPUT, KW | 744.000 | 74.400 |
| AVG POWER PER ROD, KW | 24.000 | 2.400 |
| MAX POWER PER ROD, KW | 25.600 | 2.560 |
| MIN POWER PER ROD, KW | 22.400 | 2.240 |
| FLOW PER BUNDLE =, KG/SEC | .873 | .087 |
| HELIUM INLET TEMPERATURE, C | 325.0 | 325.0 |
| HELIUM INLET PRESSURE, MPA | 9.000 | 9.000 |
| **THERMAL OUTPUT PARAMETERS** | | |
| AVERAGE BUNDLE OUTLET TEMPERATURE, C | 489.2 | 489.2 |
| AVERAGE BUNDLE TEMPERATURE RISE, C | 164.2 | 164.2 |
| OUTLET TEMPERATURE - AVG POWER ROD, C | 520.9 | 520.9 |
| TEMPERATURE RISE - AVG POWER ROD, C | 195.9 | 195.9 |
| OUTLET TEMPERATURE - MAX POWER ROD, C | 534.0 | 534.0 |
| TEMPERATURE RISE - MAX POWER ROD, C | 209.0 | 209.0 |
| OUTLET TEMPERATURE - MIN POWER ROD, C | 507.9 | 507.9 |
| TEMPERATURE RISE - MIN POWER ROD, C | 182.9 | 182.9 |
| MAX SURFACE TEMPERATURE, C (AT X/L = ) | 579.4 ( .940) | 574.1 ( .960) |
| FILM DROP AT MAX SURFACE, C | 52.1 | 44.3 |
| MAX POWER DENSITY, W/CM | 309.8 | 31.0 |
| SMOOTH H. T. COEF, W/M*M/C | 7088. | 1201. |
| ROUGTH H. T. COEF, W/M*M/C | 15870. | 1761. |
| **FLOW OUTPUT PARAMETERS** | | |
| BUNDLE AVG. RE | 94694. | 9469. |
| LOCAL RE | 106107. | 10611. |
| TOTAL BUNDLE PRESSURE DROP, KPA | 408.401 | 3.772 |
| INLET, KPA | 2.151 | .022 |
| UPPER BLANKET, KPA | 42.442 | .673 |
| SMOOTH CORE LENGTH, KPA | 19.307 | .299 |
| ROUGHENED CORE LENGTH, KPA | 171.881 | 1.311 |
| LOWER BLANKET, KPA | 112.986 | .882 |
| ACCELERATION LOSS, KPA | 6.042 | .059 |
| SPACERS LOSS, KPA | 39.880 | .390 |
| OUTLET LOSS, KPA | 13.711 | .137 |

**THERMAL EXPANSION PARAMETERS**

| THERMAL INPUT AS FABRICATED | | TEST TEMPERATURE DUCT | TEST TEMPERATURE ROD | TEST TEMPERATURE DIF | TEST TEMPERATURE DUCT | TEST TEMPERATURE ROD | TEST TEMPERATURE DIF |
|---|---|---|---|---|---|---|---|
| AVERAGE, MM | 2100.5 | 2115.2 | 2116.4 | 1.2 | 2115.2 | 2116.3 | 1.1 |
| HOTTEST, MM | 2100.5 | 2115.4 | 2116.7 | 1.3 | 2115.4 | 2116.6 | 1.2 |
| COLDEST, MM | 2100.5 | 2115.0 | 2116.1 | 1.1 | 2115.0 | 2116.0 | 1.0 |
| MAX BOW DISPLACEMENT, MM | | | 10.0 | | | 10.0 | |

## TABLE 4-1 (continued)

INITIAL AXIAL PRESSURE, POWER, AND TEMPERATURE VALUES

| LOCATION | X MM | X/L | DP KPA | AVERAGE POWER W/CM | AVERAGE HELIUM C | AVERAGE CLAD C | MAXIMUM POWER W/CM | MAXIMUM HELIUM C | MAXIMUM CLAD C | MINIMUM POWER W/CM | MINIMUM HELIUM C | MINIMUM CLAD C |
|---|---|---|---|---|---|---|---|---|---|---|---|---|
| INLET | .0 | | 2.151 | .0 | 325.0 | 325.0 | .0 | 325.0 | 325.0 | .0 | 325.0 | 325.0 |
| CORE INLET | 650.5 | .000 | 56.944 | 144.7 | 325.0 | 411.1 | 154.4 | 325.0 | 417.2 | 135.1 | 325.0 | 405.0 |
| SMOOTH | 775.5 | .125 | 69.009 | 205.1 | 342.9 | 468.0 | 218.7 | 344.1 | 478.3 | 191.4 | 341.8 | 457.8 |
| SMOOTH | 899.5 | .249 | 80.979 | 251.1 | 366.2 | 521.7 | 267.8 | 368.9 | 535.9 | 234.3 | 363.4 | 507.7 |
| ROUGH | 901.5 | .251 | 80.979 | 251.7 | 366.6 | 440.5 | 268.4 | 369.3 | 448.5 | 234.9 | 363.8 | 432.6 |
| ROUGH | 1150.5 | .500 | 142.847 | 290.4 | 423.0 | 508.6 | 309.8 | 429.5 | 521.1 | 271.0 | 416.4 | 496.1 |
| ROUGH | 1250.5 | .600 | 167.693 | 284.0 | 446.5 | 530.0 | 303.0 | 454.6 | 543.9 | 265.1 | 438.4 | 516.1 |
| ROUGH | 1350.5 | .700 | 192.540 | 265.2 | 469.0 | 546.5 | 282.9 | 478.6 | 561.5 | 247.5 | 459.4 | 531.6 |
| ROUGH | 1450.5 | .800 | 217.387 | 234.8 | 489.5 | 557.7 | 250.4 | 500.4 | 573.3 | 219.1 | 478.5 | 542.0 |
| ROUGH | 1550.5 | .900 | 242.234 | 194.0 | 507.0 | 562.9 | 206.9 | 519.2 | 578.9 | 181.1 | 494.9 | 547.0 |
| ROUGH | 1600.5 | .950 | 254.657 | 170.3 | 514.5 | 563.3 | 181.7 | 527.1 | 579.3 | 159.0 | 501.9 | 547.4 |
| CORE OUTLET | 1650.5 | 1.000 | 267.080 | 144.7 | 520.9 | 562.3 | 154.4 | 534.0 | 578.1 | 135.1 | 507.9 | 546.4 |
| OUTLET | 2100.5 | | 408.401 | .0 | 520.9 | 520.9 | .0 | 534.0 | 534.0 | .0 | 507.9 | 507.9 |

FINAL AXIAL PRESSURE, POWER, AND TEMPERATURE VALUES

| LOCATION | X MM | X/L | DP KPA | AVERAGE POWER W/CM | AVERAGE HELIUM C | AVERAGE CLAD C | MAXIMUM POWER W/CM | MAXIMUM HELIUM C | MAXIMUM CLAD C | MINIMUM POWER W/CM | MINIMUM HELIUM C | MINIMUM CLAD C |
|---|---|---|---|---|---|---|---|---|---|---|---|---|
| INLET | .0 | | .022 | .0 | 325.0 | 325.0 | .0 | 325.0 | 325.0 | .0 | 325.0 | 325.0 |
| CORE INLET | 650.5 | .000 | .815 | 14.5 | 325.0 | 376.8 | 15.4 | 325.0 | 380.4 | 13.5 | 325.0 | 373.2 |
| SMOOTH | 775.5 | .125 | .988 | 20.5 | 342.9 | 417.4 | 21.9 | 344.1 | 423.8 | 19.1 | 341.8 | 411.0 |
| SMOOTH | 899.5 | .249 | 1.160 | 25.1 | 366.2 | 458.2 | 26.8 | 368.9 | 467.5 | 23.4 | 363.4 | 449.0 |
| ROUGH | 901.5 | .251 | 1.160 | 25.2 | 366.6 | 432.9 | 26.8 | 369.3 | 440.3 | 23.5 | 363.8 | 425.5 |
| ROUGH | 1150.5 | .500 | 1.642 | 29.0 | 423.0 | 499.7 | 31.0 | 429.5 | 511.5 | 27.1 | 416.4 | 487.8 |
| ROUGH | 1250.5 | .600 | 1.836 | 28.4 | 446.5 | 521.3 | 30.3 | 454.6 | 534.6 | 26.5 | 438.4 | 508.0 |
| ROUGH | 1350.5 | .700 | 2.030 | 26.5 | 469.0 | 538.5 | 28.3 | 478.6 | 552.9 | 24.8 | 459.4 | 524.1 |
| ROUGH | 1450.5 | .800 | 2.223 | 23.5 | 489.5 | 550.7 | 25.0 | 500.4 | 565.8 | 21.9 | 478.5 | 535.5 |
| ROUGH | 1550.5 | .900 | 2.417 | 19.4 | 507.0 | 557.2 | 20.7 | 519.2 | 572.8 | 18.1 | 494.9 | 541.7 |
| ROUGH | 1600.5 | .950 | 2.513 | 17.0 | 514.5 | 558.4 | 18.2 | 527.1 | 574.0 | 15.9 | 501.9 | 542.8 |
| CORE OUTLET | 1650.5 | 1.000 | 2.610 | 14.5 | 520.9 | 558.1 | 15.4 | 534.0 | 573.7 | 13.5 | 507.9 | 542.5 |
| OUTLET | 2100.5 | | 3.772 | .0 | 520.9 | 520.9 | .0 | 534.0 | 534.0 | .0 | 507.9 | 507.9 |

## TABLE 4-1 (continued)

TRANSIENT TEST SERIES RUN NO. - 1

INITIAL AXIAL VALUE FOR AVERAGE ROD

AVG POWER PER ROD = 24.000 KW
STORED ENERGY BASE TEMPERATURE = 325.0 C
AVG STORED ENERGY PER ROD = 69.553 KW-S
STORED ENERGY/POWER FOR AVG ROD = 2.9 S

| LOCATION | X MM | X/L | POWER W/CM | STORED ENERGY W*S/CM | ENERGY/POWER S | HELIUM C | CLAD C | WALL DT C | HT*A/L W/CM/C | TEMP/TIME C/S | ROD CENTER C |
|---|---|---|---|---|---|---|---|---|---|---|---|
| INLET | .0 | | .0 | .0 | .0 | 325.0 | 325.0 | .0 | 1.79 | .0 | 325.0 |
| CORE INLET | 650.5 | .000 | 144.7 | 267.6 | 7.1 | 325.0 | 411.1 | 86.1 | 1.68 | 8.2 | 587.9 |
| SMOOTH | 775.5 | .125 | 205.1 | 416.1 | 8.7 | 342.9 | 468.0 | 125.0 | 1.64 | 11.7 | 718.4 |
| SMOOTH | 899.5 | .249 | 251.1 | 547.7 | 10.2 | 366.2 | 521.7 | 155.6 | 1.61 | 14.3 | 828.4 |
| ROUGH | 901.5 | .251 | 251.7 | 405.0 | 8.4 | 366.6 | 440.5 | 73.9 | 3.40 | 14.3 | 747.9 |
| ROUGH | 1150.5 | .500 | 290.4 | 556.0 | 11.4 | 423.0 | 508.6 | 85.6 | 3.39 | 16.5 | 863.2 |
| ROUGH | 1250.5 | .600 | 284.0 | 588.6 | 13.0 | 446.5 | 530.0 | 83.5 | 3.40 | 16.1 | 876.9 |
| ROUGH | 1350.5 | .700 | 265.2 | 602.7 | 15.0 | 469.0 | 546.5 | 77.5 | 3.42 | 15.1 | 870.4 |
| ROUGH | 1450.5 | .800 | 234.8 | 598.0 | 17.7 | 489.5 | 557.7 | 68.2 | 3.44 | 13.3 | 844.4 |
| ROUGH | 1550.5 | .900 | 194.0 | 574.7 | 21.9 | 507.0 | 562.9 | 55.9 | 3.47 | 11.0 | 799.9 |
| ROUGH | 1600.5 | .950 | 170.3 | 556.4 | 25.0 | 514.5 | 563.3 | 48.9 | 3.49 | 9.7 | 771.3 |
| CORE OUTLET | 1650.5 | 1.000 | 144.7 | 534.0 | 29.2 | 520.9 | 562.3 | 41.3 | 3.50 | 8.2 | 739.0 |
| OUTLET | 2100.5 | | .0 | 403.2 | .0 | 520.9 | 520.9 | .0 | 1.79 | .0 | 520.9 |

FINAL AXIAL VALUES FOR AVERAGE ROD

AVG POWER PER ROD = 2.400 KW
STORED ENERGY BASE TEMPERATURE = 325.0 C
AVG STORED ENERGY PER ROD = 49.239 KW-S
STORED ENERGY/POWER FOR AVG ROD = 20.5 S

| LOCATION | X MM | X/L | POWER W/CM | STORED ENERGY W*S/CM | ENERGY/POWER S | HELIUM C | CLAD C | WALL DT C | HT*A/L W/CM/C | TEMP/TIME C/S | ROD CENTER C |
|---|---|---|---|---|---|---|---|---|---|---|---|
| INLET | .0 | | .0 | .0 | .0 | 325.0 | 325.0 | .0 | .29 | .0 | 325.0 |
| CORE INLET | 650.5 | .000 | 14.5 | 102.8 | 7.1 | 325.0 | 376.8 | 51.8 | .28 | 8.2 | 394.4 |
| SMOOTH | 775.5 | .125 | 20.5 | 179.3 | 8.7 | 342.9 | 417.4 | 74.5 | .28 | 11.7 | 442.4 |
| SMOOTH | 899.5 | .249 | 25.1 | 254.9 | 10.2 | 366.2 | 458.2 | 92.1 | .27 | 14.3 | 488.9 |
| ROUGH | 901.5 | .251 | 25.2 | 210.3 | 8.4 | 366.6 | 432.9 | 66.3 | .38 | 14.3 | 463.6 |
| ROUGH | 1150.5 | .500 | 29.0 | 331.1 | 11.4 | 423.0 | 499.7 | 76.7 | .38 | 16.5 | 535.1 |
| ROUGH | 1250.5 | .600 | 28.4 | 368.8 | 13.0 | 446.5 | 521.3 | 74.8 | .38 | 16.1 | 556.0 |
| ROUGH | 1350.5 | .700 | 26.5 | 397.6 | 15.0 | 469.0 | 538.5 | 69.5 | .38 | 15.1 | 570.9 |
| ROUGH | 1450.5 | .800 | 23.5 | 416.6 | 17.7 | 489.5 | 550.7 | 61.2 | .38 | 13.3 | 579.3 |
| ROUGH | 1550.5 | .900 | 19.4 | 424.9 | 21.9 | 507.0 | 557.2 | 50.2 | .39 | 11.0 | 580.9 |
| ROUGH | 1600.5 | .950 | 17.0 | 425.0 | 25.0 | 514.5 | 558.4 | 43.9 | .39 | 9.7 | 579.2 |
| CORE OUTLET | 1650.5 | 1.000 | 14.5 | 422.4 | 29.2 | 520.9 | 558.1 | 37.2 | .39 | 8.2 | 575.8 |
| OUTLET | 2100.5 | | .0 | 403.2 | .0 | 520.9 | 520.9 | .0 | .29 | .0 | 520.9 |

## TABLE 4-1 (continued)

TRANSIENT TEST SERIES RUN NO. - 1

LINEAR POWER AND FLOW RAMP

| | FRACTION (1) | FRACTION (2) | FRACTION (3) | START TIME (S) | DECAY TIME (S) (2)-(1) | DECAY TIME (S) (3)-(2) |
|---|---|---|---|---|---|---|
| POWER | 1.000 | .400 | .100 | .2 | .7 | 2.2 |
| FLOW | 1.000 | .290 | .100 | 2.2 | 3.8 | 39.0 |

APPROXIMATE TRANSIENT HISTORY

| TIME | AVG POWER PER ROD | FLOW | EQ. STORED Q PER ROD | EQ. STORED Q CHANGE/T | TIME CONSTANT | OUTLET TEMPERATURE EQ. | OUTLET TEMPERATURE ACT. | CLAD TEMPERATURE, AVG EQ. AVG. | CLAD TEMPERATURE, AVG ACT. AVG. | CLAD TEMPERATURE, AVG ACT. MAX. |
|---|---|---|---|---|---|---|---|---|---|---|
| S | KW | KG/S | KW-S | KW | S | C | C | C | C | C |
| .0 | 24.000 | .873 | 69.555 | .000 | 2.9 | 521. | 521. | 454. | 454. | 562. |
| 1.4 | 7.672 | .873 | 22.161 | -32.817 | 2.9 | 388. | 468. | 366. | 420. | 499. |
| 2.9 | 2.946 | .760 | 9.357 | -8.061 | 3.2 | 353. | 423. | 343. | 390. | 444. |
| 4.5 | 2.400 | .501 | 10.375 | .471 | 4.3 | 359. | 398. | 347. | 373. | 413. |
| 6.6 | 2.400 | .250 | 18.393 | 2.093 | 7.7 | 393. | 396. | 367. | 370. | 410. |
| 10.5 | 2.400 | .234 | 19.537 | .281 | 8.1 | 398. | 397. | 370. | 370. | 410. |
| 14.5 | 2.400 | .217 | 20.940 | .322 | 8.7 | 404. | 400. | 374. | 372. | 413. |
| 18.9 | 2.400 | .198 | 22.717 | .375 | 9.5 | 411. | 404. | 378. | 374. | 418. |
| 23.6 | 2.400 | .178 | 25.065 | .450 | 10.4 | 421. | 411. | 384. | 378. | 426. |
| 28.9 | 2.400 | .156 | 28.362 | .558 | 11.8 | 435. | 420. | 393. | 384. | 437. |
| 34.8 | 2.400 | .131 | 33.449 | .730 | 13.9 | 456. | 434. | 406. | 392. | 454. |
| 41.7 | 2.400 | .101 | 42.722 | 1.042 | 17.8 | 494. | 458. | 429. | 407. | 482. |
| 50.6 | 2.400 | .087 | 49.241 | .636 | 20.5 | 521. | 483. | 446. | 422. | 512. |
| 60.9 | 2.400 | .087 | 49.241 | .000 | 20.5 | 521. | 498. | 446. | 431. | 530. |
| 71.2 | 2.400 | .087 | 49.241 | .000 | 20.5 | 521. | 507. | 446. | 437. | 541. |
| 81.4 | 2.400 | .087 | 49.241 | .000 | 20.5 | 521. | 512. | 446. | 441. | 548. |
| 91.7 | 2.400 | .087 | 49.241 | .000 | 20.5 | 521. | 516. | 446. | 443. | 552. |
| 101.9 | 2.400 | .087 | 49.241 | .000 | 20.5 | 521. | 518. | 446. | 444. | 554. |
| 112.2 | 2.400 | .087 | 49.241 | .000 | 20.5 | 521. | 519. | 446. | 445. | 556. |
| 122.4 | 2.400 | .087 | 49.241 | .000 | 20.5 | 521. | 520. | 446. | 445. | 557. |
| 132.7 | 2.400 | .087 | 49.241 | .000 | 20.5 | 521. | 520. | 446. | 445. | 557. |
| 143.0 | 2.400 | .087 | 49.241 | .000 | 20.5 | 521. | 521. | 446. | 446. | 558. |
| 153.2 | 2.400 | .087 | 49.241 | .000 | 20.5 | 521. | 521. | 446. | 446. | 558. |

and rod cladding) at locations between the inlet and outlet of the test bundle; the fourth sheet lists the predicted power-energy-temperature relationships at the same locations noted on the third sheet; the fifth sheet gives an approximate transient history for the test bundle, i.e., power, flow, energy, and temperatures, for a period of about 2-1/2 min. The data indicate that equilibrium should be attained within less than 50 s of scram initiation for this particular sample transient test.

### 4.2.2. Accelerated Normal Transient Cycling

Calculations indicate that more than 1300 hr of testing time would be required for the GCFR normal transient load changes at a rate of 3%/min, as noted in Ref. 4-1. One approach being considered to reduce the quantity of tests to an acceptable number and still provide the information needed for the design and safety assessment of GCFR fuel assemblies is that of accelerated "normal" transient tests. Early analysis using the computer code TSPEC indicates that the results of transient cyclic tests with load changes at a rate of 1-1/2% per second should provide the needed information. The testing time for that part of the test program would be reduced by ∿94%.

### 4.2.3. CFTL Dynamic Simulation

Drafts of users' manuals were prepared for two programs used in the dynamic simulation of the CFTL. The programs for which users' manuals were written are CFTL*SIM, which is used for total loop simulation, and ROD*SIM, (formerly known as GCFR-RODS*CFTL-HEATERS), which is used to simulate bundles of GCFR fuel rods or CFTL heater rods. Each users' manual contains a brief description of the model on which the program is based, a detailed description of the input data, and a sample problem.

## 4.3. TEST SPECIFICATION

### 4.3.1. Preliminary Test Specification Summary

There are 15 groups of tests that have tentatively been planned for the CFTL preliminary test series. Tables denoting test conditions for steady-state tests are included in Ref. 4-2. The tabular information is for an estimated maximum steady-state test program for the preliminary test series, which includes steady-state and transient tests on 37-rod bundles with unheated and heated rods. The tables for the steady-state tests and the recently completed tables for the transient tests are being revised to reflect the requirements for a low-pressure-drop GCFR core. In addition, the revisions will show a reduction in the quantity of tests to an acceptable number which will still provide the requested information, as discussed in Section 4.2.2.

### 4.3.2. Low Flow Requirements

The requirements for testing at low coolant flow rates are being reviewed. Laminar flow conditions with a minimum Reynolds number of about 500 [mass flow on the order of 4 g/s ($\sim$0.009 lbm/s)] have been requested by GA. ORNL has indicated a need for trace heating to be able to satisfactorily control the system at low flow and power levels. An alternative suggested by ORNL is the use of a once-through loop for the low flow tests.

## 4.4. TEST BUNDLE DESIGN AND FABRICATION

### 4.4.1. Low-Pressure-Drop Core

If accepted, a low-$\Delta$P [155 kPA (22.5 psi)] fuel element which is seriously being considered for the GCFR reference design will influence the design of the CFTL fuel assembly heater rods. The major changes are a reduction in the core length of 20 mm (0.8 in.) to 980 mm (38.6 in.) and a reduction in the cladding thickness of 0.12 mm (0.005 in.) to

0.38 mm (0.015 in.). For the CFTL, the reduction in cladding thickness would be beneficial in allowing for more boron nitride insulation between the heater ribbon and the cladding, which should minimize the possibility of an electrical short between the cladding and the heater element.

### 4.4.2. Blanket Element Revision

The GCFR reference design for blanket elements has been modified to reduce the number of rods from 127 to 61. The major dimensional change being considered which will be applicable to CFTL blanket heater rod design is an increase in the diameter of 7 mm (0.28 in.) to 19.8 mm (0.78 in.).

### 4.4.3. Design and Fabrication

A proposed division of responsibilities between GA and ORNL for test bundle design and fabrication activities was prepared for consideration. The aim of the proposal is to obtain an agreed upon list of detailed activities which will preclude duplication of efforts and will be documented in the CFTL management plan.

Table 4-2 summarizes six major areas of responsibility, which are primarily hardware oriented, and the suggested responsible organizations. Figure 4-1 denotes the suggested areas of responsibility, and Figs. 4-2 through 4-6 aid in defining the components listed in Table 4-2 and noted in Fig. 4-1.

## 4.5. LIAISON WITH ORNL

A CFTL review meeting was held at ORNL from March 2-5, 1976. The highlights of the meeting were as follows:

1. Presentation of the status of program activities included information on the prototype circulator, heater rod development, power supply test preparations, instrumentation, design,

TABLE 4-2

SUMMARY OF DESIGN AND FABRICATION ACTIVITIES

| Responsibility | Activity |
|---|---|
| GA | 1. Reference GCFR fuel assembly design |
| GA | 2. CFTL fuel test section design |
| ORNL | 3. Test bundle design (integrates test section into loop) |
| ORNL | 4. Instrumentation design and test integration |
| | 5. Component design, procurement, and quality assurance |
| ORNL | A. Heater rod (all activities except heater roughening, which would be GA's responsibility) |
| GA | B. Intermediate spacer grids |
| GA | C. Inlet spacer grid |
| GA | D. Spacer hanger rods |
| GA | E. Test section duct |
| GA | F. Test section outlet |
| GA | G. Test section duct flange |
| ORNL | H. Test section flange to test vessel adapter |
| ORNL | I. Test bundle pressure closure |
| ORNL | J. Test section instrumentation (except prototypical GCFR temperature instrumentation at test section outlet); GA to specify test section instrumentation type and location |
| ORNL | K. Test bundle instrumentation (routing of leads and all other bundle instrumentation not identified as test section instrumentation) |
| ORNL | 6. Test bundle assembly |

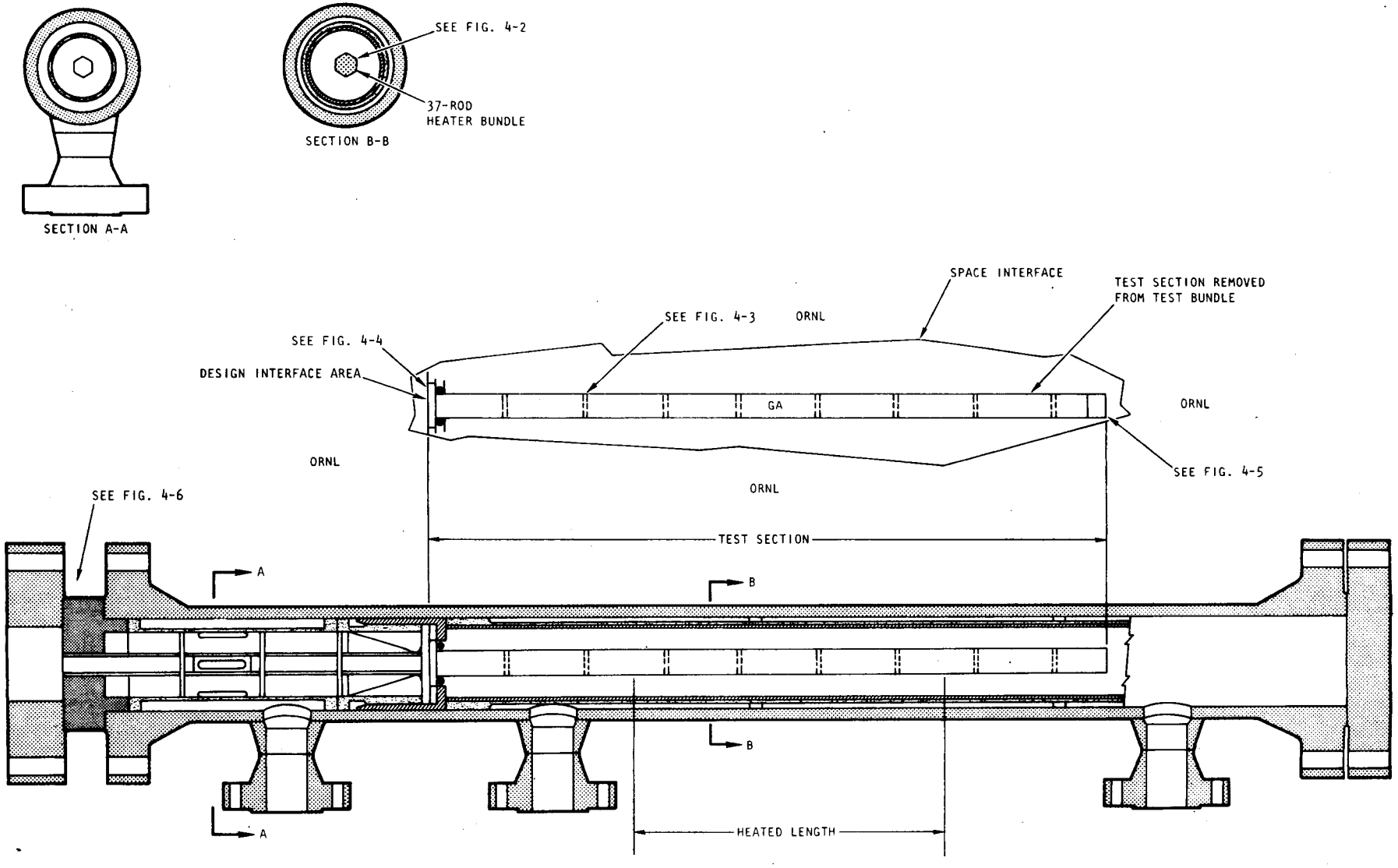


Fig. 4-1 Suggested design and space interface areas for GA and ORNL CFTL vessel, bundle, and test section responsibilities

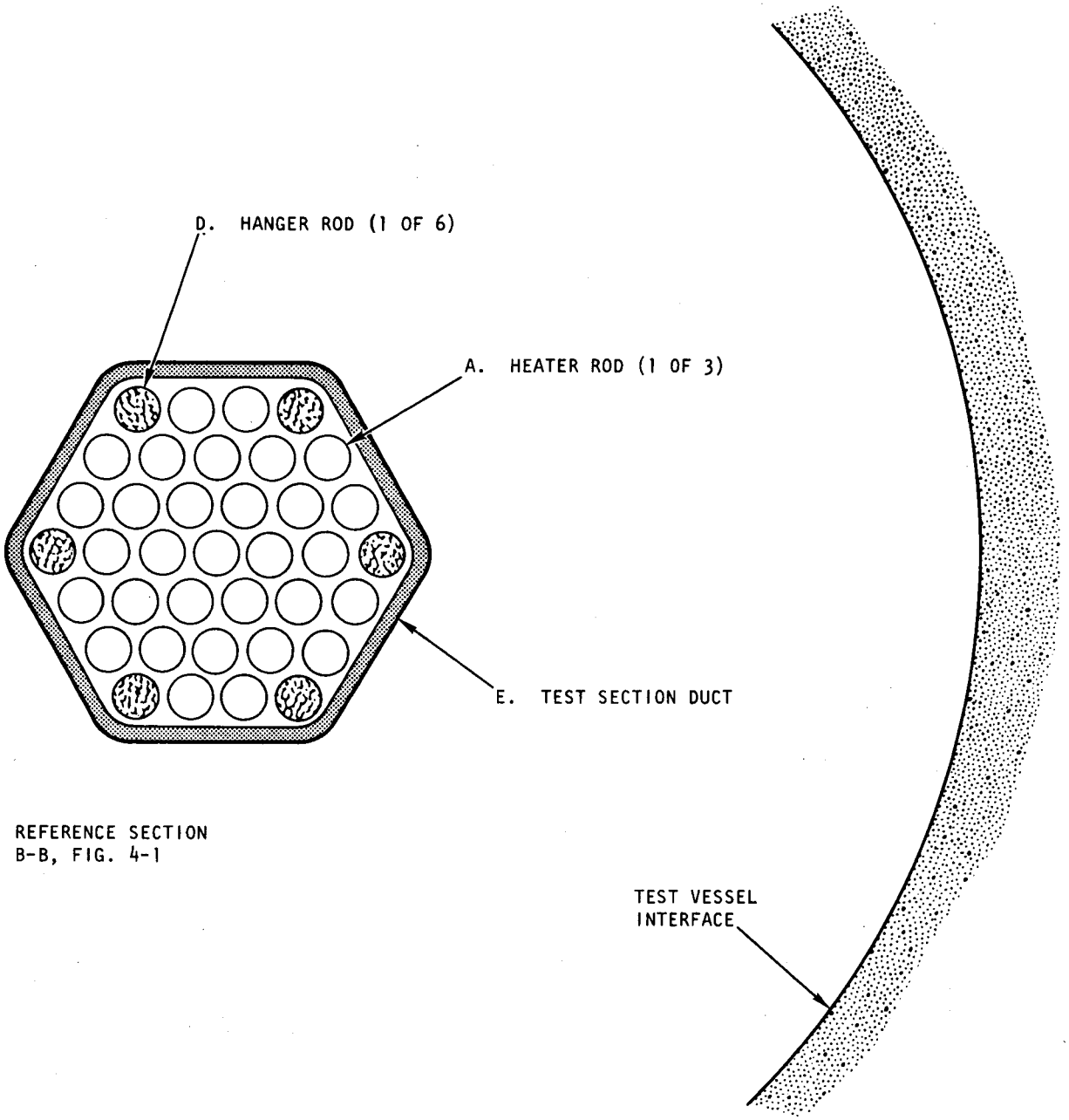


**Fig. 4-2 Cross section of 37-rod fuel assembly model**

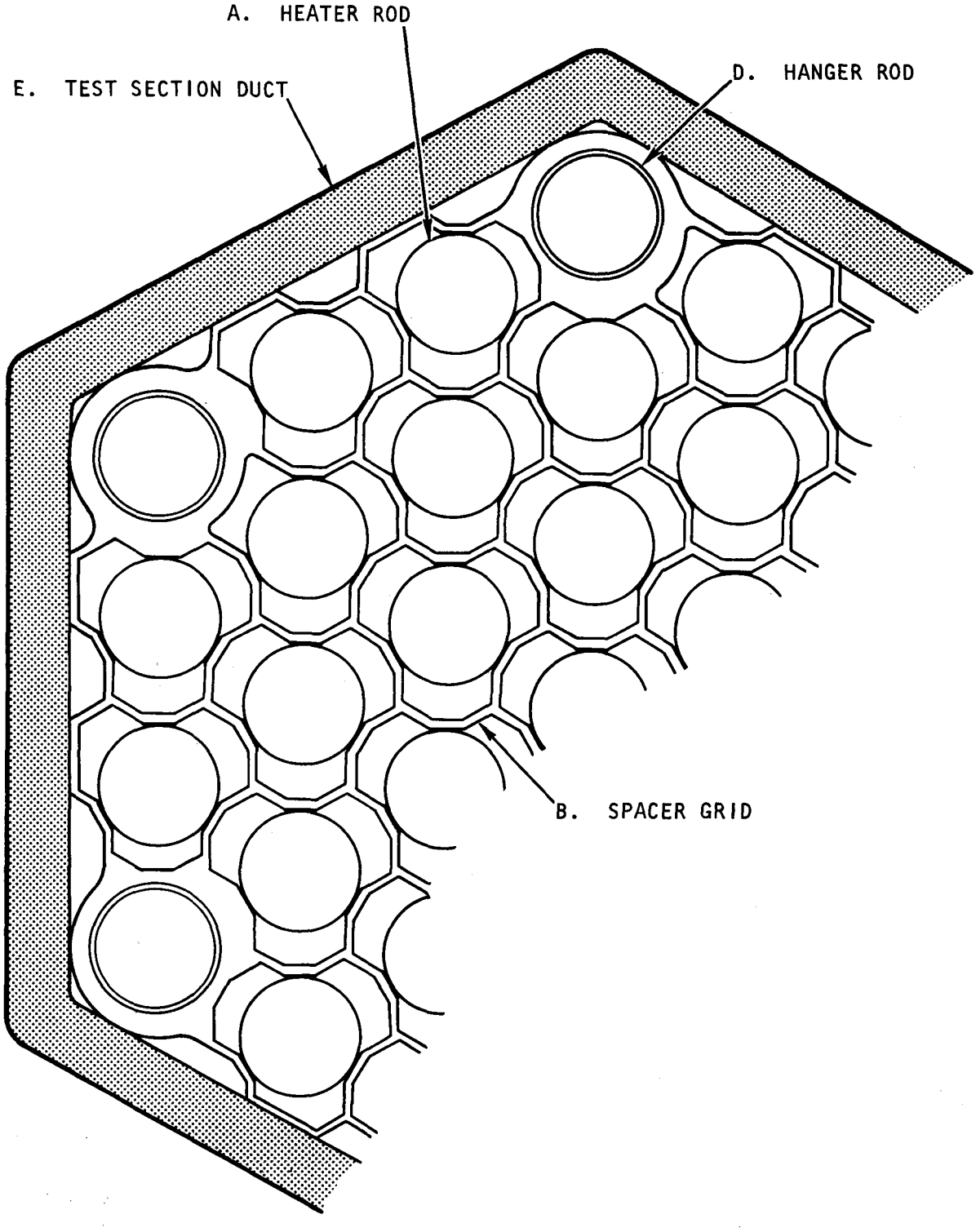


Fig. 4-3 Section of fuel rod bundle at intermediate spacer

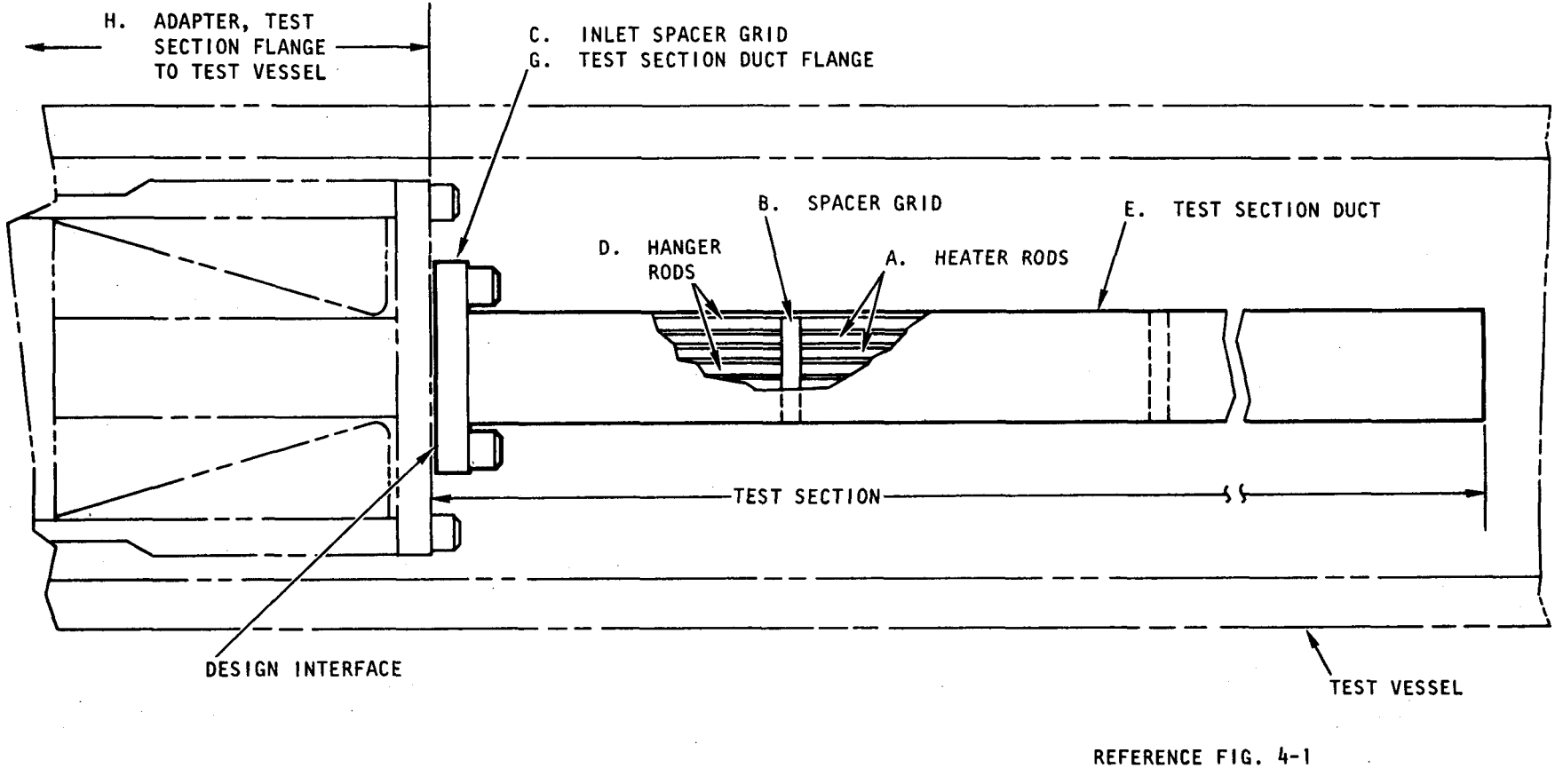


**Fig. 4-4 Typical model evaluation**

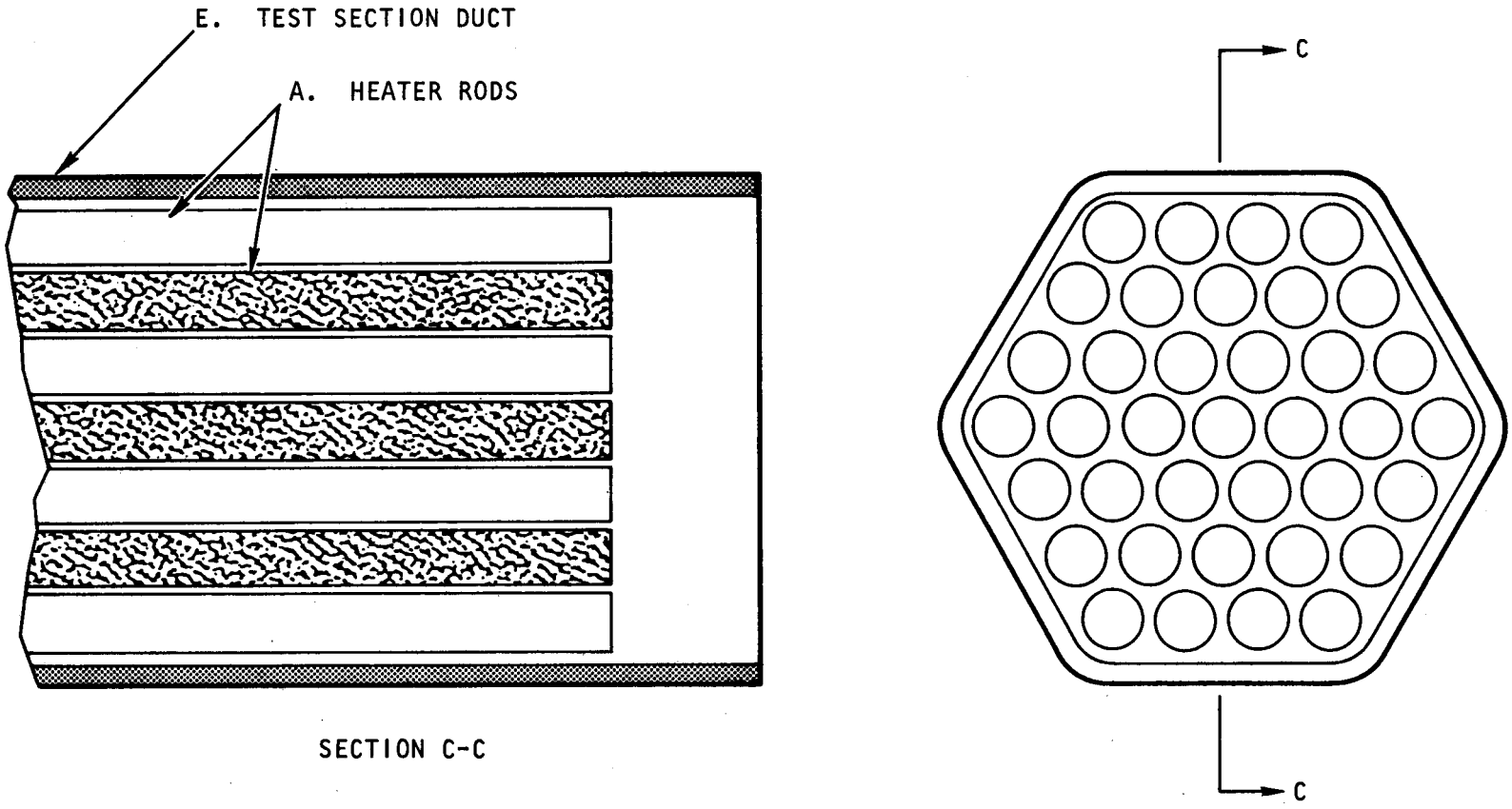


Fig. 4-5 Test section outlet

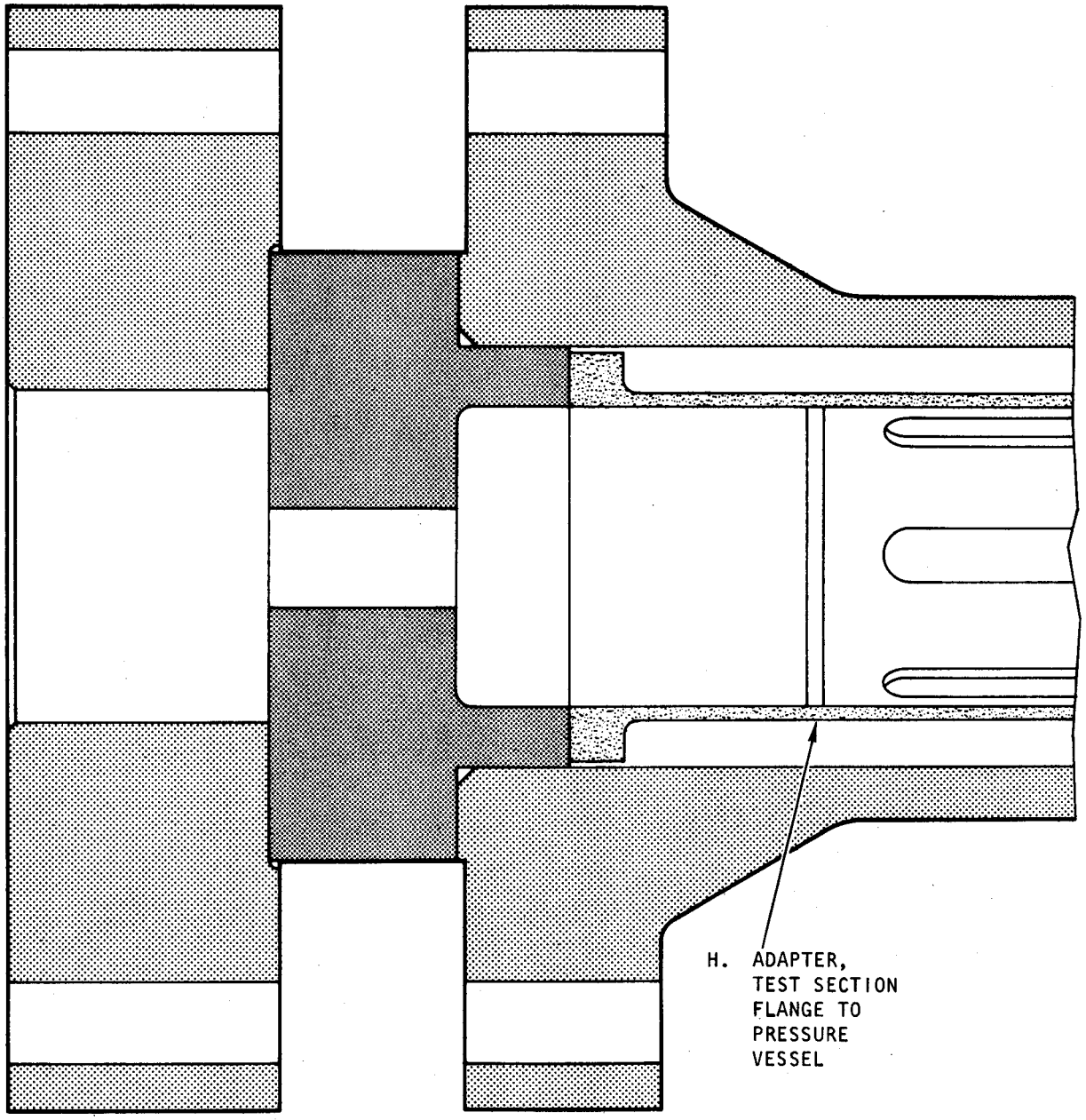


Fig. 4-6 Test bundle pressure closure

computer codes, test specifications, and progress of international test programs.

2. Budgets and schedules were discussed, and ERDA - Oak Ridge Operations personnel gave a presentation on "line item funding and scheduling."

3. There were detailed discussions on heater rod power and helium flow requirements.

4. The fuel failure mock-up (FFM) and blowdown heat transfer (BDHT) test facilities were visited to view hardware and associated instrumentation.

5. Fabrication of heater rod insulation preforms was demonstrated at a laboratory facility.

## 4.6. GCFR PROTOTYPE CORE ASSEMBLY TEST PLANNING

The program planning for the testing of the full-size prototype core assemblies has been initiated. The preliminary draft of the program outline has been issued and is undergoing internal review in the GCFR Fuel Element Design and Development Department. The prototype core assembly tests will be the final series of out-of-pile tests conducted on the core assemblies. These tests will be conducted on full-size core assemblies and will provide assurance that the assemblies meet design qualification requirements prior to fabrication of the GCFR demonstration plant initial core. The prototype assembly designs, materials, and fabrication techniques will duplicate the GCFR demonstration plant core assemblies as specified by the preliminary design for each assembly.

One core assembly of each type (fuel, control, and blanket) will be subjected to long-term endurance testing. Each assembly will be tested for the equivalent of 1 yr of reactor operation (250 full-power

days). The prototype assemblies will be tested in a helium test loop that will simulate the reactor core environment of temperature and pressure. The helium temperature will be maintained by heaters in the test loop since fuel rod heating will not be simulated in these tests. The loop will have the capability of testing the assemblies at maximum GCFR flow conditions. In addition, the loop will be used to qualify the initial production run core assemblies for the GCFR demonstration plant core.

The basic objectives of the prototype test program will be to evaluate the preliminary design of the full-size assemblies and to explore for discrepancies that cannot be uncovered in the testing of individual components and reduced-size models. The data and information obtained from the prototype tests will be applied to establish the final core assembly design prior to the fabrication of the GCFR core assemblies.

Typical test section operating conditions required to simulate full power of the 300-MW(e) GCFR demonstration plant are as follows:

| | |
|---|---|
| Fluid | Helium |
| System pressure | Ambient to $9.1 \times 10^6$ MPa (1320 psia) |
| Test section pressure drop/ system pressure | ~0.018 $\Delta P/P$ |
| Inlet temperature | 325° to 550°C (617° to 1022°F) |
| Flow | |
| Fuel assembly | 0 to 7.5 kg/s (0 to 16.5 lbm/s) |
| Control assembly | 0 to 6.5 kg/s (0 to 14.3 lbm/s) |
| Blanket assembly | 0 to 0.7 kg/s (0 to 1.5 lbm/s) |
| Test duration | 250+ days per assembly |

REFERENCES

4-1 Hopkins, H. C., Jr., "Program Plan for GCFR Core Flow Test Loop," USAEC Report GA-A13080, General Atomic, August 9, 1974.

4-2 "Gas-Cooled Fast Breeder Reactor Quarterly Progress Report for the Period November 1, 1975 Through January 31, 1976," ERDA Report GA-A13815, General Atomic, March 22, 1976.

# 5. FUELS AND MATERIAL ENGINEERING (189a No. SU007)

## 5.1. OXIDE FUEL, BLANKET, AND GRID PLATE SHIELDING MATERIALS TECHNOLOGY

It is the responsibility of this subtask to maintain liaison with and surveillance of other ERDA and non-ERDA programs, especially the liquid metal fast breeder reactor (LMFBR) program, to ensure the availability of all relevant information for the GCFR design. The areas included in this subtask are

1. Oxide fuel technology.
2. $UO_2$ (axial) blanket technology.
3. $ThO_2$ and $UO_2$ (radial) blanket technology.
4. Grid plate shielding technology.

During this quarter, corrections to the recently updated test matrices of current GCFR fast flux irradiation experiments F-1 (X094) and F-3 (X206) were provided to the Fuel Cladding Chemical Interaction Program Steering Group, which is compiling data on fast flux irradiations.

In other studies, Argonne National Laboratory (ANL) has concluded that the tentative test matrix for the F-5 (prototype) irradiation test will have to be modified because three additional bypass flow positions will be required to achieve acceptable subassembly outlet temperatures. Consequently, the F-5 subassembly will use only 31 fuel rods, reducing the total number of rods irradiated by six. The number of rods to be irradiated to high burnup (>16 at. % burnup) will remain the same (17), but the number of rods in the modified design subgroups and those exposed to low burnup will decrease. However, the change will not significantly alter attainment of the statistical objectives of the experiment.

## 5.2. CLADDING TECHNOLOGY

### 5.2.1. Coordinated Mechanical Testing Program

A meeting of the representatives of ANL, Pacific Northwest Laboratory (PNL), and GA was held at GA on January 25 and 26, 1976 to review the results and progress in the mechanical testing programs and to formulate policies and plans for future work. Agreements on future plans and policies were obtained from all participants.

### 5.2.2. Mechanical Testing Program at Argonne National Laboratory

The purpose of this program is to determine the effects of the following factors on the behavior and mechanical properties of GCFR cladding:

1. Ribs, rib geometry, and fabrication technique.
2. Impurity levels in helium typical of the GCFR.

Additionally, the effects of end cap design and length of test specimens have been determined in tests which have already been completed. These mechanical tests are being conducted in a quasi-static helium environment at ANL. General Atomic participates in an advisory, consultative, and evaluative role. Testing of the initial test matrix has been completed.

During this quarter, tests of the second test matrix were begun. This test is being conducted at 650°C (1200°F) in highly purified helium. The test matrix is shown in Table 5-1 for reference. All the smooth specimens (groups A and C) failed in 81 to 131 hr. The chemically etched, ribbed, mechanically ground, smooth specimens started to rupture after about 360 hr. The mechanically ground, ribbed specimens have not failed yet. The approximate test time at present is about 480 hr. Only four specimens from group B and all of group D remain intact and are in the secondary stage of creep. These data lead to the preliminary conclusion that the ribs strengthen the cladding regardless of the fabrication technique.

TABLE 5-1

GENERAL TEST MATRIX FOR THE SECOND TEST SERIES AT ARGONNE NATIONAL LABORATORY

| Group | Specimen Quantity[a] | Nominal Length [cm (in.)] | Nominal I.D. [cm (in.)] | Nominal Stress[b] [MPa (psi)] | Temperature [°C (°F)] |
|---|---|---|---|---|---|
| A - chemically etched, smooth | 9 | 9.83 (3.875) | 0.668 (0.263) | 238 (34,000) | 650 (1200) |
| B - chemically etched, ribbed | 8 | 4.45 (1.75) | 0.668 (0.263) | 238 (34,000) | 650 (1200) |
| C - chemically etched, smooth | 8 | 4.45 (1.75) | 0.668 (0.263) | 238 (34,000) | 650 (1200) |
| D - mechanically ground, ribbed | 4 | 4.45 (1.75) | 0.711 (0.280) | 238 (34,000) | 650 (1200) |
| E - mechanically ground, smooth | 5 | 4.45 (1.75) | 0.711 (0.280) | 238 (34,000) | 650 (1200) |

[a] Commercially bottled helium (99.99% pure). Activated charcoal at liquid nitrogen temperature is used for additional purification. Cover gas is also pure helium, purified in the same way, at atmospheric pressure and a flow rate of ~400 $cm^3$/min.

[b] The nominal stress is based on the root diameter for the ribbed specimens.

Partial shipment of ribbed cladding fabricated at the Swiss Federal Institute (EIR) by electrochemical grinding was received during this quarter. The end caps and reinforcing collars for the third test at ANL and the first test at PNL have been machined at PNL. Welding of the end caps for ANL and PNL specimens has been started at ANL. The cooperative machining and welding programs were instituted to minimize experimental errors and to maximize the comparability of the two test programs.

### 5.2.3. Helium Loop Test Program at Pacific Northwest Laboratory

The primary objectives of this program are (1) to permit comparison of the mechanical properties determined in recirculating helium at PNL to those determined in quasi-static helium in the mechanical properties testing program at ANL and (2) to ensure that the ANL tests are in fact representative of the conditions in a GCFR. The scope of work has been agreed upon, and the evaluation of techniques for detection of pinhole leaks and ruptures has been completed.

Modification of the loop for unattended operation has been completed. The water and hydrogen injection systems and impurity monitoring system have been installed, and the loop has been operated with impurity levels predicted to be typical of the GCFR demonstration plant. Analysis of the simulation of the steam inleakage accident has been completed.

The test train and specimen end caps have been fabricated and welding of the end caps is presently being done at ANL. In addition to the biaxial test specimens, three miniature tensile specimens made from 20% cold-worked 316 stainless steel are included in the test. These will be used as oxidation samples. Start of the initial test is expected by the end of May.

## 5.3. F-1 FAST FLUX IRRADIATION EXPERIMENT

Irradiation of the encapsulated seven-fuel-rod F-1 (X094B) experiment has now achieved a maximum burnup exposure of 121 MW/kg (13.0 at. %), and irradiation has been terminated for final postirradiation examination.

The conditions under which the fuel rods were irradiated and the burnup exposures achieved are listed below.

| Capsule/Rod | Cladding I.D. Temperature [°C (°F)] | Heat Rating [W/cm (kW/ft)] | Fuel O/M | Burnup [MWd/kg (at. %)] |
|---|---|---|---|---|
| G-4 | 680 (1257) | 456 (13.9) | 1.983 | 121 (13.0) |
| G-8 | 672 (1242) | 486 (14.8) | 1.985 | 97 (10.4) |
| G-9 | 727 (1341) | 480 (14.6) | 1.968 | 73 (7.7) |
| G-10 | 727 (1341) | 480 (14.6) | 1.968 | 73 (7.7) |
| G-11 | 729 (1326) | 504 (15.4) | 1.947 | 73 (7.7) |
| G-12 | 735 (1355) | 454 (13.9) | 1.976 | 73 (7.7) |
| G-13 | 772 (1422) | 504 (15.4) | 1.973 | 73 (7.7) |

Rods G-9 and G-10 have ribbed cladding; the other rods have smooth cladding. Rods G-12 and G-13 have solid pellet fuel; the other rods have annular pellet fuel.

Gamma scanning of the capsule plenums for Xe-133 has shown no presence of Xe-137, indicating that all of the rods are intact. Neutron radiography will be performed before shipment of the capsule to ANL-E for postirradiation examination.

A final report describing work done on the measurement of cladding operating temperatures using the Kr-85 annealing techniques on the rods removed from F-1 at 50 MWd/kg (5.4 at. %) was completed and circulated for review.

As a consequence of a funding shortage, the remaining planned work on dosimetry from the five rods removed at 50 MWd/kg (5.4 at. %) has been deferred until the fiscal year transition quarter. A minor effort to more firmly document the tritium yield values measured and reported in Ref. 5-1 will be completed.

A review copy of the final report on the postirradiation examination of the fuel rods removed from the F-1 (X094) experiment after an exposure of 50 MWd/kg (5.4 at. %) was received from Argonne National Laboratory East (ANL-E). Some of the information has been incorporated into a paper (Ref. 5-2).

## 5.4. F-3 FAST FLUX IRRADIATION EXPERIMENT

The F-3 experiment was irradiated in location 4B3 in EBR-II to an exposure of 46 MWd/kg (4.9 at. %); the burnup goal is 100 MWd/kg (10.8 at. %). These capsules share a type J19A subassembly (X206) with the ANL Group-08 high-temperature chemistry experiment. The experiment reached an exposure of 46 MWd/kg (4.9 at. %) on February 11, 1976, at which time it was removed from the core for a planned interim examination.

Gamma counting for Xe-133 in the F-3 capsule plenums has shown that nine of ten capsule plenums contain xenon, indicating a leak from the fuel rod to the capsule. No evidence explaining the leaks is available yet. Neutron radiography on four fuel rod capsules has been completed. Three were leakers and one was intact based on the gamma counting. The leakers exhibited gross failures in the fueled region, and fuel was observed adjacent to the capsule wall. The intact rod had a bulge near the upper end of the fueled region. It is planned to initially send intact capsule G-18 and three failed capsules (G-14, G-19, and G-20) which were due to be removed during the interim change to ANL-E for disassembly. The sodium bond in the G-18 rod capsule will then be eddy current tested and pulse laser tested, and the capsule will be slit to check for voids or bubbles. De-encapsulation will then be done, and the bulged region of the G-18 rod will be examined to determine the possible cause of the leaks in the other rods.

The F-3 replacement and fabrication plan prepared by ANL-E was reviewed by GA. Some changes and additions were made, and the plan was approved by GA contingent upon these changes and additions. Assembly of the three F-3 replacement fuel rod capsules, planned to be inserted after the interim

examination at 50 MWd/kg (5.4 at. %), was started at ANL-E, but has been placed in "hold" until a decision is reached on the future of the experiment.

## 5.5. F-5 PROTOTYPE IRRADIATION EXPERIMENT

The F-5 prototype design fuel rod experiment is to be performed for experimental study of the performance of fuel rods irradiated under simulated GCFR conditions to high burnups for the purposes of (1) determining the reliability of the GCFR fuel rod design, (2) discovering what failure modes may exist, and (3) studying the effect of a step power increase that simulates the 180-deg rotation of a subassembly at the core blanket interface in the proposed GCFR demonstration plant.

A preliminary fuel rod design proposed by ANL-E for the F-5 experiment was reviewed by GA, and comments were forwarded to ANL. The physics and thermal designs are currently being reviewed at GA, and efforts to establish fuel specifications are under way at ANL. Efforts are also being made to find a source of funding for new cladding tubing that needs to be ordered for the F-5 experiment. The tubing will have the same root thickness [0.38 mm (0.015 in.)] as the cladding used for the LMFBR.

## 5.6. GB-10 VENTED FUEL ROD EXPERIMENT

Fission product release and transport in GCFR fuel are being measured and studied in capsule GB-10, which is being irradiated in the ORR. The burnup of the pressure-equalized and vented fuel rod in capsule GB-10 has reached approximately 90 MWd/kg (9.9 at. %); the exposure goal is 100 MWd/kg (10.9 at. %). The first 27 MWd/kg (3.0 at. %) were accumulated at a heat generation rate of 39.4 kW/m (12 kW/ft) at a cladding outside surface temperature of 565°C (1049°F); from 27 MWd/kg (3.0 at. %) to 75 MWd/kg (8.2 at. %) have been accumulated at 44.3 kW/m (13.5 kW/ft) at a cladding outside surface temperature of 630°C (1166°F), and from 75 MWd/kg (8.2 at. %) to the current burnup have been accumulated at 48 kW/m (14.8 kW/ft) and a cladding outside temperature of 685°C (1265°F).

Because of funding limitations, it was necessary to postpone special tests (tritium measurements, power cycling, and simulated leak flow rate tests). In addition it was necessary to postpone further routine measurements of fission gas release and venting and flow conductance measurements. The capsule continued its irradiation and accumulation of burnup because this procedure is the best means of storage until postirradiation examination (PIE) is done, and it retained the option for resumption of test data acquisition if funding is made available. In mid-March, additional funds were allocated, which will permit all but the tritium tests to be conducted and a reduced volume of data to be acquired. Additional funding of tritium data acquisition is being considered. The capsule is expected to reach its revised goal of 100 MWd/kg (10.9 at. %) at the end of June 1976, at which time it is planned to terminate the irradiation and start the PIE with fiscal year transition quarter funds.

## 5.7. HEDL CLADDING IRRADIATIONS

General Atomic requested that Hanford Engineering Development Laboratory (HEDL) provide the capability for and perform the postirradiation tests on the GCFR cladding samples which HEDL has irradiated in EBR-II under the conditions listed below.

| Irradiation Temperature [°C (°F)] | Fluence ($n/cm^2$) | Type of Specimen | Date of Removal from EBR-II | Postirradiation Tests | |
|---|---|---|---|---|---|
| | | | | Environment Temperature | Stress[a] [MPa (psi)] (Root of Rib) |
| 704 (1300) | $2.6\text{-}3.6 \times 10^{22}$ | 5 smooth 5 ribbed By etching | 9/75 | 704°C (1300°F) 1 atm static helium[b] | 138 (20,000) |
| 704 (1300) | $4.2\text{-}6 \times 10^{22}$ | 2 smooth 3 ribbed By etching | 3/76 | 704°C (1300°F) 1 atm static helium[b] | 138 (20,000) |

[a] The hoop stress to axial stress ratio shall be equal to one.

[b] Experimental research grade 99.995% pure.

These conditions are expected to result in specimen creep rupture lifetimes in the range of 100 to 200 hr.

Hanford Engineering Development Laboratory has some smooth and electrochemically etched ribbed samples previously provided by GA. It was requested that five of the smooth and five of the ribbed samples be used for the purpose of determining the comparative behavior of unirradiated ribbed samples in static helium at 704°C (1300°F) and a stress of 138 MPa (20,000 psi). HEDL responded to the requests indicating that ~$90K in separate GCFR funding would be required to perform the tests.

REFERENCES

5-1 "Gas-Cooled Fast Breeder Reactor Quarterly Progress Report for the Period November 1, 1975 Through January 31, 1976," ERDA Report GA-A13815, General Atomic, March 22, 1976.

5-2 Lindgren, J. R., et al., "Fast Flux Irradiation Tests Performed at High Temperature," Paper Presented at the Annual Meeting of the American Ceramic Society, Cincinnati, May 5, 1976.

# 6. FUEL ROD ENGINEERING (189a No. SU007)

The objective of this task is to evaluate the steady-state and transient performances of the fuel, blanket, and control rods for the determination of the performance characteristics, operating limits, and design criteria. To this end, analytical tools (such as the LIFE-III code) are being adapted and/or developed and applied to the analysis of the GCFR prototypical rods and experimental rods. In addition, continuous surveillance of the LMFBR fuels and materials development programs and technology is maintained to maximize the use of developing technology and material properties. Support is also given for the planning and designing of irradiation experiments.

## 6.1. FUEL, BLANKET, AND CONTROL ROD ANALYTICAL METHODS

### 6.1.1. Gas-Cooled Version of LIFE Code

Although the LIFE-III computer code is designed to predict the in-pile thermal, mechanical, and nuclear performance of cylindrical fast-reactor fuel rods, it was specifically developed for the analysis of the LMFBR fuel rods whose coolant is liquid sodium. As a result, LIFE-III is not directly applicable to the study of the GCFR fuel rods which use helium as a cooling medium. Until recently, this difficulty was overcome by a code option which allows users to specify the cladding outer surface temperature as an input to the code. To remove this limitation on the usage of the LIFE code for analyses of the GCFR fuel rods, modifications have been made to substitute gaseous helium coolant for the liquid sodium by providing empirical Nusselt number (Nu) correlations for the determination of the film heat transfer coefficient. A schematic of the GCFR fuel rod is shown in Fig. 6-1. The active length, 44% of the total rod length, consists of a 24.9-cm (9.80-in.) smooth section and a 74.7-cm (29.41-in.) roughened section.

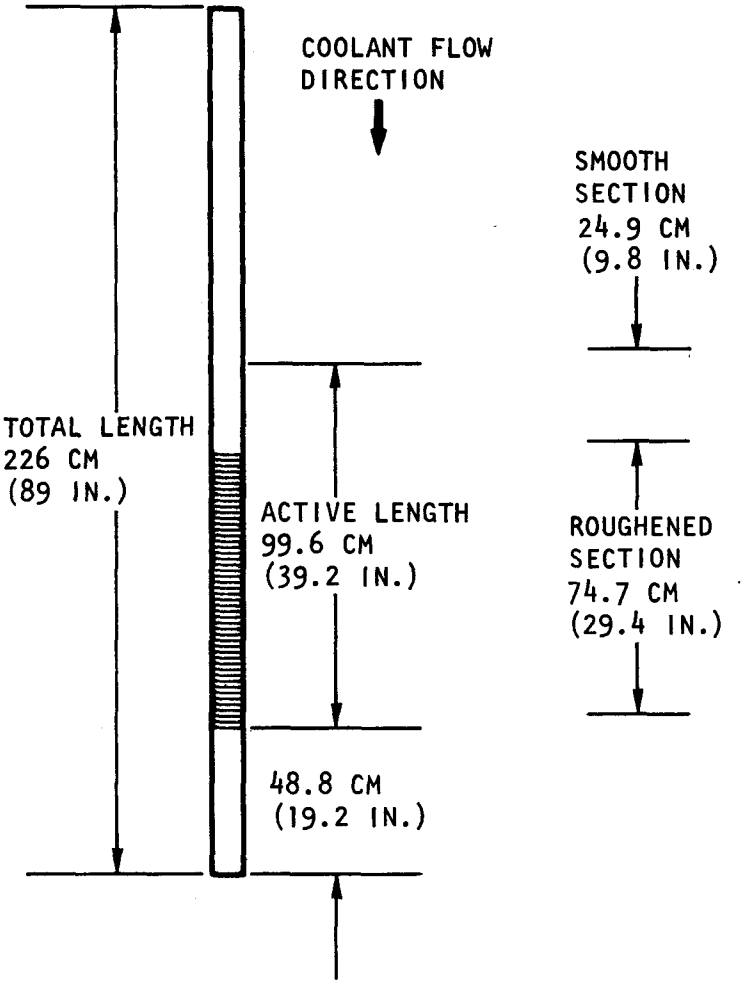


Fig. 6-1 GCFR fuel rod

In the LIFE code, the fueled part of the rod is divided into sections of equal length, whereas the plenum always forms a simple axial section regardless of length. In the current GCFR analysis, the fueled region of the rod is modeled to have four sections, so that one is a smooth section and the other three sections are surface-roughened.

The heat transfer between the outer cladding surface and the bulk coolant is calculated by the subroutine GOLDN. The coolant flow rate is obtained from specified end point temperatures, coolant specific heat, and input rod power. Sectional coolant bulk temperatures are calculated based on the integrated rod power from the top of the fueled region to the midpoint of the sections. From the local coolant temperature, helium thermal conductivity (k), viscosity ($\mu$), and Prandtl number (Pr) are found using the following correlations (Ref. 6-1):

$$k = 2.774 \times 10^{-3} T^{0.701} \text{ W/m-K} ,$$

$$= 1.062 \times 10^{-3} T^{0.701} \text{ Btu/hr-ft-R} ,$$

$$\mu = 3.953 \times 10^{-7} T^{0.687} \text{ N-sec/m}^2 ,$$

$$= 6.388 \times 10^{-4} T^{0.687} \text{ lbm/ft-hr} ,$$

$$Pr = 0.740 T^{-0.014} ,$$

where T is temperature in degrees Kelvin. Assuming an infinite fuel bundle with equilateral triangle rod spacing, the average flow area A and hydraulic diameter $D_h$ for a rod are

$$A = 0.5p^2 \tan 60 - 0.25\pi d^2 ,$$

$$D_h = 4A/P = (2p^2 \tan 60 - \pi d^2)\pi d ,$$

where p is the rod center-to-center pitch, and d is the rod diameter. The user may input the flow area or input the pitch and allow the program to calculate the flow area. With the above information, a Reynolds number

(Re) based on the hydraulic diameter is determined. The program then applies appropriate Nu correlations for the smooth and roughened sections. For the smooth section, the Nu is obtained from the Dittus-Boelter equation (Ref. 6-2),

$$Nu_{DB} = 0.023Re^{0.8}Pr^{0.4} \quad ,$$

and corrected for lattice effects by the relationship of Ref. 6-3:

$$\frac{Nu}{Nu_{DB}} = 1 + 1.322Re^{-0.139}\left[1 - 2.065\ \exp\left(\frac{-V_c}{1 - V_c}\right)\right] \quad ,$$

where $V_c$ is the void volume fraction in the lattice. For the roughened section, an Nu correlation developed from data on roughened rods in a smooth tube was used:

$$Nu = 12.3 + 0.0133Re^{0.882} \quad .$$

The film heat transfer coefficient (h) is related to Nu by the form

$$h = Nu\frac{k}{D_H} \quad .$$

After subroutine GOLDN determines the temperature of the outer cladding surface, other routines subsequently calculate the temperature gradients inward to the center of the fuel. These calculations required no modification.

The above helium heat transfer formulation has been incorporated into LIFE-III and successful runs have been obtained. The accuracy of calculational results is currently being evaluated.

## 6.2. ANALYSIS OF IRRADIATION TESTS

### 6.2.1. Evaluation of General Electric F-20 Rods

The analysis of fuel rods E-1, E-3, and S-4 from the General Electric (GE) F-20 fast flux irradiation program was completed, and the results were reported to the National LIFE-III Working Committee and the National Experiment Evaluation Program (NEEP) (see Tables 6-1 through 6-3). The analysis was performed using the LIFE-III code. In the analysis, the fueled region of the experimental rods was divided into five axial sections.

Because of the limited availability of the experimental measurements, only partial comparison of the LIFE-III results and the measured data was possible (Table 6-3). Considering that the irradiation was of very short duration (~4 hr) for rod S-4, the agreement of the predicted and the experimental measurements is quite good since, for the most part, it is within the standard deviation of the measurements. However, more experimental data are needed to better define this agreement. As more experimental data are made available, the comparison will be expanded and completed.

### 6.2.2. Evaluation of General Atomic F-3 Rods

The collection and analysis of the preirradiation and postirradiation data for the G-19 rod in the F-3 series irradiation tests in EBR-II have been initiated. The TAC-2D program is being used to find the rod cladding outside diameter temperature for the input of the LIFE-III analysis. In addition, the LAMDA code is being used to generate the rod power history from the measured fission rate density of the fuel rod.

## 6.3. DESIGN CRITERIA

Work is continuing on publication of a draft version of the GCFR fuel, blanket, and control component structural criteria. During this quarter, comments on the draft version of the criteria have been reviewed. The

TABLE 6-1

LIFE-III CALCULATED DATA, ROD E-1[a]

| | Axial Section | | | | |
|---|---|---|---|---|---|
| | 1 (Bottom) | 2 | 3 | 4 | 5 (Top) |
| Linear power level [W/cm (kW/ft)] | 537.92 (16.4) | 613.36 (18.7) | 636.32 (19.4) | 606.80 (18.5) | 528.08 (16.1) |
| Central void diameter [mm (in.)] | 1.1989 (0.0472) | 1.3665 (0.0538) | 1.4427 (0.0568) | 1.4072 (0.0554) | 0.1250 (0.0492) |
| Columnar grain diameter [mm (in.)] | 1.2497 (0.0492) | 3.7440 (0.1474) | 3.9116 (0.1540) | 3.8659 (0.1522) | 3.2106 (0.1264) |
| Equiaxed grain diameter [mm (in.)] | 1.3513 (0.0532) | 3.8456 (0.1514) | 4.0132 (0.1580) | 3.9675 (0.1562) | 3.3122 (0.1304) |
| Fuel diameter [mm (in.)] | 5.4661 (0.2152) | 5.4610 (0.2150) | 5.4610 (0.2150) | 5.4610 (0.2150) | 5.4610 (0.2150) |
| Melt diameter [mm (in.)] | -- | -- | 1.9573 (0.07706) | 1.7379 (0.06842) | -- |
| End of life (EOL) $\Delta D$ (%) | 0.0016 | 0.0016 | 0.0016 | 0.0016 | 0.0016 |
| Fuel cladding diametral gap [mm (in.)] | 0.1204 (0.00474) | 0.1280 (0.00504) | 0.1250 (0.00492) | 0.1250 (0.00492) | 0.1234 (0.00486) |
| EOL gas composition (% fission gas) | 0.015 | | | | |
| Fission gas released (%) | 3.3 | | | | |
| Fission gas released (moles) | $7.7 \times 10^{-8}$ | | | | |
| Plenum pressure at EOL [Pa (psia) at 0°C] | 116,509 (16.9) | | | | |
| Initial helium (moles) | 0.00052020 | | | | |
| Total gas at EOL (helium + fission gas) (moles) | 0.0005203 | | | | |

[a] Experimental results not measured yet.

TABLE 6-2

LIFE-III CALCULATED DATA, ROD E-2[a]

| | Axial Section | | | | |
|---|---|---|---|---|---|
| | 1 (Bottom) | 2 | 3 | 4 | 5 (Top) |
| Linear power level [W/cm (kW/ft)] | 541.20 (16.5) | 616.64 (18.8) | 639.60 (19.5) | 613.36 (18.7) | 513.36 (16.2) |
| Central void diameter [mm (in.)] | 1.3945 (0.0549) | 1.5189 (0.0598) | 1.5545 (0.0612) | 1.5545 (0.0612) | 1.4783 (0.0582) |
| Columnar grain diameter [mm (in.)] | 3.6043 (0.1419) | 4.0234 (0.1584) | 4.1859 (0.1648) | 4.1554 (0.1636) | 3.8760 (0.1526) |
| Equiaxed grain diameter [mm (in.)] | 3.7440 (0.1474) | 4.0437 (0.1592) | 4.2875 (0.1688) | 4.1758 (0.1644) | 4.0030 (0.1576) |
| Fuel diameter [mm (in.)] | 5.5626 (0.2190) | 5.5626 (0.2190) | 5.5677 (0.2192) | 5.5677 (0.2192) | 5.5728 (0.2194) |
| Melt diameter [mm (in.)] | -- | -- | -- | -- | -- |
| End of life (EOL) ΔD (%) | 0.0021 | 0.0024 | 0.0026 | 0.0025 | 0.0023 |
| Fuel cladding diametral gap [mm (in.)] | 0.0254 (0.0010) | 0.0234 (0.00092) | 0.0208 (0.00082) | 0.0183 (0.00072) | 0.0147 (0.00058) |
| EOL gas composition (% fission gas) | 15.3 | | | | |
| Fission gas released (%) | 48.0 | | | | |
| Fission gas released (moles) | $9.4 \times 10^{-5}$ | | | | |
| Plenum pressure at EOL [PA (psia) at 0°C] | 142,016 (20.6) | | | | |
| Initial helium (moles) | 0.0005209 | | | | |
| Total gas at EOL (helium + fission gas) (moles) | 0.000615 | | | | |

[a] Experimental results not measured yet.

TABLE 6-3

COMPARISON OF EXPERIMENTALLY MEASURED RESULTS AND LIFE-III CALCULATED DATA, ROD S-4

| | Calculated | | | | | Experimentally Measured[a] | | | | |
|---|---|---|---|---|---|---|---|---|---|---|
| | Axial Section | | | | | Axial Section | | | | |
| | 1 (Bottom) | 2 | 3 | 4 | 5 (Top) | 1[b] | 2 | 3 | 4 | 5[c] |
| Linear power level [W/cm (kW/ft)] | 557.60 (17.0) | 663.04 (19.3) | 659.28 (20.1) | 626.48 (19.1) | 544.58 (16.6) | | | | | |
| Central void diameter [mm (in.)] | 0.6741 (0.02654) | 0.9764 (0.03844) | 1.0617 (0.0418) | 1.0279 (0.04047) | 0.7876 (0.0314) | 0.0711 (0.0028) | | | | 1.9101 (0.0752) |
| Columnar grain diameter [mm (in.)] | 3.1521 (0.1241) | 3.7516 (0.1477) | 3.9522 (0.1556) | 3.8913 (0.1532) | 3.4849 (0.1372) | 3.6906 (0.1453) | | | | 4.1250 (0.1624) |
| Equiaxed grain diameter [mm (in.)] | 3.2537 (0.1281) | 3.8532 (0.1517) | 4.0538 (0.1596) | 3.9929 (0.1572) | 3.5865 (0.1412) | 4.7066 (0.1853) | | | | 5.2070 (0.2050) |
| Fuel diameter [mm (in.)] | 5.4788 (0.2157) | 5.4813 (0.2158) | 5.4788 (0.2157) | 5.4762 (0.2156) | 5.4762 (0.2156) | 5.4889 (0.2161) | | | | 5.4254 (0.2136) |
| Melt diameter [mm (in.)] | -- | 1.9812 (0.078) | 2.3622 (0.093) | 2.2250 (0.0876) | 1.4021 (0.0552) | 1.3691 (0.0539) | | | | 2.0523 (0.0808) |
| End of life (EOL) ΔD (%) | 0.0014 | 0.0014 | 0.0014 | 0.0014 | 0.0014 | 0.0[d] | | | | 0.04[e] |
| Fuel cladding diametral gap [mm (in.)] | 0.1082 (0.00426) | 0.1057 (0.00416) | 0.1097 (0.00432) | 0.1113 (0.00438) | 0.1123 (0.00442) | 0.0889 (0.0035) | | | | 0.1600 (0.0063 |
| EOL gas composition (% fission gas) | ← 0.036 → | | | | | ← 0.425 → | | | | |
| Fission gas released (%) | ← 3.62 → | | | | | | | | | |
| Fission gas released (moles) | ← $8.9 \times 10^{-8}$ → | | | | | ← $1.42 \times 10^{-6}$ → | | | | |
| Plenum pressure at EOL [PA (psia) at 0°C] | ← 56,531 (8.2) → | | | | | ← 96,516 (14.0) → | | | | |
| Initial helium (from decks) (moles) | ← 0.00024550 → | | | | | ← 0.0002453 → | | | | |
| Total gas at EOL (helium + fission gas) (moles) | ← 0.0002456 → | | | | | ← 0.000396 → | | | | |

[a] Reference 6-1.

[b] These measurements are at 17.27 mm (0.680 in.) above core bottom.

[c] These measurements are at 327.15 mm (12.88 in.) above core bottom.

[d] Average of five measurements on the bottom 17.27 mm (0.680 in.) of core.

[e] Average of five measurements on the top 17.78 mm (0.7 in.) of core.

responses have taken the form of either modification of the criteria or delay of a decision until specific LMFBR criteria verification tests have been completed and analyzed. The areas of major activity have been the design margins and the strain limit sections.

### 6.3.1. Design Margins

The effect of the design margins is to quantify the set of guidelines. Thus, there is considerable concern over their value and application. A new philosophy of correlating component type with design margins for the various types of operating conditions has been incorporated into the criteria. The recommended approach classifies components according to safety and reliability considerations of the individual component relative to the core system requirements. This classification is consistent with the guidelines of RDT standard C16-1 for event classifications and associated severity levels. The core designer is now responsible for classifying each core component into one of three classes based on the level of structural integrity required to satisfy system damage severity limits under the events classification of RDT C16-1. Class A components have the most stringent safety requirements and Class C the least. For each component event classification, values of $\alpha$ (time-independent stress intensity margin) and $\beta$ (damage and strain limit design margin) are specified. The designer may substitute less conservative margins if they can be justified. An extended description of the basis for choosing the existing values of $\alpha$ and $\beta$ is being prepared as part of the recommended application procedures. The design margins are not intended to indicate the threshold of catastrophic failure, but rather the bounds below which the material behavior is adequate to ensure that component response does not violate the system safety requirements. In view of this, it may be desirable to establish values of $\alpha$ and $\beta$ for events classified as extremely unlikely based on the latest thinking on margins which would ensure a coolable configuration. These values are not presently specified, but this position is being evaluated.

### 6.3.2. Strain Limits

Various aspects of the strain limit section of the preliminary design criteria were revised. This section contains a normalized strain summation rule intended to protect against a ductile-tensile instability when loading and unloading occur at different levels. Data exist for 304 and 316 stainless steel subjected to biaxial creep and then to a uniaxial tensile test. These data are being analyzed as part of a justification for the above rule. However, in the absence of more extensive tests (presently contemplated by HEDL by FY-77), this section is now considered an uncertain criterion which reflects the latest consensus on this type of failure. In addition, a cautionary note emphasizing the importance of proper modeling and analysis in the event of large strains or large deflections has been inserted. An expanded treatment of large strain/deflection techniques will be included in the application procedures. Finally, the philosophy of considering irradiation creep strains as not being ductility limited was reviewed and supported on the basis that no rupture failures have occurred on irradiated pressurized tubes with strains as large as 3%.

The application of these strain limit criteria has also been revised. Originally, the limits of this section applied regardless of the analysis type. It is now felt that application of these rules in conjunction with an "elastic only" or an "elastic irradiation creep-swelling" analysis is redundant since the time-independent stress limits are more restrictive. Consequently, the current draft of the criteria requires satisfaction of strain limits only when a nonlinear analysis (plasticity, thermal creep, and geometric nonlinearities) is performed.

## 6.4. ROD ANALYSIS AND PERFORMANCE

### 6.4.1. Fuel Rod Parametric Studies

The preliminary parametric study to evaluate the effects of the variation of design parameters (i.e., fuel pellet geometry, fuel cladding gap size, cladding thickness, fuel density, etc.) has continued. To study

the effect of cladding thickness on fuel rod performance, LIFE-III was used to analyze fuel rods with cladding thicknesses of 0.508 (0.02), 0.457 (0.018), 0.380 (0.015), 0.305 (0.012), and 0.254 (0.01) mm (in.). In order to compare the results from the different cladding thicknesses, the rod outside diameter and the fuel cladding gap were kept constant, so that the fuel pellet outside diameter was accordingly increased for the lower values of cladding thickness. However, to compensate for the increased fuel pellet diameter, the fuel enrichment was proportionally decreased rather than decreasing the fuel density. The LIFE-III computer runs were obtained, and analysis of the computer output is in progress to obtain and interpret the effect of the cladding thickness on fuel rod performance.

### 6.4.2. Rod Analysis and Performance

The rod cladding creep collapse study of simulated, accidentally sealed GCFR fuel rods continued during this quarter. Various rod parameters have been evaluated with respect to internal fission gas buildup in these sealed GCFR rods using the LIFE-III computer code. These pressure data are then used to evaluate the possibility of creep collapse using the CREBUCK code.

Preliminary results indicate that low-power rods with a cladding thickness of 0.38 mm (0.015 in.) may suffer creep collapse after 3000 to 4000 hr because the internal pressure does not increase fast enough to counter the external coolant pressure. As a precaution against such failure, the rods could initially be prepressurized by an amount sufficient to retard the collapse progression in these low-power rods. The prepressurized low-power rods are currently being analyzed with respect to creep collapse. However, preliminary runs using the CREBUCK code have revealed inadequacies in accommodating time-pressure histories. A new code is expected to be implemented shortly by HTGR Engineering, which has accurately handled problems of this type of steam generator tubing. At that time, the prepressurized low-power rod collapse will be analyzed.

REFERENCES

6-1 Goodman, J., et al., "The Thermodynamic and Transport Properties of Helium," General Atomic Report GA-A13400, October 1975.

6-2 Rohsenow, W. M., and J. P. Hartnett, Handbook of Heat Transfer, McGraw-Hill, New York, 1973, pp. 7-32.

6-3 Rapier, A. C., and L. White, "Forced-Convection Heat Transfer From a Cluster of Rods to an Axial Coolant Flow," UKAEA TRG Report 438(W), 1963.

## 7. NUCLEAR ANALYSIS AND REACTOR PHYSICS (189a No. SU008)

The scope of activities planned under this subtask encompasses the validation and verification of the nuclear design methods that will be applied to the GCFR core design. This will primarily be done by direct evaluation of the methods with a critical assembly experimental program specifically directed toward GCFR development. Program planning and coordination activities, critical assembly design and analysis, and the necessary methods development will be carried out during the course of this program.

During the previous quarter, planning for the inclusion of a steel reflector surrounding the Phase II and all subsequent assemblies was completed. Recalculation of steam and control boron worth with the reflector in place was accomplished. Postanalyses of the Phase I assembly, and in particular the steam zone experiment, were refined and continued. Methods development proceeded with the inclusion in data files of Version IV delayed-neutron data and initial efforts at speeding convergence of the 2DB two-dimensional diffusion code, to be used as a possible replacement for the more slowly converging ADGAUGE code.

During this quarter, the design of the three-zone Phase III core was finalized and the experimental program was specified in conjunction with ANL. Postanalysis of the $CH_2$ zone experiment in the Phase I core was completed, and initial comparisons with the experimental results for whole-core steam entry worths were undertaken. The 2DB diffusion code and the associated perturbation code PERT were implemented as production codes. Development of the PINDF3 code, which correctly computes bidirectional diffusion coefficients in pin geometry, was completed.

## 7.1. PHASE I CRITICAL ASSEMBLY

### 7.1.1. Analysis of Steam Zone Experiment

The effort on the central steam zone analysis in the Phase I core was concluded with the publication of an extensive memorandum discussing various methods of analysis. Several conclusions were drawn from this study:

1. Spectra must be recomputed at each steam density and cross sections reaveraged in order for perturbation calculations to be accurate. The attempted technique of mixing dry and full-density $CH_2$ cross sections to achieve intermediate-density cross sections does not give good results. Exact perturbation (EP) methods using reaveraged cross sections give reactivity worths which are in good agreement with experimental results (Table 7-1). In fact, EP calculations using a 28-group energy mesh exhibit the central-worth discrepancy characteristic of light scatterers, as would be expected.

2. Accurate calculation of the adjoint flux depends upon the group structure, with a larger number of energy groups generally giving a better calculation. Since collapsing the cross sections (which are used to compute the adjoint) with a real flux weighting does not conserve the adjoint fluxes between a few- and a many-group calculation, the only way to avoid this problem at present is to use many groups in any calculation involving hydrogen.

## 7.2. PHASE II CRITICAL ASSEMBLY

### 7.2.1. Whole-Core Steam Flooding

The effect of insertion of $CH_2$ in the full core and blanket regions at two different densities has been analyzed and compared with experimental

TABLE 7-1
SUMMARY OF EXPERIMENTAL AND CALCULATED RESULTS FOR PHASE I STEAM ZONE EXPERIMENTS

| Case Number | Measured Weight of $CH_2$ in Zone (g) | Calculated Weight of $CH_2$ in Zone (g) | Approximate Channel Density ($g/cm^3$) | Experimental[a] Reactivity Worth (Ih/kg) | Calculated Reactivity Worth (Ih/kg) | | |
|---|---|---|---|---|---|---|---|
| | | | | | Exact Perturbation Method, 10 Groups | Exact Perturbation Method, 28 Groups | Eigenvalue Difference Method, 10/28 Groups |
| 1 | 784.0 | 768.7 | 0.035 | 200.52 ± 3.32 | 194.8 | 239.6 | 215.4/266.0 |
| 2 | 408.2 | | 0.035/2 | 169.01 ± 6.66 | | | |
| 3 | 373.8 | 384.35 | 0.0175 | 160.17 ± 8.77 | 155.3 | 184.1 | -- |
| 4 | 194.4 | 192.2 | 0.0175/2 | 134.30 ± 14.76 | 128.2 | 155.8 | -- |

[a] Reference 7-1.

results. Table 7-2 gives the results calculated by Δk techniques. These results are conservative; i.e., the calculated reactivity insertions are greater than the experimentally measured values.

### 7.2.2. Analysis of Control Boron Worth in a Dry and a Steam-Flooded Core

Comparison of experimental measurements with calculations are shown in Table 7-3. The calculations were done in a 10-group energy mesh using eigenvalue difference techniques and give satisfactory agreement for the two cases reported to date.

### 7.2.3. Postanalysis of Central Reactivity Worths

Central worths have been recomputed for the as-built Phase II core (without reflector) and are shown in Table 7-4. For comparison, the corresponding postanalysis values for the first core are also shown. Somewhat better agreement is uniformly evident; this is believed to be due to the fact that the smaller Phase II core, although unreflected at this measurement stage, is much more decoupled from reflective effects of the bed and knee structure of the assembly machine than the large Phase I core. Further investigation is under way.

## 7.3. PHASE III CRITICAL ASSEMBLY

### 7.3.1. Planning and Liaison

Working meetings with ANL were held in March to fix the configuration of the three-zone Phase III core and to establish the experimental program within the limited time available for completion of the program.

### 7.3.2. Critical Assembly Design

Specifying the Phase III design involved a lengthy analysis of many possibilities for core zone configurations and enrichments, with the demonstration plant parameters as a general target. However, limitations of

TABLE 7-2
ANALYSIS OF SIMULATED STEAM FLOODING EXPERIMENTS
IN PHASE II GCFR CRITICAL ASSEMBLY

| Nominal Density of $CH_2$ in Void Channels ($g/cm^3$) | Full Core and Blanket Regions in Phase II | |
|---|---|---|
| | Calculated Flooding Worth (Ih)[a] | C/E[b] |
| 0.0088 | 278 | 1.34 |
| 0.0175 | 855 | 1.62 |
| 0.0350 | 1850 | Not measured |

[a] Using eigenvalue difference from 10-group, RZ diffusion calculations. Core radius slightly different than experiment.

[b] Experimental values from Ref. 7-2.

TABLE 7-3
CALCULATED VERSUS EXPERIMENTAL BORON CARBIDE ROD WORTHS IN PHASE II GCFR ASSEMBLY WITH VARYING SIMULATED STEAM FLOODING

| Nominal $CH_2$ Density in Void Channels ($g/cm^3$) | Central $B_4C$ Column[a] Replacing Void Can | | 9 Distributed $B_4C$ Columns[a] (center + 8-rod ring) | |
|---|---|---|---|---|
| | Calculated Worth ($) | C/E | Calculated Worth ($) | C/E |
| Dry | -1.32 | 0.93 | -7.16 | --[b] |
| 0.0088 | -1.49 | 0.95 | -- | Not measured |
| 0.0175 | -1.67 | --[b] | -9.16 | --[b] |
| 0.0350 | -1.89 | Not measured | -- | Not measured |

[a] Columns averaging 4.6 g boron-10 per inch axially with cross section of 0.25 x 2.0 in.

[b] Experimental data not yet available.

TABLE 7-4
ANALYSIS OF CENTRAL WORTH MEASUREMENTS IN
INITIAL GCFR CRITICAL ASSEMBLIES

| Material | Core Center Reactivity Coefficient | | | |
|---|---|---|---|---|
| | Phase I Assembly | | Phase II Assembly | |
| | Calculation (Ih/kg) | C/E | Calculation (Ih/kg) | C/E |
| He | -108.4 | -- | -191 | 1.22 |
| B-10 | -2434 | 1.19 | -3804 | 1.11 |
| C | -21.33 | 1.75 | -35.91 | 1.69 |
| Fe | -4.879 | 1.45 | -8.63 | 1.35 |
| Th | -17.19 | 1.32 | -27.18 | 1.27 |
| U-233 | -- | -- | 374 | 1.27 |
| U-235 | 127.1 | 1.28 | 207.5 | 1.23 |
| U-238 | -8.69 | 1.32 | -13.18 | 1.15 |
| Pu-239 | 168.3 | 1.23 | 279.6 | 1.21 |
| Pu-240 | 25.94 | 1.16 | 48.57 | 1.15 |

the ZPR-9 facility and the core void fraction adopted (45 versus 55 vol %) produce a smaller core volume. The core void fraction and heavy metal density were fixed by the intended pin-zone loading at the center of zone 1, thereby also fixing the matching enrichment for the zone 1 plate-type loading.

A second target goal was the demonstration of power flattening in the zoned core. To accomplish this, searches on the (outer) zone 3 enrichment and the radial thicknesses of all zones were carried out. The final loading specifications and core zone parameters are shown in Tables 7-5 and 7-6, respectively. In addition to meeting the target design goals, this configuration utilizes the existing Phase II core drawer loadings as core zone 2, thus eliminating some loading time otherwise needed.

For this three-zone model, with a total fissile loading of 913.5 kg, the calculated 2DB eigenvalue was 0.9980 using cross sections from the Phase II analysis. This is comparable to the 2DB results for the as-built Phase II core.

## 7.4. METHODS DEVELOPMENT

### 7.4.1. Diffusion Code Development

The 2DB code has been modified by the addition of convergence acceleration algorithms. Optimum inner iteration overrelaxation factors are now internally computed for each energy group at the problem start. Improvements in I/O and data management schemes were also added. With these changes, the 2DB code now runs considerably faster than the previously used ADGAUGE code, and, along with the associated perturbation code package PERT, it is being utilized as the standard production code.

### 7.4.2. Bidirectional Modifiers Code

The auxiliary code PINDIF-II, which generates bidirectional diffusion coefficient modifiers for RZ geometries with nonvoided axial channels,

TABLE 7-5
LOADING SPECIFICATIONS FOR PHASE III CORE

| Region | Drawers Per Half | Volume (liters) | Outer Radius (cm) |
|---|---|---|---|
| Core | 229 | 853.2 | 47.17 |
| Core | 192 | 715.3 | 63.95 |
| Core | 100 | 372.6 | 71.14 |
| Radial blanket | 500 | 2793 | 99.59 |
| Reflector | 256 | 1430 | 111.38 |
| Core Total | 521 | 1941.1 | 71.14 |

TABLE 7-6
CORE ZONE PARAMETERS FOR PHASE III CORE

| | Zone 1 | Zone 2 | Zone 3 |
|---|---|---|---|
| Fraction of core (%) | 44.0 | 36.8 | 19.2 |
| Cell width | 1 drawer | 3 drawers | 1 drawer |
| Nominal enrichment (%) | 13.1 | 17.5 | 26.2 |
| Pu-U-Mo columns/cell | 1 | 4 | 2 |
| Fissile mass, (kg Pu-239 + Pu-241) | 305.8 | 340.6 | 267.1 |
| Average zone power density | 100.2 | 97.5 | 104.4 |
| In-zone peak/average power | 1.422 | 1.492 | 1.396 |
| Zone peak/core average | 1.425 | 1.454 | 1.457 |
| Midplane peak/average power | 1.122 | 1.145 | 1.147 |

was found to have significant errors in cases involving low material density in the channels. Extensive revisions were made, and the code has been reissued as PINDF3. This code will handle voided and nonvoided channel cases.

REFERENCES

7-1 Smith, D. M., et al., Argonne National Laboratory, private communication.

7-2 Bohn, E. M., Argonne National Laboratory, private communication.

# 8. SHIELDING REQUIREMENTS (189a No. SU008)

The purpose of the shielding task is to verify the adequacy of the methods and data (physics and engineering) for the design of GCFR shields and to evaluate the effectiveness of various shield configurations. In addition, this task coordinates and provides liaison with the analytical and experimental GCFR shielding activities at ORNL.

During the last quarter, a detailed analysis of the GA and ORNL shielding benchmark was carried out, wherein the sources of difference in the absolute magnitude of the neutron transport and heating results were examined. Additional analysis of the two-row blanket radial shield was conducted. The feasibility of incorporating a removable shield reflector element adjacent to the radial blanket was analyzed, and the effect of recent damage function data on the radial shield was investigated.

During this quarter, effort was directed to the following:

1. Extensive review and analysis of the lower shield and wraparound shield were performed. A model of the revised lower shield and wraparound was developed and sent to ORNL for two-dimensional calculations with the DOT III code (Ref. 8-1).

2. Preliminary calculations were performed for fluence and neutron-induced embrittlement in the grid plate of the 300-MW(e) GCFR with the current $B_4C$ grid plate shield design. The model was an RZ, two-dimensional mock-up of a grid plate cylindrical equivalent cell at the location of the central fuel element. The transport calculation used a highly forward-biased quadrature set in order to accurately treat the axially peaked streaming. Recent damage function data from Ref. 8-2 were utilized

to estimate the time to reach specific residual ductility levels in the grid plate.

## 8.1. LOWER SHIELD AND WRAPAROUND SHIELD

The initial lower shield and wraparound shield assembly that was reviewed for study is shown in Fig. 8-1 (also, see Ref. 8-3). A model of the region shown in Fig. 8-1 was also used in the DOT III two-dimensional calculations of the entire reactor cavity performed at ORNL in 1974 and 1975 (Ref. 8-4). The approach used in the present review was (1) study present ORNL two-dimensional results; (2) perform approximate one-dimensional slab calculations in appropriate regions of the lower shield and wraparound region; (3) obtain and study the current design being considered by the Vessel and Internals Branch using the one- and two-dimensional results as a guide for fluxes and fluence damage for 24 yr at full power; and (4) propose a revised model of the lower shield and wraparound shield for two-dimensional calculations at ORNL.

### 8.1.1. Two-Dimensional Calculations

Two-dimensional transport calculations were performed for GA by ORNL, as reported in Ref. 8-4. The ORNL calculations were performed with DOT in RZ geometry using the 50-group cross-section library employed at ORNL. The GA calculations were performed with $S_6$ angular quadratures and $P_1$ anisotropic scattering. Additional calculations for the lower shield - wraparound region were made with a biased quadrature set containing 306 angles in order to more accurately treat the transport below the outer radial shield and above the outer annular region. Calculations were performed for the reference shield and a revised shield that contained $B_4C$ in the outer part of the outer radial shield. Isoflux plots of total neutron flux and neutron flux with energy $E > 1.0$ MeV, $E > 0.1$ MeV, and $E < 2.38$ eV were generated at ORNL and transmitted to GA for study.

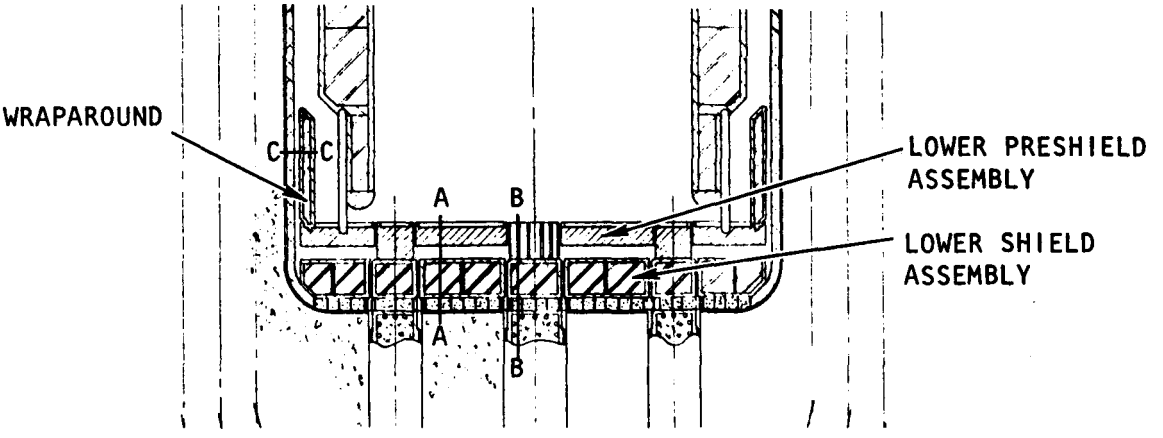


Fig. 8-1 Vertical section through reactor cavity

### 8.1.2. One-Dimensional Slab Calculations

The parts of the lower shield and wraparound region chosen for one-dimensional slab calculations are shown in Fig. 8-1 as cuts A-A and B-B in the lower shield region and C-C in the wraparound region. Several material and dimension configurations were considered. The criterion used for assessing the degree of conservatism in the calculations at the liner was the 75°C (167°F) nil ductility temperature shift (NDTS). In the stainless steel, the 10% residual ductility (RD) damage response function for a temperature of about 575°C (1067°F) was used. In both cases, the nominal response functions were used. The use of the above damage functions was described in Ref. 8-5.

The final one-dimensional slab configurations considered along cuts A-A, B-B, and C-C are given in Fig. 8-2. Cut A-A involved the study of two configurations, one without fused silica and one with fused silica below the preshield as shown. Along cut B-B, there is essentially a hole in the preshield above the central plug of the access hole for the fuel transfer machine. (The vertical lines in the central hole of the preshield of Fig. 8-1 represent vertical fins for radially directing the helium gas into the coolant passage between the preshield and the lower shield.) Along cut C-C, the wraparound configuration includes a 2.9-cm (1.14-in.) thickness of $B_4C$ + C, with $B_4C$ at 19.5 wt %.

### 8.1.3. Results of One-Dimensional Calculations

The one-dimensional neutron transport calculations were performed with the 1DFX computer program (Refs. 8-6, 8-7) in slab geometry with 24 neutron groups, $S_{16}$,$P_3$ angular quadratures, and anisotropic scattering. The incident neutron spectra above the lower shield and at the wraparound were obtained from previous ORNL calculations. The damage functions for the 75°C (167°F) NDTS and the 10% RD were collapsed to the 24 neutron groups from the corresponding 75-group damage functions reported in Ref. 8-2. The one-dimensional gamma heating calculations were performed with the

LOWER SHIELD AND PRESHIELD

NO. 1, SECTION A-A, WITHOUT $SiO_2$

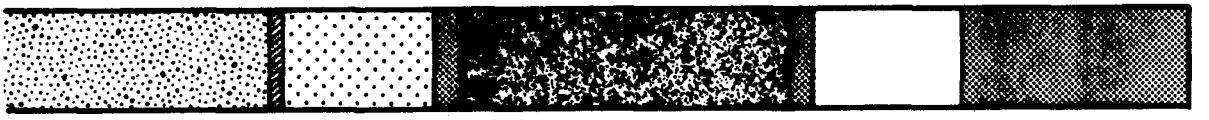

NO. 2, SECTION A-A, WITH $SiO_2$

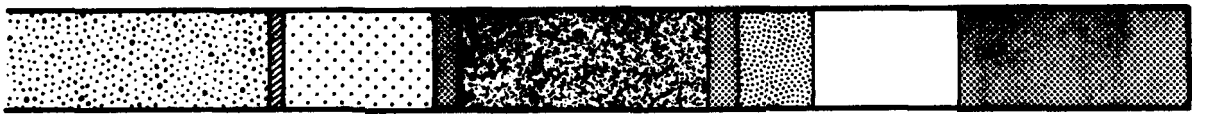

LOWER SHIELD CENTRAL PLUG

SECTION B-B

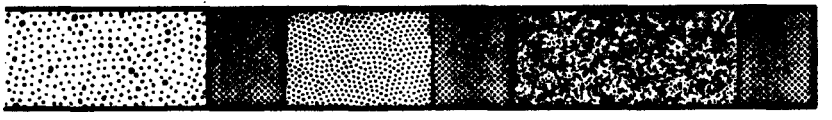

WRAPAROUND

SECTION C-C

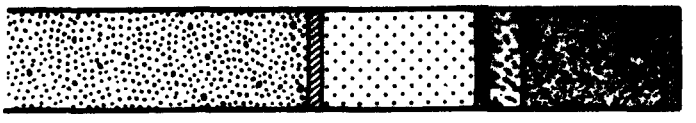

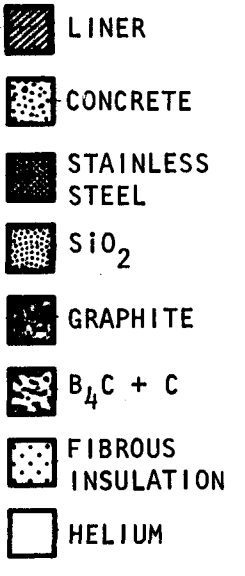


Fig. 8-2 Slab configurations for lower shield and wraparound shield

GA 24-neutron group - 15-gamma-ray group coupled set (Refs. 8-8, 8-9) with $S_{16}$,$P_3$ angular quadratures and anisotropic scattering.

Of primary interest from the neutron transport results was the calculation of the limiting total fluences at the liner and on the top of the stainless steel preshield. These limits were compared with the calculated fluences resulting from the one- and two-dimensional calculations. In these comparisons, a conservative factor of three to five or more was acceptable for the present stage of the shielding program. For a 75°C (167°F) NDTS in the liner, the conservative factor for the total fluence at the liner below the lower shield was about nine; at the radius of the central plug, the conservative factor at the liner was about eight; and behind the wraparound, about four. Because of the possible narrow streaming paths through the preshield construction joints and lower shield joints and around the radius of the central plug, it was decided to consider the present conservative shield configurations for gamma heating and two-dimensional calculations at this stage rather than search for a thinner, less conservative lower shield configuration.

At the top of the stainless steel preshield, however, the calculated total fluence limit was approximately $10^{22}$ n/cm$^2$ for a 10% RD, which is comparable to the fluence calculated by ORNL. This calculated fluence limit also agrees with the measured fluence limit for 10% RD in 316 stainless steel given in Ref. 8-10. Consequently, if a 10% RD is required in the preshield, further analysis and study will have to be given to this preshield problem, with particular attention given to the appropriate damage function determinations, damage measurements, and more detailed two-dimensional calculations of the GCFR reactor and cavity.

The gamma ray heating results along cut A-A of Fig. 8-1 are given for the lower shield without and with fused silica in Figs. 8-3 and 8-4, respectively, and for the configurations given in Fig. 8-2. In both calculations, it is noted that the heating rate in the concrete is about 0.5 mW/cm$^3$ (4.8 x $10^4$ Btu/hr-ft$^3$). This indicates that in this region of the prestressed concrete reactor vessel (PCRV), the shield configuration

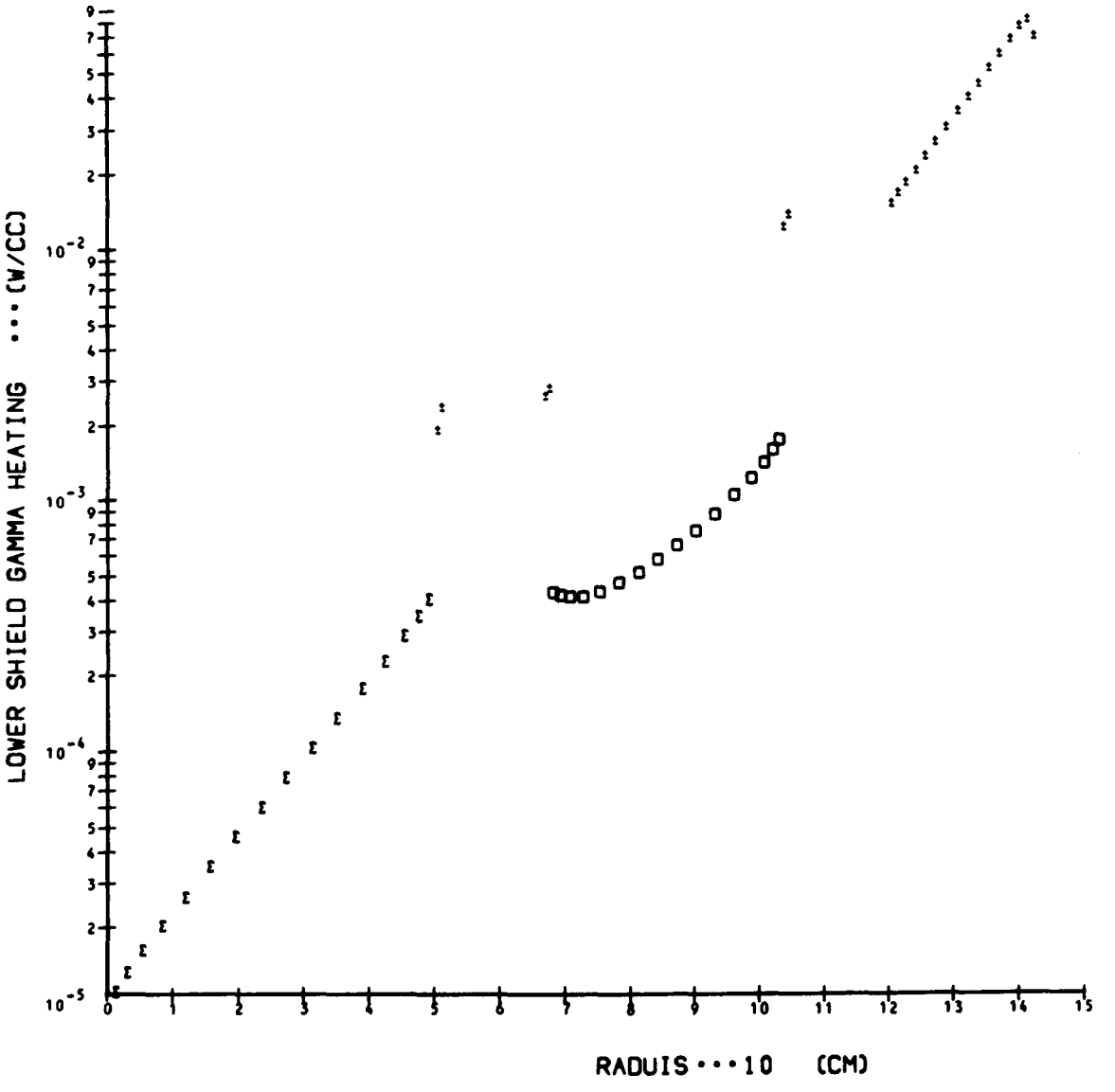


Fig. 8-3 Gamma ray heating for lower shield without fused silica

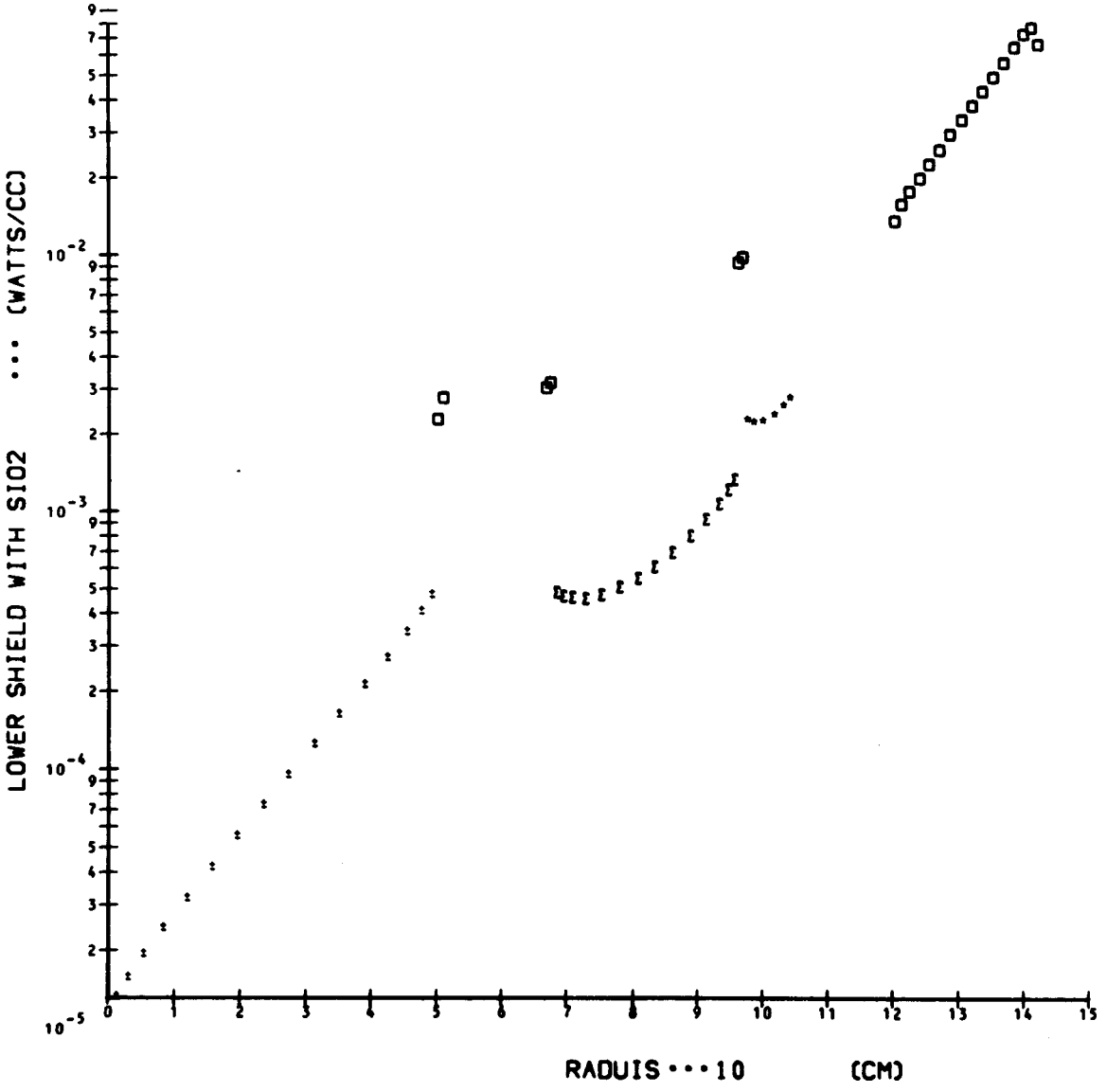


Fig. 8-4 Gamma ray heating for lower shield with fused heating

may be determined by the heating of the concrete rather than by the 75°C (167°F) NDTS in the liner.

The gamma ray heating results along cut C-C of Fig. 8-1 are given in Fig. 8-5 for the wraparound region. In Fig. 8-5, the maximum gamma ray heating rate in the concrete is about 0.3 $mW/cm^3$ ($2.9 \times 10^4$ $Btu/hr\text{-}ft^3$). However, the concrete heating rate above the wraparound shield will have to be determined in the two-dimensional calculations at ORNL. The gamma ray heating results given in Figs. 8-3, 8-4, and 8-5 were given to the Vessel and Internals Branch for use in the analysis of the revised lower shield. The wraparound region is discussed below.

### 8.1.4. Revised Model of the Lower Shield and Wraparound Region

As a result of communication with the Vessel and Internals Branch regarding its current engineering analysis and using the above results from the Nuclear Analysis and Reactor Physics Branch, a revised model of the lower shield and wraparound region was proposed for two-dimensional calculations at ORNL; this model is presented in Fig. 8-6. Two major changes are (1) the outer radial shield rests on a graphite base, and (2) the central hole of the preshield is modified with a rounded stainless steel piece and a stainless steel "cover" placed on the central plug to provide a shield for the liner at the plug radius. The "steps" in the wraparound and the outer radial shield are merely an approximation for a tapered shield design. Finally, the graphite base for the outer radial shield as shown in Fig. 8-6 mitigates the effects of streaming observed in the initial two-dimensional calculations.

## 8.2. GRID PLATE SHIELDING ANALYSIS

The regions from the fuel rods through the grid plate are geometrically complex and represent one of the most challenging shielding problems in the GCFR (Ref. 8-11). Streaming up through the axial blanket and the grid plate region determines source intensities for neutrons, which eventually determine the flux levels at the reactor inlet ducts leading to

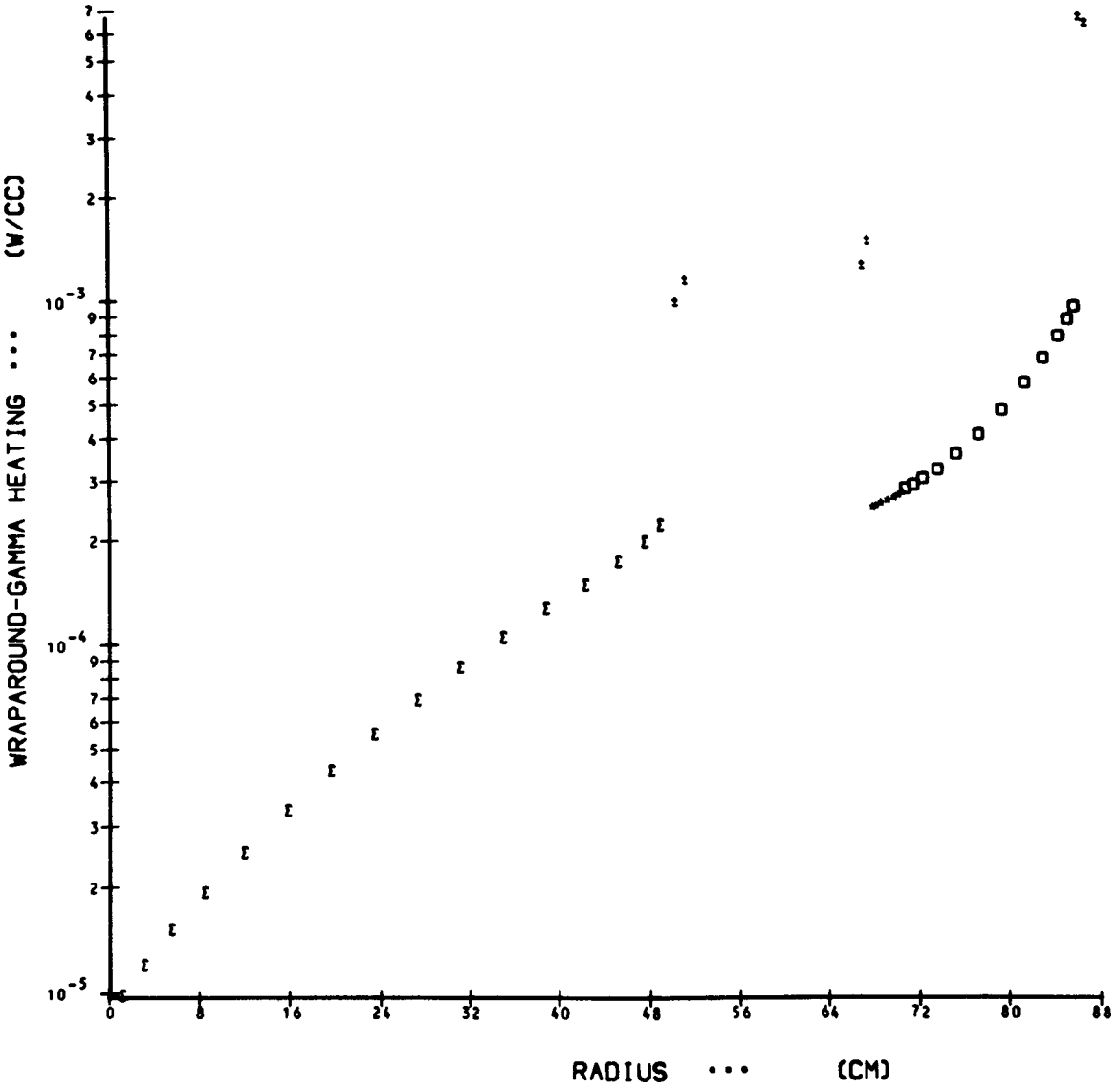


Fig. 8-5 Gamma ray heating for wraparound region

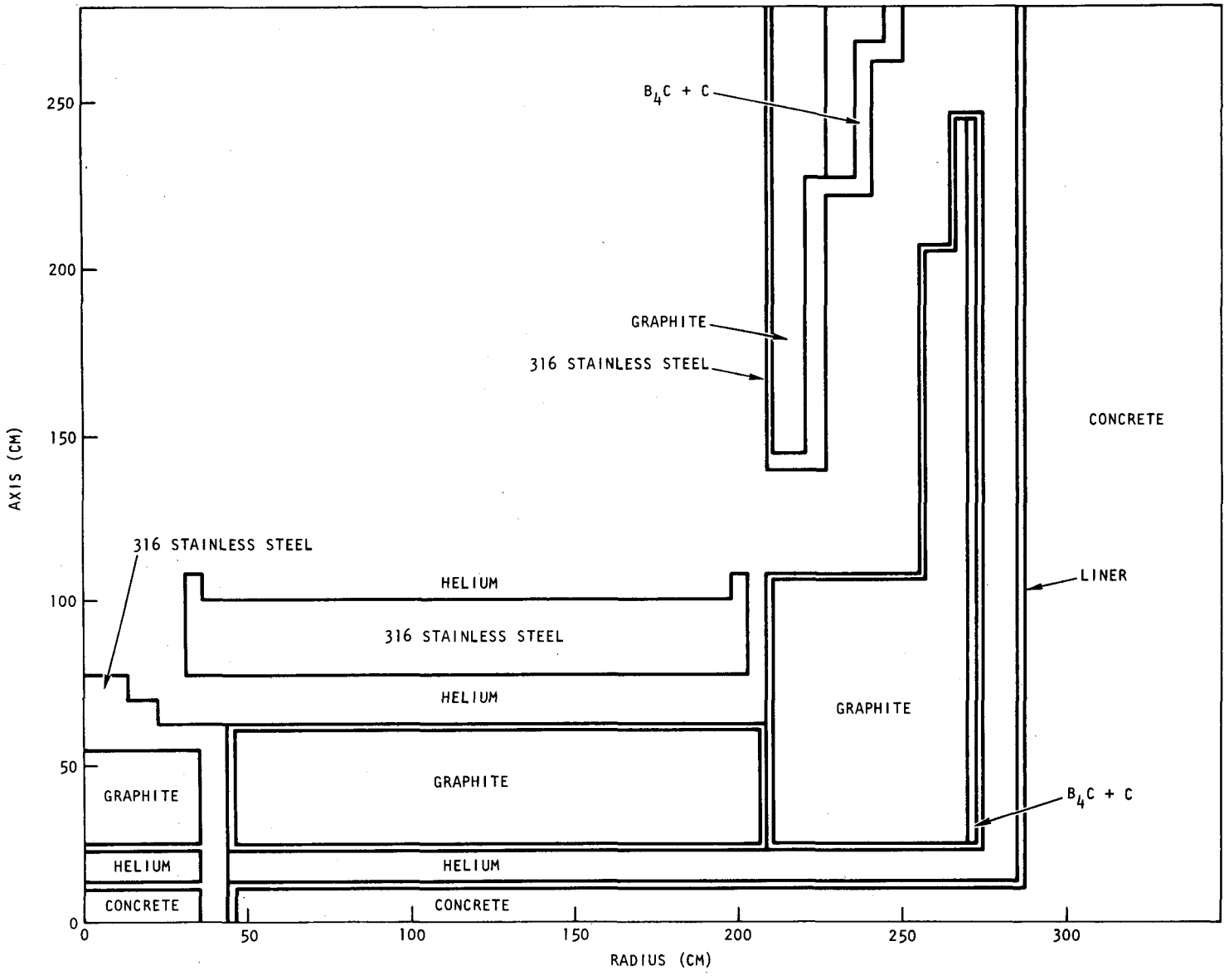


Fig. 8-6 300-MW(e) GCFR lower axial shield and wraparound model for two-dimensional calculations

the helium circulators. Shielding of the grid plate must be provided to prevent excessive irradiation damage to the grid plate. The grid plate shielding is geometrically complex owing to the necessity of eliminating direct streaming paths and, at the same time, minimizing pressure drop across the fuel elements. A detailed analytical program is required to qualify the design methods for the upper shields. For the most part, these geometric configurations may be calculated with two-dimensional discrete ordinates and three-dimensional Monte Carlo methods. The problem of neutron streaming from the fuel rods will continue to receive careful attention in the experimental program in order to bound the streaming effect and therefore minimize design margins.

### 8.2.1. Transport Calculations

For this preliminary analysis, advantage was taken of the fuel element symmetry to perform a two-dimensional discrete ordinates calculation for the maximum flux through the grid plate. The RZ model of a cylindrical grid plate equivalent cell at the location of the central fuel element is shown in Fig. 8-7. The mock-up extends from 30 cm (11.8 in.) above the core blanket interface to the top of the grid plate. The DOT-II (Ref. 8-12) code was modified to utilize the extended core capability of the UNIVAC 1110. The calculation was then performed with $P_3$ anisotropic scattering and a highly forward peaked, asymmetric quadrature set with 76 forward angles and 24 backward angles.

The most energetic and therefore damaging neutrons which reach the grid plate are those which stream in the grid plate shield region and therefore suffer few collisions. In addition, the angular flux emerging from the blanket is peaked in the forward direction for the higher energy groups. Therefore, use of the asymmetric quadrature set enhances the accuracy of the $S_N$ approximation by providing a relatively more accurate treatment of the axially streaming neutrons which induce the largest damage response in the grid plate (Ref. 8-13).

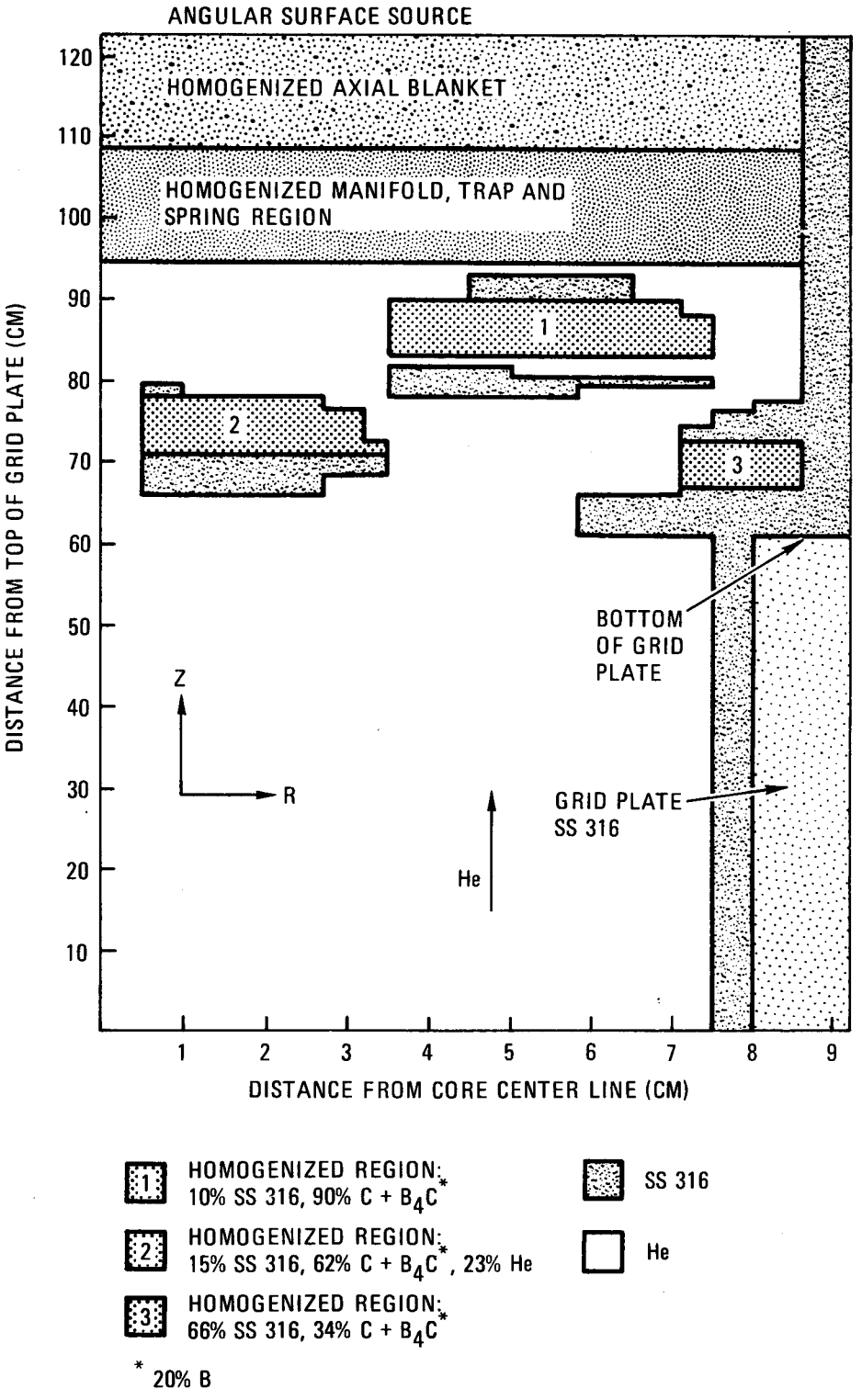


Fig. 8-7 RZ mock-up of cylindrical grid plate equivalent cell for DOT-II calculation

The 1DFX code (Ref. 8-6) was modified to use an asymmetric quadrature set. The two-dimensional, 100-angle quadrature set in $\mu$ and $\eta$ was reduced to an equivalent one-dimensional, 20-angle set in $\mu$ (Ref. 8-14), and the 1DFX calculation was performed in plane geometry for the configuration shown in Fig. 8-8. The two-dimensional angular boundary source at 30 cm (11.8 in.) above the core blanket interface was then obtained by assuming azimuthal ($\eta$) flux symmetry.

All cross sections used in the transport calculations were generated from ENDF/B-Version-IV data. The broad group cross sections were obtained using the GGC-5 code (Ref. 8-15) with $B_3$ calculations for single-region homogenized mixtures. The transport calculations used a 10-group structure (9 fast and 1 thermal).

### 8.2.2. Neutron Damage Functions

Energy-dependent damage functions from Ref. 8-2 were used to compute fluence levels to attain specific levels of residual ductility in the grid plate. The total fluence ($\phi t$) required to attain the property level P is computed from the relation

$$\phi t = \frac{P}{\sum_{g=1}^{G} \bar{G}_g^P \phi_g} \quad , \tag{8-1}$$

where $\bar{G}_g^P$ is the average damage function in the $g^{th}$ broad group, and $\phi_g$ is the group g scalar flux normalized such that

$$\sum_{g=1}^{G} \phi_g = 1.0 \quad . \tag{8-2}$$

The damage functions are divided by the property level for which they were derived and hence have units of $(n/cm^2)^{-1}$. Therefore, P in Eq. 8-1 has a value of 1.0.

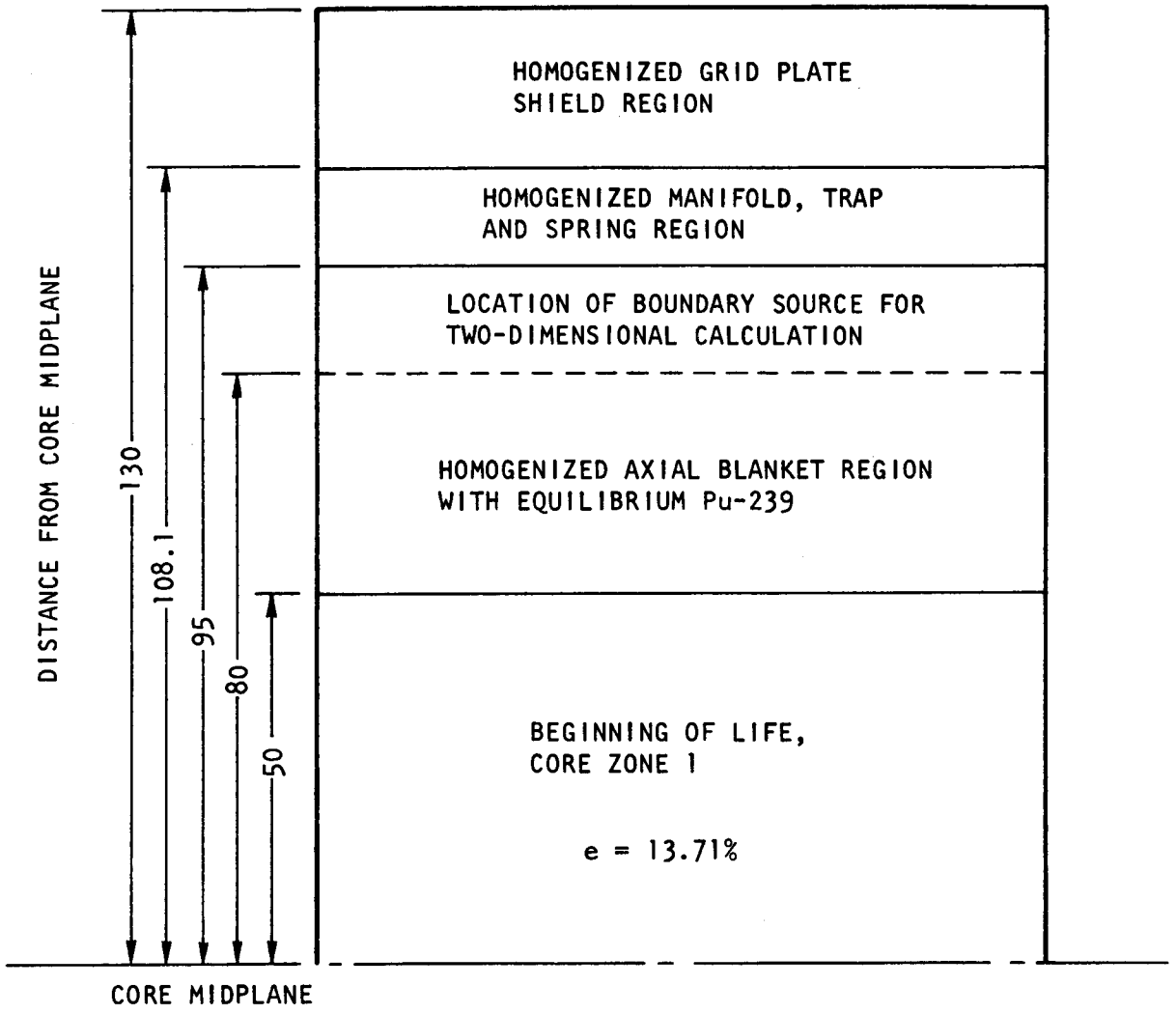


Fig. 8-8 Slab geometry mock-up of core, axial blanket, and grid plate shield region for 1DFX calculation

Three sources of error in the damage function which are propagated to the fluence limit prediction are (1) uncertainties associated with the characterization of the test spectrum, (2) measurement of the material property, and (3) lack of mathematical uniqueness of the damage function solution (Refs. 8-2, 8-16). Error analysis produces the upper bound solution to the damage function which is defined as the $2\sigma$ (95%) confidence level. The upper bound solution is used to compute the lower bound fluence which provides the most conservative estimate of the limiting exposure to obtain the material property level P in a given spectrum. In general, the inequality

$$\phi t_N - \phi t_{LB} \leq 2/3\ \phi t_N \quad , \tag{8-3}$$

where $\phi t_N$ is the nominal fluence limit and $\phi t_{LB}$ is the lower bound fluence limit, should be satisfied. This means that the tolerable error at the 95% confidence level is ~66%. If the inequality is not satisfied, the lower bound fluence limit should be considered indeterminate. This occurs because of insufficient data to accurately determine the energy dependence of the damage function and when the spectrum in question is considerably different from the test spectra used to determine the energy dependence.

The computer program DMGFCN was written to collapse the 75-fine-group damage functions given in Ref. 8-2 with GGC-5 generated spectra to obtain the desired 10-broad-group constants. Nominal and lower bound fluence limits for 5% and 10% uniform elongation (UE) were determined for annealed type 316 stainless steel irradiated at 399°C (750°F).

### 8.2.3. Results

Figure 8-9 shows a plot of the total, E > 0.1 MeV, and E > 1.0 MeV flux through the GCFR grid plate above the central fuel element. The total flux emerging from the axial blanket is $5.0 \times 10^{14}$ n/cm$^2$-s, with 42% of the total having E > 0.1 MeV. The total flux incident on the bottom of the grid plate is $4.0 \times 10^{13}$ n/cm$^2$-s, with about 37% of the total having E > 0.1 MeV. The grid plate shielding, which averages about 14 cm (5.5 in.)

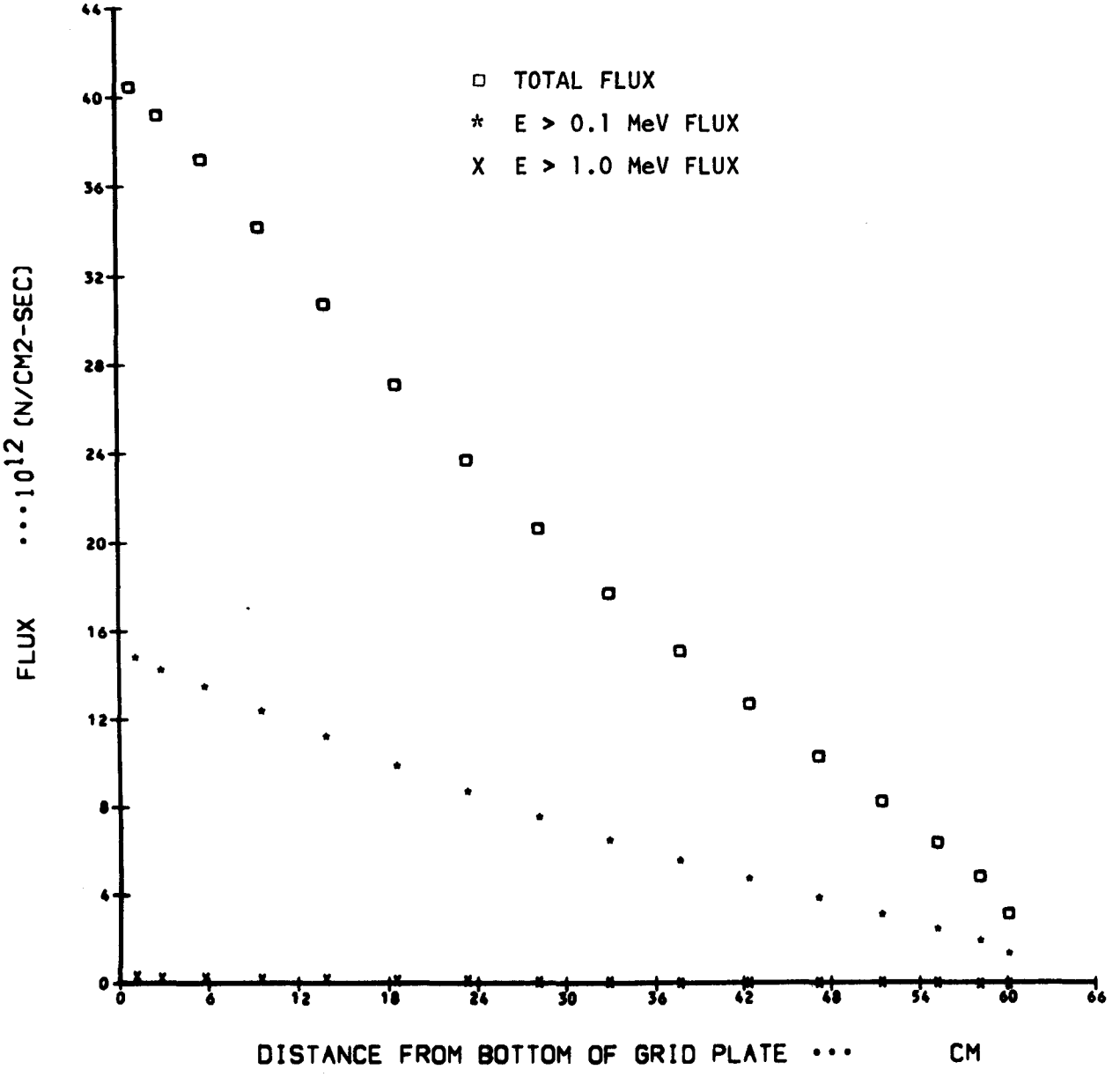


Fig. 8-9 Flux through GCFR grid plate above central fuel element

in thickness, reduces the flux emerging from the axial blanket by somewhat more than an order of magnitude. The spectrum impinging on the grid plate is very similar to that emerging from the blanket, with about 90% of the flux between 1 keV and 1 MeV. About 2.5% of the neutrons leaving the blanket and 1% of those striking the grid plate have $E > 1.0$ MeV. This indicates that the effect of inelastic scattering in steel dominates any direct streaming of any high-energy neutrons in the grid plate shield region. The thermal flux remains insignificant, and therefore embrittlement due to helium production is not important in the GCFR grid plate.

The results of the damage response calculations at the grid plate bottom and midplane are given in Table 8-1. The total fluence impinging on the bottom surface of the grid plate is $3.1 \times 10^{22}$ n/cm$^2$. The results show that 5% residual uniform elongation (RUE) would be attained at 25 and 48 effective power years (EPY, years at 0.8 load factor) based on the lower bound and the nominal fluence limit, respectively. The corresponding times required to attain 10% RUE are 19 and 35 EPY. At the center of the grid plate, 5% RUE is attained at 51 and 94 EPY based on the lower bound and the nominal fluence limit, respectively. The corresponding times to attain 10% RUE are 38 and 68 EPY. For all cases, the damage response contribution due to $E > 1.0$ MeV neutrons is small (3% to 5%). Neutrons with $1.0 \text{ MeV} > E > 1.0$ keV contribute about 95% of the damage. The relatively larger contribution to the damage for the lower bound fluence limits due to neutrons with $E < 0.1$ MeV is a result of somewhat greater uncertainty of the energy dependence of the damage function in this spectral range. Note that all cases satisfy the tolerable error criteria defined by Eq. 8-3. The error in the lower bound fluence limit is about 45% at the $2\sigma$ confidence level for all cases, which indicates a reasonably accurate determination of the maximum damaging effectiveness of the grid plate spectrum.

Figure 8-10 shows a plot of total fluence and the total fluence limits through the grid plate. The damaging effectiveness of the spectrum remains essentially constant through the grid plate, increasing somewhat toward

TABLE 8-1
SUMMARY OF DAMAGE RESPONSE CALCULATIONS IN GCFR GRID PLATE ABOVE CENTER

| Location | Residual Uniform Elongation (%) | Damage Function Type | Total Fluence Limit ($n/cm^2$) | Total Fluence (30 yr at 0.8 load factor) ($n/cm^2$) | Percent of Damage Response Due To | | | | Calculated Time to Reach Fluence Limit[a] (yr at 0.8 load factor) |
|---|---|---|---|---|---|---|---|---|---|
| | | | | | E > 1.0 MeV Flux | E > 0.1 MeV Flux | 2.38 < E < 0.1 MeV Flux | E < 2.38 eV Flux | |
| Bottom of grid plate | 5 | Upper bound | 2.6 + 22 | 3.1 + 22 | 4 | 63 | 33 | ~0 | 25 |
| | 5 | Nominal | 4.9 + 22 | 3.1 + 22 | 5 | 73 | 22 | ~0 | 48 |
| | 10 | Upper bound | 1.9 + 22 | 3.1 + 22 | 4 | 62 | 34 | ~0 | 19 |
| | 10 | Nominal | 3.6 + 22 | 3.1 + 22 | 5 | 72 | 23 | ~0 | 35 |
| Grid plate mid-plane | 5 | Upper bound | 2.7 + 22 | 1.6 + 22 | 3 | 62 | 35 | ~0 | 51 |
| | 5 | Nominal | 5.0 + 22 | 1.6 + 22 | 4 | 72 | 24 | ~0 | 94 |
| | 10 | Upper bound | 2.0 + 22 | 1.6 + 22 | 3 | 62 | 35 | ~0 | 38 |
| | 10 | Nominal | 3.6 + 22 | 1.6 + 22 | 4 | 72 | 24 | ~0 | 68 |

[a] With no margin for calculational uncertainty.

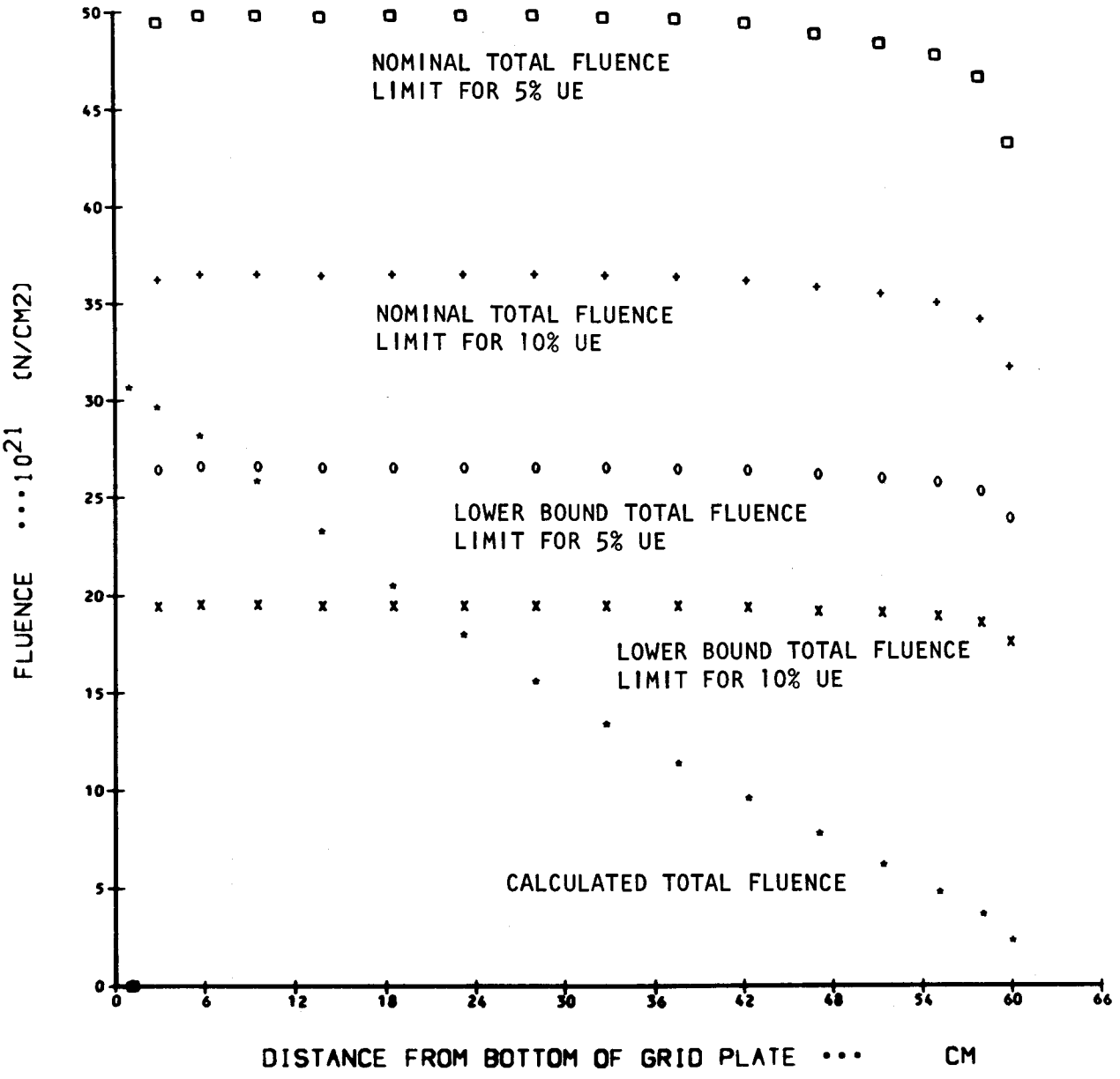


Fig. 8-10 Calculated total fluence and total fluence to attain specified uniform elongation vs distance from bottom of grid plate

the top owing to a slight hardening of the spectrum. Figure 8-10 can be used to evaluate the axial dependence of neutron embrittlement in the grid plate.

In this preliminary analysis, no determination of errors associated with the calculational method or with the effect of pin streaming has been made. Use of the high-order biased quadrature is considered to provide a reasonably accurate treatment of the angular flux variation in a streaming problem of this general nature; the method will be checked by Monte Carlo calculation performed at ORNL. The results indicate that the fluence limits based on the upper bound damage functions provide a conservative lower bound to the fluence required to attain the specified material property levels. The effect of pin streaming in the core and blanket, which will be determined in the experimental program, is believed to have a small effect on the angular flux source emerging from the axial blanket. The effect of the pin streaming on the grid plate damage will be mitigated in any case owing to a lack of direct streaming paths in the grid plate region. The primary error source is probably the coarse 10-energy-group approximation; however, experience has shown that the 10-group approximation yields conservative results. In addition, the global effect of radial leakage, not treated in this analysis, would tend to lower peak fluence levels near the grid plate centerline. A bias factor of 2.0 applied to the total calculated fluence levels and used in conjunction with the lower bound fluence limits should provide a conservative upper bound to the neutron-induced embrittlement of the grid plate.

REFERENCES

8-1 Mynatt, F. R., et al., "The DOT-III Two-Dimensional Discrete Ordinates Transport Code," Oak Ridge National Laboratory Report ORNL-TM-4280, 1973.

8-2 Nuclear Systems Materials Handbook, v. I, II, Hanford Engineering Development Laboratory (TID-2666).

8-3 "300-MW(e) Gas-Cooled Fast Breeder Reactor Demonstration Plant," General Atomic Report GA-A13045, July 15, 1974, p. 47.

8-4 Bartine, D. E., et al., "Preliminary Shielding Analysis of a Reference Design 300-MW(e) Gas-Cooled Fast Breeder Reactor," Trans. Am. Nucl. Soc. 21, 525-527 (1975).

8-5 "Gas-Cooled Fast Breeder Reactor Quarterly Progress Report for the Period November 1, 1975 Through January 31, 1976," ERDA Report GA-A13815, General Atomic, March 22, 1976.

8-6 Archibald, R., K. D. Lathrop, and D. Mathews, "1DFX - A Revised Version of the 1DF (DTF-IV) SN Transport Theory Code," Gulf General Atomic Report Gulf-GA-B10820, September 27, 1971.

8-7 Mathews, D., and R. Archibald, "DTFX Code Description," General Atomic, unpublished data.

8-8 Nagel, M., and R. J. Cerbone, "Neutron-Coupled Gamma-Ray Cross-Section Requirements for Gas-Cooled Fast Breeder Reactors," in Proceedings of the Conference on Cross-Section Technology, Washington, D.C., March 5, 1975.

8-9 Cerbone, R. J., et al., "Shielding Analysis of the 300-MW(e) GCFR," ERDA Report GA-A13558, General Atomic, August 12, 1975.

8-10 Soo, P., "Analysis of Structural Materials for LMFBR Coolant-Boundary Components - Materials Property Evaluations," USAEC Report WARD-3045T3-5, Westinghouse Electric, November 1972.

8-11 Cerbone, R. J., G. A. Ducat, and M. T. Simnad, "Development Program Plan for GCFR Shielding," ERDA Report GA-A13291, General Atomic, February 14, 1975.

8-12 Mynatt, F. R. "DOT Two-Dimensional Discrete Ordinates Transport Code," Oak Ridge National Laboratory Report ORNL-CCC-89, K1694, October 1969.

8-13 Cerbone, R. J., and K. D. Lathrop, "$S_N$ Calculation of Highly Forward Peaked Neutron Angular Fluxes Using Asymmetric Quadrature Sets," Nucl. Sci. Eng. 35, 139 (1969).

8-14 Rouse, C. A., and D. R. Mathews, "The Use of 1DFX Results in Cylindrical Geometry as a Surface Source for 1DFX Calculations in Slab Geometry," ERDA Report GA-A13095, General Atomic, August 22, 1974.

8-15 Mathews, D. R., et al., "GGC-5, A Computer Program for Calculating Neutron Spectra and Group Constants," General Atomic, unpublished data.

8-16 McElroy, W. N., et al., "Damage Function Analysis," Hanford Engineering Development Laboratory Report HEDL-SA-755, September, 1974.

# 9. REACTOR SYSTEMS ENGINEERING (189a No. SU019)

Under this task, reactor system development activities are being defined and carried out; analytical methods and models applicable to the assessment of thermal-hydraulic performance of the GCFR reactor core are being developed and utilized to define operating strategies; methods and materials behavior models are being evaluated to assess the capability of the PCRV internal structures to serve as a postaccident fuel containment (PAFC); and GCFR plant control systems are being developed, including establishment of the interface requirements between these control systems, the plant protection system, the operational protection system, and the plant operator.

## 9.1. CORE THERMAL-HYDRAULIC PERFORMANCE

Activities in this subtask are devoted to the development of accurate computer models for the evaluation of core thermal-hydraulic performance. In addition, the requirements for and methods of core temperature monitoring are being investigated.

During previous quarters, the development of the core thermal-hydraulics computer program GACOOL was described, and preliminary results were reported. During this quarter, computer program development and documentation were continued. GACOOL development to date in terms of its available options is summarized, and the results of some core parametric studies are reported. The GACOOL draft document is in review. Efforts to define the feasibility of an alternate core temperature monitoring concept and to quantify the system benefits from the use of an alternate concept were continued.

### 9.1.1. GACOOL Development

GACOOL development activities continued during this quarter. The improved core pressure drop model described in Ref. 9-1 was made fully operational for all GACOOL performance options. An additional option was added which allows the calculation of core performance (pressure drop, element flow distribution, and axial hot spot temperature distribution for the maximum powered fuel pin of each element) for a fixed total core flow rate; it permits the calculation of core flow redistribution at off-design-point conditions. The flow distribution is affected because of the slight dependence of orifice performance on Reynolds number. Results obtained from this option will also be available for other system analysis and performance computer programs to simulate the core pressure drop characteristics over a wide range of flow rates and core powers. The three other GACOOL options can predict core thermal-hydraulic performance for (1) "ideal" orificing conditions, (2) a specified pressure drop, and (3) off-design-point conditions.

In the ideal orificing option, the individual core element flow rates are determined consistent with the midwall cladding hot spot temperature limit. The design pressure drop is established by the maximum pressure drop element, and every other element is orificed consistent with this pressure drop. The second option allows the prediction of core performance for a specified pressure drop and orifice sizes. This option is useful in performing orifice grouping studies at the design pressure drop. These studies consist of grouping core elements having similar flow requirements into a set; each element in the set is fitted with an identical standard-size orifice. This grouping results in overcooling of some core elements and a slight degradation in the mixed-mean core coolant outlet temperature; however, it reduces the number of different orifice types which must be handled within the reactor cavity during refueling. The off-design-point option allows core performance to be determined for the case of specified orifice sizes and a specified maximum midwall hot spot cladding temperature. At off-design-point power levels, this option calculates pressure

drop, total core flow rate, and, in turn, power-to-flow ratio necessary to cool the core consistent with the specified cladding limit. All the options have been verified by checking whether they yield consistent results.

Table 9-1 shows the input and output for the various GACOOL options. Figure 9-1 is a flowchart of all major GACOOL subroutines. A brief explanation of the subroutines shown in the flowchart is given below.

1. MAIN. This is the main program. MAIN sets up the logic sequence for all GACOOL options.

2. INPUT. This routine reads and prints out all information necessary to define the problem under consideration.

3. FLOCAL. This subroutine contains the heat transfer models for core and blanket elements. It determines the flow rate required by each element to cool its maximum powered fuel pin consistent with the midwall cladding hot spot temperature limit. FLCAL1 is an entry point in FLOCAL called by TDIS to give the axial hot spot temperature distribution for the maximum powered fuel pin in each element.

4. PDROP. PDROP calculates the plenum-to-plenum pressure drop across each element, excluding the orifice pressure drop. PDROP1 is an entry point to PDROP.

5. HOLS1Z. For LOPT = 1, the subroutine sizes element orifice diameters. For fixed orifice areas (LOPT = 2,3,4), HOLSZ1, an entry point in HOLS1Z, is used to predict the orifice pressure drop.

6. HFLUX. HFLUX is used to calculate node point heat fluxes from midnode point power densities.

TABLE 9-1
INPUT AND OUTPUT FOR GACOOL OPTIONS

| Ideal Orificing Option, LOPT = 1 | Off-Design-Point Option, LOPT = 2 | Specified Core Pressure Drop, LOPT = 3 | Specified Total Core Flow Rate, LOPT = 4 |
|---|---|---|---|
| **Input** | | | |
| Fuel rod and core element geometric data | Fuel rod and core element geometric data | Fuel rod and core element geometric data | Fuel rod and core element geometric data |
| Power distribution data | Power distribution data | Power distribution data | Power distribution data |
| Inlet temperature and pressure | Inlet temperature and pressure | Inlet temperature and pressure | Inlet temperature and pressure |
| Midwall cladding hot spot temperature limit | Midwall cladding hot spot temperature limit | Core pressure drop | Total core flow rate |
| | Orifice sizes | Orifice sizes | Orifice sizes |
| **Output, Element** | | | |
| Outlet temperature | Outlet temperature | Outlet temperature | Outlet temperature |
| Flow rate | Flow rate | Flow rate | Flow rate |
| Pressure drop | Axial hot spot temperature distribution for maximum powered fuel rod | Axial hot spot temperature distribution for maximum powered fuel rod | Axial hot spot temperature distribution for maximum powered fuel rod |
| Orifice sizes | | | |
| Axial hot spot temperature distribution for maximum powered fuel rod | | | |
| **Output, Core** | | | |
| Pressure drop | Pressure drop | Total flow rate | Pressure drop |
| Total flow rate | Total flow rate | Outlet temperature | Outlet temperature |
| Outlet temperature | Outlet temperature | | |

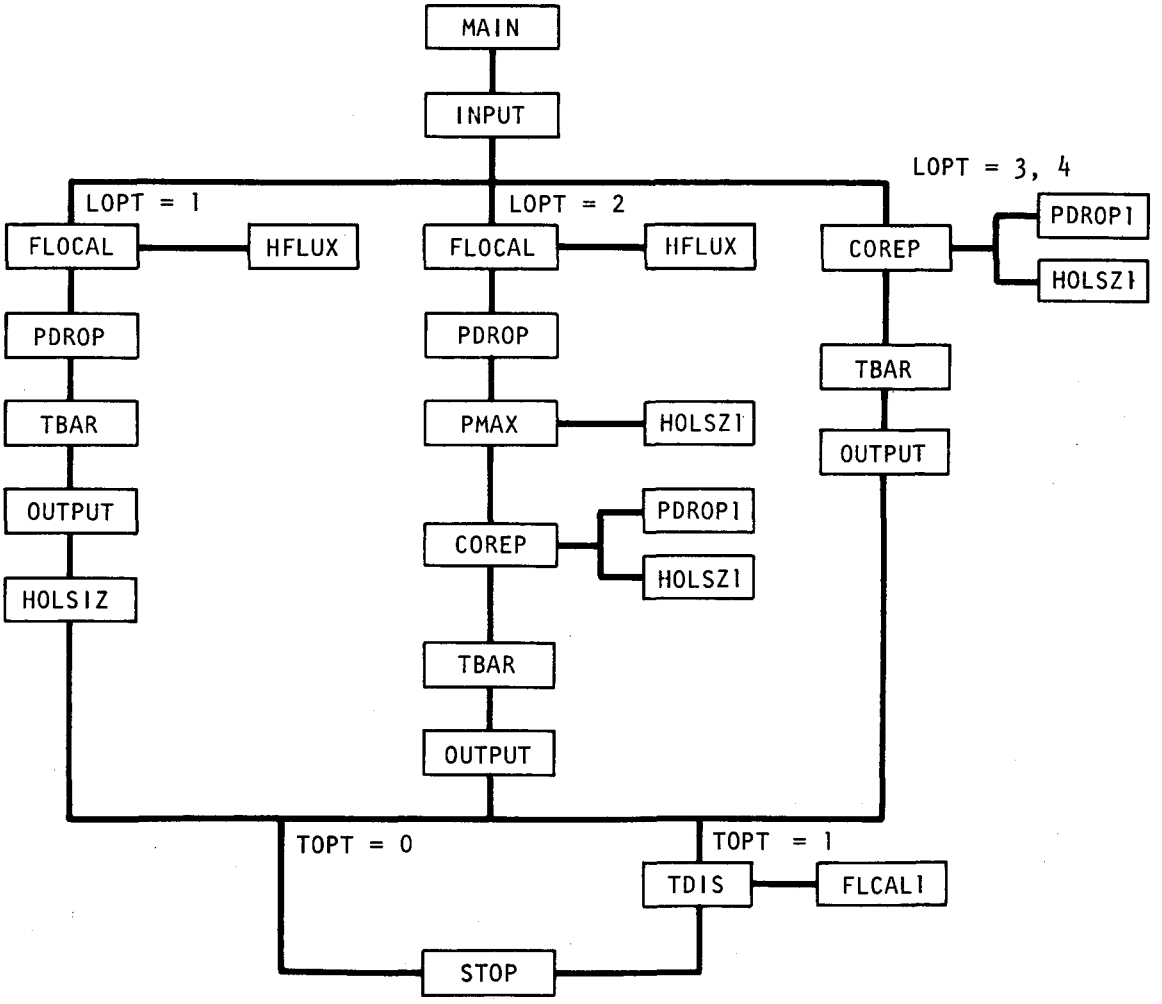


Fig. 9-1 GACOOL flow chart

7. COREP. This subroutine sets up all iterative calculations for fixed orifice cases (LOPT = 2,3,4).

8. PMAX. PMAX determines the reactor pressure drop necessary to cool all elements consistent with the specified midwall cladding hot spot temperature limit for a fixed orifice case.

9. TBAR. TBAR calculates the mixed mean coolant outlet temperature for the reactor at each time point.

10. TDIS. This subroutine performs setup functions and calls FLCAL1 to calculate the axial hot spot temperature distribution for the maximum powered fuel pin in each element and prints the axial temperature distribution output.

11. EST. EST is a general purpose subroutine for the solution of an iteration loop for a specified tolerance.

13. OUTPUT. This subroutine prints output information generated by GACOOL.

Additional development activity during this reporting period included the obtaining of new correlations from the Fuel Element Development Branch for Stanton numbers and friction factors as a function of Reynolds number and relative roughness for the roughened portion of the fuel rod. These data will be used in conjunction with the GACOOL off-design-point option to define the upper operating limit for the power-to-flow ratio. Hot spot factors, pressure drop, and heat transfer information obtained from the Fuel Element Development Branch for the spiral wire-wrapped blanket elements was used to improve GACOOL modeling of the radial blanket. The wire wrapping is treated as a multiplier to the normal smooth tube friction factor and heat transfer coefficient. Verification of the improved blanket model with results that have been obtained from the detailed heat transfer and subchannel analysis computer programs is still in process.

Other modifications to the program included the addition of a core bypass model, the improvement of input and output routines, and removal of unnecessary debugging output. A sample output for the axial hot spot temperature distribution of the maximum powered fuel pin in a representative element is shown in Section 9.1.2. The draft GACOOL users' manual was finished and is in review.

### 9.1.2. Preliminary Core Performance and Orificing Results

Core design and system performance analyses have shown the desirability of going to a lower pressure drop core configuration. This is accomplished by increasing the fuel rod pitch. For the lower pressure drop core [0.155 MPa (22.5 psi)], GACOOL predicts a reactor outlet temperature of 544°C (1011°F) and a coolant mass flow rate of $2.99 \times 10^6$ kg/hr ($6.59 \times 10^6$ lbm/hr). These results are based on each element having its own individually tailored orifice, a midwall cladding hot spot temperature limit of 700°C (1292°F), a channel hot spot factor of 1.23, and a film hot spot factor of 1.14. A simplified blanket model and a core bypass model are also included in these results. For this design, orifice diameters range from 10.7 to 16.7 cm (4.2 to 6.6 in.) for fuel and control elements.

The sensitivity of the core outlet temperature (not including bypass flow and blanket elements) to independent variations in the channel and film hot spot factors is shown in Fig. 9-2 for a fixed core configuration, a fixed cladding temperature limit, and a fixed reactor power. As can be seen, the outlet temperature is much more sensitive to the channel hot spot factor than to the film hot spot factor. This is because the core temperature rise is much greater than the film temperature drop at the axial location of the maximum midwall cladding hot spot temperature. Hence, changing the channel hot spot factor which is applied to the core temperature rise will have a greater effect than changing the film hot spot factor which is applied to the film temperature drop. If the channel and film hot spot factors are assumed to be 1.0, the core outlet temperature is 594°C (1101°F). Figure 9-3 shows the sensitivity of core outlet

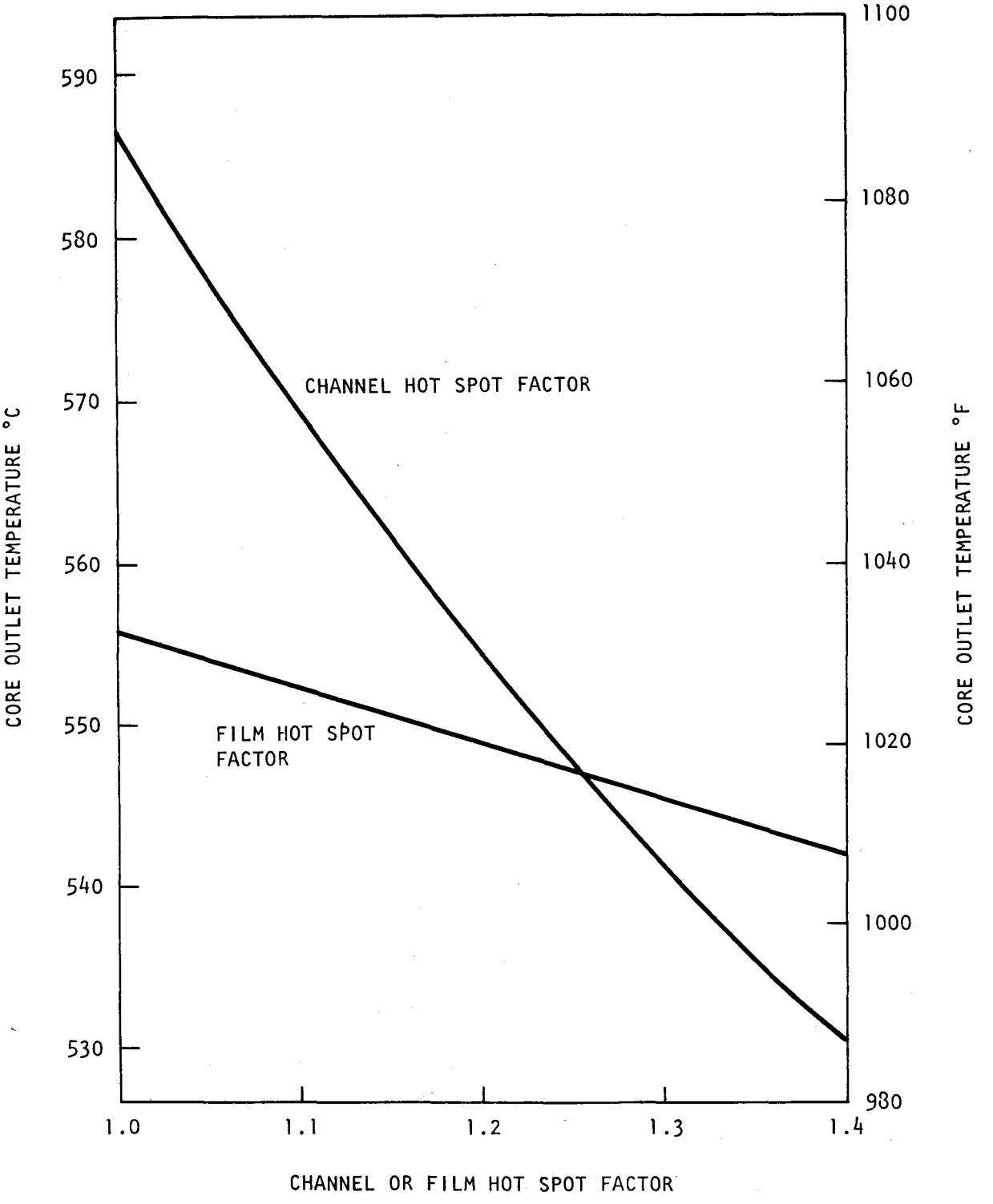


**Fig. 9-2 Sensitivity of core outlet temperature to channel and film hot spot factors**

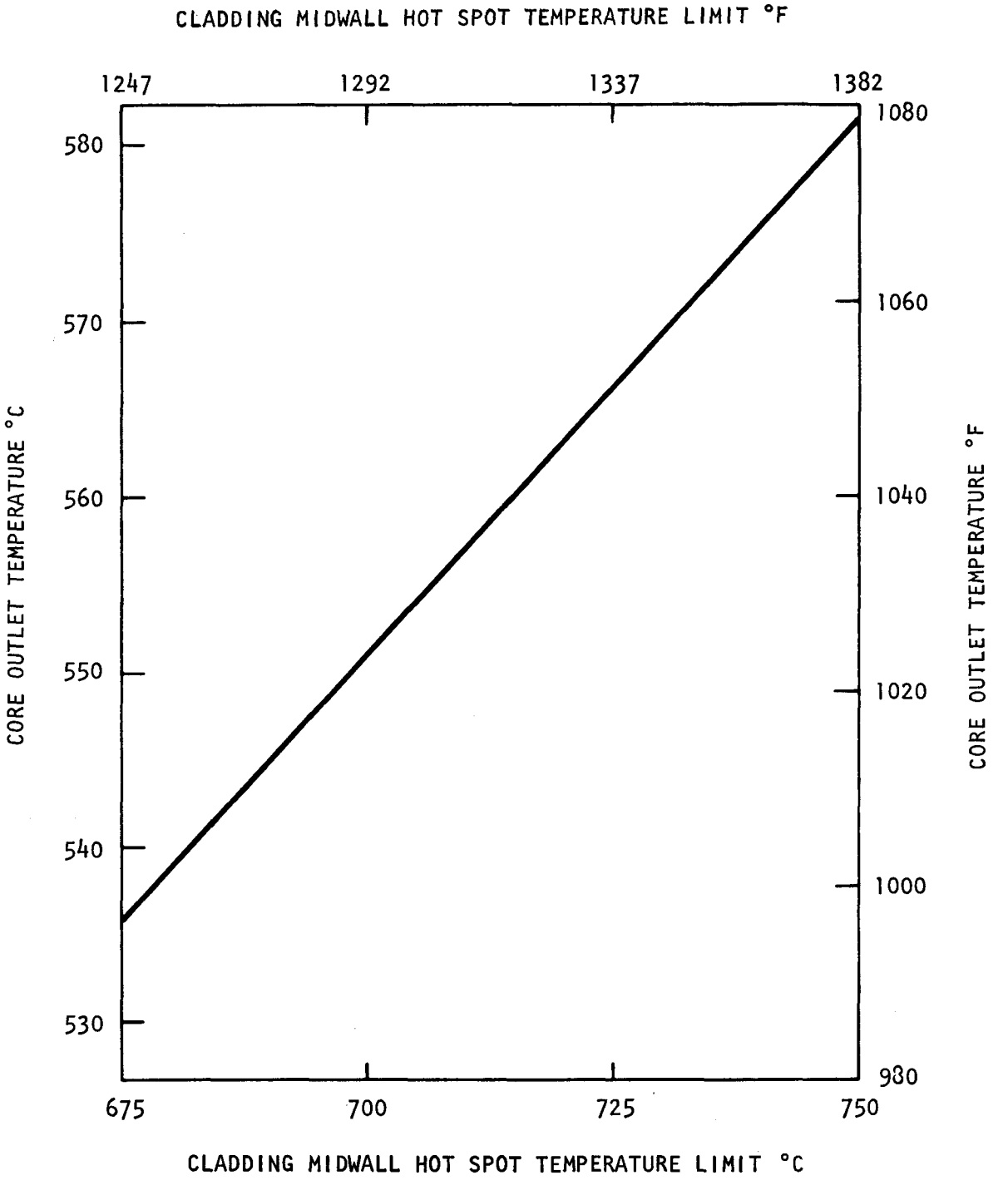


Fig. 9-3 Sensitivity of core outlet temperature to cladding midwall hot spot temperature limit

temperature (not including bypass flow and blanket elements) to the cladding midwall hot spot temperature limit. A sample axial hot spot temperature distribution output for the maximum powered fuel pin in a representative element is shown in Table 9-2.

### 9.1.3. Alternate Core Temperature Monitoring Concepts

The function of the core temperature monitoring system is to provide beginning-of-cycle verification of thermal-hydraulic predictions and verification of fuel and orifice loading patterns. Since this system accomplishes its functional requirements at the beginning of each burnup cycle, failure of a temperature sensor during the burnup cycle does not necessitate reactor shutdown; the system must, however, have maintenance and calibration capabilities during periods of reactor shutdown. The continuous availability of element-by-element coolant outlet temperature information is not considered essential.

The current temperature monitoring system in the GCFR demonstration plant reference design consists of a thermocouple at the bottom end (outlet end) of the central fuel pin position of each standard fuel and blanket element. The leads for the thermocouples extend through the core region and out of the PCRV via the individual element locking mechanism extension tubes. The replaceability of the temperature monitoring sensors through the locking mechanism penetrations during shutdown periods provides a means of assuring the availability of this system to perform its required function.

Development of an alternate temperature monitoring concept may be justified on the basis of anticipated performance and/or overall cost advantages. Although the reference system does provide a means of accurately monitoring core outlet temperature, it does have several disadvantages, particularly with regard to the mechanical complexity (and therefore cost) of providing maintenance capabilities and paths for the thermocouple leads.

TABLE 9-2
SAMPLE AXIAL HOT SPOT TEMPERATURE DISTRIBUTION FOR MAXIMUM POWERED FUEL PIN IN A REPRESENTATIVE CORE ELEMENT

TIME POINT 1
ELEMENT 15

| AXIAL INCREMENT | AXIAL DISTANCE[a] | COOLANT TEMPERATURE WITH HOT SPOTS | SURFACE TEMPERATURE[b] WITH HOT SPOTS | CLAD MIDWALL TEMPERATURE[b] WITH HOT SPOTS |
|---|---|---|---|---|
| 1 | .738180+00 | .672800+03 | .672800+03 | .672800+03 |
| 2 | .147636+01 | .672800+03 | .940856+03 | .956019+03 |
| 3 | .163625+01 | .690457+03 | .992098+03 | .100920+04 |
| 4 | .179614+01 | .710237+03 | .104376+04 | .106271+04 |
| 5 | .195603+01 | .731956+03 | .109404+04 | .111467+04 |
| 6 | .211592+01 | .755412+03 | .114249+04 | .116462+04 |
| 7 | .227580+01 | .780389+03 | .957912+03 | .981321+03 |
| 8 | .243569+01 | .806656+03 | .991694+03 | .101617+04 |
| 9 | .259558+01 | .833969+03 | .102475+04 | .105007+04 |
| 10 | .275547+01 | .862075+03 | .105680+04 | .108273+04 |
| 11 | .291536+01 | .890714+03 | .108756+04 | .111385+04 |
| 12 | .307525+01 | .919621+03 | .111677+04 | .114318+04 |
| 13 | .323514+01 | .948527+03 | .114416+04 | .117045+04 |
| 14 | .339503+01 | .977167+03 | .116950+04 | .119543+04 |
| 15 | .355492+01 | .100527+04 | .119258+04 | .121789+04 |
| 16 | .371481+01 | .103259+04 | .121318+04 | .123766+04 |
| 17 | .387469+01 | .105885+04 | .123113+04 | .125454+04 |
| 18 | .403458+01 | .108383+04 | .124627+04 | .126840+04 |
| 19 | .419447+01 | .110729+04 | .125846+04 | .127910+04 |
| 20 | .435436+01 | .112901+04 | .126760+04 | .128656+04 |
| 21 | .451425+01 | .114879+04 | .127359+04 | .129069+04 |
| 22 | .467414+01 | .116645+04 | .127692+04 | .129209+04 |
| 23 | .541232+01 | .116645+04 | .116645+04 | .116645+04 |
| 24 | .615050+01 | .116645+04 | .116645+04 | .116645+04 |

[a] In feet. [b] In degrees Fahrenheit.

One alternate temperature monitoring concept which may be useful in the GCFR system is Johnson noise thermometers. These temperature probes have the same general configuration as thermocouples (i.e., small-diameter temperature sensors with two leads) and have been reported to be accurate and drift-free even in high-temperature radiation environments. If performance is sufficiently high, noise thermometers could replace thermocouples in the current reference configuration and could possibly eliminate the requirement for temperature sensor maintenance capabilities. An independent evaluation of the potential performance advantages of noise thermometry as compared with thermocouples should provide the basis for pursuing or not pursuing a development and qualification program for this concept in a GCFR. One significant problem for the application of this concept in the GCFR may be the length of the leads [over 15 m (50 ft)] between the temperature probe and the first point of signal amplification.

Another alternate concept which is under consideration is an infrared system. The essential elements of this system would include an imaging device for viewing the outlet of the core, a means of transmitting the collected signal outside the PCRV, and a detector/processor for converting the signal into temperature information. Such a system would allow the thermocouples of the reference design to be replaced by fissile-bearing fuel pins and would thus slightly improve the nuclear and thermal performance of the core. These system gains, however, would be small in comparison to the potential capital cost savings resulting from simplified mechanical designs of the element locking mechanisms. In fact, an alternate element locking mechanism concept currently under investigation could eliminate any convenient path for leads to the temperature probes. Incorporation of this alternate locking mechanism into the reference design could in turn significantly increase the incentive for developing the infrared temperature monitoring system. In any event, the development and qualification of an infrared system would require a significant expenditure (several hundred thousand dollars) over several years.

An overall consideration of the incentive for developing alternate core temperature monitoring concepts has led to the following three conclusions:

1. Developments in the field of noise thermometry will be monitored for their impact on the applicability of this concept to the GCFR. Contacts with ORNL in this area will be continued.

2. The proposed core temperature monitoring philosophy will be reviewed to ensure that it is realistic in terms of operating and licensing requirements. This activity is in progress.

3. A brief overview study of the feasibility of an infrared system will be conducted prior to a final development decision.

## 9.2. POSTACCIDENT FUEL CONTAINMENT

The objectives of this subtask are (1) to assess the capability of the structures within the reactor cavity of the PCRV to contain core debris associated with a postulated core melt-down arising from a series of very-low-probability failures and (2) to define the analytical and experimental studies needed to verify thermal processes associated with core debris containment.

Results of the study of upward heat removal without helium circulation are reported in Ref. 9-1. During this quarter, work has been completed on upward heat removal by natural helium circulation at depressurized conditions. Results of the base case analysis with natural helium circulation through all three core auxiliary cooling loops indicated the feasibility of removing all upward-flowing decay heat. However, the safety margin was shown to be small. It was found that a 1/2-hr delay of natural helium circulation, e.g., by a stuck isolation valve, slightly increases all temperatures. With only two core auxiliary cooling loops operating, the natural convective helium flow is insufficient, and some melting of the internal structures would eventually occur. Owing to the limited helium flow, any mechanical enhancement of the heat transfer coefficient would have an insignificant effect on the convective cooling. It was also found that

a decrease of the radial shield thermal conductivity, i.e., considering gas gaps in the radial shield, would increase the surface temperatures in the central cavity region.

The present transient analysis used a two-dimensional model of the reactor cavity and applied natural convection of helium induced by the density difference between a pair of hot and cold gas columns as the mode of heat transfer. The helium flow is upward through the core and downward through the core auxiliary heat exchanger.

A base case using the most probable input data was analyzed first, followed by a parametric study. Owing to the preliminary nature of the reference design, there are uncertainties in the loop pressure drop calculations. For this reason and also because of some other assumptions in the PAFC analyses, it is not the intent of this study to conduct a detailed analysis of the core auxiliary cooling loop pressure drop. Therefore, needed pressure drop information was obtained from existing core auxiliary cooling loop pressure drop data in Ref. 9-2. For the same reason, detailed calculations of heat transfer in the core auxiliary heat exchanger were avoided by using a constant helium inlet temperature into the cavity. The validity of this assumption was checked at the end of the analysis.

### 9.2.1. Initial Configuration and Assumptions

The same computational model and initial conditions as those for the previous upward heat removal analysis with forced circulation (Ref. 9-3) were assumed except that the helium flow direction was reversed (see Fig. 9-4). Further assumptions related to the natural convection heat transfer are listed below.

1. The system is depressurized to an equilibrium pressure of 179 KPa (26 psia), and none of the core auxiliary helium circulators are operating.

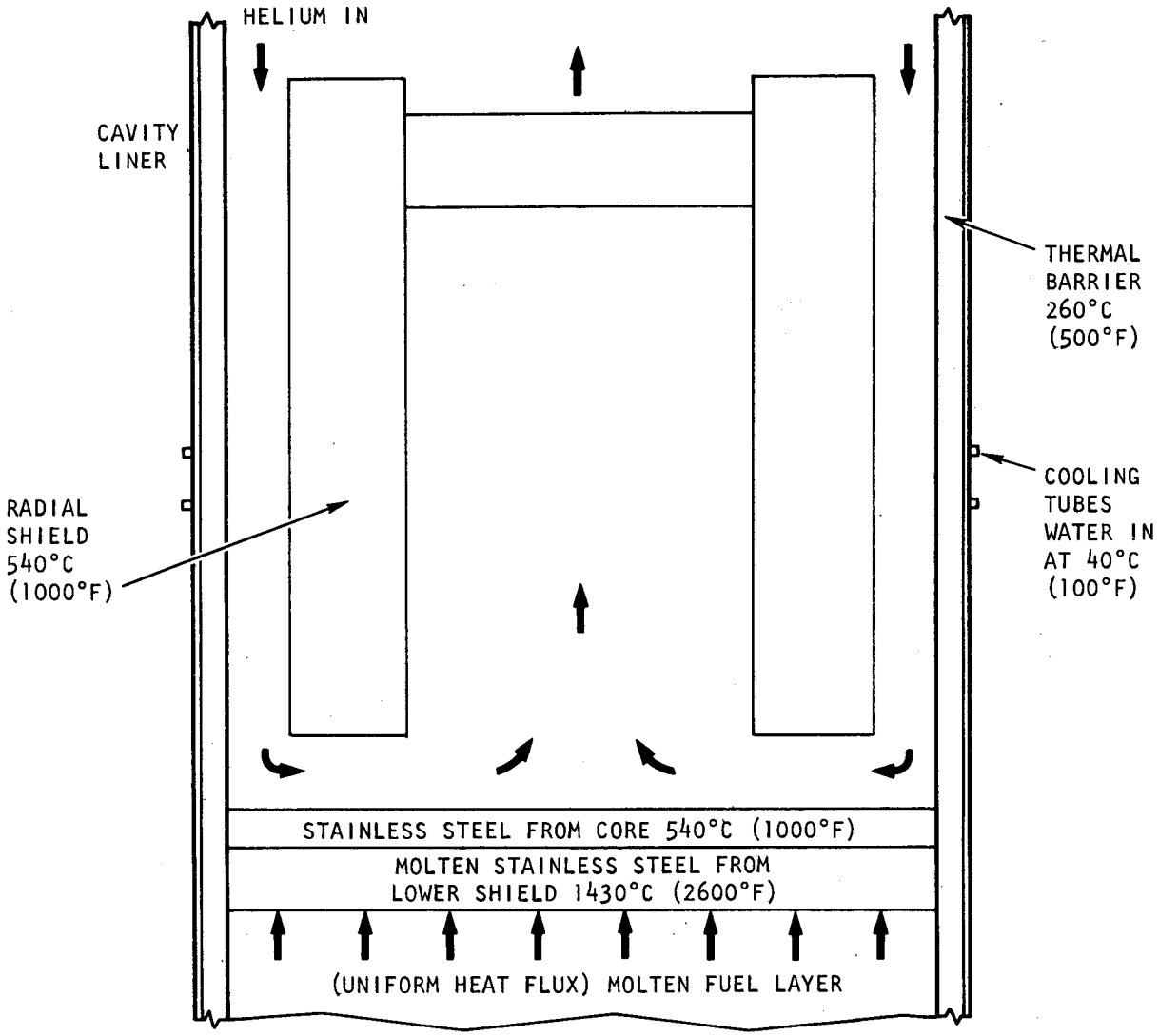


**Fig. 9-4 Computational model (with initial temperatures)**

2. The core auxiliary cooling loop isolation valves are manually opened to permit helium flow.

3. Cooling water is circulated through all three core auxiliary heat exchangers at the specified design conditions (Ref. 9-2).

4. The PCRV cooling system functions properly.

5. The downward portion of the decay heat is effectively removed.

6. The overall flow resistance coefficients in the core auxiliary cooling loops are constant so that the system pressure drop at other mass flow rates, temperatures, and system pressures can be obtained by mass continuity and ideal gas relationships.

7. In the auxiliary cooling loops, the flow resistance in the reverse flow direction is the same as that in the normal flow direction. This assumption is optimistic because the flow resistance through a stalled auxiliary helium circulator is expected to be higher.

8. Core pressure drop is contributed only by the grid plate since with a complete melt-down the entire core structure falls onto the top of the preshield.

9. During natural circulation of helium, the flow direction is reversed. Therefore, the continuous release of fission products from the molten pool surface causes the central cavity region to be nontransparent, so that the previously assumed transparency in this region is not quite correct. However, in order to use simple radiative heat transfer relations for a gray enclosure, the helium-aerosol mixture in this region is assumed to remain transparent. This assumption is conservative because a non-transparent gas absorbs thermal radiation, so that less heat reaches the reactor cavity internals.

### 9.2.2. Natural Circulation of Helium

The driving force for natural circulation is determined by the difference between the helium density in the central region of the reactor cavity and the annulus formed by the outer radial shield and the thermal barrier. The height of hot and cold gas columns is calculated from the difference in elevation between the lower end of the outer radial shield and the midplane of the core auxiliary heat exchangers (see Fig. 9-5).

The effective pressure differential for natural circulation is

$$\Delta p_g = H\,(\rho_c - \rho_h) \quad , \tag{9-1}$$

where $H$ = height of hot and cold gas columns,

$\rho_c$ = helium density in cold leg,

$\rho_h$ = helium density in hot leg.

From the ideal gas law,

$$\left.\begin{aligned} p &= \rho_c R T_c \quad , \\ p &= \rho_h R T_h \quad , \end{aligned}\right\} \tag{9-2}$$

where $p$ = helium pressure,

$R$ = gas constant,

$T_c$ = cold leg temperature,

$T_h$ = hot leg temperature,

and Eq. 9-1 becomes

$$\Delta p_g = H \cdot \frac{p}{R}\left(\frac{1}{T_c} - \frac{1}{T_h}\right) \quad . \tag{9-3}$$

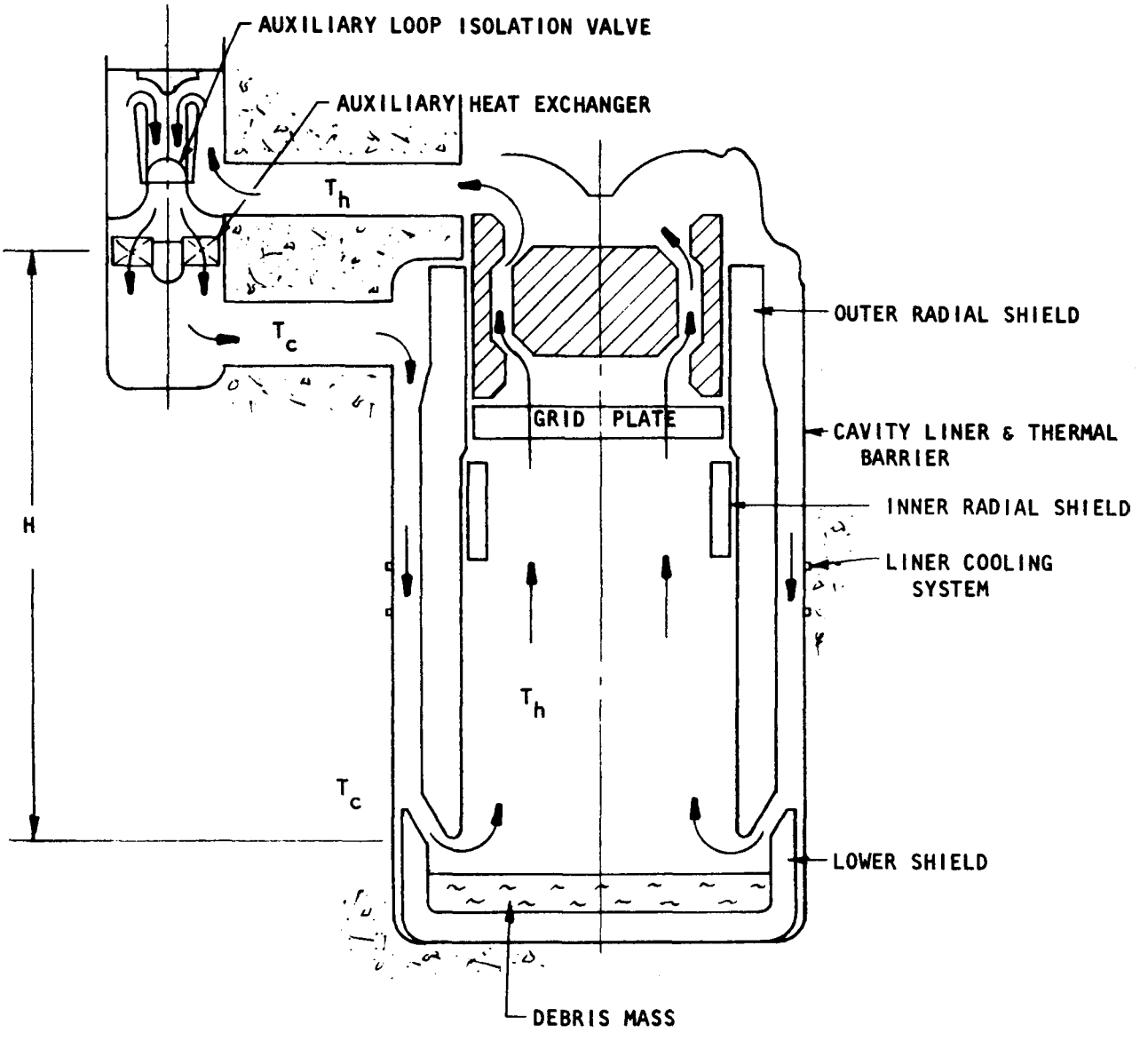


Fig. 9-5 Natural circulation flow path within PCRV

The pressure drop along the complete helium flow path is the sum of the pressure drops through the reactor cavity ($\Delta p_1$) and the core auxiliary cooling loop ($\Delta p_2$); i.e.,

$$\Delta p = \Delta p_1 + \Delta p_2 \quad . \tag{9-4}$$

The reason for distinguishing between the two pressure drops is that the complete helium flow path may include either one, two, or all three core auxiliary cooling loops, in which case the pressure drop through the reactor cavity will be different each time.

The pressure loss along a flow path is

$$\Delta p = \alpha \frac{L}{D} \frac{\rho V^2}{2g} \quad , \tag{9-5}$$

where L = length of flow path,
D = diameter of flow path,
V = flow velocity,
g = acceleration due to gravity,
$\alpha$ = overall flow resistance coefficient.

Based on assumption 6 in Section 9.2.1, $\alpha$ is constant. Mass flow is given by

$$\dot{m} = \rho A V \quad , \tag{9-6}$$

where A is the cross-sectional flow area.

Using Eq. 9-6 and the ideal gas law $p = \rho RT$, Eq. 9-5 can be written as:

$$\Delta p = \beta \frac{\dot{m}^2 T}{p} \quad , \tag{9-7}$$

where $\beta$ is $\alpha RL/2gDA^2$. Mass flow, temperature, system pressure, and pressure drop are known for a given design condition, so that $\beta$ can be found by

$$\beta = \frac{\Delta p \cdot P}{\dot{m}^2_T} \quad . \tag{9-8}$$

Thus, for the reactor cavity and the core auxiliary cooling loops, different values of $\beta$ can be found; i.e.,

$$\left.\begin{aligned} \beta_1 &= \frac{\Delta p_1 \cdot P}{\dot{m}^2_1 T_1} \quad , \\ \beta_2 &= \frac{\Delta p_2 \cdot P}{\dot{m}^2_2 T_2} \quad , \end{aligned}\right\} \tag{9-9}$$

where the subscripts 1 and 2 refer to the reactor cavity and the core auxiliary cooling loops, respectively.

The natural convection helium mass flow can be determined by equating Eqs. 9-3 and 9-4 and substituting for $\Delta p_1$ and $\Delta p_2$ from Eq. 9-9. For simplicity and conservatism, $T_1$ and $T_2$ can be replaced by $T_h$ in Eq. 9-9, since higher temperatures lead to a larger pressure drop. Since $m_2 = m_1/n$, where n is the number of cooling loops used, then

$$\dot{m}^2_1 = \left(\beta_1 + \frac{\beta_2}{n_2}\right) R \frac{1}{T_h} \left(\frac{1}{T_c} - \frac{1}{T_h}\right) \quad . \tag{9-10}$$

### 9.2.3. Heat Convection at Reactor Internal Surfaces

The helium flow induced by natural convection is laminar along its flow path. Equations for the heat transfer coefficients at various reactor internal surfaces are obtained from Refs. 9-4 through 9-6. These equations are based on helium flowing over a constant temperature surface, which is more conservative than some other possible surface conditions.

9.2.3.1. Grid Plate. The thermal entry length solutions for laminar flow through tubes have been tabulated in Ref. 9-4 and are shown below.

| $X^+$ | 0 | 0.001 | 0.004 | 0.01 | 0.04 | 0.08 | 0.10 |
|---|---|---|---|---|---|---|---|
| $Nu_m$ | ∞ | 22.96 | 12.59 | 8.99 | 5.87 | 4.89 | 4.66 |

$X^+$ is the dimensionless axial distance, and $Nu_m$ is the mean Nusselt number over $X^+$. $X^+$ is defined by

$$X^+ = \frac{X/r_o}{RePr} \quad ,$$

where X = axial distance,

$r_o$ = inside diameter of tube,

Re = Reynolds number,

Pr = Prandtl number.

9.2.3.2. Inner Surface of Outer Radial Shield. Helium flow along this surface may be treated as laminar boundary layer flow along a flat plate. An equation for this type of flow is the well known expression

$$h = 0.664\ k \sqrt{\frac{\dot{m}}{\mu AL}}\ Pr^{1/3} \quad , \qquad (9\text{-}11)$$

where h = average heat transfer coefficient,

k = thermal conductivity of helium,

$\dot{m}$ = mass flow rate of helium,

$\mu$ = dynamic viscosity,

A = cross-sectional area of flow path,

L = axial length of surface.

9.2.3.3. Upper Surface of Debris Mass. A laminar stagnation flow may be assumed for this flow condition. An equation cited in Ref. 9-5 is

$$h = 1.52\ k \sqrt{\frac{\dot{m}}{\mu AL}}\ Pr^{0.4} \quad , \qquad (9\text{-}12)$$

where h = average heat transfer coefficient,

L = radial distance to the inner edge of radial shield.

Other quantities are defined in Eq. 9-11.

9.2.3.4. Lower Surface of Outer Radial Shield. Helium flow passing along this surface may be considered as laminar flow between two parallel surfaces. An equation cited in Ref. 9-6 is

$$h = 1.85 \frac{k}{D_e} \left( \frac{4}{\pi} \frac{C_p \dot{m}}{k L} \right)^{1/3} , \qquad (9\text{-}13)$$

where $D_e$ = equivalent diameter, which, for this case is two times the space between the two surfaces,

$C_p$ = specific heat of helium,

L = lower width of radial shield.

Other quantities are defined in Eq. 9-11.

9.2.3.5. Annular Space Between Outer Radial Shield and Thermal Barrier. For the design under consideration, the ratio of the inner to outer radius of the annulus is nearly unity. Therefore, Eq. 9-13, which applies to laminar flow between two parallel surfaces, is also valid.

9.2.4. Pressure Drop Through the Core Auxiliary Cooling Loops.

The core auxiliary cooling loop pressure drop is

$\Delta p$ = 9.38 kPa (1.36 psi),

as shown in Ref. 9-2. This value was calculated for the maximum design condition, i.e., depressurized and all three core auxiliary cooling loops operating. The corresponding data are

| | |
|---|---|
| Helium flow per loop | 5.1 kg/s (11.1 lb/s) |
| Helium temperature at inlet of core auxiliary heat exchanger | 768°C (1414°F) |
| Helium temperature at exit of core auxiliary heat exchanger | 204°C (400°F) |
| Average system pressure | 179 kPa (26 psia) |

The design condition core pressure drop is 290 kPa (42 psi). Converting this value to the maximum design conditions of the core auxiliary cooling loops yields 6.76 kPa (0.98 psi). According to assumption 8 of Section 9.2.1., the only core pressure contribution is by the grid plate because of complete core melt-down. The calculated grid plate pressure drop is 0.07 kPa (0.01 psi). Therefore, the total pressure drop across the core auxiliary cooling loop, without core, is

$$\Delta p = 9.38 - 6.76 + 0.07 = 2.69 \text{ kPa } (0.39 \text{ psi}) \quad .$$

The auxiliary heat exchanger pressure drop is 1.72 kPa (0.25 psi) (Ref. 9-2). The pressure drop across a core auxiliary cooling loop without the core and the auxiliary heat exchanger is 0.90 kPa (0.13 psi), of which 0.83 kPa (0.12 psi) is allocated to the reactor cavity region and 0.07 kPa (0.01 psi) to ducting, etc. Therefore, the pressure drop in the reactor cavity (with core melt-down) is 0.9 kPa (0.13 psi). The pressure drop in the rest of the core auxiliary cooling loop is 1.79 kPa (0.26 psi). These two pressure drop values (reactor cavity and auxiliary loop) are used along with Eqs. 9-9 and 9-10 to establish the natural convection helium mass flow.

### 9.2.5. Input Data for Computation

Along with the pressure drop data from Section 9.2.4, some additional information is required for calculating the helium flow:

| | |
|---|---|
| Height of hot and cold gas columns | 11.58 m (38 ft) |
| Gas constant for helium | 2075 N-m/kg-K (386 lbf-ft/lbm-°F) |
| Helium inlet temperature | 120°C (250°F) |

Other input data not listed above are identical to those used for upward heat removal by forced helium circulation (Ref. 9-2).

### 9.2.6. Results and Discussions

Four parametric cases have been investigated:

1. Base case, in which there is helium flow through all three core auxiliary cooling loops.
2. Two core auxiliary cooling loops operational.
3. Heat transfer coefficients at grid plate, lower end, and inner surface of radial shield increased by 50%.
4. Compound thermal conductivity of radial shield decreased by 70%; i.e., a helium gap of 18 mm/m (0.2 in./ft) is considered in the radial shield.

For the base case, surface temperatures for various locations within the reactor cavity are shown in Fig. 9-6. These specific locations are

A = upper surface of molten debris mass (stainless steel).

B = lower surface of outer radial shield.

C = inner surface [0.3 m (1.0 ft) from lower end] of outer radial shield.

D = inner surface (midpoint of outer radial shield elevation).

E = lower surface of grid plate.

F = same as D, but outer surface.

G = inner surface (midpoint) of thermal barrier.

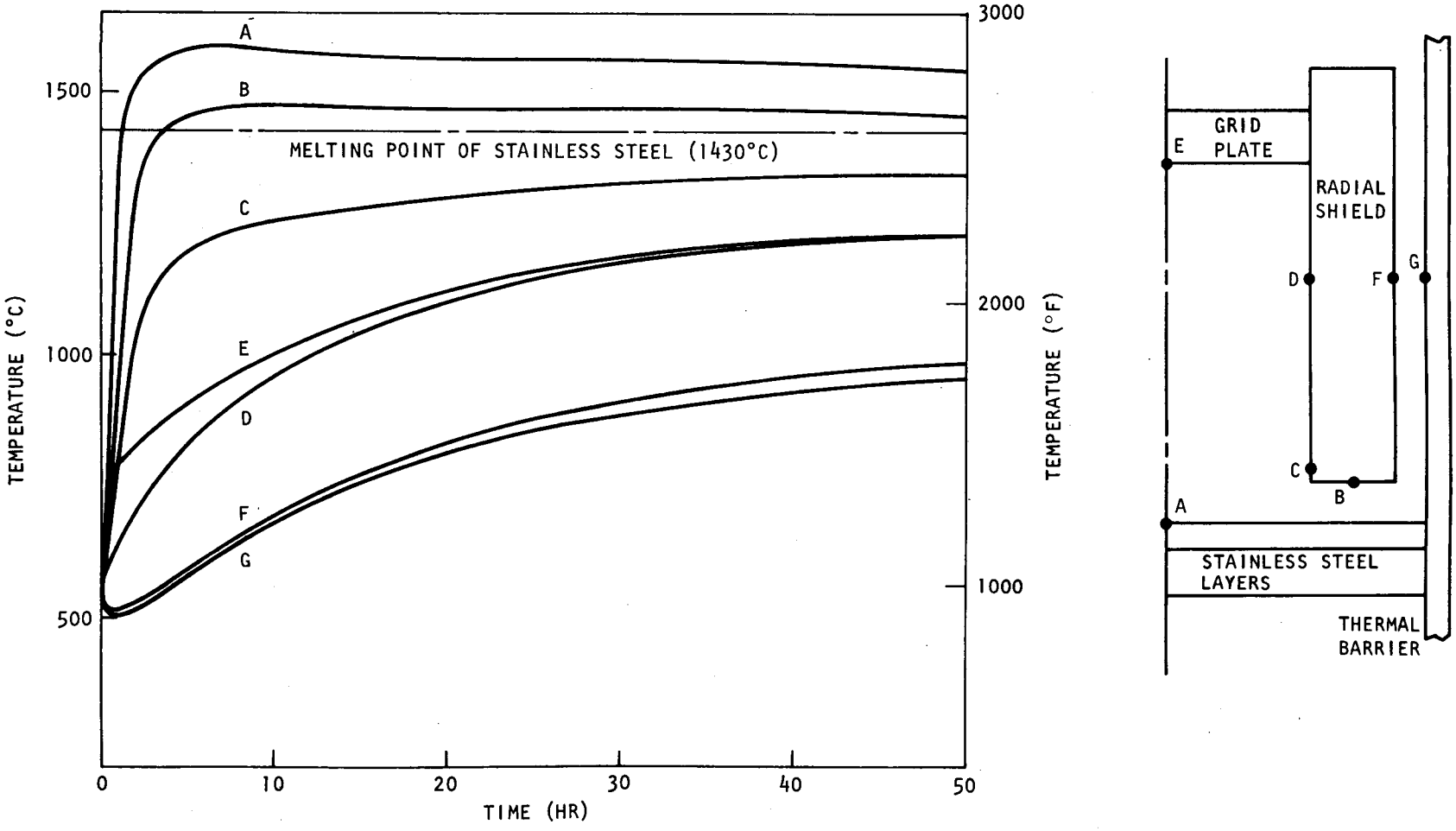


Fig. 9-6 Surface temperature history at various locations within reactor cavity

From Fig. 9-6 it can be seen the lower end of the outer radial shield starts to melt about 4 hr after the accident and reaches maximum temperature after about 10 hr. The surface temperature at 0.3 m (1.0 ft) above the lower end always remains below the melting point. Maximum surface temperatures at the midpoint of the outer radial shield facing the reactor cavity and at the lower side of the grid plate are about 1200°C (2190°F). At this temperature, stainless steel has about 3% of its original strength (Ref. 9-7), which is sufficient for holding the structural member together. However, these temperatures are much higher when compared with the case of forced helium circulation. Therefore, the calculated margin for preventing melt-down of the internal structures is much smaller than that for the case with forced helium circulation. Surface temperatures in the annulus are much lower and are still increasing after 50 hr, thus permitting more heat to be stored in the structural members in this region.

The same base case with an assumed 0.5-hr delay of the helium circulation was also investigated; this delay may be caused by a delay in the opening of the isolation valves. For comparison of this and the previous case, temperatures at two locations are shown in Fig. 9-7. Temperatures for the delayed cooling case are somewhat higher. This difference is not as negligibly small as it was in the case of forced helium circulation. Owing to the much smaller helium mass flow in the case of natural convection, the influence of this change in the initial conditions tends to continue for a very long time, whereas for the case of forced helium circulation, the initial impact is smoothened out within a few hours.

For the other parametric cases, the maximum temperatures and their times of occurrence are given in Table 9-3. The amount of helium flow due to natural convection is shown in Fig. 9-8; helium exit temperatures above the grid plate level are shown in Fig. 9-9. Finally, upward heat removal by natural convection cooling is shown in Fig. 9-10. The base case and the other cases are compared in the following paragraphs.

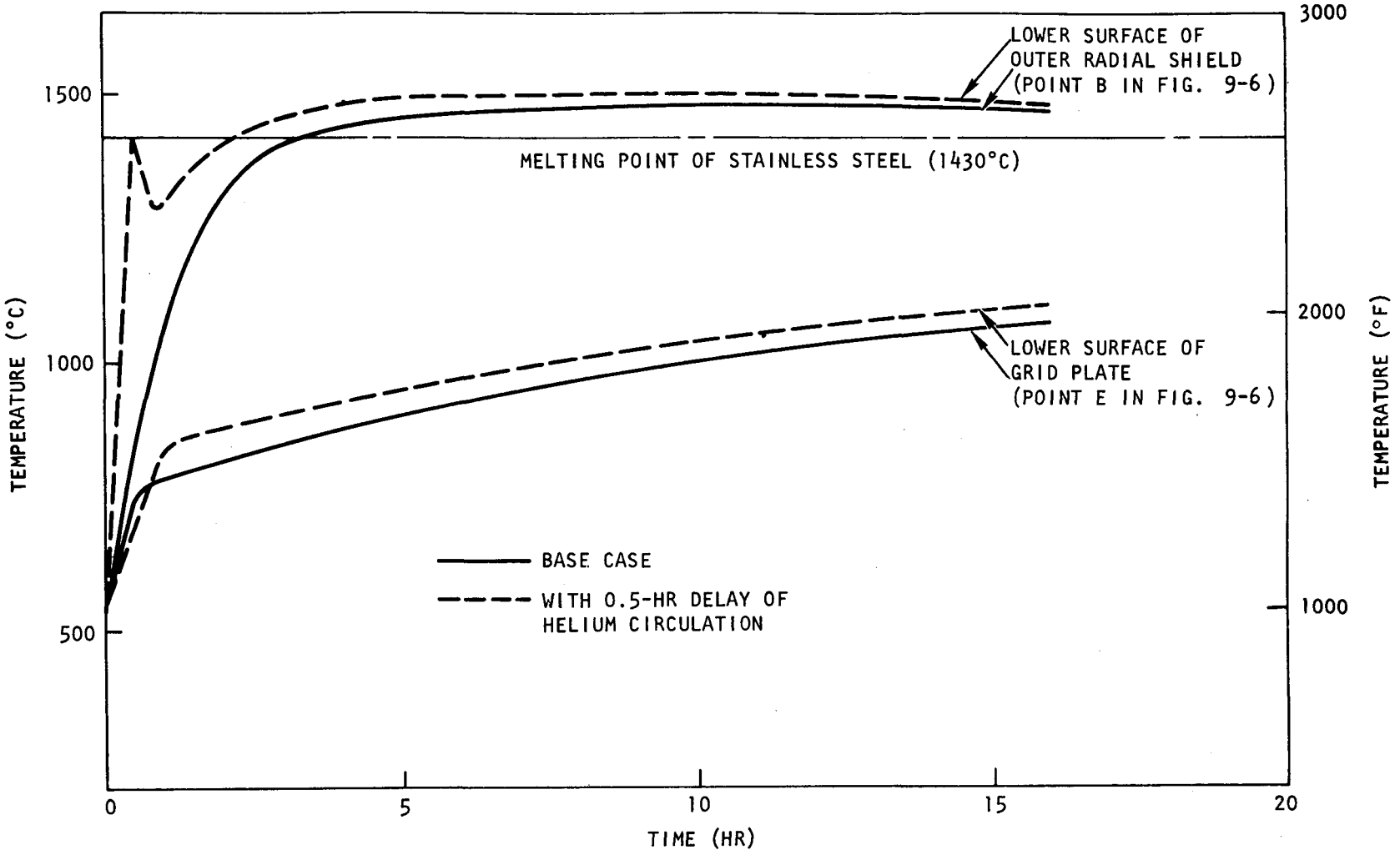


Fig. 9-7 Surface temperature history with 0.5-hr delay in helium circulation

TABLE 9-3
MAXIMUM TEMPERATURES AT SPECIFIC LOCATIONS AND THEIR TIMES OF OCCURRENCE FOR VARIOUS ACCIDENT CASES UNDER CONSIDERATION

| Location | Case 1 | | Case 2 | | Case 3 | | Case 4 | |
|---|---|---|---|---|---|---|---|---|
| | Maximum Temperature [°C (°F)] | Time (hr) | Maximum Temperature [°C (°F)] | Time (hr) | Maximum Temperature [°C (°F)] | Time (hr) | Maximum Temperature [°C (°F)] | Time (hr) |
| A | 1585 (2803) | 6 | 1656 (3013) | 50 | 1579 (2770) | 6 | 1652 (2895) | 10 |
| B | 1477 (2654) | 10 | 1592 (2897) | 50 | 1453 (2597) | 10 | 1565 (2743) | 10 |
| C | 1346 (2453) | 45 | 1498[(a)] (2729) | 50 | 1326 (2412) | 45 | 1427 (2589) | 40 |
| D | 1236 (2257) | 50 | 1419[(a)] (2587) | 50 | 1213 (2215) | 50 | 1347 (2454) | 45 |
| E | 1223 (2234) | 50 | 1426[(a)] (2598) | 50 | 1202 (2195) | 50 | 1308 (2383) | 40 |
| F | 983[(a)] (1801) | 50 | 1155[(a)] (2111) | 50 | 963[(a)] (1766) | 50 | 828[(a)] (1522) | 50 |
| G | 957[(a)] (1754) | 50 | 1136[(a)] (2077) | 50 | 936[(a)] (1717) | 50 | 805[(a)] (1480) | 50 |

[(a)] Maximum temperature has not been reached yet.

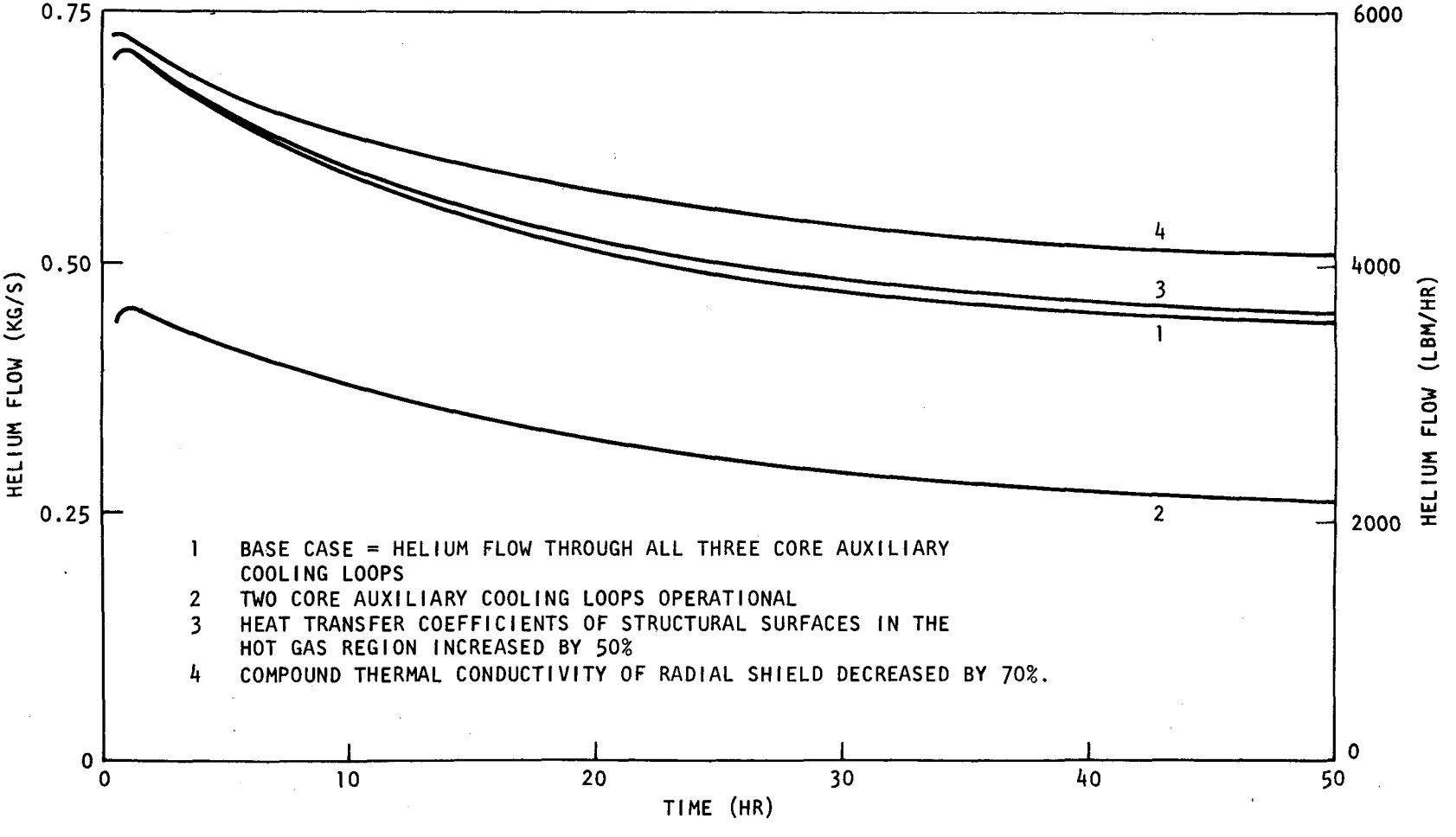


Fig. 9-8 Natural convection helium flow for various accident cases under consideration

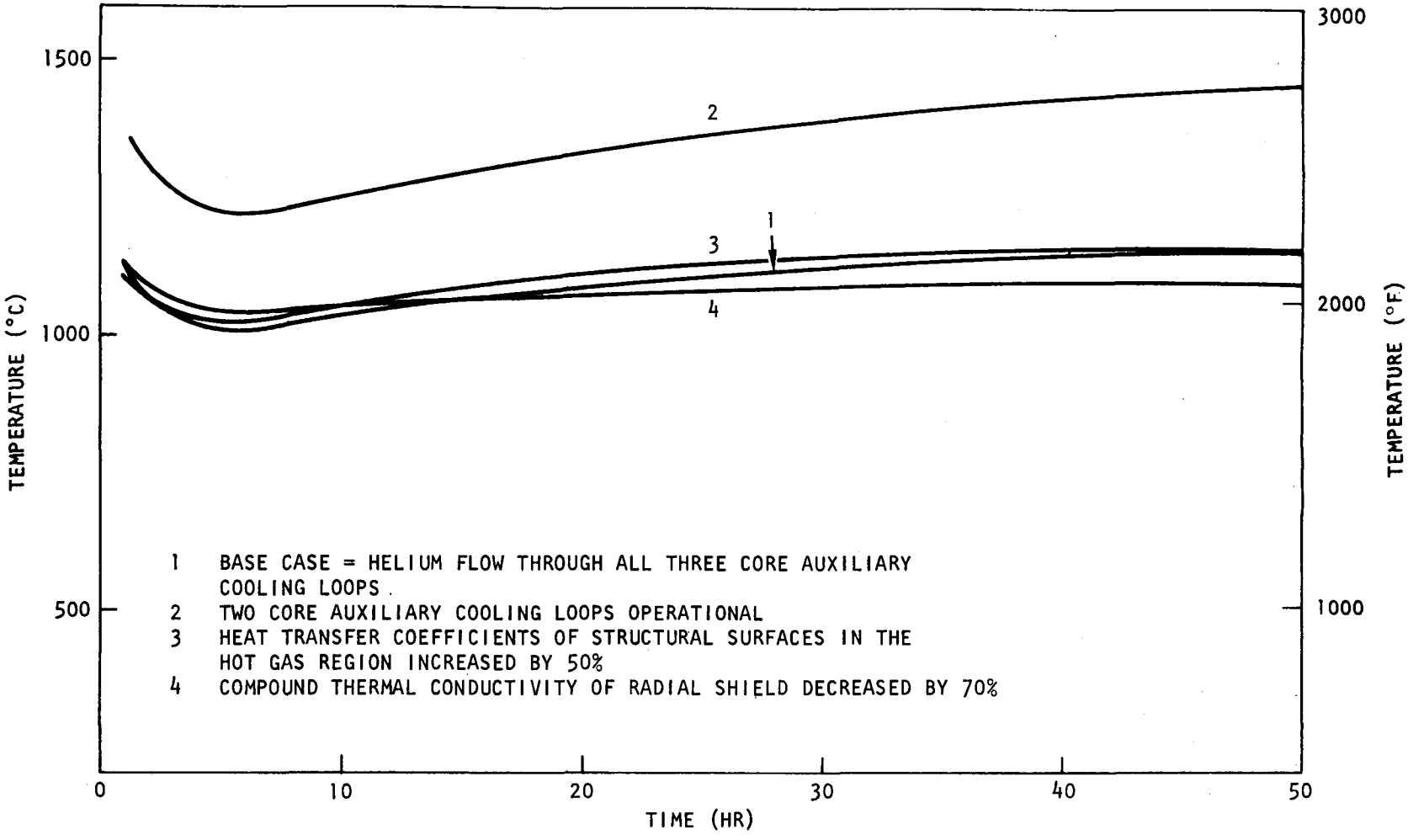


**Fig. 9-9 Helium temperature at top of grid plate**

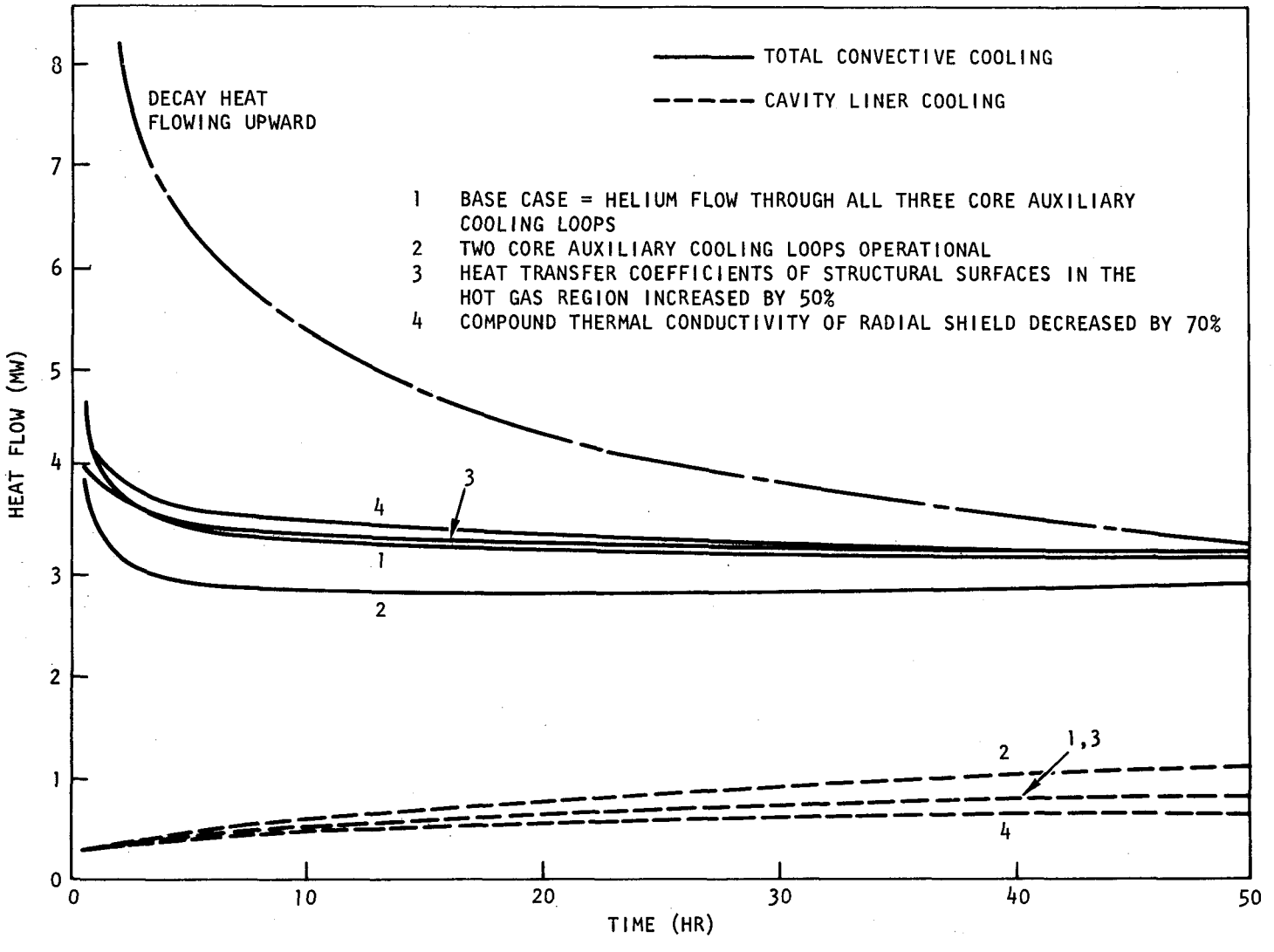


Fig. 9-10 Upward heat removal by convective cooling

For case 2, with only two core auxiliary cooling loops operating, the helium flow through the reactor cavity is decreased owing to increased friction. Therefore, the helium temperature as well as the surface temperatures of the internal structures are considerably higher, and melt-down of the grid plate and radial shields is likely to begin about 50 hr after the accident.

Case 3 shows the effect of a 50% enhancement of the heat transfer coefficients at the structural surfaces (except in the annular region). The influence of this change is not as significant as would be expected. The improved heat transfer coefficient upstream of the point of interest, i.e., at the surface of the outer radial shield facing the reactor cavity, increases the heat removal rate from the structures and thus contributes to a significant increase in helium coolant temperature rise. The available temperature difference for heat transfer at the point of interest is thus diminished, and the surface temperature is not greatly reduced.

Case 4 shows the effect of a 70% decrease in radial shield thermal conductivity. The decreased thermal conductivity of the shield reduces its capability to conduct heat. Therefore, a greater fraction of the heat radiated from the molten debris surface to the structures is transferred to the helium flow. This causes a slight increase in helium flow, but the controlling effect is the greater heat flux on the surface of the shields, which yields higher surface temperatures.

Figure 9-10 shows the total upward heat flow due to natural convection and the heat removed by the cavity liner cooling system. The difference between the two is the heat removed by the helium flow; this includes the convective heat removal from the structural surface and also the heat released from the volatile fission products. The area between the curve of decay heat flowing upward and the curve of total convective cooling is the heat stored in the structures. For all cases except case 2, an almost quasi-steady state (intercept between the two curves) is reached in about 50 hr. In case 2, more heat is stored in the structures until further temperature increases cause melt-down of the structures.

### 9.2.7. Validity of Assumed Helium Inlet Temperature

Design data for the core auxiliary heat exchanger (Ref. 9-2) were used to check the validity of the assumed helium inlet temperature [120°C (250°F)] for the base case and the case of only two core auxiliary cooling loops operating. The cooling capacity of the core auxiliary heat exchanger is approximated and compared with the amount of heat removed by the helium in Table 9-4. A margin of four was found for the base case; for the case of two operating core auxiliary cooling loops, the margin is reduced to three. The margin for both cases increases with time.

## 9.3. CONTROL SYSTEMS

Equations describing the dynamic behavior of the major reactor and steam system components, i.e., the core, the steam generator, the steam turbine/helium circulator, and the resuperheater, have been written. It is not intended at this time to provide a complete closed path for the secondary (steam) system. Instead, only the dominant dynamic characteristics of the main turbine and the feedwater pumps have been included in the descriptive equations for these two components.

Digital coding for the steam generator model is complete. At the full-power operating point, steady-state values of key output parameters are within 1% of those obtained with more detailed analytical models. Comparisons of model transient response characteristics were in good agreement without model "tuning." More careful attention will be given to the transient response after the complete plant model has been assembled and the effects of individual model responses can be evaluated in terms of the critical overall system parameters. Coding and input parameter generation for the other model components are continuing.

TABLE 9-4

COMPARISON OF HELIUM HEAT REMOVAL RATE AND COOLING CAPACITY OF THE CORE AUXILIARY HEAT EXCHANGER [HELIUM INLET TEMPERATURE = 120°C (250°F)]

| Case | Time (hr) | Helium Heat Removal Rate (MW) | Cooling Capacity of Core Auxiliary Heat Exchanger (MW) | Margin[(a)] |
|---|---|---|---|---|
| Base case | 1 | 3.8 | 14.6 | 3.8 |
| | 10 | 2.8 | 12.6 | 4.4 |
| | 50 | 2.3 | 11.7 | 5.0 |
| With two core auxiliary cooling loops | 1 | 3.1 | 8.6 | 2.8 |
| | 10 | 2.3 | 7.4 | 3.3 |
| | 50 | 1.8 | 6.9 | 3.8 |

[(a)]Margin = helium heat removal rate/cooling capacity of core auxiliary heat exchanger.

REFERENCES


9-1 "Gas-Cooled Fast Breeder Reactor Quarterly Progress Report for the Period November 1, 1975 Through January 31, 1976," ERDA Report GA-A13815, General Atomic, March 22, 1976.

9-2 300-MW(e) Gas-Cooled Fast Breeder Reactor Demonstration Plant, General Atomic, unpublished data.

9-3 Menzel, H. F., and C. S. Kang, Status of Post-Accident Fuel Containment Studies for a 300-MW(e) GCFR Demonstration Plant, General Atomic Report GA-A13734, December 18, 1975.

9-4 Kays, W. M., Convective Heat and Mass Transfer, McGraw-Hill, New York, 1966, p. 120.

9-5 Ibid., p. 211.

9-6 Jakob, M., Heat Transfer, John Wiley & Sons, New York, 1949, p. 462.

9-7 Sutton, G. P., Rocket Propulsion Elements, 2nd ed., John Wiley & Sons, New York, 1956, p. 143.

# 10. COMPONENT DEVELOPMENT (189a No. SU025)

## 10.1. REACTOR VESSEL

The scope of this subtask is to assure that the design of the PCRV and the related components which contribute to the integrity of the pressure boundary is satisfactory and to test critical component configurations to make certain that they attain the design objectives. This subtask will demonstrate by analyses and tests that the PCRV and its penetrations and closures meet the design criteria. It will also provide assurance that the design of the thermal barrier satisfactorily protects the liner and PCRV from the effects of high temperatures and the flow restrictors for the large penetrations can be developed to limit the flow of helium from the primary coolant systems to acceptable levels in the event of structural failure of a penetration or closure component.

Work accomplished during the previous quarter included the completion of a drawing showing the placement and sizes of the reinforcing bars for the prototype steam generator closure. A copy was sent to ORNL for use in the scale model testing program for PCRV closures. Based on the reference design for the reactor cavity closure, drawings were initiated for the prototype configuration using shear rings inside the cylindrical wall to transfer the shearing forces. To reduce deflections on the lower plate, the plate will be internally braced.

The results of the structural analysis of the PCRV using a three-dimensional creep-crack computer code were reviewed. The model is being revised to have the liner more realistically reflect the stress distribution around the cavities and penetrations.

In coordination with the designers of the fuel element locking mechanism, layouts were prepared for an updated PCRV reactor cavity closure

configuration. The concept uses 27 penetrations for the control rod drive mechanisms and 7 large-size penetrations for a proposed latching machine. This machine is inserted through a penetration when it is necessary to latch or unlatch a core element from the grid plate. The control drive mechanisms are attached to a casting recessed within the closure. This concept is being evaluated for its effect on the structural integrity of the closure.

Preliminary studies were initiated for the 300-MW(e) reactor to determine the PCRV configurations for accommodating helical coil steam generators with and without resuperheaters. Concepts which placed the steam generator in one cavity and the helium circulator in a separate cavity were also studied. Economic comparisons were prepared for the NSS systems from the various configurations showing the PCRVs and the resulting sizes of the secondary containments. The configuration to be used for the updated NSS system design will be selected from these data. In addition, drawing layouts were prepared for the PCRV to determine the location and sizes of the components of the HPS and the PES.

In connection with the development plan for preparing the test plan of PCRV closure flow restrictors, calculations are being made to determine the clearances required for the structural-type flow restrictor used in the reference reactor design. In order to assess the effect of the PCRV concrete movements of creep and initial prestressing on the clearances, a review was made of methods used in calculating the construction and operational movements of the PCRV.

## 10.2. CONTROL AND LOCKING MECHANISMS

The primary objective of this task is the preparation of a comprehensive development plan for the control and locking mechanisms for a 300-MW(e) GCFR demonstration plant. During this reporting period, after completion of the system description portion of the plan, an effort was made to describe the development and test requirements. The following sections of the development and test requirements portion of the plan were completed in draft form:

- 4.1 Element Locking Mechanism Development and Tests
- 4.2 Reactivity Control Systems Development and Tests
- 4.4 Primary Seal Development and Tests
- 5.0 Test Facility Requirements

## 10.3. FUEL HANDLING DEVELOPMENT

### 10.3.1. Conceptual Studies and System Optimization

Activities in this primary subtask increased during this quarter. Alternate schemes for spent fuel transfer between the reactor and the spent fuel storage pool were analyzed on a qualitative basis with the aid of trade-off comparisons and system layouts. A significant factor in these comparisons is the relative cost impact, due to required interfacing, on the demonstration plant design compared with the refueling system reference design for initial capital costs. The operational or functional cost impact which would be experienced by the user utility is also of prime importance and is included in the draft of the summary report for this subtask, which underwent finalization during the latter part of this quarter.

One alternative scheme consists of a vertical chute within the concrete pad below the PCRV which receives the spent fuel through a gate-type floor valve from the fuel transfer cask. At the bottom of this chute is a chamber which enables an upending operation to allow the fuel to pass into a horizontal pipe tunnel through the concrete pad and isolating valves into the spent fuel storage pool. Another upending operation returns the fuel to a vertical position, which enables the spent fuel transporter and positioner to properly store the fuel. Associated with this scheme are mechanisms to support and transfer the element at all times while it is submerged in water. The upending device supports the element in a cradle-type device, and drives are employed to horizontally transfer the cradle on tracks. This scheme is contained within an area which is located considerably below the refueling floor level and is depicted in a simplified manner in Fig. 10-1.

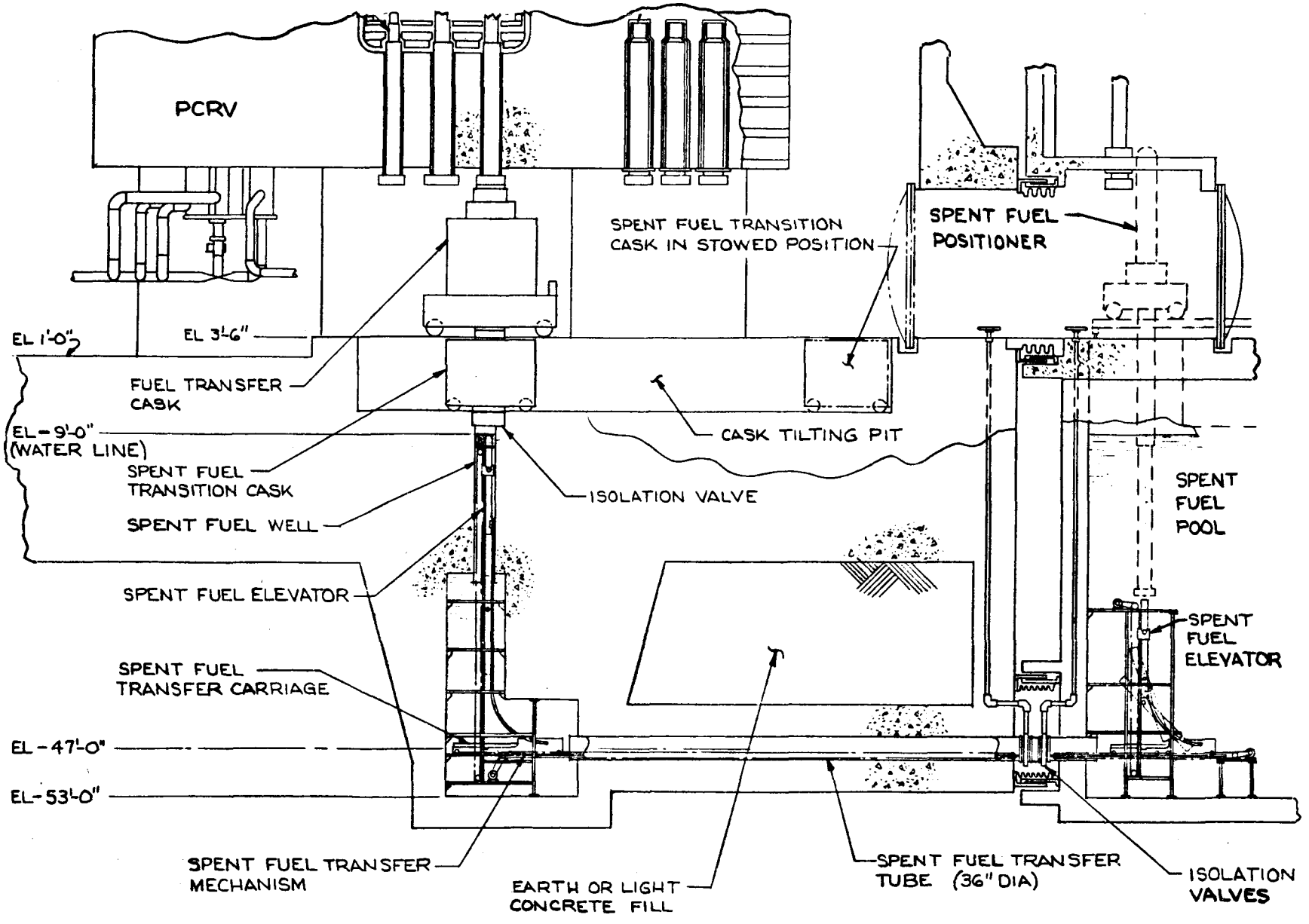


Fig. 10-1 Alternate spent fuel transfer scheme

Component conceptual design studies were also initiated during this quarter, with particular attention directed at the development of in-vessel refueling component mechanisms. The major component is the fuel transfer machine (FTM), and studies of the lifting mechanism design included realistic determination of its major dimensions. With the aid of analysis and layout, the primary components capable of supporting the design loads encountered during the operation of the FTM were selected. This enabled the arrangement and packaging of these components into a dimensional envelope compatible with the interfaces involved. A schematic arrangement, including a grapple assembly, depicting the extending and lifting mechanisms is shown in Fig. 10-2.

Using these data and the related layouts, construction of a quarter-scale plastic working model of the FTM extending and lifting mechanisms was initiated and completed. This model will serve as an engineering tool in the development phase and is expected to be a valuable asset for assuring that interferences do not exist under any operating condition. The model may also be used to demonstrate the various interrelated functions of the FTM operating mechanisms.

### 10.3.2. Postirradiation Examination Facility Evaluations

There were no results to report during this quarter, and we are awaiting specific input data.

### 10.3.3. Spent Fuel Shipping Studies

Technical visits to observe spent fuel shipping activities at an operating LWR plant, San Onofre, occurred during April. Activities observed included the movement of spent fuel assemblies from their storage pool positions (under water) to the shipping cask loading pit and the loading of the assemblies into the cask and their subsequent transfer to the truck transport loading area.

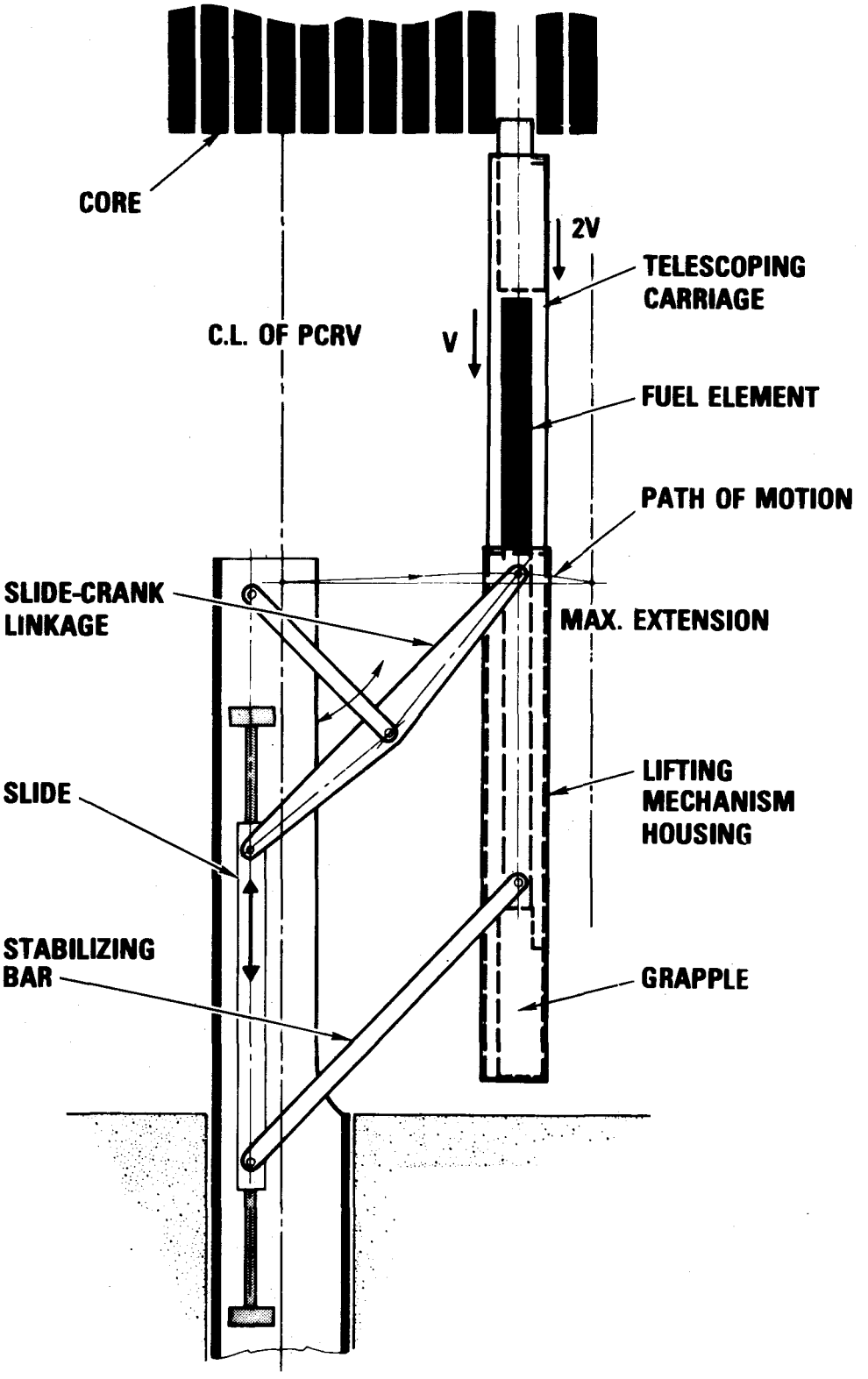


Fig. 10-2 Fuel transfer machine lifting mechanism

## 10.4. CORE SUPPORT STRUCTURE

The purpose of this subtask is to assure the availability of structural analysis methods and materials mechanical behavior required to assess the structural integrity of the GCFR core support structure under all anticipated operational and safety-related loading conditions in the GCFR environment.

During the previous quarter, the problem of the structural interaction between the grid plate and the support cylinder was investigated. An analytical solution was obtained to determine the interactive movement between the grid plate and the lower flange and the discontinuity shear force and bending moment at the junction between the lower flange and the support cylinder. The setup for the grid plate model test was constructed, and some preliminary test data were taken and analyzed during the checkout of the fixture. During this quarter, the static part of the grid plate model test was completed, and the dynamic test is in progress. In order to correlate the effective elastic constants of the grid plate with the measured static test data, an analytic solution was obtained to include the outer solid rim effect as an addition to the anisotropic elasticity solution of the equivalent solid plate of the grid plate.

### 10.4.1. Structural Analysis

An anisotropic elasticity solution of the simply supported equivalent solid plate of the grid plate with the outer solid rim effect neglected was obtained in Ref. 10-1. During the course of the grid plate test model analysis, it was found that the outer solid rim can increase the grid plate deflection stiffness as much as 60%. It is therefore important that the effect of the outer solid rim be included in the solution for the determination of the effective elastic constants from the test data.

Consider the simply supported grid plate subjected to a uniform pressure p, as shown in Fig. 10-3. Applying the equivalent solid material concept to the central perforated region, discontinuity bending moment M and radial force H are introduced owing to material property discontinuity, as shown

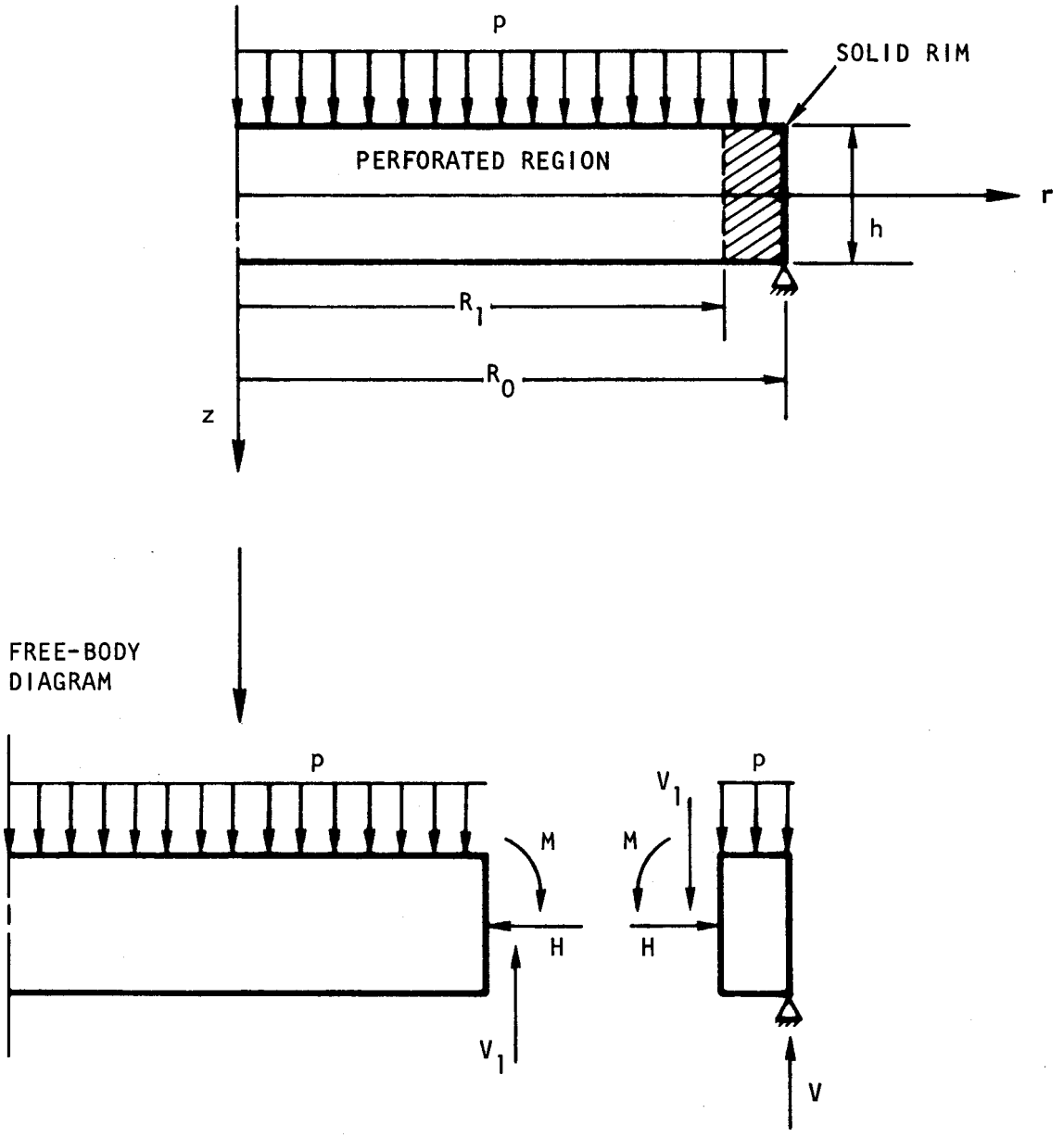


Fig. 10-3 Simply supported reactor grid plate

in the free-body diagram of Fig. 10-3. M and H are then determined by equalizing the rotation and radial displacement of the central perforated plate and the outer rim. Using the notation of Ref. 10-1, the analyses are summarized as follows:

## Perforated Plate

### Radial Displacement

$$U^P = U_1^P + U_2^P + U_3^P \quad , \tag{10-1}$$

where $U^P$ = radial displacement due to p (Ref. 10-1),

$$U_2^P = - \frac{12\ (1 - \nu^*)rz}{E^* h^3} M \quad ,$$

$$U_3^P = - \frac{2\nu_z^*\ z}{E_z^* h} H \quad .$$

### Axial Displacement

$$W^P = W_1^P + W_2^P + W_3^P \quad , \tag{10-2}$$

where $W_1^P$ = axial displacement due to p (Ref. 10-1),

$$W_2^P = - \frac{6}{h^3} \left[ \frac{(1 - \nu^*)}{E^*} (R_1^2 - r^2) - \frac{2\nu_z^*}{E_z^*} z^2 \right] M \quad ,$$

$$W_3^P = \frac{2\nu_z^*\ z}{E_2^*\ h} H \quad .$$

Outer Solid Rim (as a Ring)

Radial Displacement

$$U^r = \frac{R_1 R_2}{hE\Delta R} H \quad , \tag{10-3}$$

where $\Delta R = R_0 - R_1$ .

Rotation of the Ring Cross Section

$$\Theta^r = \Theta_1^r + \Theta_2^r \quad , \tag{10-4}$$

where $\Theta_1^r = \frac{R_2 \Delta R (R_1^2 + R_0^2)}{4EI} p$ ,

$$\Theta_2^r = \frac{R_1 R_2}{EI} M \quad ,$$

$$I = \frac{\Delta R h^3}{12} \quad .$$

Compatibility Conditions

$$U^p \Big|_{\substack{z=0 \\ r=R_1}} = U^r \Big|_{\substack{z=0 \\ r=R_1}} \quad , \tag{10-5}$$

$$-\frac{\partial W^p}{\partial r} \Big|_{\substack{z=0 \\ r=R_1}} = \Theta^r \Big|_{\substack{z=0 \\ r=R_1}} \quad . \tag{10-6}$$

Substituting Eqs. 10-1 and 10-3 into 10-5 and Eqs. 10-2 and 10-4 into 10-6 gives two simultaneous algebraic equations from which M and H are found to be

$$M = \frac{\dfrac{pR_1^3}{8D(1+\nu^*)} - \dfrac{pR_2(R_1^2 + R_0^2)\Delta R}{4EI} + \dfrac{3pR_1}{5h}\left[\dfrac{1}{G_2^*} - \dfrac{\nu_z^*(7-\nu^*)}{4E_2^*}\right]}{\dfrac{R_1R_2}{EI} + \dfrac{12R_1(1-\nu^*)}{E^*h^3}} , \qquad (10\text{-}7)$$

$$H = \frac{pEE^*\nu_z^* h\Delta R}{2E_z^*\,[E^*R_2 + (1-\nu^*)\,E\Delta R]} . \qquad (10\text{-}8)$$

Finally, the deflection of the grid plate is

$$W^G = W^P + \text{outer ring deflection}$$

$$= W^P + \Delta R\theta^r .$$

The result is being used for the analysis of the grid plate model test data to determine the effective elastic constants.

### 10.4.2. Core Support Structure Model Test

The static test of the grid plate model was completed and the results transmitted from San Diego State University to GA. Axial deflection measurements were made along two different radial lines, which were chosen to represent the stiffest and the least stiff directions. This was done in order to evaluate the effect of the nonuniform width of the outer rim. Deflections at five points (1 to 5) along the stiffest direction and eight points (6 to 13) along the least stiff direction were measured, as shown in Fig. 10-4. The results are given in Table 10-1. Because there is no noticeable difference in deflection between the two different radial directions, only the result of the stiffest direction was plotted in Fig. 10-5, and it is shown that the maximum deflection at the plate center due to the 414-kPa (60-psi) uniform pressure is about 0.13 mm ($5 \times 10^{-3}$ in.).

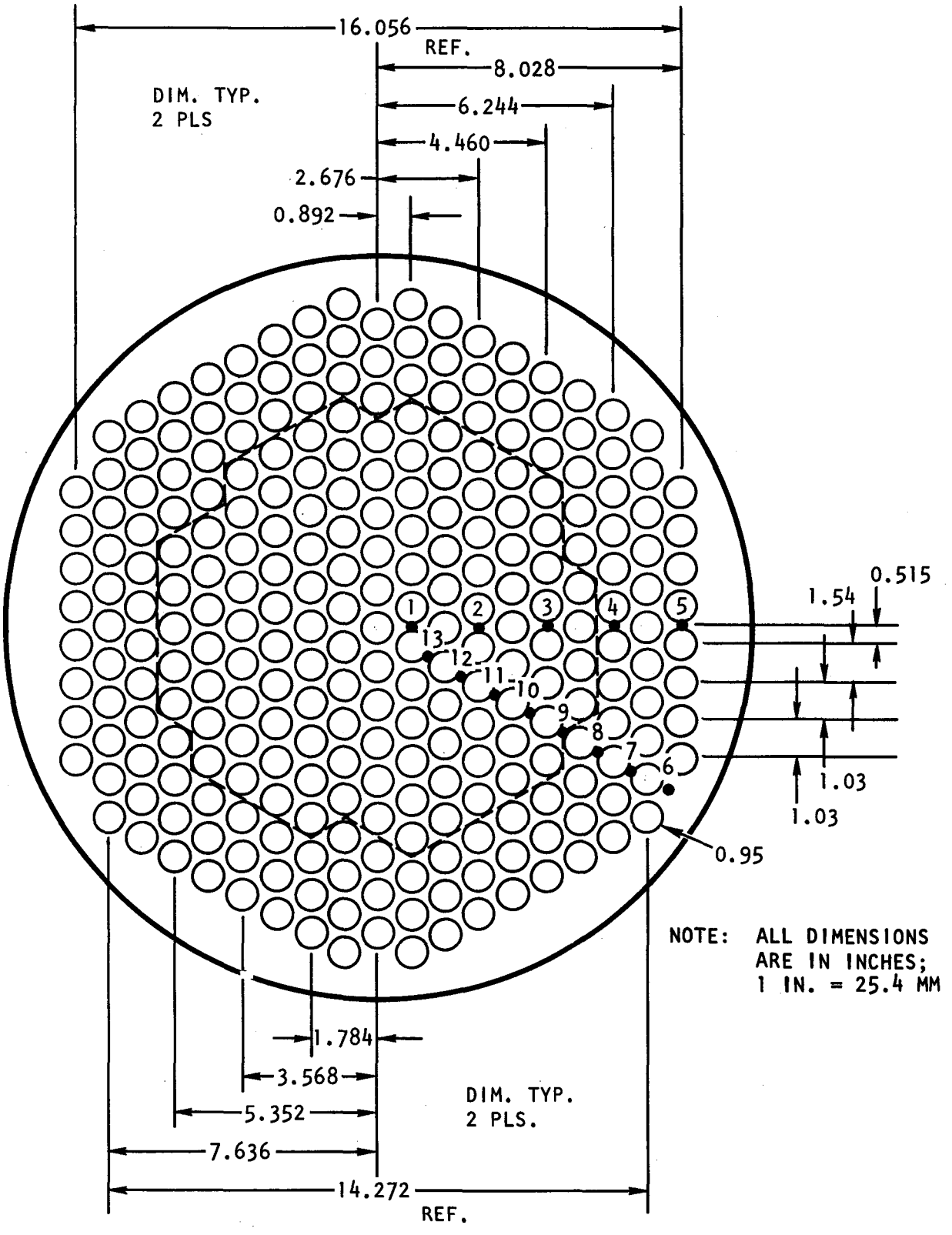


Fig. 10-4 Point location code of profile data

TABLE 10-1

READINGS OF DIAL INDICATOR (IN. x $10^{-3}$)[a]

| Pressure [kPa(psi)] | Point | | | | | | | | | | | | |
|---|---|---|---|---|---|---|---|---|---|---|---|---|---|
| | 1 | 2 | 3 | 4 | 5 | 6 | 7 | 8 | 9 | 10 | 11 | 12 | 13 |
| 0 | 0.0 | 0.0 | 0.0 | 0.0 | 0.0 | 0.0 | 0.0 | 0.0 | 0.0 | 0.0 | 0.0 | 0.0 | 0.0 |
| | 0.1 | 0.0 | 0.0 | 0.0 | -0.2 | 0.1 | 0.0 | -0.1 | 0.0 | 0.0 | 0.0 | 0.0 | -0.2 |
| | 0.0 | 0.0 | 0.0 | 0.0 | 0.0 | 0.0 | 0.0 | 0.0 | 0.0 | 0.0 | 0.0 | 0.0 | 0.0 |
| | 0.0 | 0.0 | 0.0 | 0.0 | 0.0 | 0.0 | 0.0 | 0.0 | 0.0 | 0.0 | 0.0 | 0.0 | -0.1 |
| | 0.025[b] | 0.0[b] | 0.0[b] | 0.0[b] | -0.05[b] | 0.025[b] | 0.0[b] | -0.025[b] | 0.0[b] | 0.0[b] | 0.0[b] | 0.0[b] | -0.075[b] |
| 68.95 (10) | 0.6 | 0.5 | 0.1 | 0.0 | -0.1 | 0.0 | 0.0 | 0.0 | 0.0 | 0.0 | 0.5 | 0.2 | 0.2 |
| | 0.8 | 0.8 | 0.3 | 0.0 | -0.1 | 0.1 | 0.0 | 0.0 | 0.3 | 0.4 | 0.5 | 0.6 | 0.5 |
| | 0.6 | 0.6 | 0.2 | 0.0 | 0.0 | 0.0 | 0.0 | 0.0 | 0.0 | 0.1 | 0.5 | 0.2 | 0.4 |
| | 0.7 | 0.7 | 0.2 | 0.0 | 0.1 | 0.0 | 0.0 | 0.0 | 0.2 | 0.5 | 0.5 | 0.5 | 0.6 |
| | 0.675[b] | 0.65[b] | 0.2[b] | 0.0[b] | -0.025[b] | 0.025[b] | 0.0[b] | 0.0[b] | 0.125[b] | 0.25[b] | 0.5[b] | 0.375[b] | 0.425[b] |
| 137.90 (20) | 1.2 | 1.0 | 0.8 | 0.2 | -0.1 | 0.1 | 0.0 | 0.0 | 0.6 | 0.7 | 0.9 | 0.9 | 0.8 |
| | 1.5 | 1.5 | 0.9 | 0.5 | 0.1 | 0.1 | 0.0 | 0.4 | 0.9 | 1.1 | 1.0 | 1.1 | 1.2 |
| | 1.2 | 1.0 | 0.8 | 0.1 | 0.0 | 0.0 | 0.1 | 0.1 | 0.3 | 0.4 | 1.0 | 0.9 | 1.1 |
| | 1.5 | 1.4 | 0.8 | 0.3 | 0.3 | 0.0 | 0.1 | 0.5 | 0.9 | 1.1 | 1.5 | 1.1 | 1.3 |
| | 1.35[b] | 1.225[b] | 0.825[b] | 0.275[b] | 0.075[b] | 0.05[b] | 0.05[b] | 0.25[b] | 0.675[b] | 0.825[b] | 1.1[b] | 1.0[b] | 1.1[b] |
| 206.84 (30) | 2.0 | 1.9 | 1.0 | 0.6 | -0.1 | 0.1 | 0.0 | 0.3 | 1.0 | 1.0 | 1.5 | 1.3 | 1.6 |
| | 2.4 | 2.2 | 1.3 | 0.9 | 0.2 | 0.1 | 0.1 | 0.9 | 1.2 | 1.4 | 1.5 | 2.0 | 1.9 |
| | 1.9 | 1.9 | 1.0 | 0.5 | 0.0 | 0.0 | 0.2 | 0.4 | 0.8 | 1.0 | 1.5 | 1.4 | 1.7 |
| | 2.3 | 2.1 | 1.1 | 0.8 | 0.4 | 0.0 | 0.4 | 0.9 | 1.1 | 1.5 | 2.0 | 2.0 | 2.1 |
| | 2.15[b] | 2.025[b] | 1.1[b] | 0.7[b] | 0.125[b] | 0.05[b] | 0.175[b] | 0.625[b] | 1.025[b] | 1.225[b] | 1.625[b] | 1.675[b] | 1.825[b] |
| 275.79 (40) | 2.8 | 2.6 | 1.6 | 1.0 | 0.0 | 0.1 | 0.1 | 0.9 | 1.3 | 1.4 | 2.0 | 2.0 | 2.3 |
| | 3.2 | 3.0 | 2.0 | 1.1 | 0.4 | 0.1 | 0.2 | 1.0 | 1.8 | 2.0 | 2.5 | 2.5 | 2.7 |
| | 2.7 | 2.5 | 1.5 | 0.9 | 0.2 | 0.0 | 0.5 | 0.9 | 1.2 | 1.5 | 2.0 | 2.1 | 2.5 |
| | 3.2 | 2.9 | 1.8 | 1.1 | 0.6 | 0.0 | 0.7 | 1.1 | 1.7 | 2.0 | 2.5 | 2.5 | 2.8 |
| | 2.975[b] | 2.75[b] | 1.725[b] | 1.025[b] | 0.3[b] | 0.05[b] | 0.375[b] | 0.975[b] | 1.5[b] | 1.725[b] | 2.25[b] | 2.275[b] | 3.2[b] |
| 344.74 (50) | 3.7 | 3.2 | 2.1 | 1.4 | 0.2 | 0.1 | 0.4 | 1.1 | 1.9 | 2.0 | 2.5 | 3.0 | 3.2 |
| | 4.0 | 3.7 | 2.4 | 1.6 | 0.5 | 0.1 | 0.4 | 1.3 | 2.0 | 2.5 | 3.0 | 3.1 | 3.4 |
| | 3.7 | 3.2 | 2.0 | 1.2 | 0.4 | 0.0 | 0.8 | 1.2 | 1.8 | 2.0 | 3.0 | 3.0 | 3.3 |
| | 3.9 | 3.6 | 2.2 | 1.5 | 0.7 | 0.0 | 0.9 | 1.4 | 2.0 | 2.3 | 3.0 | 3.0 | 3.5 |
| | 3.825[b] | 3.425[b] | 2.175[b] | 1.425[b] | 0.45[b] | 0.05[b] | 0.625[b] | 1.25[b] | 1.925[b] | 2.2[b] | 2.875[b] | 3.025[b] | 3.35[b] |
| 413.68 (60) | 4.7 | 4.1 | 2.9 | 1.9 | 0.5 | 0.1 | 0.8 | 1.7 | 2.2 | 2.8 | 3.5 | 4.0 | 4.1 |
| | 4.7 | 4.1 | 2.9 | 1.8 | 0.7 | 0.0 | 1.0 | 1.9 | 2.2 | 2.8 | 3.5 | 3.8 | 4.2 |
| | 4.7[b] | 4.1[b] | 2.9[b] | 1.85[b] | 0.6[b] | 0.05[b] | 0.9[b] | 1.8[b] | 2.2[b] | 2.8[b] | 3.5[b] | 3.9[b] | 4.15[b] |

[a] 1 in. = 25.4 mm.

[b] Averaged values.

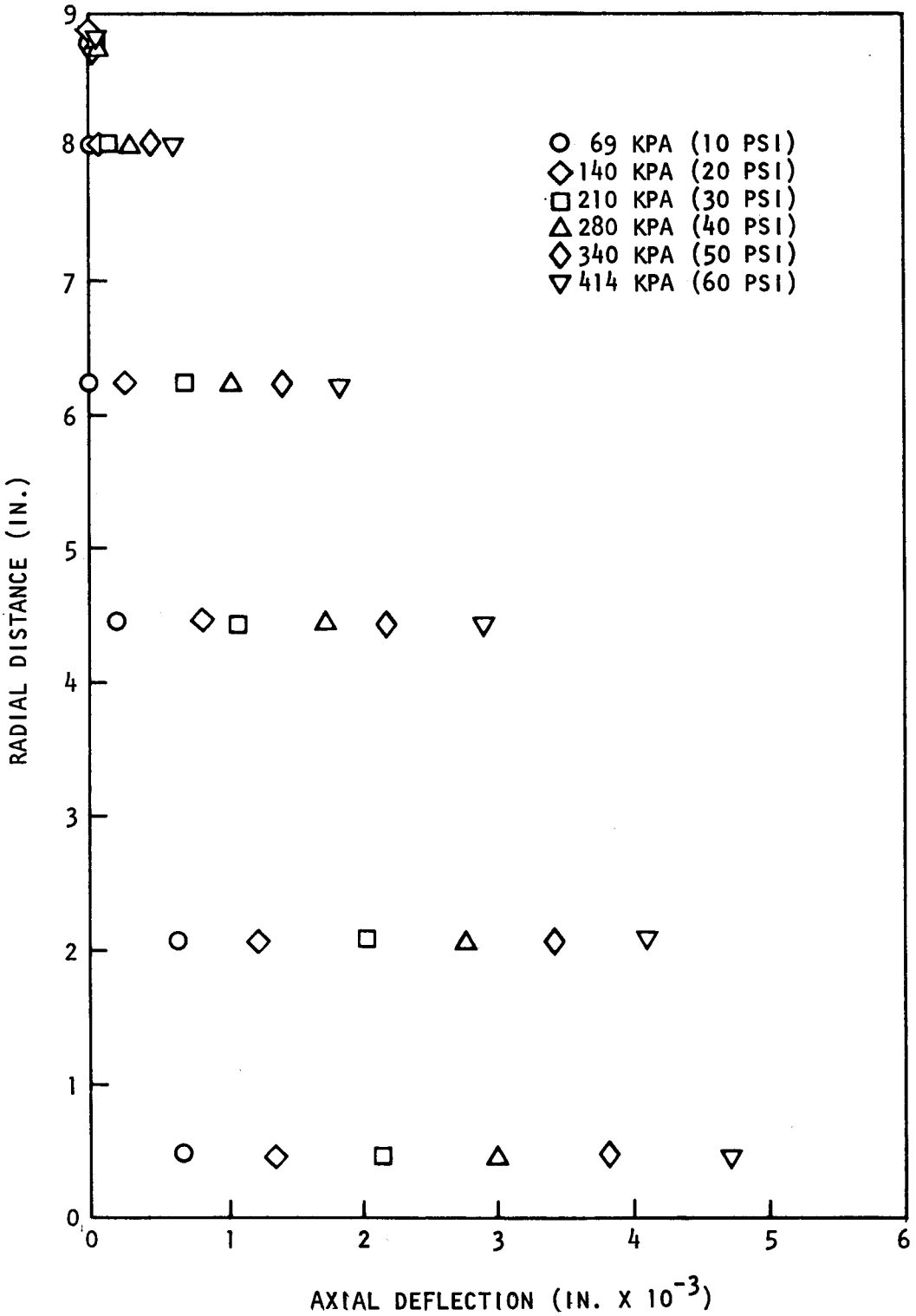


Fig. 10-5 Measured axial deflections of the grid plate (1 in. = 25.4 mm)

First, the SAP IV computer program was used to analyze the test data. The plate was modeled using an axisymmetric solid element with an orthotropic material. The effective elastic constants of the plate were obtained from Ref. 10-2, and the effective elastic constants in the axial direction were found from Ref. 10-3. Figure 10-6 shows the deflections of the plate from the SAP IV calculations for various test pressure loadings. It is seen that the deflections calculated by SAP IV with the input of the effective constants from Ref. 10-2 are about twice as much as those measured in the test.

The second approach for analyzing the test data was to use the analytical solution developed in Section 10.4.1. With the effective elastic constants from Refs. 10-2 and 10-3, the deflection at the center of the plate was 0.21 mm ($8.4 \times 10^{-3}$ in.) for a pressure loading of 414 kPa (60 psi). This is in good agreement with the SAP IV results.

A factor of two discrepancy between the experimental results and the analytical calculations is too great to be ignored and explained as a result of test fluctuation. Therefore, it is felt that the difference could result from the conservatism of the effective elastic constants in Ref. 10-2. In addition, a partial clamping of the test plate in the setup could reduce the deflections. Based on these conclusions, a best-estimated set of the effective elastic constants for the grid plate is being developed using the analytical solution of Section 10.4.1.

The objective of the second part of the test program is to determine the dynamic response of the core support structural model during a simulated earthquake excitation. In achieving this task, some of the important parameters of the core model system will also be determined. As the first part of the free vibration test, the lowest natural frequencies of the perforated plate model were determined. The plate was freely supported by an inflated rubber tire and excited by a magnetic shaker and independently excited by acoustic excitation. The two measured lowest frequencies of the plate were 1500 and 4440 Hz. The dynamic model of the fuel and blanket elements was

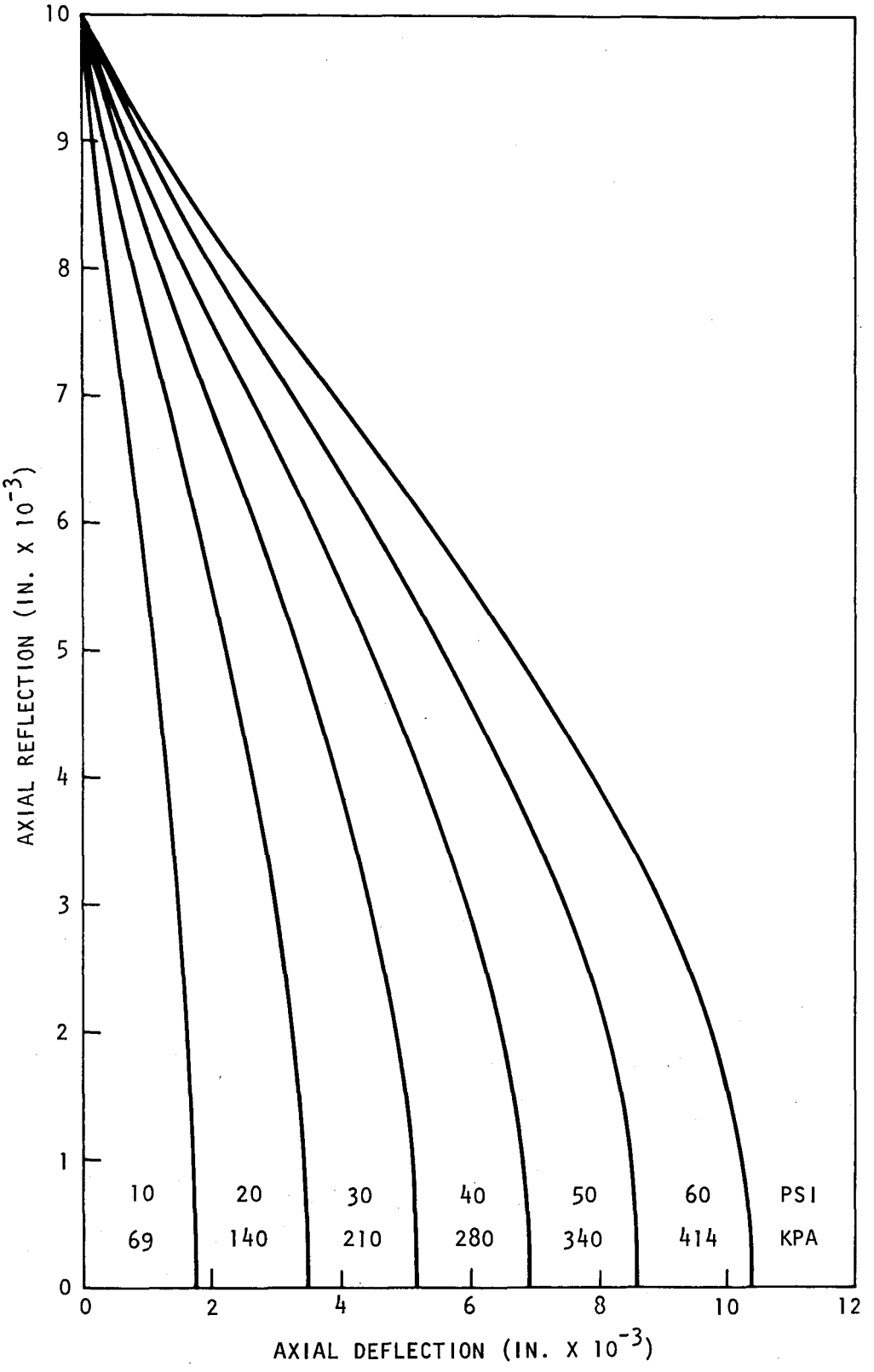


Fig. 10-6 Grid plate deflection calculated by the SAP IV computer program (1 in. = 25.4 mm)

simulated by aluminum tubes which were 22 mm (0.875 in.) in diameter. To achieve the proper ratio of the model grid plate and core elements, steel inserts were placed in the tubes. The cantilever mode of the individual core element was also determined by mounting the individual elements into a rigid steel block. The observed frequencies of the fuel and blanket elements were 56.7 and 41 Hz, respectively. These frequencies are in the expected ranges, which were determined from dimensional analysis.

## 10.5. REACTOR SHIELDING

The purpose of this task is to develop analytical methods and experimental programs to evaluate the reference design of the reactor shields. This evaluation considers heating and cooling of the shields, materials evaluation, seismic effects, need for flow tests, and structural analysis. The evaluation also includes alternate shield configurations as necessary to develop a satisfactory design.

During the previous quarter, a simplified stress analysis of the radial shield based on stress and ductility limits was discussed. In parallel with this effort, a review of the shield design was also briefly mentioned. During this quarter, this effort was continued to include different design concepts and problem areas of the shield design.

### 10.5.1. Shield Design

The shield assembly is designed to protect the PCRV and core support from excessive radiation-induced effects, including radiation-induced heating and degradation of material properties. An additional function of the assembly is the minimization of neutron-induced activation of primary loop components, thereby simplifying maintenance operations. The reference shield design includes the upper, radial, and lower shields. The radial shield may be further classified as the inner and outer radial shields.

The reference shield design was studied and compared with alternate shield configurations. The alternate design concepts were

1. Variations of the removable inner radial shield.
2. An outer radial shield as a continuous cylindrical shell.
3. A segmented outer shield with a protective cylindrical shell close to the thermal barrier.

The second part of this effort included an assessment of the problem areas in the shield design:

1. Methods of structural analysis.
2. Material and radial damage effects.
3. Seismic loads on the support structure.
4. Radial heat generation, cooling, and pressure drop.
5. Effect of thermal barrier on the shield design.
6. Fabrication, construction, and cost effectiveness.

The structural analysis of the shield assembly employs simplified methods assuming steady-state loads. Two failure mechanisms were reviewed in some detail: (1) creep rupture and (2) residual ductility. The creep rupture curves of Ref. 10-4 (LMFBR) were applied to determine the allowable stress limits of the stress calculations, and the ductility criteria of Ref. 10-5 (Clinch River breeder reactor) were used to study the effect of radiation on the shielding material. A review of the existing material data was performed, and the pertinent test data were applied to the simplified stress analysis. Although more material information is desirable, the results of the analysis appear satisfactory even with the existing limited test data. The concept of a different shield support was evaluated, and it was concluded that the "best support" of the shields should be determined on the basis of a seismic analysis and the cost effectiveness of the system.

As a verification of the pressure drop calculation, flow model tests are being considered for the upper shield. Some of the important aspects

of the manufacturing and related cost were reviewed, and the possibility of cost reduction by utilizing the different shield design concepts was investigated.

### 10.5.2. Heat Transfer and Hydrodynamic Analyses

The objectives of this subtask are (1) to define and validate (as necessary) the analytical methods for determining the flow distribution and pressure drops related to coolant flow in and around the GCFR shielding structures and (2) to define methods for and perform evaluations of the temperature distribution in the shield structures.

During the previous quarter, a thermal analysis of the radial shielding structures was performed for the alternative design configurations with two-row blankets. The steady-state temperature distributions in the radial shields at the core midplane were reported in Section 10.5.3. of Ref. 10-6. During this quarter, the configuration of the upper axial shield was investigated to determine if a modular shield design can be devised for this region, as discussed in Section 10.5.1. The effect of several proposed designs on the pressure drop is being studied. Preliminary calculations for one proposed upper axial shield configuration indicate that a pressure drop reduction of ~7 kPa (1 psi) is possible in comparison with the reference design; the overall pressure drop for this region was calculated to be 17 kPa (2.5 psi) for the reference design. A thermal analysis of several lower shield conceptual designs has been initiated. The purpose of this analysis is to determine temperature profiles for the shielding configurations and to assess the cooling requirements for the shield and the preshield. In conjunction with this effort, a hydrodynamic analysis will be performed to ensure that the coolant flow requirements can be satisfied.

The thermal model basically includes a stainless steel preshield, a helium coolant channel, a graphite shield with stainless steel cladding (with and without a fused silica layer), a thermal barrier, and a liner

with a cooling coil system. The one-dimensional gamma ray heating calculations for the above configurations have been performed, and these heating rates will be used in the analysis.

## 10.6. MAIN HELIUM CIRCULATOR, VALVE AND SERVICE SYSTEM

The objective of this task is to prepare a topical report evaluating alternate main loop isolation valve conceptual designs. The purpose is to develop components for the main helium circulator valve and service system and to demonstrate their performance and reliability by testing them under anticipated operating conditions.

A number of conceptual design alternatives have been evaluated in lieu of the pressure-operated louver-type valve located at the cross duct of the GCFR reference design. Criteria applied to the alternate designs and evaluation include

1. Mechanical actuation, including a motor-driven or solenoid-operated valve.
2. Valve-positioning indicator systems to satisfy operating functions and in-service inspection requirements.
3. Replacement of the circulator leaves the valve in a fail-safe condition in the closed position.
4. Seismic Category 1 qualification.

Several basic alternative valve configurations have been considered, including

1. A flapper-type valve located in the inlet duct to the circulator.
2. A valve concept similar to that proposed for the large HTGR design.
3. A butterfly-type valve installed in the circulator outlet duct. Actuation is by means of a vertical shaft extending through the circulator support and cavity closure and installed at the top of the PCRV.

4. A gate valve installed at the exit of the circulator outlet duct. Actuation is similar to that of item 3.

A draft of the FY-77 work plan for the main helium circulator valve and service system (Subtask 23.66.100.77) has been prepared.

## 10.7. STEAM GENERATOR

The purpose of this task is to develop a steam generator which meets the operational, performance, and safety requirements of the GCFR. During this fiscal year, several steam generator designs will be analyzed and evaluated, and the merits of each design will be compared.

Since the last reporting period, cycle evaluations have shown that for the 300-MW(e) GCFR, the most desirable cycle is one in which the primary loop helium pressure drop is reduced from 0.37 MPa (54 psi) to approximately 0.28 MPa (40 psi). For this cycle, the helium temperatures into and out of the steam generator are 543°C (1010°F) and 337°C (639°F), respectively. Using the condition of this cycle, helical coil steam generators without a resuperheater were sized for various frontal areas with corresponding bundle lengths. For example, a 3.05-m (10-ft) diameter bundle has an 8.1-m (26.6-ft) length, whereas a 2.6-m (8.5-ft) diameter bundle is 16.6 m (54.5 ft) in length. These steam generator sizes were used in various component arrangements in the PCRV (i.e., circulator and steam generator in one cavity or in separate cavities) to evaluate the effect of component sizes and locations on helium and steam ducting and PCRV cost.

In the steam generator study it was found that by appropriate selection of tube sizes in the various sections, it is possible to make the all-liquid pressure drop approximately equal to the two-phase pressure drop. Such a pressure drop distribution is desirable in that it reduces the need for inlet tube orificing. Because the allowable stress for Incoloy 800 does not significantly decrease with increasing temperature as it does for 2-1/4 Cr - 1 Mo, the desirable pressure drop distribution can be obtained with a superheater tube which is only slightly larger than the economizer tube.

A review of steam generator design and operating experience in domestic PWRs and the LMFBR was performed in order to obtain background material for the GCFR steam generator design. Reference 10-7 describes the results of a 4000-hr development test on the Atomics International modular steam generator. Because this steam generator design was chosen for the Clinch River LMFBR plant and its operating conditions are similar to those of the GCFR, the information on design, material behavior, and thermal-hydraulic performance is of interest. Of note are the findings that (1) at low flow and pressure, boiling is stable and (2) the mechanical and corrosion performance of the 2-1/4 Cr - 1 Mo steel tubing is satisfactory on the sodium and water sides. Continuing tests on the LMFBR steam generator (Ref. 10-8) and the single-tube boiling tests to be performed at Argonne National Laboratory (Ref. 10-9) will be monitored for their applicability to the GCFR program.

A draft of the FY-77 work plan for steam generator Subtask 23.67.100.77 has been prepared. The scope of the work has been increased to include first-of-a-kind engineering design of the steam generator, including thermal-hydraulics and structural aspects.

## 10.8. AUXILIARY CIRCULATOR, VALVE AND SERVICE SYSTEM

The general objective of this task is to prepare and issue a CACS component development plan document. The purpose is to develop components for the CACS system to meet the reliability and safety criteria and to demonstrate the performance and reliability of critical components by testing under anticipated operating conditions.

The draft copy of the CACS development plan is approximately 90% complete. The cost and schedule for the tasks and subtasks in the development schedule include interfacing requirements with the design, fabrication, qualification, and installation of the CACS components.

A draft of the FY-77 work plan for auxiliary circulator valve and service system (CACS) components Subtask 23.68.100.77 has been prepared.

REFERENCES


10-1 "Gas-Cooled Fast Breeder Reactor Quarterly Progress Report for the Period August 1, 1975 Through October 31, 1975," ERDA Report GA-A13766, General Atomic, January 5, 1976.

10-2 "ASME Boiler and Pressure Vessel Code," Section III, (ASME 111/2), 1974.

10-3 Slot, T., Stress Analysis of Thick Perforated Plates, Technomic Publishing, Westport, Connecticut, 1972.

10-4 Soo, P., "Analysis of Structural Materials for LMFBR Coolant-Boundary Components," Westinghouse Electric Report WARD-3045T3-5, November 1972.

10-5 "Clinch River Breeder Reactor Plant, Preliminary Safety Analysis Report," v. 4, Amendment 1, Project Management Corporation, July 1975.

10-6 "Gas-Cooled Fast Breeder Reactor Quarterly Progress Report for the Period November 1, 1975 to January 31, 1976, ERDA Report GA-A13815, General Atomic, March 22, 1976.

10-7 Harty, R. B., "Modular Steam Generator Final Project Report," Atomics International Report TR-097-330-010, September 1974.

10-8 "The Clinch River Breeder Reactor Project: A Briefing for Engineers," Proceedings of the Breeder Reactor Corporation, Information Session, April 1975.

10-9 Stevens, H. C., "System Design Description for Steam Generator Test Facility - AI Test Section," Argonne National Laboratory Report ANL-G0033-0004-SA-00, April 1975.

## 11. HELIUM CIRCULATOR TEST FACILITY (189a SU046)

The objective of this task is to develop a test facility for qualification testing of the GCFR main helium circulator, and the scope of this task involves (1) evaluation of alternative test facility concepts in terms of technical feasibility and cost, (2) identification of the most promising test facility concept, (3) an A/E preliminary design study, and (4) final design, construction, and checkout of the facility.

The final draft of the topical report describing the full-power (100%) helium circulator test facility concept scoping and cost evaluation study is in final review prior to publication. The 25%-power helium circulator test facility scoping study is complete and documented in a topical report which has been submitted for internal GA review. A draft version of the FY-77 work plan for helium circulator test facility Subtask 23.91.100.77 has been prepared.

The 100%-power closed steam loop helium circulator test facility sized for the GCFR reference design circulator, $\Delta P$ = 0.37 MPa (54 psi), has been reviewed for compatibility with the low-$\Delta P$ circulator for the updated 300-MW(e) GCFR design in which the primary coolant system $\Delta P$ has been reduced. The closed steam loop system concept uses two parallel steam compressors to circulate steam to and from the circulator turbine. The review showed that the closed loop test facility conceptual design from the full-power scoping study could be modified to accommodate the low-helium-$\Delta P$ circulator, with cost adjustments for different piping and heat exchanger sizes. The only area of technical concern is the increase in steam compressor exit temperature from 738 to 783 K (868° to 950°F), which requires the manufacturer to do additional research and development. The magnitude of the cost increase is difficult to define at this time since only a preliminary response concerning the steam compressors for

the reference design has been obtained from the manufacturer. The estimated cost for the two reference test facility design steam compressors is $\$3.2 \times 10^6$, which includes $\$1.2 \times 10^6$ for research and development. Until a firm commitment to supply the steam compressors is obtained from a supplier, the technical feasibility of the steam compressors and the associated closed loop test facility must be considered an open question. It is therefore recommended that the open loop concept using a high-pressure utility steam supply be kept as a viable alternative.

# 12. REACTOR SAFETY (189a No. SU021)

The purpose of this task is to study the reactor safety aspects of the GCFR. Logical probabilistic methods are employed to determine the probabilities associated with various accident initiation and progression sequences and to identify potential design modifications that would help reduce risks. The thermal behavior of the fuel element duct walls under conditions of loss of shutdown heat removal is studied to determine the relative timing of duct wall melting and fuel melting. Scoping studies are performed to determine test requirements for duct melting experiments. This task also includes liaison between GA and the ERDA-funded GCFR safety task at ANL.

## 12.1. ACCIDENT INITIATION AND PROGRESSION STUDIES

Applying the accident initiation and progression analysis (AIPA) techniques developed in FY-74, work is being directed toward the probabilistic analysis of potential accident sequences leading to low-probability, high-consequence sequences of events; this is also under study at ANL under the task "GCFR Safety Aspects on Fuel and Core." The principal AIPA effort is directed at the 300-MW(e) demonstration plant, with scoping-type analyses to be performed for larger plant sizes. The three principal accident classes under investigation are loss of flow (LOF) with shutdown, LOF with failure to shut down, and transient overpower (TOP). The objective of this work is to provide a best estimate assessment of accident sequences within each of these classes. This assessment will be reported in detail by June 1976, and therefore only a brief summary of this work is given below. Work during this quarter has been directed at the first two accident classes, i.e., LOF with and without shutdown.

### 12.1.1. Loss of Flow With Shutdown Accidents

Emphasis in this area has been directed at identifying the means and probability of decay heat removal failure in the GCFR. The analysis of sequences within this accident class was essentially completed during this quarter, and details will be reported in the year-end report (June 1976). Summaries of this work have appeared in previous quarterly progress reports and show that accidents in this class have a frequency of less than $10^{-5}$/yr.

### 12.1.2. Loss of Flow without Shutdown Accidents

The approach developed for consideration of LOF without shutdown accidents involves two principal parts: (1) establishing the reliability of the two diverse GCFR systems to perform a rapid shutdown and (2) determining the frequency of initiating events requiring rapid shutdown. Because of a lack of design information (design schematics of the plant protection system have not yet been developed for the GCFR), the approach taken to the first part has been to consider and compare the GCFR design approach with that of other reactor types to provide a reasonable target reliability for the GCFR systems. Table 12-1 presents a summary of the shutdown system failure probabilities or goals for other reactor types. Based on such information, it appears that the GCFR diverse system approach could achieve an unavailability in the range of $10^{-7}$ to $10^{-8}$ per demand. The achievement of such a goal requires that there be no higher order linking common mode failures between the systems, an aspect currently being considered in more detail.

Consideration of the frequency of initiating events requiring immediate reactor shutdown has identified a total loss of feed event as most limiting. This event has been calculated to have a frequency of less than once in 10 yr. Barring the occurrence of intersystem common mode failures, the total likelihood of an LOF without shutdown accident should be in the range of $10^{-8}$ to $10^{-9}$/yr, or less than 0.1% of the sequences leading to core damage with shutdown.

TABLE 12-1
SUMMARY OF SHUTDOWN SYSTEM FAILURE PROBABILITIES

| Source | Failure Probability | | |
|---|---|---|---|
| | Normal | Backup | Total |
| Reference 12-1 | | | |
| PWR | $3 \times 10^{-5}$ | $10^{-2}$ | $3 \times 10^{-7}$ |
| BWR | $1 \times 10^{-5}$ | $10^{-1}$[a] | $1 \times 10^{-6}$ |
| HTGR-AIPA | $1 \times 10^{-5}$ | $10^{-3}$[a] | $1 \times 10^{-8}$ |
| Kaman Sciences-Fort St. Vrain | $4 \times 10^{-5}$ | (b) | (b) |
| Reference 12-2 (anticipated transient without scram) | $<1 \times 10^{-4}$ | $<10^{-3}$ | $<1 \times 10^{-7}$ |
| Clinch River breeder reactor(Ref.12-4) | $<1 \times 10^{-4}$ | $<5 \times 10^{-4}$ | $<5 \times 10^{-8}$ |

[a] Requires operator action.

[b] Analysis reported in Ref. 12-3 on the Fort St. Vrain HTGR backup system was not analyzed.

## 12.2. SAFETY-RELATED ANALYTICAL AND EXPERIMENTAL STUDIES

Under this subtask, analyses are in progress to determine the heat-up and melting of duct walls relative to the fuel during a loss of coolant flow in a shutdown reactor. Analyses during previous quarters have indicated that the duct wall will melt prior to any fuel melting within the element and the time lag between duct melting and fuel melting is insensitive to uncertainties in the physical parameters. During this quarter, analyses of duct melting progression in core elements during an LOF in a shutdown reactor have been completed, and a topical report is being drafted.

### 12.2.1. Two-Dimensional Analysis of a Control Fuel Element

The previous quarterly progress report (Ref. 12-5) documented detailed analyses of the circumferential duct melting progression in a standard fuel element. It was concluded that the delay in the melting of the duct corner relative to the midflat region was approximately 20 s for an element design with fueled corner rods, and for the current reference design with unfueled corner support rods, the delay was about 50 s.

During this quarter, a detailed duct melting progression analysis was completed for a control fuel element. In the GCFR, the control fuel element is identical to the standard fuel element except that the central 37 fuel rods are removed and replaced by a hexagonal guide tube and the steel-clad $B_4C$ control rod. The fuel element design using unfueled corner support rods was used for this analysis. Table 12-2 compares the results for the control fuel element with those for the standard fuel element. The six remaining rows of fuel rods in a control fuel element are sufficient to thermally decouple the guide tube from the element duct, as indicated by the identical duct melting sequence in both element types (the first six items of Table 12-2). The last section of the guide tube melts about 10 s after the duct corner, but this additional delay is more than compensated for by the significant delay in the beginning of fuel melting (261 versus 198 s). The element duct and the control rod guide tube melt significantly earlier than the control rod cladding, and no early control rod reactivity effects are anticipated.

TABLE 12-2
CALCULATED DUCT AND FUEL MELTING TIME NEAR THE CORE CENTER FOLLOWING A LOSS OF FLOW (IN 2 S) WITH SCRAM

| Melting Time (50% Heat of Fusion) (s) | Fuel Element Type | |
|---|---|---|
| | Standard | Control[a] |
| First cladding | 40 | 40 |
| Last cladding | 111 | 111 |
| First tie rod section | 135 | 137 |
| Last tie rod section | 156 | 157 |
| First duct wall section | 118 | 119 |
| Last duct wall section | 169 | 169 |
| First guide tube section | -- | 144 |
| Last guide tube section | -- | 179 |
| Control rod cladding | -- | 265 |
| First fuel | 198 | 261 |

[a]Control rod initially withdrawn.

The control fuel element analysis assumed an initial control rod temperature of 315°C (600°F), which is typical of a control rod in the withdrawn position. A reactivity balance shows that only the control rods withdrawn prior to the accident are required to maintain the core subcritical up to fuel melting. Thus, the behavior of the initially inserted control rods which are at a higher initial temperature is not crucial to the accident progression. Nevertheless, the melting sequence in a control fuel element where the control rod is initially at 1100°C (2000°F) was also analyzed. The significant difference is a more rapid heat-up of the control rod and its guide tube, such that the control rod cladding melts shortly after the last duct section melts. For an initially hot control rod, it appears that duct fall-away would occur at about the same time as a control rod failure. An initially cold control rod would fail much later.

### 12.2.2. Axial Duct Melting Progression

During the delay in melting the duct corner relative to the duct midflat, the melt front also progresses axially upward and downward. Owing to the flat axial power distribution near the core midplane, the axial melt progression is relatively fast. During the 20-s corner delay in an element with fueled corner rods, the duct melt front reaches a level approximately 17 cm (6.7 in.) above and below the core midplane, and for the 50-s corner delay in an element with unfueled corner support rods, the melt front reaches about 32 cm (12.6 in.) above and below the midplane.

### 12.2.3. Radial Duct Melting Progression

In elements which are further removed from the core center, the radially decreasing power density delays the melting of the duct side oriented away from the core center. However, across an enrichment boundary, the power density increases stepwise, as shown in the bottom of Fig. 12-1 for a three-zone core. The resulting thermal coupling between elements significantly reduces the incoherence across the fuel elements in rings 3 and 4, as shown at the top of Fig. 12-1. Duct melting in all duct flats begins within about 20 s in all fuel elements except those adjacent to

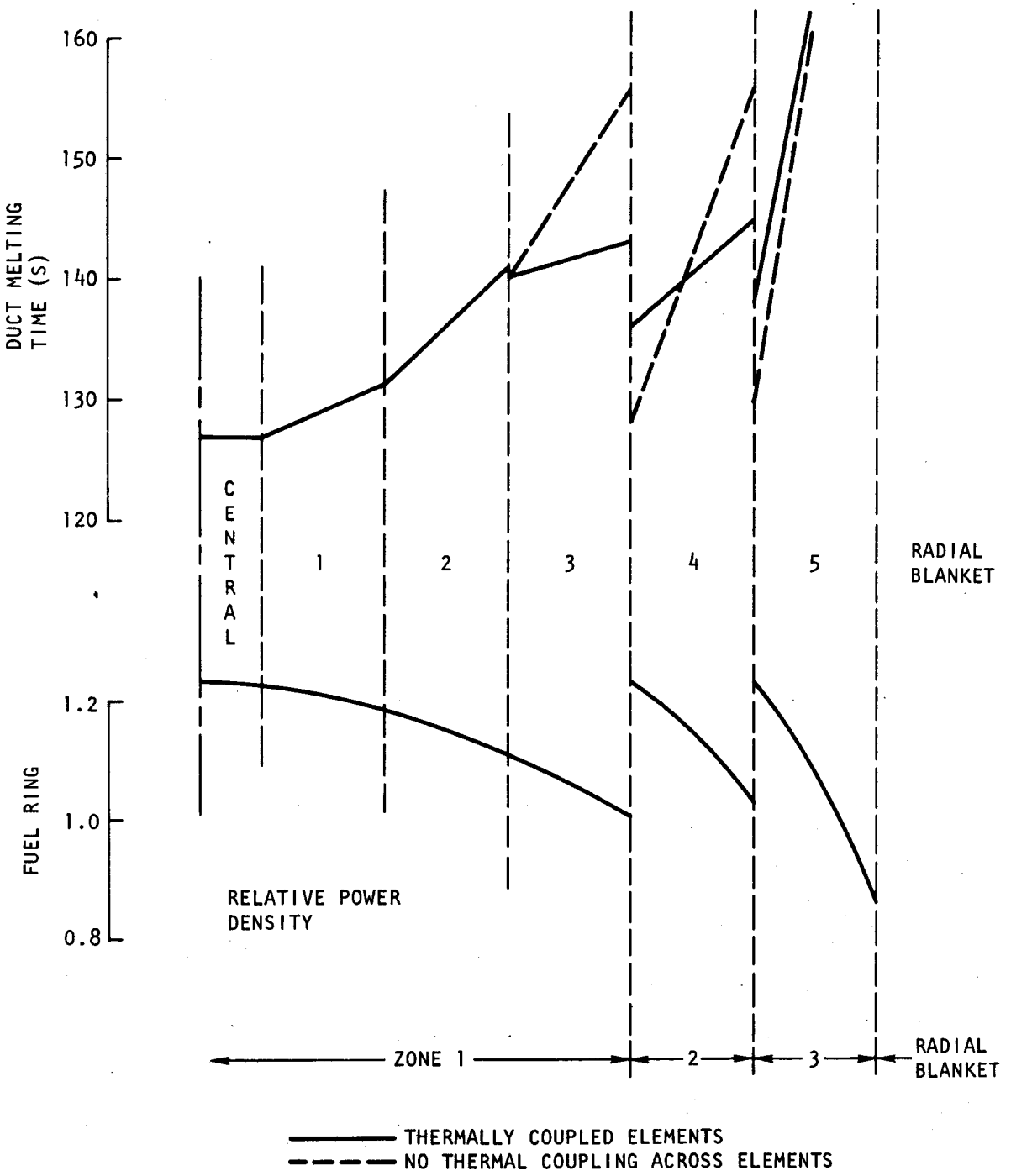


**Fig. 12-1 Radial distribution of duct midflat melting time**

the radial blanket. This incoherence would increase for an equilibrium cycle core with fuel elements of three different ages. Within an individual element in zones 1 or 2, duct melting begins in all six flats within 10 s, and the longest delay occurs in fuel ring 2. In a four-zone core, there would be an enrichment boundary between rings 2 and 3, which would further reduce this delay. Thus, the corner melting delay of about 50 s is the dominant incoherence within an individual element.

### 12.2.4. Conclusions

It is concluded that circumferential duct melting will occur prior to fuel melting in all fuel elements except possibly those adjacent to the radial blanket. In an initially withdrawn control fuel element, the control rod cladding will melt after the duct wall and the guide tube have melted circumferentially. Thus, if the individual elements are free to fall away from the core after duct melting has occurred, sufficient fuel can be removed prior to control rod or fuel melting to prevent recriticality at the core level. However, owing to the 50-s corner melting delay, a significant portion of the duct wall melts prior to dropout. If some molten steel should relocate into the gap between the fuel elements, the possibility of bridging between adjacent elements exists. Furthermore, thermal expansion during duct heat-up can bring adjacent duct walls into contact, and the resulting mechanical interference could also cause a delay in duct dropping. The definition of conditions under which melted ducts can fall out of the core is an important future element in the GCFR safety program. Primarily out-of-pile experiments supported by analyses are considered to be the most promising approach to investigate this phenomenon. These analyses define the thermal conditions which such tests must reproduce.

## 12.3. SAFETY RESEARCH AND DEVELOPMENT LIAISON

On March 9, 1976, the semiannual GCFR Safety Program Review Meeting was held at ANL with the participation of ERDA, ANL, Nuclear Regulatory Commission (NRC), Aerojet Nuclear Corporation (ANC), ORNL, LASL, Brookhaven

National Laboratory (BNL), Northwestern University, and Rand Corporation. Technical presentations were made by ANL and GA.

On March 10 and 11, 1976, the GCFR Safety Program Review Committee (GSPRC) met at ANL. Two major committee recommendations were made:

1. To pursue experimental verification of duct melting and dropping during an LOF with scram with high priority; out-of-pile tests are preferred for this purpose.

2. For unprotected accidents, to focus the primary experimental emphasis on tests in a transient facility rather than in a steady-state facility.

REFERENCES


12-1 "Reactor Safety Study - An Assessment of Accident Risks in U.S. Commercial Nuclear Power Plants," NRC Report WASH-1400 (NUREG-75/014), October 1975.

12-2 "Anticipated Transients Without Scram for Water-Cooled Power Reactors," USAEC Report WASH-1270, September 1973.

12-3 Becar, N. J., et al., "Reliability Analysis of an HTGR Scram System Including Human Interfaces," Kaman Sciences Report KSC-1037-1, March 1975.

12-4 "Clinch River Breeder Reactor Project Preliminary Safety Analysis Report," v. 9, Project Management Corporation (NRC Docket 50-537), Appendix C.

12-5 "Gas-Cooled Fast Breeder Reactor Quarterly Progress Report for the Period November 1, 1975 Through January 31, 1976," ERDA Report GA-A13815, General Atomic, March 22, 1976.

# 13. IN-PILE SAFETY TEST PROGRAM GRIST (189a No. SU015)

## 13.1. INTRODUCTION

The gas reactor in-pile safety test (GRIST) program is being evaluated by ERDA, ANL, ANC, and GA as a potential follow-on to analytical and experimental programs being conducted under the LMFBR and GCFR programs. Important data for the design basis of the GCFR demonstration plant will be provided by in-pile endurance testing of the 12-rod GCFR test assemblies in the BR-2 in Mol, Belgium, and out-of-pile testing with the CFTL, described in Section 4. The GRIST program has the objective of going beyond the design basis accidents, in particular, investigating the behavior of melted cladding and fuel. However, testing of GCFR-type fuel assemblies in the GRIST program may include less severe transients of core power, coolant flow, and coolant pressure in order to investigate the effects of upset, emergency, and faulted conditions on the performance of GCFR fuel assemblies. These tests would provide information that is projected to be of importance for improving the performance of commercial GCFR plants.

Studies were initiated in FY-74 and included (1) a comprehensive review of potential program objectives, (2) design trade-off studies, (3) schedule and cost estimates for the in-pile loop facility to be installed in the ETR at Idaho National Engineering Laboratory (INEL), (4) a conceptual design study for a reference test bundle, and (5) a scoping study for test space requirements of duct wall melting tests.

During this quarter, efforts were devoted to a conceptual design study of multisection test assemblies to be used for duct wall melting tests. The test assemblies being considered would be designed to prototypically simulate transient temperature behavior of the duct wall during severe temperature transients involving duct wall melting.

## 13.2. CONCEPTUAL TEST DESIGN STUDIES FOR DUCT WALL MELTING TESTS

Duct wall melting tests have been considered to experimentally verify and demonstrate that during severe operational accidents (loss of flow, loss of coolant) involving melting of cladding, flow ducts, and fuel, the GCFR fuel assembly will drop out of the core prior to gross fuel melting. Previous analyses and conceptual design considerations indicated that duct wall melting tests with multisection test assemblies could only demonstrate and verify certain aspects of the dropping hypothesis. Phenomena that may be separately tested are, for example, the melt-through rate and melting progression of (1) the flat sections of the flow ducts and (2) the corner sections behind the unfueled spacer support rods. The results of these tests may be employed to check calculational methods and analytical approaches to the dropping phenomenon.

A conceptual design effort was initiated on double-section test assemblies. Two design concepts evolved which are currently being analyzed to determine their advantages and disadvantages. Since the test objectives have not yet been fully defined, it is anticipated that both concepts will be carried along until the basis for a decision has been provided. During the design evolution of double-section test assemblies, triple-section test assemblies were considered to ensure that the design features can be applied to the more complicated structure of a triple-section assembly. The advantages of a common design concept are seen in common fabrication and handling criteria. Detailed design features will be reported during the next quarter.

## 13.3. FABRICATION COST AND SCHEDULE ESTIMATES FOR 37-ROD AND 61-ROD SINGLE-SECTION TEST ASSEMBLIES

A detailed estimate of the fabrication cost and schedules has been prepared for the conceptual design of 37-rod and 61-rod single-section test assemblies, which have been described in previous quarterly reports.

Because of many uncertainties in the GRIST program, and especially because of the lack of an accepted program plan, the cost estimates have been prepared as a sensitivity study to provide cost ranges rather than single cost data. The cost estimates were prepared in cooperation with potential vendors. The fuel rods were costed by HEDL, the costs of the flow ducts were estimated by Carpenter Technology (Santee, California), and spacer costs were provided by Mertoc Tool Engineering.

The estimated cost per bundle is summarized in Tables 13-1 and 13-2. The parameters used to present the cost estimates are bundle size, enrichment zone, lot size, and type of flow duct. The ranges obtained indicate that 61-rod assemblies may cost about $315 K and 37-rod assemblies about $225 K.

The cost data that lead to the cost estimates are currently being used to prepare cost estimates for multisection test assemblies which are in the conceptual design stage. The schedule estimates are presented in Fig. 13-1. The lead time for one, five, and ten bundles per lot is estimated at 1-1/2, 2-1/4, and 3-1/2 yr, respectively.

TABLE 13-1
COST PER BUNDLE AS A FUNCTION OF LOT SIZE, NUMBER OF ENRICHMENT ZONES, AND RODS PER BUNDLE

| Lot Size | Type of Duct | Cost per Bundle ($) | | | | | |
|---|---|---|---|---|---|---|---|
| | | 37-Rod Bundle | | 61-Rod Bundle | | Dummy Bundle | |
| | | 3-Zone Enrichment | 5-Zone Enrichment | 3-Zone Enrichment | 5-Zone Enrichment | 37-Rod | 61-Rod |
| 1 | Weld drawn | 362,294 | 380,700 | | | 187,780 | |
| | Seamless | 407,796 | 436,202 | | | 233,282 | |
| 5 | Weld drawn | 224,897 | 244,511 | 306,771 | 335,320 | 92,768 | 128,971 |
| | Seamless | 236,320 | 254,934 | 314,194 | 346,743 | 104,191 | 140,394 |
| 10 | Weld drawn | 198,452 | 216,210 | 277,023 | 304,123 | 76,014 | 89,200 |
| | Seamless | 210,234 | 227,992 | 288,805 | 315,905 | 87,796 | 100,982 |

TABLE 13-2
COST PER LOT AS A FUNCTION OF LOT SIZE, NUMBER OF ENRICHMENT ZONES, AND RODS PER BUNDLE

| Lot Size | Type of Duct | Cost per Lot ($) | | | | | |
|---|---|---|---|---|---|---|---|
| | | 37-Rod Bundle | | 61-Rod Bundle | | Dummy Bundle | |
| | | 3-Zone Enrichment | 5-Zone Enrichment | 3-Zone Enrichment | 5-Zone Enrichment | 37-Rod | 61-Rod |
| 1 | Weld drawn | 362,294 | 391,700 | | | 187,780 | |
| | Seamless | 407,796 | 436,202 | | | 233,282 | |
| 5 | Weld drawn | 1,124,486 | 1,287,656 | 1,533,856 | 1,676,701 | 463,840 | 644,856 |
| | Seamless | 1,181,462 | 1,274,671 | 1,590,172 | 1,733,717 | 520,956 | 701,872 |
| 10 | Weld drawn | 1,984,516 | 2,162,100 | 2,770,220 | 3,041,230 | 760,139 | 892,000 |
| | Seamless | 2,102,340 | 2,279,924 | 3,159,050 | 3,159,054 | 877,960 | 1,009,820 |

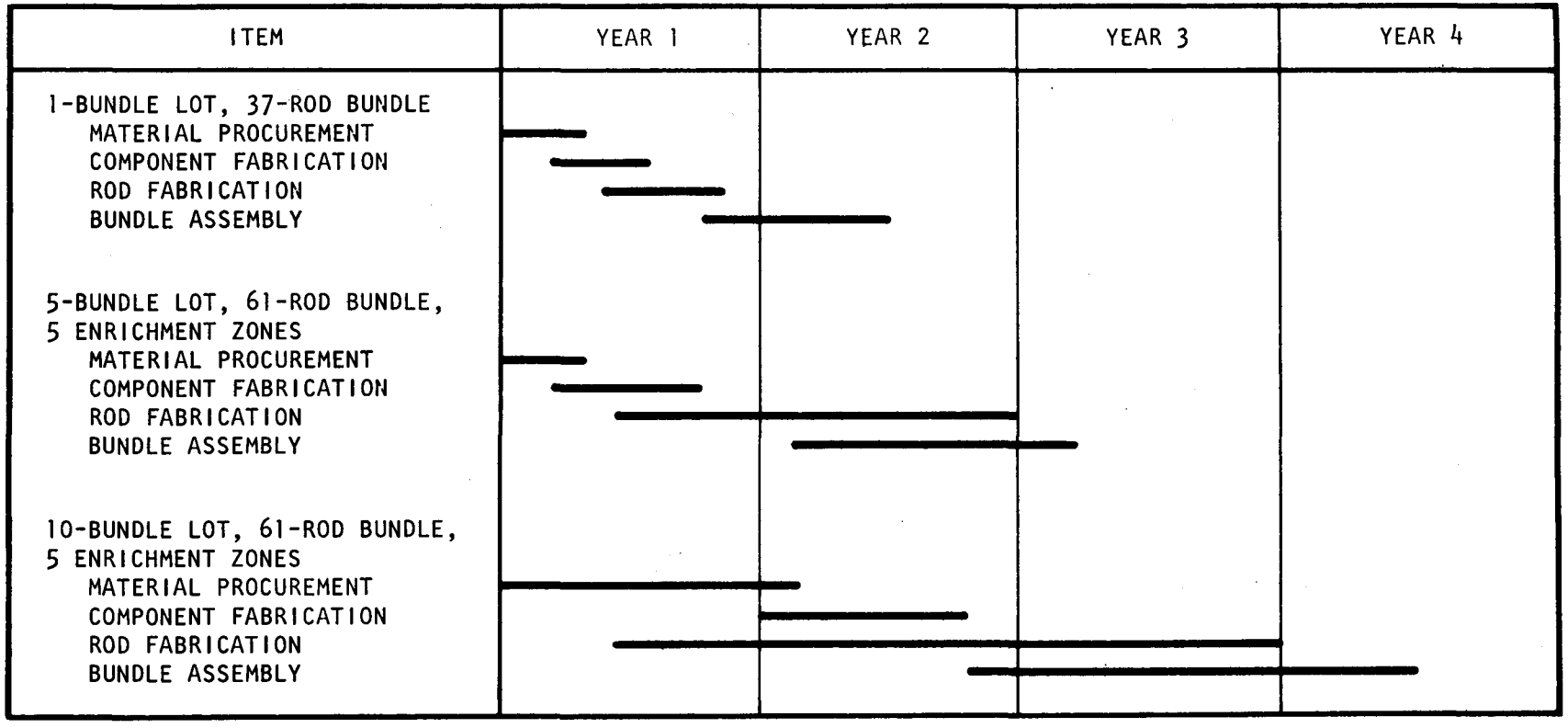


Fig. 13-1 GRIST bundle fabrication schedule